MANIPULATING NANOMAGNETS WITH SPIN-POLARIZED CURRENTS

A Dissertation

Presented to the Faculty of the Graduate School

of Cornell University

in Partial Fulfillment of the Requirements for the Degree of

Doctor of Philosophy

by

Edward Benjamin Myers

August 2002

© Edward Benjamin Myers 2002

ALL RIGHTS RESERVED

MANIPULATING NANOMAGNETS WITH SPIN-POLARIZED CURRENTS

Edward Benjamin Myers, Ph.D.

Cornell University 2002

This dissertation describes a new kind of effect that results from passing a spin-polarized current perpendicularly through a thin ferromagnetic film. Due to exchange-based spin-dependent scattering between the conduction electrons and the spin moments of the magnet, a torque can be generated on the moments. This so-called "spin-transfer" torque can, for sufficiently large ($\geq 10^6$ A/cm^2) current densities and at sufficiently small (≤ 200 nm) size scales, measurably alter the magnetization direction of a small magnetic domain.

I present data supporting this notion in two device geometries, both of which allow me to inject large spin-polarized current densities into sub-100 nm magnetic domains. At low magnetic fields, the domains can be controllably switched between two stable configurations simply by sending a current of the appropriate magnitude and sign through the magnet. If a large magnetic field is applied, the switching can be suppressed, and instead the current excites a dynamical state in the magnet.

I explore the microscopic origin of spin-transfer by showing how the torques are related to the spin-dependent scattering properties of the magnet. From calculations

of the torque within a scattering formalism, I make predictions that, depending on the kind of magnetic materials system, the torque can point in different directions and have different symmetries with respect to current direction.

I also look at the role that thermal fluctuations play in current-induced magnetic reversal. Using data on the statistics of reversal in the presence of both a current and a magnetic field, I show that spin-transfer torque operates in a qualitatively different manner than a magnetic field. This demonstrates that spin-transfer provides an independent means of studying and controlling small magnetic systems.

Biographical Sketch

Edward Benjamin Myers was born in 1975 in Milwaukee, Wisconsin. After attending a series of fine public schools, he ventured to Oberlin College in Oberlin, Ohio, where he recieved a B. A. in Physics in 1996. From there, Edward proceeded to Ithaca, New York, where the gatekeepers of the Cornell University Physics Department were kind enough to grant him entrance to their Ph.D. program. He obtained his M. S. in physics in 1999. Despite Cornell's heartbreaking triple-overtime loss to Harvard in the 2002 ECAC Championship game, Edward managed to complete his Ph.D. in the summer of that year. He will next be found (as of this writing) in a postdoctoral position at the California Institute of Technology, in the research group of Michael Roukes.

To Luc LePlae

For Your Art and Your Science

http://www.uwm.edu/~luc/

Acknowledgements

Let me start in reverse chronological order. Thank you, Spike's Bar-BQ, for a fabulous meal tonight–you truly have the best ribs available within a 50-mile radius of Ithaca.

I wish to thank my advisor, Dan Ralph, for providing me with an opportunity for learning and research that I don't think I could have found anywhere else. Dan's uncommon intellect and enthusiasm for physics has been a great source of inspiration for me, and I have only begun to appreciate the things I have learned from him about what it means to be a physicist. It is a sincere honor to be among the first to come out of his research group.

I must also thank Piet Brouwer and Bob Buhrman. It seems an astounding coincidence that a student, working in a particular field, could manage to have on their committee the three most expert physicists in the world in that same field, yet somehow I have been so fortunate. Thank you, Piet and Bob, for your deep insights and support.

Part of the great physics environment in Dan's group has come from the enormously talented students he has attracted. Thank you, Jason, Abhay, and Alex Champagne; I can only hope to once again work with people of such great ability and spirit. I wish the best of luck to Kirill, Jacob, and Jack, although you likely

will not need it. An *in absentia* thank you to Edgar Bonet as well. As for Mandar Deshmukh, he and I joined the group at the same time, in the summer of 1997, and were both witness to all that has come since then. For that I feel a special kinship with him. Thank you, Mandar, for your wisdom and your energy, your boundless generosity and your plain common sense. I wish you the best of luck at Harvard.

A hearty thank you goes out to Alex Corwin, for being a kindred spirit and, well, frankly, a genius (even though you may not realize it). Keep that guest room free for when I come to visit you in Alberquerque. I also must thank Sergey, Frank, Eric Smith, Erik, Lisa, Basudev, Donna, Lori, Marshall, and Chad. You all helped to define the texture of life in Ithaca for me both in and out of lab, which on the whole was quite a good thing. A particular thanks to Lisa and Erik, who introduced me to the wild, weird, wonderful Kim. I cannot thank you enough, Kim, for your love and support in my last year of graduate school.

Returning to my tradition of working backwards, I want to thank Cayce. Your unfailing wisdom, support, and humor made the low points here (and there were a few) bearable. I also thank Sophie Guéron. You are a great friend and mentor, and are dear to my heart. Let me know if you ever need a corny American joke to tell Juliette. There's this one about a pickle who walks into a bar...

Finally, I thank James, Barbara, Martha, Christian, and Mom and Dad, for helping me become who I am today. Sorry, folks, the damage has been done.

Table of Contents

1 Current-Induced Excitations in Ferromagnetic Nanostructures: Some Background **1**
1.1 Ferromagnetism and Spin-Polarized Electron Transport 1
1.2 Spin-Transfer: The Flip Side of GMR 10
1.3 Spin-Transfer With Two Magnetic Layers 13
1.4 Spin-Transfer and Magnetic Instabilities 16

Bibliography **21**

2 Current-Induced Excitations in Magnetic Trilayers Using the Nanoconstriction Geometry **24**
2.1 Fabrication Overview 25
2.1.1 Forming the Nanoconstriction Mold 25
2.1.2 Creating the Magnetic Trilayer 26
2.2 Experimental Set-up 31
2.2.1 Advantages of the Nanoconstriction Technique 31
2.3 Magnetoresistance of Trilayers 35
2.4 Low Field Current-Induced Excitations: Hysteresis 42
2.4.1 Comparing Hysteresis Data to Spin-Transfer Models 49
2.4.2 Temperature Dependence of Hysteresis 58
2.4.3 Suppression of Hysteresis 63
2.5 Excitations for Thick Layers and High Fields: Dynamical Excitations 67
2.5.1 Field Dependence of Dynamical Excitations 77
2.6 Other Current-Induced Features 81
2.7 Final Thoughts 87

Bibliography **88**

3 Deriving Spin-Transfer Torques from the Spin-Dependent Scattering Properties of Magnetic Layers **91**
3.1 Spin and the Landauer-Büttiker Scattering Formalism 92
3.2 Warmup Case: Single Magnetic Layer as Nonideal Spin Filter 98
3.3 Adding a Second Magnetic Layer 109

3.4 Ensemble Averaging: Ballistic and Diffusive Scattering 114
3.4.1 Ballistic Limit 114
3.4.2 Diffusive Limit: A Pedagogical Approach 115
3.4.3 Averaging in the Diffusive Limit 116
3.4.4 Spin-Transfer and Phase Coherence 119
3.4.5 Results for Diffusive Scattering 121
3.5 Applying Band Structure Calculations to the Scattering Formalism . 125
3.5.1 Torque Predictions in Diffusive Limit 130
3.5.2 Aside: Experimental Evidence for Opposite Torques? 134
3.5.3 More Realistic Torques in the Ballistic Limit 135
3.6 Final Thoughts 137

Bibliography **139**

4 Current-Induced Excitations in Magnetic Trilayers using Nanostructured Pillars **142**
4.1 Fabrication of Nanopillars and Measurement Set-Up 143
4.1.1 Nanopillar Fabrication 143
4.1.2 Measurement Set-Up 150
4.2 Nanopillars vs. Nanoconstrictions 152
4.2.1 Current-Induced Reversal of Nanopillar Magnets 152
4.2.2 Dynamical Excitations at Higher Fields 154
4.3 My Nanopillar Devices 156
4.3.1 Magnetoresistance 156
4.3.2 Current-Induced Switching 160
4.3.3 Anomalously-Small Devices 168

Bibliography **182**

5 The Role of Temperature in Excitations Induced by a Spin-Polarized Current **184**
5.1 Current-Induced Switching: a Thermally Activated Process? 185
5.1.1 Model of Thermal Activation 189
5.1.2 Statistical Switching Distributions: The Kurkijärvi Approach . 192
5.1.3 Current-Switching Data and Kurkijärvi Equations 195
5.1.4 Limitations on Statistical Measurements 198
5.1.5 Statistics and Barrier Height: Nonuniform Reversal? 202
5.2 Current-Induced Reversal Models and Thermal Fluctuations 204
5.2.1 Reversal Using Both a Current and a Field 207
5.2.2 Zero-Temperature Stability Boundaries 213
5.2.3 Field and Current in Opposition: Telegraph-Noise 218
5.2.4 Current-Induced Reversal as Both a Torque and a Field? . . . 225
5.3 Intuitive Picture of Spin-Transfer at Finite Temperature 227
5.3.1 The Langevin and Fokker-Planck Equations 228
5.3.2 Uniaxial Case 230

5.3.3 Uniaxial Plus Easy-Plane Case 233
5.3.4 Nonuniform Reversal 235
5.4 Final Thoughts 236

Bibliography **238**

6 Concluding Remarks and Future Directions **240**

Bibliography **244**

A Fabrication of Nanoconstrictions **245**

B Fabrication of Nanopillars **257**

Bibliography **274**

List of Tables

3.1 Calculated transmission probabilities for N/F materials interfaces . . 130

5.1 Summary of main devices used in thermal-activation study 237

B.1 Mill rates for various materials used in nanopillar process 263

List of Figures

1.1 Schematic of Stoner picture of itinerant ferromagnetism 4
1.2 Johnson-Silsbee experiment 5
1.3 Two-channel series resistor model 8
1.4 Schematic of spin-transfer effect 12
1.5 Spin-transfer effect with two ferromagnetic layers 15
1.6 Semiclassical depiction of torques 19

2.1 Schematic of a nanoconstriction 28
2.2 Typical nanoconstriction device 30
2.3 Block diagram of measurement apparatus 32
2.4 Differential resistance vs. applied magnetic field for two nanoconstriction devices 37
2.5 Depiction of thin magnetic layer with roughness 43
2.6 Differential resistance vs. applied current for a nanoconstriction device 45
2.7 Self-field effect vs. spin-transfer effect 50
2.8 Spin-transfer effect at two different temperatures 60
2.9 Spin-transfer effect at a range of temperatures 61
2.10 Spin-transfer effect for a thicker nanoconstriction device 65
2.11 Schematic of domain evolution as the thin layer is made thicker in a nanoconstriction device 66
2.12 Critical switching currents vs. applied field for a nanopillar device . . 68
2.13 Spin-transfer effect at large magnetic field 69
2.14 High-field features for several of magnetic fields 71
2.15 DC resistance vs. current for several large magnetic fields 73
2.16 Field dependence of high-field spin-transfer features 79
2.17 Differential resistance vs. current for a nanopillar device, showing features beyond hysteretic region 83
2.18 Multiple high-field features 86

3.1 Schematic of Landauer-Büttiker scattering formalism 95
3.2 Scattering of an incident spin-polarized electron by a single magnetic layer, for the case of general spin-filtering 99
3.3 Scattering from a magnetic layer in the clean ballistic limit 106
3.4 Scattering formalism applied to the trilayer system 111

3.5 Torque per current vs. angle for highly-polarized layers: diffusive limit 126
3.6 Torque per current vs. angle for magnetic layers of varying polarizations: diffusive limit . . . 127
3.7 Torque in diffusive limit vs. Slonczewski's formalism . . . 128
3.8 Calculated transmission coefficients vs. incident momentum for a Cu/Co interface . . . 131
3.9 Spin-transfer torque for Co/Cu/Co and Fe/Cr/Fe trilayer systems: diffusive limit . . . 133

4.1 Schematic of nanopillar fabrication . . . 146
4.2 Atomic force microscope image of an array of nanopillars . . . 147
4.3 Scanning electron microscope image of an array of nanopillars . . . 148
4.4 Optical image of a finished pillar device . . . 149
4.5 Two methods in which a magnetic field is applied to nanopillar devices in a 2-dimensional plane . . . 151
4.6 Central nanopillar results previous to this work . . . 155
4.7 Magnetoresistance loop for a nanopillar device . . . 157
4.8 Schematic of spin moment motion in the presence of in-plane and easy-plane anisotropy fields in a nanopillar device . . . 163
4.9 Current-induced hysteresis loop for a nanopillar device . . . 169
4.10 Magnetoresistance loops of a nanopillar device for two different magnetic field directions . . . 171
4.11 Schematic of Stoner-Wohlfarth model . . . 174
4.12 Magnetoresistance vs. magnetic field direction: experiment and theory 175
4.13 Coercive field vs. angle for a nanopillar device . . . 180

5.1 Distribution of switching current . . . 187
5.2 Waiting-time measurements . . . 188
5.3 Thermally-activated reversal process . . . 191
5.4 Kurkijärvi model of switching distributions . . . 194
5.5 Statistical distributions vs. temperature and sweep rate . . . 196
5.6 DC resistance vs. current at two different temperatures for a nanopillar device . . . 200
5.7 Structure in potential energy function of magnetic configuration of a nanomagnet . . . 201
5.8 Mean switching currents vs. magnetic field . . . 210
5.9 Standard deviations of switching currents vs. magnetic field . . . 211
5.10 Statistics of switching fields as a function of current . . . 215
5.11 Extrapolation of room-temperature switching data to the zero-temperature stability boundaries . . . 219
5.12 Predictions of torque and effective field models . . . 220
5.13 Telegraph noise . . . 223
5.14 Switching times of telegraph-noise data vs. field and current . . . 224

A.1 Schematic of first steps of nanoconstriction fabrication process . . . 247

A.2 Photolithography pattern 248
A.3 Schematic of later steps in nanconstriction fabrication process 252

B.1 Schematic of initial steps of nanopillar fabrication process 259
B.2 Layout of electron-beam lithography pattern 260
B.3 Images of photolithography masks 265
B.4 Schematic of later steps of nanopillar fabrication process 270

Chapter 1

Current-Induced Excitations in Ferromagnetic Nanostructures: Some Background

1.1 Ferromagnetism and Spin-Polarized Electron Transport

Electron transport in materials involving ferromagnetic metals is an interesting subject for condensed-matter physicists, because it explores the close connection between material properties traditionally associated with the charge of the electron, (currents), and those associated with the electron spin (ferromagnetism). The role that ferromagnetic ordering plays in transport can most easily be seen by considering the band structures of these materials. The modern understanding of ferromagnetism in transition metal elements such as Co, Ni and Fe tells us that the net magnetic moment in these materials arises from their partially-filled $3d$ orbitals. For

a single atom, this results in a net number of unpaired spins, due to a combination of the Pauli Exclusion Principle and Coulomb repulsion (Hund's rules). In the bulk, these influences still exist, but are now spread out over the entire material due to the overlap of electron wavefunctions on adjacent atoms. The Stoner picture of ferromagnetism [1] models this physics by a spin-split energy band (Fig. 1.1), in which a Hund's Rule-type exchange coupling lowers the energy of one spin relative to the other. As each spin band is in equilibrium filled up to the Fermi energy, this results in a greater number of electrons with one spin direction than the other, and thus a net spin moment for the material. At the same time, this exchange splitting creates an asymmetry in the densities of states at the Fermi level. Since it is the electrons at the Fermi level that determine the transport properties of a metal, we can immediately surmise that there is a spin-imbalance in the conduction electrons of the ferromagnet; in other words, the current within a ferromagnet is spin-polarized.

To be sure, the Stoner picture of ferromagnetism does not make a proper distinction between the *d*-orbital electrons and those from the *sp* orbitals, which are less localized and thus less influenced by exchange interactions. A true quantitative picture of ferromagnetic metals must consider the full band structure of the material [2]. However, the Stoner picture does capture the important notion that the spin polarization of the current is a Fermi-surface manifestation of the magnetism of the electronic system as a whole, so that the two properties are closely intertwined. Yet we can clearly separate out the two properties, simply by driving a current through the magnet via metallic leads. In this situation, the Fermi-surface electrons will freely enter or leave the magnet, while the bulk of electrons that make up the net spin moment will remain within. If this spin-polarized current enters a metal with no intrinsic exchange coupling, such as a paramagnet, it becomes an interesting

question to see how the spin-polarization survives.

The first theoretical investigation of current across the interface between a ferromagnet and a paramagnet was undertaken by Aronov [3], who, by solving the diffusion equation across the interface, found that a spin-polarized current can indeed be injected into a paramagnet. However, since the density of states of the paramagnet is equal for each spin, this nonequilibrium polarization manifests itself as a spin-split Fermi energy in the paramagnet that survives over a length scale equal to the spin-diffusion length, $L_s = \sqrt{D\tau_s}$, where D is the paramagnet's diffusion constant and τ_s is the spin relaxation time. We can thus think of the polarization as a consequence of an effective spin-dependent interface resistance, caused by the different levels of scattering for each spin to satisfy the diffusion equation [4]. This spin-dependent scattering will equivalently cause a buildup of spins in the paramagnet if a current of opposite sign is applied.

The existence of a spin-polarized current was confirmed experimentally in 1985, in the work of Johnson and Silsbee [5]. Here an interface was formed between a thin patterned Permalloy ($= Py = Fe_{81}Ni_{19}$) film (called the injector electrode) and a thick Aluminium block (Fig. 1.2a). A voltage was applied across this interface, driving a spin-polarized current into the aluminium. The polarization was then detected by using a second patterned Py film (the detector electrode), placed on the aluminium less than a spin-diffusion's length away from the injector electrode. When a current was driven across the injector interface, an open-circuit voltage developed across the detector interface, whose sign depended on the polarization direction of the current relative to the magnetization direction of the electrode (Fig. 1.2b). The origin of the voltage was explained as a consequence of the excess spins in the Al modifying the relative chemical potential of the detector electrode [6].

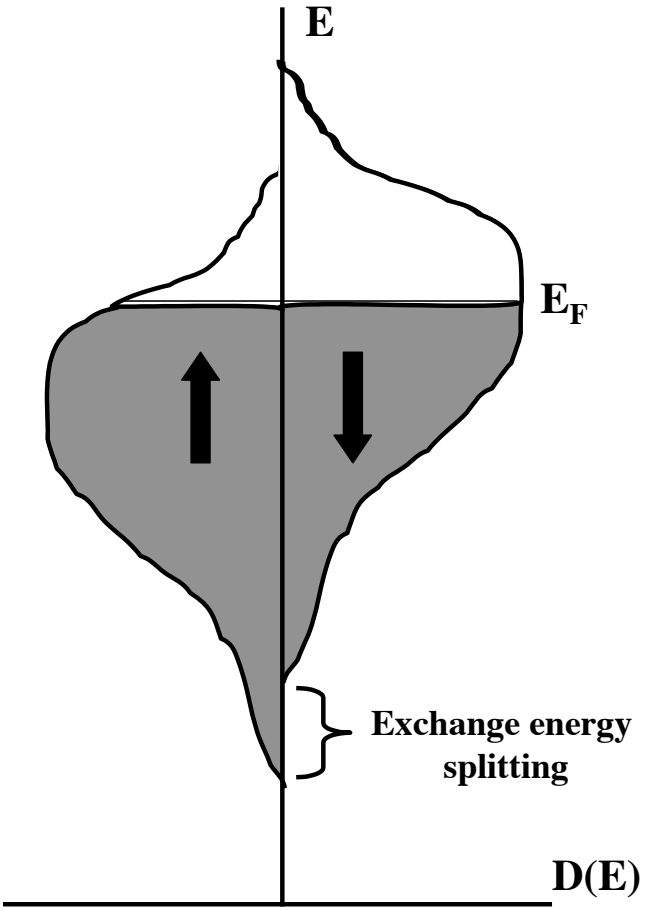


Figure 1.1: Schematic of Stoner picture of itinerant ferromagnetism. An electron band is shown here as density of states $D(E)$ on the horizontal axis and energy E on the vertical axis. A Hund's Rule-type exchange coupling lowers the energy of one spin relative to the other. As both spin bands are filled up to the same Fermi energy E_F, both a net spin moment and a spin asymmetry in the density of states at E_F is created.

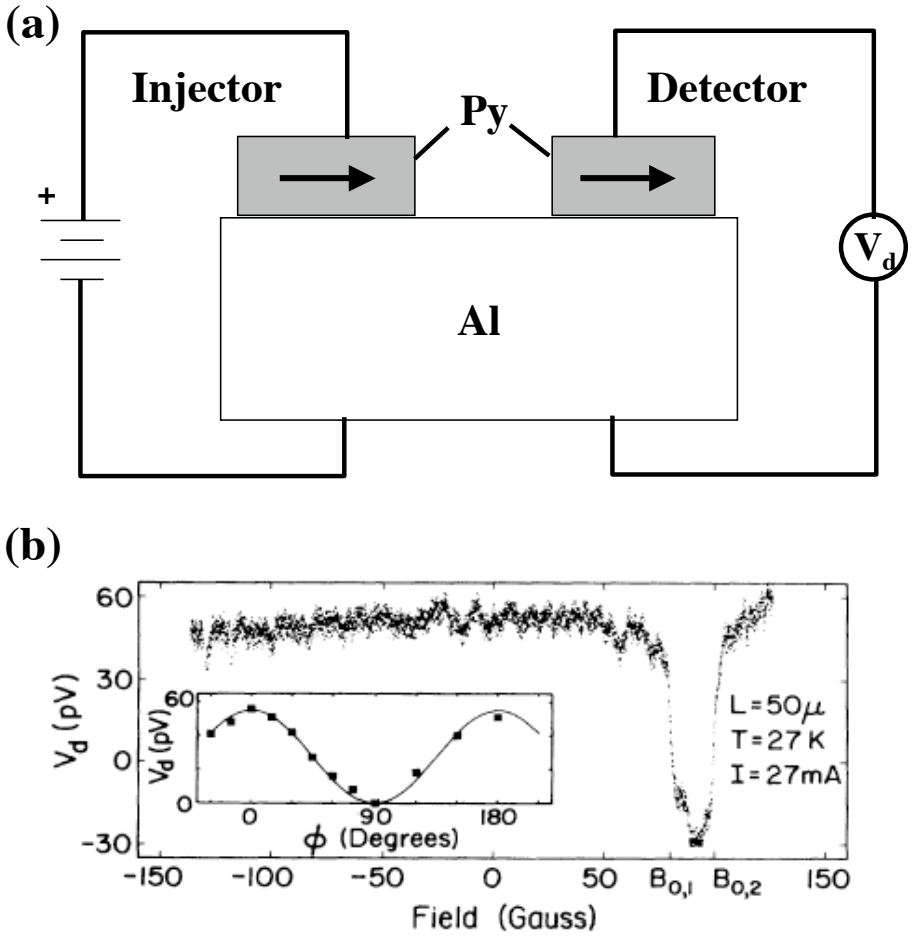


Figure 1.2: The initial experiment of Johnson and Silsbee [5]. (a) Schematic of experimental setup. A spin-polarized current is injected into an Al block by applying a voltage across an Al-Permalloy (=Py=$Fe_{81}Ni_{19}$) interface (injector), and is detected, due to the nonequilibrium buildup of spin-polarized electrons in the Al, as a voltage across a second (detector) Al-Py interface. (b) As a magnetic field is swept, the two Py electrodes switch between parallel and antiparallel alignment, which corresponds to a switch in the sign of the detector voltage (from [5]). The inset shows that the voltage is sensitive to the angle between the Py electrode moments.

The Johnson and Silsbee experiments clearly demonstrate that charge and spin are coupled in transport through ferromagnets, and, perhaps more interestingly, that spin information about one magnet can be transmitted to and detected by a second magnet, through the nonlocal nature of currents. However, the efficiency of such information transmission is quite low in these experiments: for a injector current in the 10's of mA, the typical detector voltage signal is in the 10's of picoVolts. A far more dramatic effect of spin-polarized currents was observed in 1988, with the discovery of giant magnetoresistance (GMR) [7, 8]. The geometry here consists of an alternating sequence of ferromagnetic and nonferromagnetic (spacer) layers stacked on top of one another, so-called a multilayer; the initial experiment utilized iron and chromium, but the effect has been extended to a wide variety of materials combinations, of which the most relevant to this project is cobalt and copper. If the layer thicknesses are chosen appropriately (in the few-nm range), the spin moments in successive magnetic layers align themselves so that they are antiparallel to one another (AP configuration). It was found that, as a magnetic field is applied to reorient the moments so that they lie parallel to one another (P configuration), the overall resistance of the multilayer drops dramatically, to as little as half of its zero-field value at room temperature [9].

There are two bits of new physics involved here. The first (although the second to be elucidated) is the source of the antiferromagnetic coupling between the layers. This has been explained as an interlayer exchange interaction mediated by conduction electrons in the spacer layer, somewhat in analogy to the RKKY model of metallic spin glasses [10]. As it involves electron wave interference within the spacer layer, it is highly sensitive to the exact thickness of the layer and disappears if the layer is more than a couple nanometers thick for most materials [11, 12]. In

fact, it has been shown [13] that this interaction can be understood as the zero-current, thin-layer limit of the spin-transfer effect, which is the central focus of this dissertation.

The second important aspect of GMR is, of course, the strong dependence of the resistance on the orientation of the magnetic moments. GMR has been observed both for currents applied in the plane of the layers (so-called CIP geometry) [7] and currents applied perpendicularly to the layers (CPP geometry) [14, 15, 16]. In the interests of focusing on the experimental geometry most relevant to this dissertation, I limit discussion of the effect to just two magnetic layers in the perpendicular configuration (Fig. 1.3). Experimentally, such two-magnetic-layer systems are called spin-valves. The following explanation is called the two-channel series resistor model [17], and involves assigning to each magnetic layer the spin-dependent resistances $R_\uparrow$ and $R_\downarrow$ [18]; in this model, as long as there is no spin relaxation during the electrons' journey across the layers, spin-up and spin-down electrons travel within two separate, independent conduction channels. In the high-field configuration (Figs. 1.3a and 1.3b), where the moments are parallel to one another (P configuration), the spin-up electrons see a combined resistance $2R_\uparrow$, while the spin-down electrons see a resistance of $2R_\downarrow$. The overall resistance is thus $R_P = 2R_\uparrow || 2R_\downarrow = 2R_\uparrow R_\downarrow/(R_\uparrow + R_\downarrow)$. If the field is lowered so that the magnetic layers assume an antiparallel (AP) configuration (Figs. 1.3c and 1.3d), then the resistances for the second layer essentially become inverted; "spin-up" for the first layer becomes "spin-down" for the second, etc. Here the total resistance is $R_{AP} = \frac{1}{2}(R_\uparrow + R_\downarrow)$, which in general is higher than R_P.

The series two-channel resistor model of GMR captures the qualitative features of the effect, but it has the unfortunate property of being, at best, misleading, and at

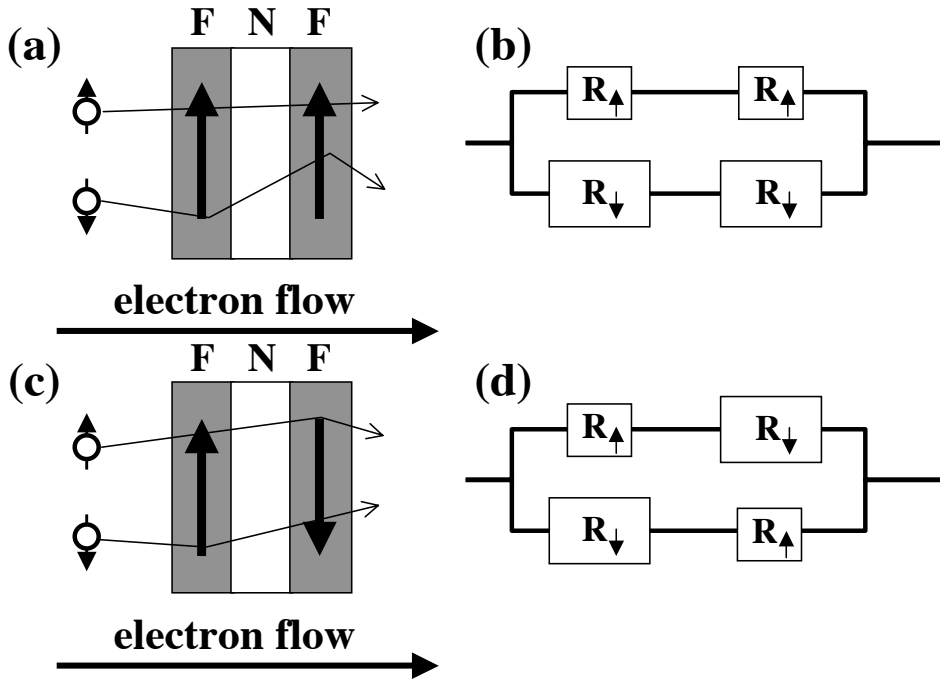


Figure 1.3: Two-channel series resistor model of the giant magnetoresistance effect, in a ferromagnetic/nonmagnetic/ferromagnetic (F/N/F) trilayer (adapted from [16]). (a) When the magnetic moments in adjacent F layers are parallel (P configuration), the equivalent resistor circuit (b) gives $R_P = 2R_\uparrow R_\downarrow/(R_{uparrow} + R_\downarrow)$, while in the antiparallel (AP) configuration (c), the resistor model (d) gives $R_{AP} = (R_\uparrow + R_\downarrow)/2 \geq R_P$.

worst, wrong. One issue this model conceals rather than illuminates is how best to think about the spin-dependent scattering at the heart of the effect. While the layer thicknesses (a few nm) are well below the spin-diffusion length, they are also below the typical mean free paths in these materials ($\sim$ 20 nm in Cu at room temperature). As a result, it is likely not appropriate (especially in the CPP geometry) to treat each magnetic layer as an independent diffusive resistor, generating simple spin-dependent chemical potential drops across the magnetic layers as in the Johnson-Silsbee experiments. Instead, it is safer to take a more microscopic viewpoint, in which individual electrons are tracked as they scatter around the multilayer. In the limit that the layers are defect-free and the interfaces between layers perfectly smooth, electron transport within the layers is ballistic. In a purely ballistic theory, spin-polarization is generated by the coherent scattering off of potential steps at the layer interfaces generated by mismatch between the electron bands of the two materials [19]. Real multilayers are certainly full of defects and rough interfaces, however, and actual electron transport in these magerials involves a combination of coherent scattering, diffuse interface scattering, and scattering from bulk impurities and defects; the relative importance of each effect is still a matter of debate [20, 21, 22]. I will not dare to resolve that debate here, but instead mention it to emphasize that a truer understanding of giant magnetoresistance comes from a focus on the types of scattering in electron transport. Taking this more microscopic approach yields possibilities not covered by the two-channel series resistor model, such as: nonlocality, in which electrons scattered by one layer return to previous layers, changing their effective resistance [23]; and mixing between the two spin channels [24, 25]. As we will soon see, we will need to treat these possibilities seriously to understand the the spin-transfer effect.

1.2 Spin-Transfer: The Flip Side of GMR

While our understanding of GMR through the resistor model is in many respects oversimplified, it at least suggests an interesting line of thought to pursue. The size of the GMR signal shows that the coupling between the spin-polarized conduction electrons and the spin moments of the magnetic layers can be made to be quite strong. As the Stoner picture makes clear, however, this current-moment coupling is more fundamentally an electron-electron coupling, so we might expect some symmetry in the interaction. We may then ask the question: If these conduction electrons can be so strongly scattered by the moment electrons, can, under some circumstances, the moments themselves be scattered by the current?

This question was first explored theoretically in the 1970's, in papers by Zaitsev [26], and, more extensively, by Berger [27], who found that a spin-polarized current can exert an effective torque on the moments of domain walls in thin ferromagnetic films via the exchange interaction, moving the walls around. More recent papers by Berger [28] and Slonczewski [29] have shown that torques are also generated on the moments of magnetic multilayers in the CPP geometry. To understand how a torque comes about from spin-dependent scattering, we adopt the analysis of Berger and Slonczewski and consider how a single electron interacts with a magnetic layer. Consider the thought experiment of Figure 1.4. An electron is traveling along the x-direction (as, say, a plane wave), and is incident upon a magnetic layer lying in the y-z plane, whose spin moment lies along the z-axis. As we know, the electron will be scattered differently depending on its spin. For simplicity, we will take the clean ballistic limit, and will assume that the layer is a perfect spin filter, meaning that all currents that emerge from it are completely spin-polarized [30]. Thus if the incident electron is spin-up ($S_z = +1/2$) then it will pass through the layer with no

scattering (Fig. 1.4a), while if it is spin-down ($S_z = -1/2$), no current will flow and the electron will be reflected (Fig. 1.4b).

An arbitrary electron, however, need not be polarized along the z-axis; a general spinor state can point anywhere along the unit sphere. Let us consider, then, an electron spinor state of the form $\begin{bmatrix} \cos(\theta/2) \\ \sin(\theta/2) \end{bmatrix}$, which describes an electron polarized in the x-z plane at an angle θ to the z-axis (Fig. 1.4c). When this electron hits the layer, the spin-dependent scattering properties of the layer demand that a quantum-mechanical separation of the electron occur, with the spin up component, $\begin{bmatrix} \cos(\theta/2) \\ 0 \end{bmatrix}$ propogating through the layer, and the spin-down component, $\begin{bmatrix} 0 \\ \sin(\theta/2) \end{bmatrix}$ reflected off the layer. The large number of degrees of freedom in the magnetic system, however, strongly suggest that this coherent separation cannot last for long after the scattering, and so the electron wavefunction is quickly collapsed into either a transmitted spin-up electron with probability $\cos^2(\theta/2)$, or a reflected spin-down electron with probability $\sin^2(\theta/2)$ before it leaves the magnet. By inspection, however, we note an interesting consequence of the scattering; the scattered electron is either completely spin-up or spin-down, while the incident electron wavefunction is neither. To be more precise, if we compare the angular momentum S carried by the incident electron with the average angular momentum carried away by the electron, we find

$$\vec{S}_{incident} = \frac{\hbar}{2}\left(\sin\theta\hat{x} + \cos\theta\hat{y}\right), \tag{1.1}$$

$$\left\langle \vec{S}_{transmitted} \right\rangle + \left\langle \vec{S}_{reflected} \right\rangle = \frac{\hbar}{2}\left(\cos^2(\theta/2)\hat{y} - \sin^2(\theta/2)\hat{y}\right) = \frac{\hbar}{2}\left(\cos\theta\hat{y}\right). \tag{1.2}$$

Thus the condition of perfect spin-filtering (combined with charge conservation, of course) demands that the component of the electron's angular momentum trans-

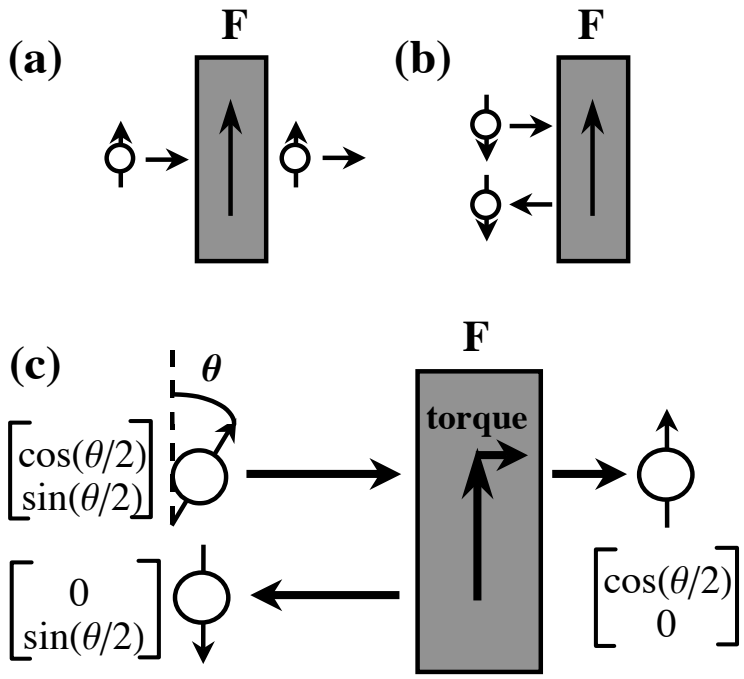


Figure 1.4: Schematic of spin-transfer effect. An electron is incident upon a magnetic layer which operates as a perfect spin-filter, so that spins aligned with the moment of the layer (spin-up) are transmitted completely (a), while spins aligned oppositely to the moment (spin-down) are completely reflected (b). If an electron that is a superposition of up and down spins is incident on the layer (c), the coherent spin-dependent scattering of the electron removes its component of angular momentum transverse to the layer moment, which is thus taken up by the moment itself. For a steady current of electrons I, this transfer of angular momentum can be thought of as an effective torque proportional to I and to $\sin(\theta)$.

verse to the spin moment axis of the magnetic layer be removed, with an average momentum change of $\Delta S_x = -\frac{\hbar}{2}\sin\theta$.

This in and of itself is not noteworthy; the change in spin-polarization of a current as it passes between magnetic and nonmagnetic metals necessarily implies a change in the spin ngular momentum. However, the type of scattering considered above involves only the coupling between the current and the magnetic moment (as in [19]), and not interactions like spin-orbit coupling, which can channel spin momentum to the lattice [31]. In our thought experiment, then, any spin momentum lost by the electron must be taken up by the magnetic moment alone. For individual electrons, the total angular momentum transferred to the moment will vary depending on whether it is transmitted or reflected. If however a steady current I is sent through the layer, the probabilities of scattering can be treated as a true average, and the rate of angular momentum transfer to the moment is $dS/dt = \frac{I}{e}\Delta S = \frac{I}{e}\frac{\hbar}{2}\sin\theta$, which has the units and symmetry of a torque that favors a parallel alignment of the layer moment with the incident current polarization [32]. This process of transfering spin angular momentum from the current to the moment is known as spin transfer, and the torque generated is called spin-transfer torque. This is the central phenomenon studied in this dissertation.

1.3 Spin-Transfer With Two Magnetic Layers

To perform the above kind of thought experiment in reality, one of course needs a source of the spin-polarized electrons that are sent to the magnetic layer. Although experiments have indeed been performed injecting an external beam of spin-polarized electrons generated by a photocathode into a magnetic layer [33], it is simpler, and closer in analogy to the magnetic multilayer experiments, to use a sec-

ond ferromagnetic layer as a source. When a second layer is added, however, an interesting asymmetry of spin-transfer torque arises with respect to the direction that electrons are sent through the layers, due to multiple scattering events between the layers. Consider the magnetic trilayer device of Figure 1.5, where two magnetic layers, which we will continue to treat as perfect spin-filters, are separated by a nonmagnetic spacer [28, 29]. The ferromagnetic layer thicknesses, t_{F1} and t_{F2}, are chosen so that $t_{F1} >> t_{F2}$, while the normal metal spacer layer thickness t_N is kept thinner than the spin-diffusion length. When a current is run through the layers, spin-transfer torques will be generated within both layers; however, since the total spin moment of layer $F1$ is much larger than that in layer $F2$, the fractional effect of any torque generated in $F1$ is comparatively much smaller. We may thus take layer $F1$ to be essentially fixed, and consider only the torques that are exerted on layer $F2$. We consider the case that the moments in layer $F2$ are aligned in the $+z$ direction, while the $F1$ moments lie at an angle θ to the $z-$axis in the $z-x$ plane. First consider a left-going current, which is a right-going electron flow (this will be known as negative current in our experimental sign convention) (Fig. 1.5a). Electrons emerge from $F1$ polarized along its moment direction, and scatter off of $F2$. This is precisely the situation of the single-layer scattering of Fig. 1.4, so we conclude that the torque (in the $-x$ direction) favors parallel alignment of $F2$ with the spin polarization, and thus parallel alignment with $F1$. I should note that the magnitude of the torque here is different than that in the single-layer case, as there are further scatterings of the electron between the magnetic layers; however, the fundamental symmetry of the torque is unchanged. I take a more quantitative look at spin-transfer torque in the trilayer system in Chapter 3.

Now let us consider what happens when the sign of current is reversed (made

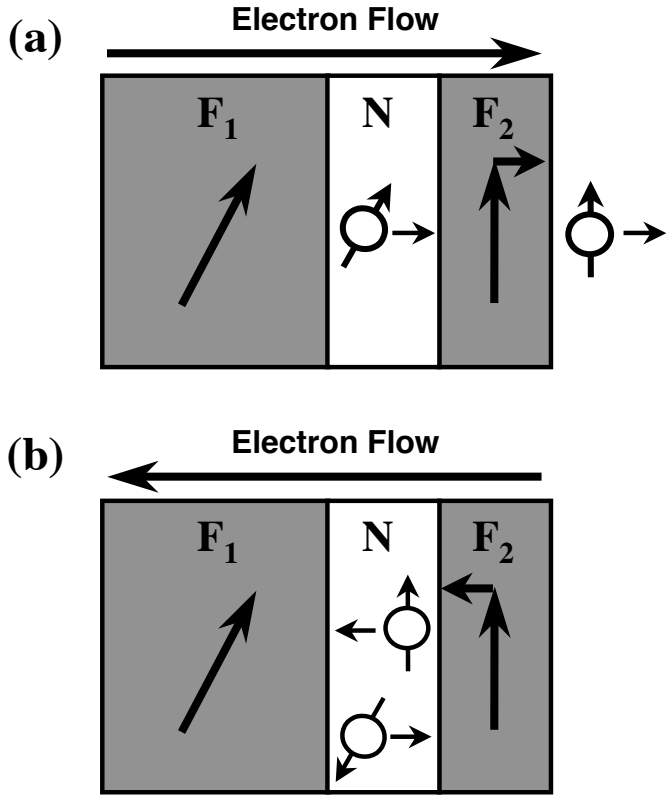


Figure 1.5: Spin-transfer effect with two ferromagnetic layers, one thick (F_1) and one thin (F_2), with a normal metal spacer layer (N). If current flow is from F_1 to F_2 (a), the electrons polarized by F_1 exert a torque on F_2 which favors a parallel alignment of the layers. If the current is reversed (b), electrons that are initially polarized by F_2 get partially reflected by F_1 and return to F_2. Since these are reflected electrons, their spin-polarization is opposite to the transmitted electrons in (a) and thus the torque they exert is opposite. For this current direction, then, an antiparallel alignment of the layer moments is favored by the torque.

positive). In this case, the electrons are first polarized by layer $F2$ (Fig. 1.5b). This initial act of polarization generates no net torque on $F2$ in this model. We can see this by noting that the torque generated by two oppositely-polarized electrons (to represent an unpolarized current) in the single-layer case of Fig. 1.4, added incoherently, is zero. However, once the current is polarized, it subsequently scatters off of layer $F1$, and some of the current is reflected *back* to $F2$. In the perfect spin-filter limit, this portion of the current is polarized exactly oppositely to the moment of $F1$ (since it is reflected), so that it subsequently generates a torque on $F1$ that is opposite (in the $+x$ direction) to the earlier (negative current) case, and thus encourages the moments of layer $F2$ to align *antiparallel* with layer $F1$. The overall effect of using a second, fixed, magnetic layer as a polarizer is thus to generate a torque in the original magnetic layer whose magnitude and sign are governed by, respectively, the magnitude and sign of the current passing perpendicularly through it. Following Slonczewski [29, 44], the symmetry of this torque can be expressed in coordinate-free form as

$$\text{torque} \propto \frac{I}{e}\vec{S}_{F1} \times \left(\vec{S}_{F2} \times \vec{S}_{F1}\right), \tag{1.3}$$

where $\vec{S}_{F1,2}$ are the spin moments for layers $F1$ and $F2$.

1.4 Spin-Transfer and Magnetic Instabilities

The above picture, first established by Slonczewski and Berger, suggests that spin-transfer torques, if large enough, can alter the magnetization state of a thin magnetic film. But exactly how much is "large enough"? To answer that question, spin-transfer torques have to be placed in the context of all the other influences on the spin moments of magnetic layers, which on the whole will oppose spin-transfer-

induced deviations from magnetic equilibrium. The most straightforward way to accomplish this is to incorporate spin-transfer into the Landau-Lifschitz-Gilbert (LLG) equation[34, 35], a 3-component differential equation that describes magnetic dynamics semiclassically. In words, the LLG equation simply expresses Newton's Second Law in angular form: the rate of change of angular momentum of layer $F2$'s spin moment, $d\vec{S}_{F2}/dt$, must be equal to the sum of all the torques on it. Typically the equation takes the form

$$\frac{d\vec{S}_{F2}}{dt} = \gamma \vec{S}_{F2} \times \vec{H}_{eff} - \alpha \hat{s}_{F2} \times \frac{d\vec{S}_{F2}}{dt}, \tag{1.4}$$

where $\gamma = -\frac{g\mu_B}{\hbar}$ is the gyromagnetic ratio. Figure 1.6 depicts this equation graphically. The first term is the net torque exerted on the moment by conservative influences, which are incorporated into a total effective field H_{eff}. By conservative influences I mean any effect that can be expressed in terms of a potential energy U which can be written as $U = \gamma \vec{S}_M \cdot \vec{H}_{eff}$. An external magnetic field most clearly falls under this category, but other magnetic influences such as magnetic anisotropy or exchange can be written in terms of an effective field (which may depend on $\vec{S}_M$) [36]. The torque in this first term thus drives the moment to precess along an equipotential orbit, so that the moment neither gains nor loses energy during its motion. The second term on the RHS of Fig. 1.4 is a phenomenological term that describes the dissipative processes that drive the moment towards its stable energy minimum direction, which is aligned with $\vec{H}_{eff}$. There are a variety of processes which contribute to the decay of a magnetic excitation, including eddy currents generated by the time-varying moment, magnon-magnon couplings, and magnon-phonon couplings via the spin-orbit interaction [37, 38]. The overall strength of these dissipative processes is parametrized by the dimensionless constant α, called the Gilbert damping parameter, which can be thought of as the inverse of the quality factor of the

magnetic oscillations sustained by the precession torque term. Typically $\alpha << 1$, so to a good approximation equation (1.4) can be rewritten

$$\frac{d\vec{S}_{F2}}{dt} = \gamma \vec{S}_{F2} \times \vec{H}_{eff} - \gamma\alpha\hat{s}_{F2} \times \left(\vec{S}_{F2} \times \vec{H}_{eff}\right). \tag{1.5}$$

The damping torque thus acts perpendicularly to the precession torque and tends to damp out any magnetic excitations.

If we now include spin-transfer torque in the LLG equation, it becomes

$$\frac{d\vec{S}_{F2}}{dt} = \gamma \vec{S}_{F2} \times \vec{H}_{eff} - \left[\gamma\alpha\hat{s}_{F2} \times \left(\vec{S}_{F2} \times \vec{H}_{eff}\right) + \frac{cI}{e}\vec{S}_{F2} \times \left(\hat{s}_{F1} \times \vec{S}_{F2}\right)\right], \tag{1.6}$$

where c is a proportionality constant (that may depend on the spin moment direction) and $\hat{s}_{F1}$ is a unit vector in the direction of $\vec{S}_{F1}$. In situations of high symmetry (such as if both magnetic layers have aligned anisotropy axes), $\hat{s}_{F1} || \vec{H}_{eff}$, in which case the damping term and the spin-transfer term lie along the same axis. The threshold for magnetic excitations is thus set by the damping. Depending on the sign of the current, spin-transfer will either pump energy into or draw energy out of the magnet by changing its angular momentum. If the current has the right sign and is large enough, the amount of energy pumped into the system will overcome the dissipative processes and a magnetic excitation will occur.

In parallel to the work reported in this dissertation, there have been reports of current-induced magnetic switching in manganite nanoparticles [39] and nickel nanowires [40], as well as switching [41] and spin-wave excitations [41, 42] in magnetic multilayers. However, the torque model as I have presented it in this chapter is not the only accepted approach to interpreting these observations. Indeed, theorists have taken various approaches to describe how spin-transfer torques translate into magnetic excitations [28, 43, 44, 45, 46]; within each approach the type of excitation depends on the geometry, material properties, and external parameters set by the

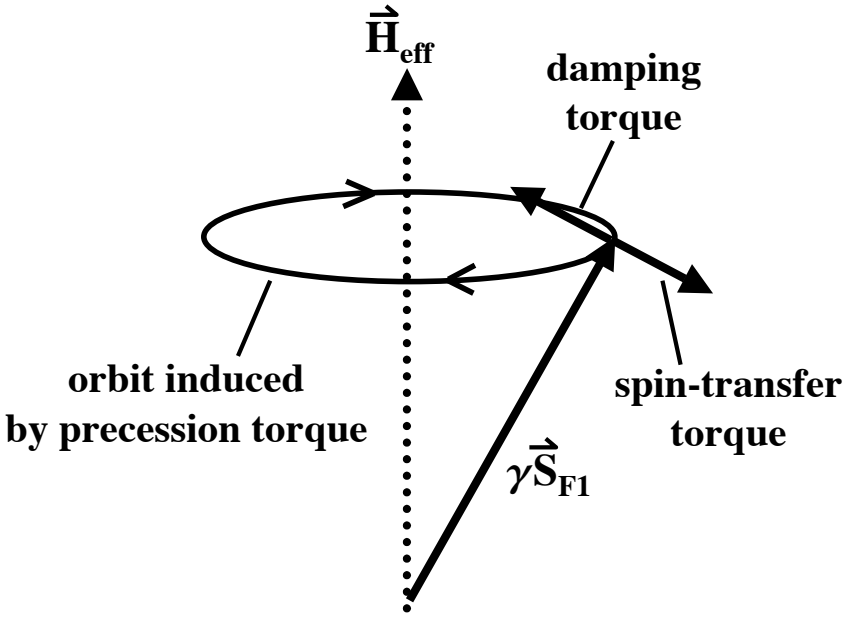


Figure 1.6: Semiclassical depiction of torques exerted on the spin moment of a magnetic layer. Conservative torques such as magnetic field, anisotropy, and exchange cause the moment to precess around an effective field H_{eff}. Dissipative couplings of the moment to the environment are expressed as a damping torque, which causes the moment to rotate towards its energy minimum. The symmetry of spin-transfer causes it to point along the damping torque axis. If the current has the right sign, it can generate a torque which will overcome the damping and cause a magnetic excitation.

experimentalist. This is to say nothing of more recent models [47, 48, 49, 50] that consider an additional interaction between the current and magnetic moments which operates as an effective magnetic field, with a qualitatively different symmetry than spin-transfer torque. This dissertation does its best to use the data within to address these differences; in particular, a considerable part of Chapter 5 will consider the torque model vs. effective field models. Primarily, however, Slonczewski's torque model will be used to interpret the data, for the simple reason that, apparently, it works the best.

It suffices to conclude this chapter by noting that all models of spin-current-induced magnetic excitations, regardless of their origins, are bound by this fact: in order to change the magnetization in some particular way (such as magnetic reversal), a finite, known amount of angular momentum must be imparted to the magnet, an amount which scales with the cross-sectional area of the magnet. The models thus all speak of an intrinsic critical current density that is required to generate an excitation; taken in the aggregate, the models predict values for this current density in the range of $10^6 - 10^9 A/cm^2$. This corresponds to a 1 mA current being confined to a cross-sectional width of 10-300 nm. In the following chapter I will describe one method used to inject currents at these densities into a magnetic trilayer, and will compare the results to the predictions for spin-transfer torques.

Bibliography

[1] E. Stoner, Proc. R. Soc. A **165**, 372 (1938).

[2] D. A. Papaconstantopoulos, Handbook of the Band Structure of Elemental Solids, Plenum, NY (1986).

[3] A. G. Aronov, JETP Lett. **24**, 32 (1976).

[4] P. C. van Son, H. van Kempen, and P. Wyder, Phys. Rev. Lett. **58**, 2271 (1987).

[5] Mark Johnson and R. H. Silsbee, Phys. Rev. Lett **55**, 1790 (1985).

[6] Mark Johnson and R. H. Silsbee, Phys. Rev. B **37**, 5312 (1988); Phys. Rev. B. **37**, 5326 (1988).

[7] M. N. Baibich *et al.*, Phys. Rev. Lett. **61**, 2472 (1988).

[8] G. Binasch *et al.*, Phys. Rev. B **39**, 4828 (1989).

[9] S. S. P. Parkin, Z. G. Li, and D. J. Smith, App. Phys. Lett. **58**, 2710 (1991).

[10] P. Bruno, Phys. Rev. B **52**, 411 (1995).

[11] S. S. P. Parkin, N. More, and K. P. Roche, Phys. Rev. Lett. **64** 2304 (1990).

[12] S. S. P. Parkin, Phys. Rev. Lett. **67**, 3598 (1991).

[13] J. C. Slonczewski, J. Magn. Magn. Mater. **126**, 374 (1993).

[14] W. P. Pratt *et al.*, Phys. Rev. Lett. **66**, 3060 (1991)

[15] J. Bass and W. P. Pratt, J. Magn. Magn. Mater. **200**, 274 (1999).

[16] Martin A. M. Gijs and Gerrit E. W. Bauer, Adv. Phys **46**, 285 (1997).

[17] T. Valet and A. Fert, Phys. Rev. B. **48**, 7099 (1993).

[18] N. C. Mott, Adv. Phys **13**, 325 (1964).

[19] Kees M. Schep, Paul J. Kelly, and Gerrit E. W. Bauer, Phys. Rev. Lett. **74**, 586 (1995); Phys. Rev. B. **57**, 8907 (1998).

[20] S. S. P. Parkin, Phys. Rev. Lett. **71**, 1641 (1993).

[21] Shashi K. Upadhyay, Richard N. Louie, and R. A. Buhrman, App. Phys. Lett. **74**, 3881 (1999).

[22] C. Vouille *et al.*, Phys. Rev. B. **60**, 6710 (1999).

[23] Didier Bozec *et al.*, Phys. Rev. Lett. **85**, 1314 (2000).

[24] A. Brataas, Yu. V. Nazarov, G. E. W. Bauer, Phys. Rev. Lett. **84**, 2481 (2000).

[25] D. H. Hernando *et al.*, Phys. Rev. B **62**, 5700 (2000).

[26] A. N. Zaitsev, Fiz. Tverd. Tela **18**, 129 (1976) (Sov. Phys. Solid State **18**, 72 (1976)).

[27] L. Berger, J. App. Phys. **49**, 2156 (1978); J. App. Phys. **55**, 1954 (1984); Phys. Rev. B. **33**, 1572 (1986).

[28] L. Berger, Phys. Rev. B **54**, 9353 (1996).

[29] J. C. Slonczewski, J. Magn. Magn. Mater. **159**, L1 (1996).

[30] In chapter 3 we will consider theoretically systems with non-ideal spin filters and diffuse scattering, and find that spin-transfer torques can still be generated on magnetic layers.

[31] Albert Fert, Jean-Luc Duvail, and Thierry Valet, Phys. Rev. B **52**, 6513 (1995).

[32] Note that the $\sin\theta$ symmetry of this torque makes it invisible in the two-channel series resistor model, which at all times treats electrons as only spin-up ($\theta = 0$) or spin-down ($\theta = \pi$).

[33] W. Weber, S. Riesen, and H. C. Siegmann, Science **291**, 1015 (2001).

[34] L. D. Landau and E. M. Lifshitz, Physik. Z. Sowjetunion **8**, 153 (1935).

[35] T. L. Gilbert, Phys. Rev. **100**, 1243 (1995).

[36] T. H. O'Dell, Ferromagnetodynamics, Wiley, New York (1981).

[37] H. B. Callen, Phys. Chem. Solids **4**, 256 (1957).

[38] V. Kambersky, Can. J. Phys, **48**, 2906 (1970).

[39] J. Z. Sun, J. Magn Magn. Mater. **202**, 157 (1999).

[40] J.-E. Wegrowe *et al.*, Europhys. Lett. **45**, 626 (1999).

[41] R. N. Louie, Dissertation, Cornell University, Ithaca, NY (1997).

[42] M. Tsoi *et al.*, Phys. Rev. Lett. **80**, 4281 (1998); erratum, ibid. **81**, 493 (1998).

[43] L. Berger, J. App. Phys. **89**, 5521 (2001).

[44] J. C. Slonczewski, J. Magn. Magn. Mater. **195**, L261 (1999).

[45] Ya. B. Bazaliy, B. A. Jones, and S.-C. Zhang, Phys. Rev. B. **57**, R3213 (1998).

[46] M. D. Stiles and A. Zangwill, J. App. Phys. **91**, 6812 (2002); Phys. Rev. B **66**, 014407 (2002).

[47] C. Heide *et al.*, Phys. Rev. B **63**, 064424 (2001).

[48] C. Heide, Phys. Rev. Lett. **87**, 209 (2001); Phys. Rev. B **65**, 054401 (2002).

[49] J.-E. Wegrowe, Phys. Rev. B **62**, 1067 (2000).

[50] S. Zhang, P. M. Levy, and A. Fert, Phys. Rev. Lett. **88**, 236601 (2002).

Chapter 2

Current-Induced Excitations in Magnetic Trilayers Using the Nanoconstriction Geometry

As mentioned at the end of the previous chapter, it is predicted that, if large current densities (in the range of $10^6 - 10^9 A/cm^2$) are sent perpendicularly through magnetic/nonmagnetic/magnetic trilayers, spin-dependent scattering will generate torques on the magnetic layers (spin-transfer) large enough to measureably alter the magnetization state of the layers. Fortunately for the young experimentalist, there is a point-contact geometry quite well established at Cornell that can send very large current densities through metallic trilayers in a nondestructive manner. This is the so-called "nanoconstriction" technique [1], and this chapter will focus on studies of spin-transfer using magnetic trilayer devices fabricated in this manner. We will find that, although the nanoconstriction geometry makes a full quantitative analysis difficult, the data confirm the basic predictions of the spin-transfer torque model.

2.1 Fabrication Overview

2.1.1 Forming the Nanoconstriction Mold

As its name suggests, the nanoconstriction technique involves confining the metal of a magnetic trilayer system at a particular point to nanometer size scales, thus naturally increasing the current density through this point. This is achieved by creating an insulating mold in the shape of the device (the nanoconstriction), and then filling the mold with metal. A considerable amount of work on nanoconstriction fabrication precedes my own [1, 2, 3, 4, 5] and my devices do not provide significant deviations from these previously-established recipies. In Appendix 2.A I provide a detailed description of the current nanofabrication steps, adapted from a recipe that has been the standard in the Ralph group for the past few years, for anyone who wishes to make these (quite useful) devices. Here I present a short overview of the fabrication of the nanoconstriction mold, and then a more detailed look at how the magnetic trilayer system is filled into this mold.

We begin with a double-polished $\langle 100 \rangle$ Si wafer approximately 500 μm thick, on both sides of which a thin layer of low-stress amorphous silicon nitride approximately 100 nm thick has been grown. A combination of photolithography and reactive ion etching (RIE) is then used to open a window ≈ 80 μm wide in one of the nitride layers to expose the silicon below. In practice, an array of 9×9 windows are opened in the nitride, so that a total of 81 nanoconstriction devices can be made in parallel per wafer. The nitride etch is followed by a wet etch in a heated KOH solution which preferentially etches the exposed Si along the $\langle 111 \rangle$ planes until it reaches the other nitride layer, leaving it a suspended membrane. Since the $\langle 111 \rangle$ planes sit at an angle to the $\langle 100 \rangle$ face of the Si, the suspended membrane is smaller than that

defined by the photolithography, roughly 50 μm (Figure 2.1a).

After the suspended membrane has been thinned to a controlled thickness of 50 nm, the next, crucial, step is to effectively drill a small hole through the membrane; this hole is the nanoconstriction and defines the region of highest current density in my devices. The hole is formed by performing electron beam lithography to clear an opening 20-50 nm wide in the electron beam resist. After that, a special isotropic RIE is performed which etches through the nitride in a bowl shape (Fig. 2.1b and 2.1c). If the etch is timed correctly, the opening in the membrane at the bottom of the hole will be much narrower than that defined by e-beam lithography at the top; holes with diameters less than 10 nm can be regularly achieved. The size of the hole can be characterized by direct imaging via transmission electron microscopy (TEM) (Fig 2.1c) [6]. More typically, the hole size is inferred by measuring the resistance of homogeneous metallic point contacts made from the constriction (See section 2.2.1).

2.1.2 Creating the Magnetic Trilayer

Once the hole is formed, we can fill it with our magnetic heterostructure, created by depositing metal directly onto both sides of the membrane with thermal evaporation. We start by taking a fraction of the processed wafer, typically two or three columns of the 9×9 array of constrictions, and place them in a UHV evaporation chamber with base pressure of 5×10^{-8} torr. The samples are mounted onto a special rotating stage in the chamber so that metal may be deposited on both sides of the constrictions *in situ*. This helps to ensure that few contaminants are incorporated into the metal as it is deposited around the constriction region. One particularly troublesome contaminant is water, which becomes adsorbed onto the membrane in air, and will remain even at low pressures. To drive moisture off the membrane, it is

heated to approximately 100° C at low pressure in the evaporator for 30-45 minutes prior to metal deposition. Also, when initially mounting the nanoconstrictions, it is important to ensure that no samples that may be at the edge of the wafer portion are visible to the evaporation source, or else a metallic connection may form around the edge and short out the connection through the constriction. To avoid this, a glass slide can be mounted that overlaps the edge of the sample.

Although this dissertation will describe nanoconstriction devices with a number of different configurations of the metals, the canonical set-up, and the configuration I will focus on for most of this chapter, is that depicted in Figure 2.2. First, the bowl side of the membrane (top side in Fig. 2.2) is filled with a nonmagnetic electrode, usually copper. In order to help make sure that the bowl is thoroughly filled by the metal, the device is tilted with respect to the evaporation direction by a small amount (say 10 degrees) from normal incidence for the first 25 nm of deposition. It is then tilted a similar amount in the other direction from normal incidence for the next 25 nm, and finally returned to normal incidence for the rest of the lead deposition. Equivalently, the sample can be continuously rocked back and forth during this deposition. I estimate roughly 50 nm of Cu is needed to fill the bowl (since the nitride membrane is 50 nm thick), but because I want to ensure that the bulk of the lead contributes little to the overall resistance of the device, I usually deposit 150 nm in total.

Next, the sample is flipped over, and construction of the magnetic trilayer begins. The layers are deposited in the sequence $F_2/N/F_1$, with respective thicknesses $t_{F2}/t_N/t_{F1}$. On top of this, a capping layer of 50 nm copper is deposited to prevent oxidation of layer F_1; this completes the device. I have tried to test whether contaminants that may adsorb on the interface between the first Cu lead and layer F_2

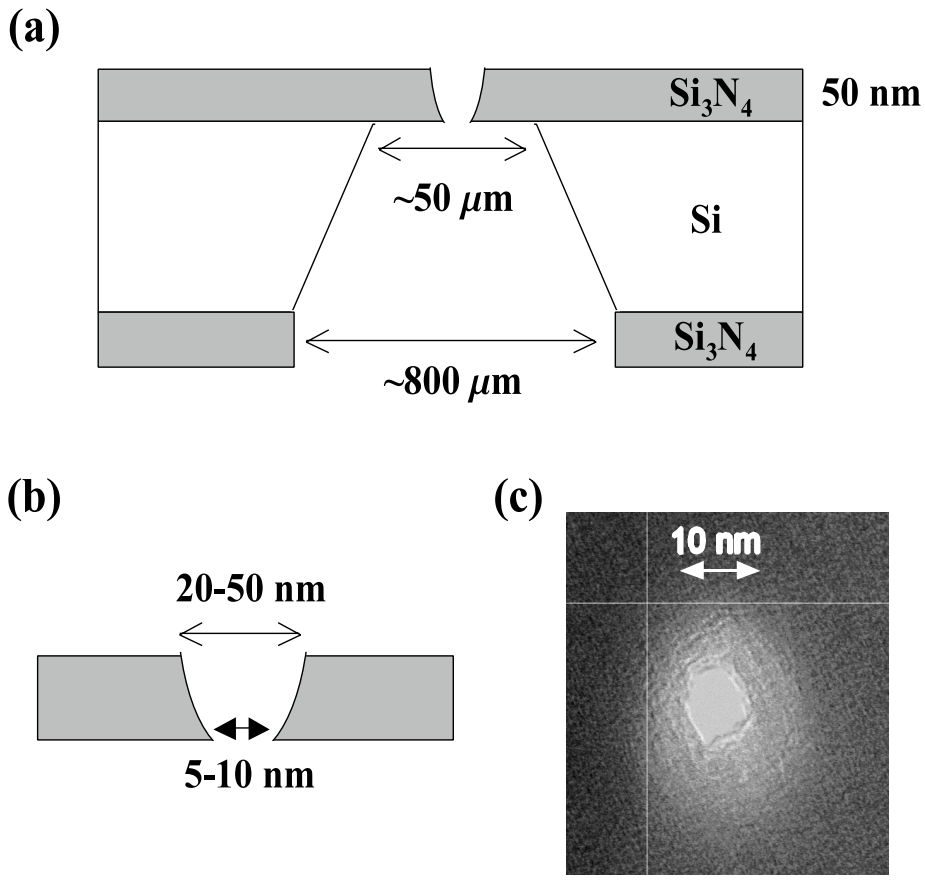


Figure 2.1: Schematic of a nanoconstriction. (a) A freely suspended silicon nitride (Si_3N_4) membrane is formed, and a combination of electron-beam lithography and an isotropic reactive ion etch form a bowl-shaped hole through the membrane. (b) The bowl shape allows the smallest part of the hole (≤ 10 nm) to be smaller than that defined by lithography (20-50 nm). (c) Scatting transmission electron microscope (STEM) image of a nanoconstriction, from [6]. Light areas indicate thinner parts of the membrane, with the center white the hole itself.

between their depositions affect the transport properties of the device by inserting a small amount (few nm) of Cu before depositing layer F_2, effectively moving this interface away from the constriction. This does not systematically alter the observed results, so in most cases I grow this interface right at the constriction, as in Fig. 2.2.

Most of my nanoconstriction devices are fabricated with $F_1, F_2 =$ Co, and $N =$ Cu; due to the relative lack of intermixing between Cu and Co [7] and their well-established use in GMR multilayers, they provide a good model system for the study of spin-transfer in a magnetic trilayer. I have also made devices employing Fe, Ni, and Py as the ferromagnetic layers, and Ag and Cr as the spacer. As this chapter is focused on the fundamental signatures of spin-transfer, I will discuss the Co/Cu/Co combination as an example system almost exclusively here. In Chapter 3, where I discuss a more microscopic theory of spin-transfer, the intrinsic electronic properties of the materials becomes a more important issue; I examine my work on different materials combinations there. In order to conform to the geometry of Slonczewski and Berger, F_1 is made much thicker than F_2; typically $t_{F1} = 100$ nm, while t_{F2} ranges from 2-10 nm. The normal layer thickness t_N is made of sufficient thickness (4-6 nm) that the quantum interference effects which give rise to interlayer exchange coupling are negligible [8]. My labeling convention is as follows: a trilayer with, for example, 4 nm of Co, 6 nm of Cu, and 100 nm of Co is called a $(Co_4/Cu_6/Co_{100})_{nm}$ device in this dissertation. I will also use the formal device name (e.g., CD05R32) in the figure captions for identification purposes.

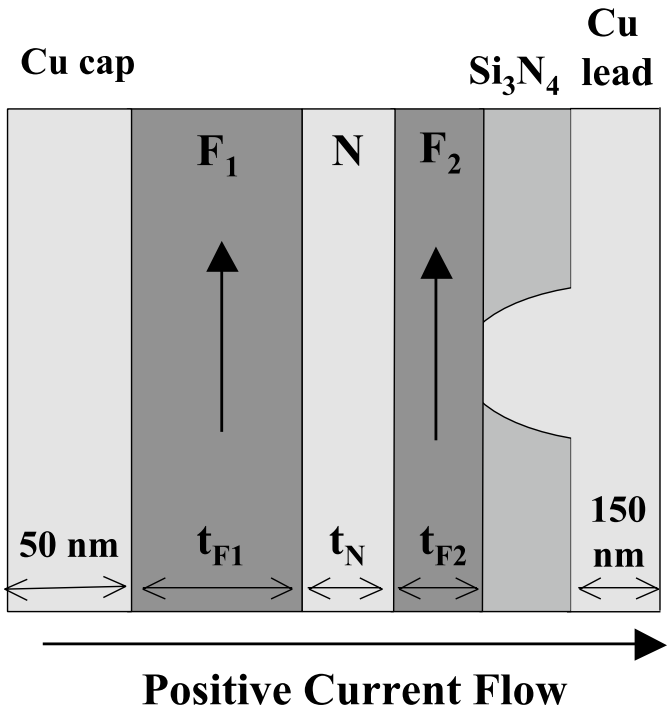


Figure 2.2: A typical nanoconstriction magnetic trilayer device. The layer thicknesses are typically chosen so that $t_{F1} >> t_{F2}$. A Cu cap on layer F_1 prevents oxidation of the magnet.

2.2 Experimental Set-up

A schematic of the circuit used to measure the transport properties of the devices is shown in Figure 2.3. As the impedence of these devices range from 10-50 Ω, it is most straightforward to send in a controlled current I, which is made up of a large DC component and a small AC component, through the device. The DC voltage V and the differential resistance dV/dI, determined from the AC signal via a lock-in amplifier, are then measured across the device. The devices are mounted on a spring-loaded contact holder which makes two connections each to top and bottom of the device, so that a four-probe measurement can be performed. This holder can be affixed either to a simple dipper for quick measurements at room temperature, nitrogen temperature (77 K) and helium temperature (4 K), or to a more sophisticated dipper made by Desert Cryogenics that includes a 3 T superconducting magnet and a heater for measurements over a large range of temperatures.

2.2.1 Advantages of the Nanoconstriction Technique

Before delving into the measurements I have made on nanoconstriction devices, it is useful to pause here and consider exactly what this point-contact geometry allows us to measure, and why. Let us first consider the issue of high current densities. A typical measurement may involve sending 2 mA through a constriction 10 nm across; this corresponds to a current density of about $2.5 \times 10^9 A/cm^2$ at the constriction. A reasonable question to ask is how such a current can be sustained without melting the device, since typical maximum current densities in larger diffusive wires are orders of magnitude smaller. The key comes in the extreme narrowness of the constriction; 10 nm is narrower than, or on the order of, typical inelastic mean

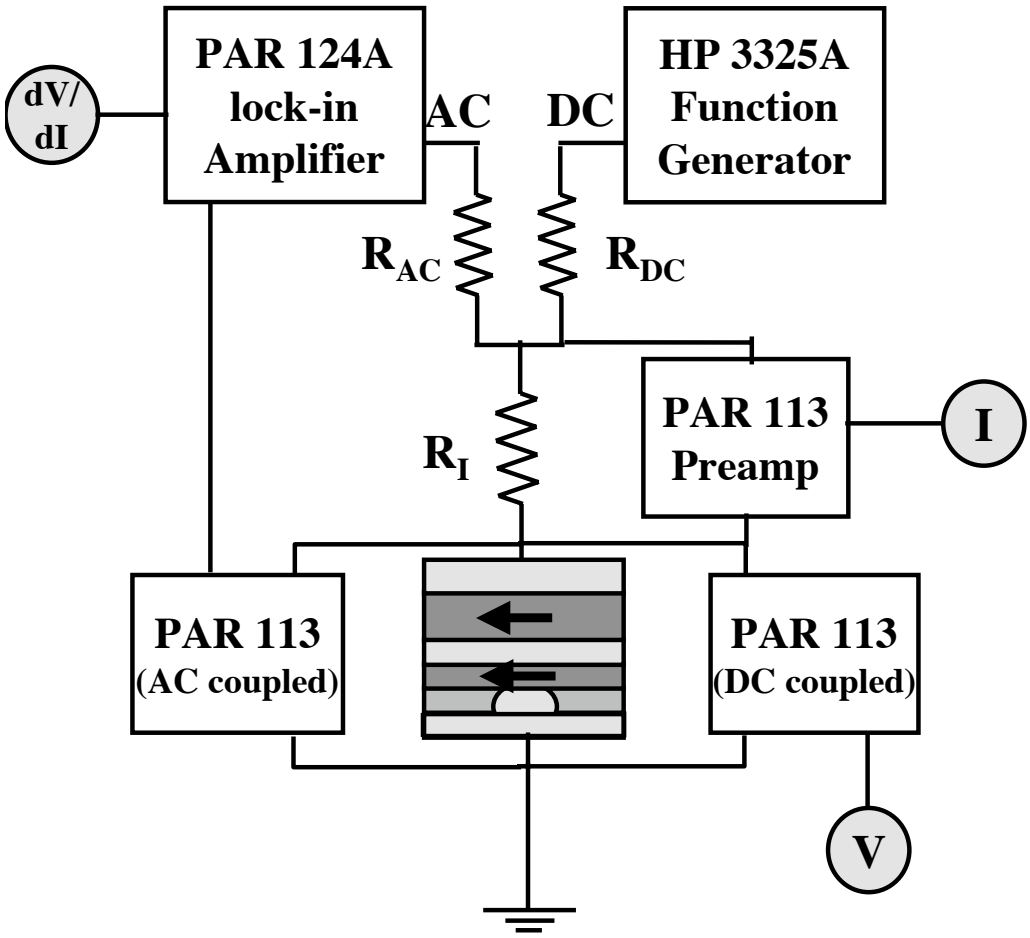


Figure 2.3: Block diagram of measurement apparatus. A DC (slow sweep) signal from a function generator and an AC lock-in reference signal are sent through the large (relative to the device) resistors R_{DC} and R_{AC} and combined as currents. The DC current I is determined from the voltage drop across a small known resistor R_I. The DC+AC current is sent through the device, and the DC voltage V and differential voltage dV/dI are measured. The gray circles represent the three quantities——I, V, and dV/dI——that are simultaneously sent to a computer system for collection.

free paths in most of the materials studied here at low temperatures. As a result, electron transport in the immediate vicinity of the constriction can, in the absence of additional sources of scattering, be thought of as ballistic or near-ballistic. For an electron to give its energy to the metallic lattice and heat the device, it must travel on average an inelastic mean free path's distance away from the constriction, where the current density is much lower. Thus the heating that we would expect at high current densities is spread out far beyond the constriction, and we can effectively generate higher current densities in the device than would be possible in purely diffusive devices.

One might think that if transport is essentially ballistic through the constriction, there should not be any measurable resistance associated with current flow there. However, the small size of the constriction provides an intrinsic resistance to current flow. An approximate expression for the resistance that applies for a large range of hole sizes is [9, 11]

$$R = \frac{h}{e^2}\frac{8}{(k_F d)^2}\left(1 + \Gamma\frac{3\pi}{16}\frac{d}{l}\right), \tag{2.1}$$

where d is the constriction diameter and l and k_F are, respectively, the mean free path and the Fermi wavenumber of the material in the constriction. Γ is a slowly-varying function of d/l that lies roughly between 0.7 and 1. The first term is the Sharvin resistance [13] that arises from the limited number of electron states (on the order of $k_F d$) that can fit through the constriction. For constrictions where l is not many times larger than d (certainly true for our devices), there is an additional resistance term coming from scattering events. Equation (2.1) can be used to self-consistently determine the diameter d of the hole, by filling the constriction with a homogeneous metal with a known k_F and l, such as Cu, and measuring the low-bias resistance [2]. This is the primary method by which I characterize the sizes of the

constrictions I create.

The dependence of the second term in Eqn. (2.1) on the mean free path l demonstrates that transport through the device is sensitive to small deviations from pure ballisticity, i.e., individual scattering events near the constriction. When a voltage is applied, a current of electrons is driven through the constriction. Due to the small size of the hole, only the electrons that are near the constriction and have the correct momentum direction can pass through at any time. If an electron that has passed through is scattered by an energy-dependent process such as the creation of a phonon or magnon, there is some probability that it will be scattered back through the hole to the original side. It will then effectively get stuck on this side, as it will take many further random scatterings on average to restore the proper position and momentum needed to get through the constriction. Thus this backscattered electron is effectively removed from the current and the resistance of the sample rises due to a single backscattering event. In this way the nanoconstriction is a sensitive probe of microscopic scattering processes, and how these processes depend on the energy of the electrons and external parameters like magnetic field. If the constriction was much larger than the mean free path, then backscattered electrons could more easily return through the constriction and the effect on the resistance would be blurred into a more general diffusive rise due to heating.

The point contact geometry, first achieved by Yanson in the early 1970's [9, 10], has long been used for spectroscopic studies of scattering processes at the nanometer scale; see [11, 12] for reviews. At Cornell nanoconstriction spectroscopy has been applied to a variety of physical phenomena, including (but not limited to) 1/f noise [14], thermoelectric effects [4], the Kondo effect [16, 17, 18], and Andreev reflection as a probe of spin-dependent scattering in ferromagnets[19, 20]. However, it is not

necessary to have good ballistic transport in the point contact to observe effects in magnetic trilayers induced by a spin-polarized current [4]. Indeed, in Chapter 3 we will find theoretically that even highly diffusive devices can exhibit spin-transfer torques, and in Chapter 4 I will discuss devices far larger than the ballistic limit in which spin-transfer signals are clear, and in fact easier to understand than in the nanoconstriction geometry. The primary signal we measure in order to track spin-transfer effects is simply that from the giant magnetoresistance effect, in which the device resistance is sensitive to the relative angle between the moments of the two magnetic layers. Since the main types of current-induced magnetic excitations I have measured involve a change in the magnetization angle of the excited magnet, the GMR effect straightforwardly connects these excitations to the resistance signal of the nanoconstriction. A number of previous GMR measurements have been performed in point-contact geometries [4, 21, 22, 23, 24].

2.3 Magnetoresistance of Trilayers

At last we have arrived at the point where we can discuss actual measurements [25]. Nearly all the measurements on Co/Cu/Co trilayers were taken at liquid helium temperature, $T = 4.2$ K. Let us first look at the magnetoresistance of these devices. Figure 2.4 shows magnetoresistance loops for two devices chosen for illustration, a $(Co_4/Cu_6/Co_{100})_{nm}$ (Fig. 2.4a) and a $(Co_4/Cu_4/Co_{100})_{nm}$ (Fig. 2.4b) trilayer, near zero current bias. Here the magnetic field field is swept in the plane of the layers. The resistance is at a minimum at a large magnetic field H, and is the same value for both signs of field. Since the device resistance is a measure of the relative alignment of the two magnetic layers via the GMR effect, this minimal resistance indicates that the two layers in each device are in parallel alignment, as expected at

high fields. As the field is reduced, the layers deviate from parallel alignment and the device resistance increases. Typically this occurs before the field reaches zero. The rise in resistance can take many forms, involving continuous transitions, abrupt jumps, or both. The resistance of the devices in this field region also is hysteretic, in that it depends on the direction in which the field is being swept. Eventually, as the field changes sign and increases in magnitude again, the resistance returns to its minimum value, as the two layers reorient themselves to the opposite field direction. The devices in Fig. 2.4 are representative of the data I have taken in the sense that there are wide sample-to-sample variations of the shape and size of the magnetoresistance loop, and that even within each device there can be quite complicated behavior. As the devices are all fabricated in a similar manner, it may at first seem troubling that there is such wide variation among devices. However, it must be remembered that, since the resistance measured in the nanoconstriction geometry is sensitive only to scattering events near the constriction, we are probing the properties of the magnetic trilayer only very locally. Typical domain structures in Co/Cu multilayers exist on size scales on the order of 100 nm [26], far larger than my constriction sizes; thus, unlike all GMR measurements on bulk devices, the micromagnetic, multidomain variations that occur in magnetic films do not average out. Consequently, we must interpret the magnetoresistance data (and, later, the current-induced resistance changes) as a measure of the relative orientations of single domains or small groups of domains between the two magnetic layers [23].

In this context, much of the magnetoresistance data, at least qualitatively, makes sense. Domains in magnetic materials are set by competitions between exchange and local anisotropy forces, which include crystalline, dipolar, and defect-driven anisotropies and are set by the microstructure of the material [27]. As a result,

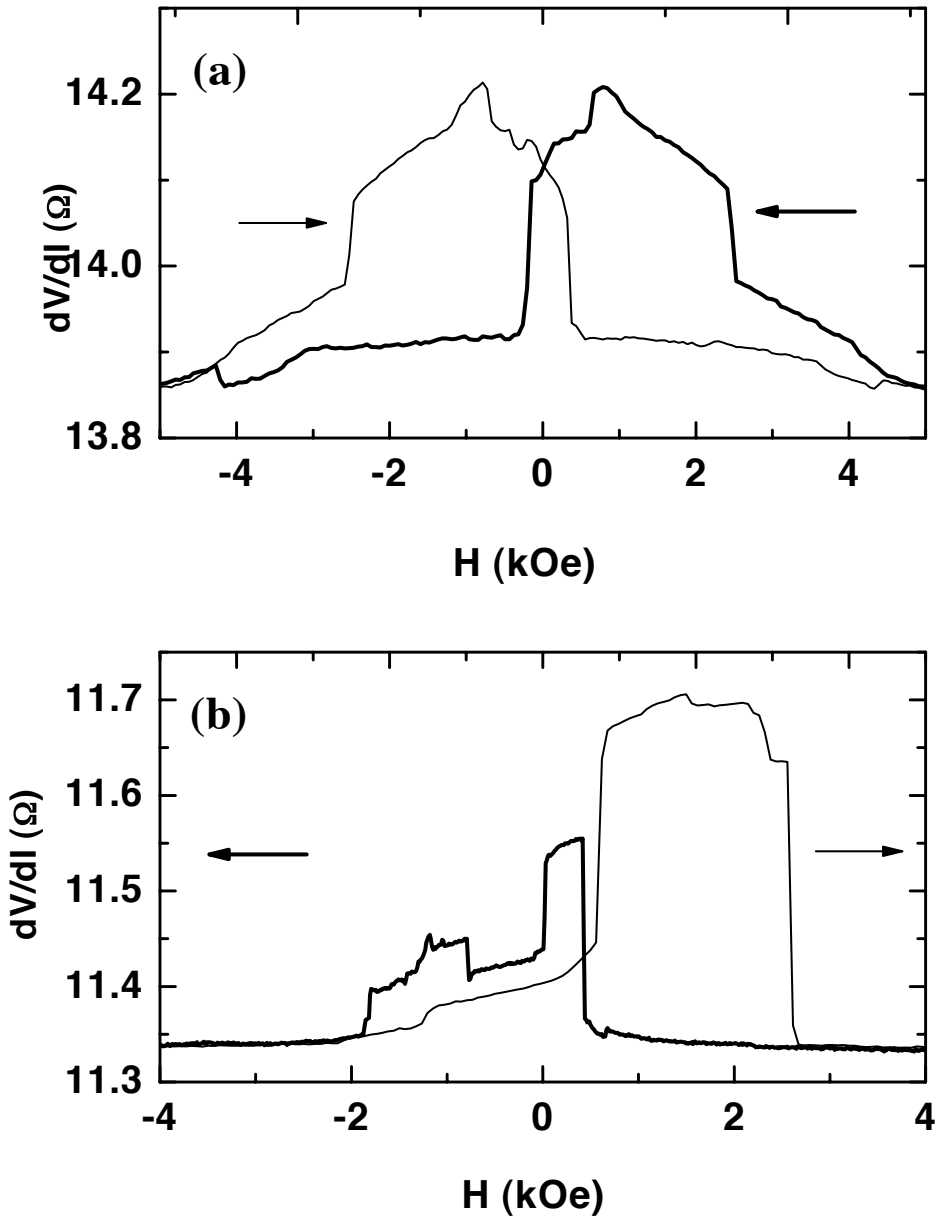


Figure 2.4: Differential resistance dV/dI vs. applied magnetic field H for two devices, (a) a $(Co_4/Cu_6/Co_{100})_{nm}$ (CD05M62) and (b) a $(Co_4/Cu_4/Co_{100})_{nm}$ (CC09R61) trilayer, at $T = 4.2$ K. The field is applied in the plane of the layers.

while a film will on average have a nonzero remanent moment at zero magnetic field, the microscopic domains will be oriented roughly randomly. As we reduce the field from large values towards zero, the domains probed by the nanoconstriction will relax to their equilibrium positions, which, assuming no intrinsic interlayer coupling, will in general have some relative angle; this explains the rise in resistance as we take H to zero. This relaxation can involve domain growth or rotation, and may be continuous or abrupt, depending on the local anisotropy fields felt by the domain. Since the two layers have different thicknessses, the domains probed by the two layers will experience different local couplings and will have different reorientation behaviors as a function of magnetic field, contributing to the structure in the magnetoresistance. Also, although the magnetization hysteresis loop for a bulk magnet is in general highly reproducible, there is no reason to expect the same for a single domain. As the exact behavior of a domain depends sensitively on what neighboring domains do, and as there are a huge number of degrees of freedom in the magnetic system as a whole, there are many ways that a domain can evolve as the field changes. Thus we do not always see the same reversal features if we change the direction of magnetic field sweep, and in some cases we observe highly asymmetric magnetoresistance loops (Fig. 2.4b).

Although we can largely explain away the complicated features we see in magnetoresistance, there are two aspects that demand closer inspection. One is the size of the magnetoresistance ratio, which I will define as

$$\mathrm{MR}(\%) = \frac{R_{max} - R_{min}}{R_{min}} \times 100, \tag{2.2}$$

where R_{max} and R_{min} are the largest and smallest resistances measured during a hysteresis loop. This differs from the typical definition of the magnetoresistance ratio, where the large field resistance is compared with the zero field resistance.

That definition is more appropriate for multilayers with strong zero-field antiferromagnetic coupling. As I use only two layers and the domains in the layers are randomly oriented at zero field, the definition above gives a better idea of the maximum magnetic contrast signal possible by manipulating the layers with a field. Typical measured magnetoresistance ratios for Co/Cu/Co trilayers are in the range of 2-5%. This is smaller than the maximum ratios measured in larger spin-valves in the current-in-plane geometry [28], which is contrary to expectations that the perpendicular-to-plane geometry should result in higher MR ratios.

The main source for the reduction in the MR ratio comes from the ballistic character of my nanoconstrictions. From Equation (2.1), we can see that when l is larger than the constriction diameter d, the majority of the nanoconstriction resistance comes from the Sharvin term. This term comes entirely from the confined geometry of the constriction and does not depend on any kind of scattering process; thus the fractional contribution of spin-dependent scattering to the total resistance is reduced. In addition, the constriction geometry effectively reduces the role of spin-dependent scattering by limiting the fraction of back-scattered electrons that return to the original side of the constriction and thus contribute to the resistance. For example, if an up-spin electron backscatters from a down-oriented magnetic layer, it requires a specific momentum direction to return through the hole. If it is not scattered in this direction, it will remain on the trilayer side of the nanoconstriction until a spin-flip process changes it into a down-spin electron, and it can pass through the down-oriented magnetic layer more easily. This reduces the dependence of the overall resistance on spin. Point-contact measurements on magnetic multilayers [24] have shown that a ballistic geometry can in certain cases *enhance* the magnetoresistance, with observations of MR ratios above 200%; however, these effects can largely

be attributed to magnetostriction affecting the contact shape (and thus the Sharvin resistance), rather than a strong change in the spin-dependent scattering.

The MR ratio I observe certainly cannot be called "giant" (although I still call the associated effect the "GMR effect"), and it is even small enough that the effects of anisotropic magnetoresistance (AMR) cannot be ignored. Anisotropic magnetoresistance is a transport effect in homogeneous ferromagnetic metals where, due to spin-orbit scattering, the resistance of the magnet depends on the relative orientations of the current and the magnetization; typically (as with Co), the resistance is highest when the current is parallel to the magnetization, and lowest when it is perpendicular [29]. This effect can be as high as a few percent. I have checked the AMR contribution by measuring magnetoresistance for a device both with the field parallel and perpendicular to the layers; the resistance of the device at high fields in these two configurations differ by much less than 0.1%, indicating that the AMR contribution to the resistance is extremely small relative to the GMR contribution.

The second aspect of the magnetoresistance that must be discussed is the size of the hysteretic region, which is much larger than expected. Although I cannot assign a well-defined coercive field H_c to the domains I am probing, as would be possible for a bulk film or an isolated single-domain magnet, I can approximate this quantity by defining an effective saturation field H_s as the point at which the resistance is independent of sweep direction, as it is this point that the domains in both layers have settled into their minimum energy configurations and will follow the field at larger magnetic field. For these devices H_s is on the order of several kOe, with some reaching as high as 9 kOe. This is far larger than is expected from the coercive fields of either of the films. For the thick layer, I have grown 100-nm-thick Co films under similar conditions and measured their coercive fields using vibrating

sample magnetometry (VSM)––the coercive fields are at most several 10's of Oe. For the thin layer, the net moment is too small to measure with VSM. However, it is expected that the coercive field in magnetic films increase with decreasing thickness [27]. Studies of coercive fields in magnetic trilayer spin-valves [23, 30] indicate that, even for a Co layer as thin as a few nanometers, the coercive field does not increase to more than a few hundred Oe, an order of magnitude smaller than the saturation fields I observe.

The discrepancies observed above can be understood if we take into account the actual structure of the magnetic thin films, and the effect that the nanoconstriction geometry may have on the growth of the films. The real layers in my trilayer devices are not the perfectly smooth slabs depicted in Fig 2.2. Deposition of Co and Cu by evaporation onto insulators like Si_3N_4 involves growth of films by surface nucleation of grains, which are oriented randomly and will have varying shapes and sizes [31]. AFM studies of my deposited Co films indicate that they have surface roughness of several nm, which for the thin layer is on the order of the film thickness itself. As a result, the domains in this thin film may not be strongly coupled, which will inhibit domain reversal due to domain wall propagation across the film at the bulk coercive field. In addition, if the bowl is not completely filled with Cu during the formation of the first lead (Figure 2.5), then there will effectively be a dimple in the first Cu electrode, which may be filled up by the first Co layer. This might cause a significant deformation in the film at the location of the constriction if the dimple is more than a couple nm deep, which will further decouple the domain at the constriction from the rest of the film. This deformation essentially acts as structural disorder, and will result in enhanced spin-independent scattering at the constriction––one can think of it as a reduction in the mean free path l for both spins in Eqn. (2.1)––and

consequently a reduced MR ratio. In addition, the dipolar fields and the strain induced on the constriction domain by the dimple may contribute to a high coercive field. Enhancements have been seen in the coercive field, as well as reductions in the magnetoresistance ratio, in point-contact measurements of magnetic multilayers by driving an STM tip down into the layers and inducing a deformation [24].

I have made attempts to fill in any dimple which might be present by depositing several nanometers of Cu before growing the first, thin Co layer, but it has not qualitatively changed the data. The deformation of the film at the constriction also appears to be insensitive to the manner of film growth. I have made devices both by thermally-evaporating and sputtering the films; in both cases the magnetoresistance curves show coercive fields in the range of several kOe, significantly higher than that of an unperturbed film. We are thus forced to reluctantly admit that, as useful as the nanoconstriction technique is, it may significantly perturb the magnetic trilayer, given the film growth method I have used. So, rather than two homogeneous films as assumed by the spin-transfer models, we likely have one thick film and a thin, rough film with a strong deformation at the constriction. As it turns out, however, this occurence is in one way fortuitous. The weak coupling of the domain at the constriction allows it to be more freely manipulated by spin current-induced torques, which has made the identification of spin-transfer much easier to achieve.

2.4 Low Field Current-Induced Excitations: Hysteresis

Now that I have established how these devices behave when only a magnetic field is applied, I can turn on the current and see if similar reorientations of the magnetic

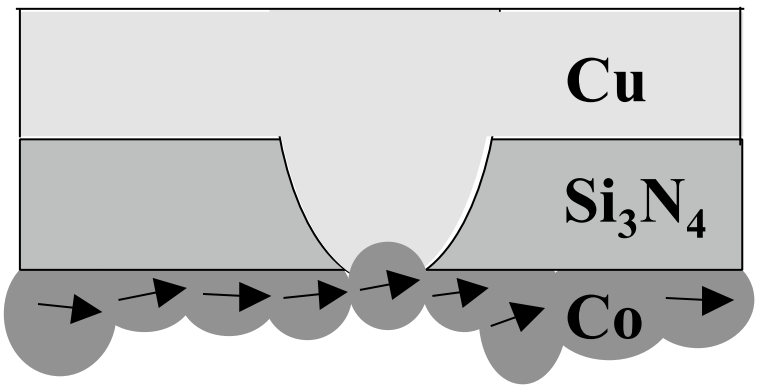


Figure 2.5: Perhaps a more realistic depiction of the thin magnetic layer than that in Fig. 2.2. Film growth during thermal evaporation is by crystalline grain nucleation and growth; this makes the layers rough. Also, a bowl partially filled with Cu can leave a dimple in the top Cu electrode, causing the domain grown at the constriction to be unusually strained and separated from the rest of the film. This may explain the high saturation fields observed in the magnetoresistance data.

moments can be induced. I will first discuss devices where the thin layer is less than 4 nm thick, and where any magnetic fields I apply are within the hysteretic region defined by the magnetoresistance data. In this regime the domain at the constriction in the thin layer can have more than one stable equilibrium point.

Figure 2.6 shows a curve of differential resistance dV/dI vs. current I for a $(Co_4/Cu_6/Co_{100})$ trilayer at zero applied field and $T = 4.2$ K, for both directions of current sweep. The magnetoresistance curve for this same device is that depicted in Fig. 2.4a. Positive current bias corresponds to electrons being injected from the Cu lead in the bowl into the trilayer (see Fig. 2.2). The data in Figure 2.6 are representative of many Co/Cu/Co trilayer devices with similar film thicknesses. The most prominent feature in these curves is the rise in dV/dI with increasing current bias for both signs of bias. This rise reflects the spectroscopic sensitivity, discussed previously, of the nanoconstriction geometry to voltage-dependent scattering events, and is common to all of my devices. Also, there is a dip in the signal at positive current bias. This dip, also seen in many of my devices, is better understood after the origin of the other signals in the dV/dI curves has been explained, so I will save discussion of it for later.

For now, I focus on the hysteresis in the resistance signal as a function of current sweep direction. Starting at negative current bias and moving towards more positive bias (the thin line in Fig. 2.6), the device follows one spectroscopic curve until a particular positive current value. At this point the differential resistance abruptly jumps, and dV/dI follows a similar-looking, but higher-resistance, spectroscopic curve. This jump is irreversible, as can be seen by reversing the direction of current sweep (thick line). As the current is made more negative, the device stays along the higher-resistance state until a particular negative current value is reached, at

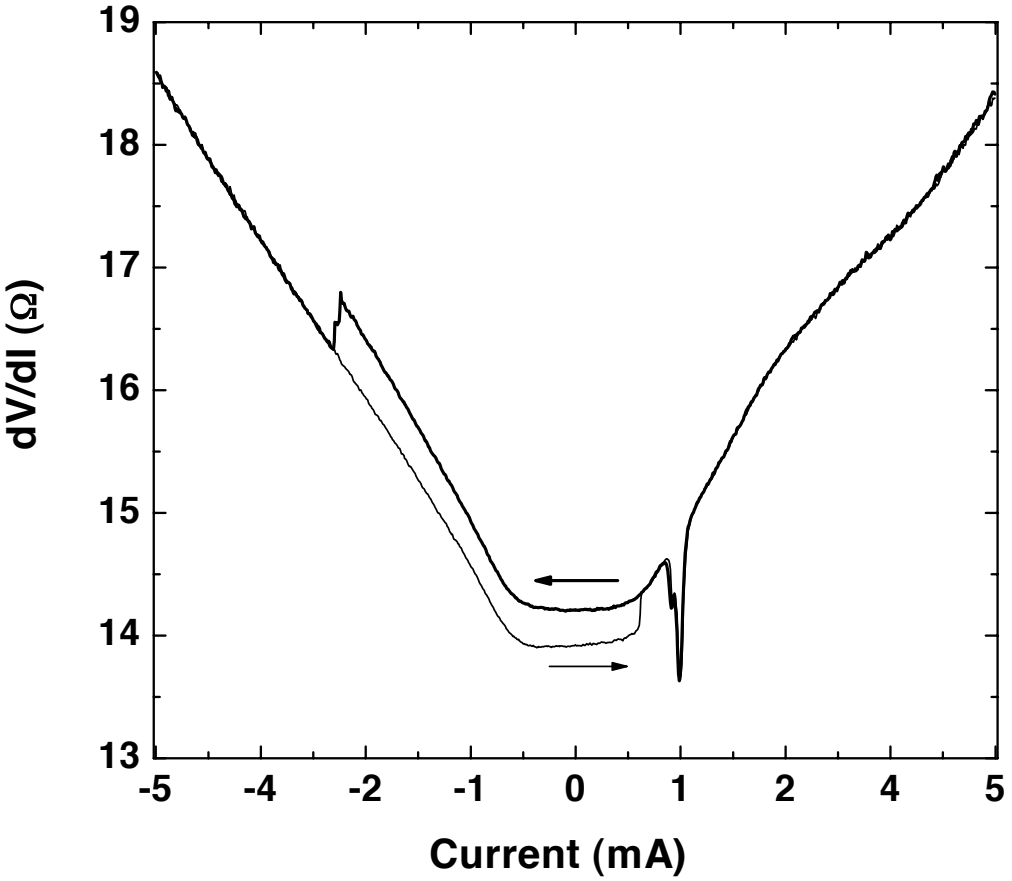


Figure 2.6: Differential resistance dV/dI vs. applied current for a $(Co_4/Cu_6/Co_{100})$ trilayer device (CD05M62) at $T = 4.2$ K and zero applied magnetic field, for both directions of current sweep.

which point the resistance jumps downward to the original spectroscopic curve. In a survey of this and many similar devices that exhibit hysteresis, the currents at which the resistance switches range in magnitude from $0.5 - 3$ mA. Similar features have been seen in multilayer nanoconstriction devices, at similar current levels, by Richard Louie [4].

If a magnetic field larger than the effective saturation field H_s is applied, the hysteresis disappears and only the lower resistance state is stable at zero current bias. I will discuss the field dependence of the hysteresis in more detail later, but for the moment this evidence immediately suggests that the hysteresis is connected to a change in the magnetic state of the trilayer. Moreover, as the GMR signal is the strongest magnetic signal in my device resistances, the hysteresis loop describes a situation in which domains in the two magnetic layers switch from a relatively parallel (lower resistance) configuration to a more antiparallel (higher resistance) configuration at positive current, and switch from a relatively antiparallel to a more parallel configuration at negative current. The two resistance states seen at zero current bias happen to correspond to the high and low resistance states seen in the magnetoresistance for this device (Fig 2.4a). It should not be surprising, however, that such correspondence is not a universal feature for my devices, due to the different reversal processes induced by a current and a field. While the current, due to its localized nature, primarily affects only the domain directly under the constriction, the magnetic field affects the thin layer as a whole. Thus the domain evolution seen in the magnetoresistance curves is typically more complex than the simple switching seen in the current sweeps, with the resistance levels often corresponding to slightly different magnetic configurations than is achieved with a current.

The symmetry seen in the hysteresis loop of Fig. 2.6 is precisely that described by

spin-transfer, in which a positive (in our sign convention) current generates a torque which favors an antiparallel alignment of the two layers, while a negative current favors a parallel alignment. However, this kind of clear symmetry is seen in only about 50% of the Co/Cu/Co devices I have made. The rest show a wide variety of more complicated current-induced effects, e.g., multiple switching events, multiple peaks and dips at zero applied field, and enhanced noise. I attribute the behavior of these devices to a magnetic structure more complex than a single relatively uniform domain sitting at the constriction in the thin layer. Such micromagnetic variations are to be expected in my growth process, which, as I have discussed previously, results in rough and disordered films. For clarity, I focus my discussion and analysis on those devices that exhibit simple current-induced features, e.g. two-level hysteretic switching. When such a device exists, it invariably exhibits a symmetry consistent with the spin-transfer model.

Before we can definitively associate these observations with spin-current-induced effects, we need to first rule out other influences that might reorient the domains in the magnetic layers. The most obvious of these is the self-field generated by the current. Indeed, transport studies of magnetic layered pillars [33, 32] have shown that, if a current is sent perpendicularly through a magnetic layer, the circumferential Oersted field can be made large enough to reorient the layer into a vortex state. However, the current-induced changes in the magnetic domains we observe are likely not due to the Oersted field, for two reasons. First, the magnetic fields generated by the current are too small to orient the domains. We can approximate the field generated at the constriction as that at the surface of an infinite cylindrical wire of radius d,

$$H_{Oersted} = \frac{\mu_0 I}{2\pi d}, \tag{2.3}$$

where $\mu_0 = 4\pi \times 10^{-7}\ N/A^2$ is the permeability of free space. For a current of 1 mA and a constriction diameter of 10 nm, the maximum field is $H_{Oersted} = 200$ Oe, an order of magnitude smaller than the fields needed to align the layer moments in the magnetoresistance measurements. It is conceivable that a field of this magnitude could reorient the low-coercivity thick layer while the high-coercivity thin layer domain remains fixed, but it is important to note that, unlike the pillar experiments [32, 33], the current density distribution is not uniform——it falls off roughly as $1/l^2$ with distance l from the constriction [11]. As a consequence, the fields in the thicker layer are smaller by approximately a factor of 4 for the sample in Fig. 2.6 and are mostly concentrated at the interface nearest the constriction, quickly falling to negligible levels across the 100-nm thickness of the film. There is thus insufficient field energy to induce a vortex state in the thicker layer, despite its low coercive field [34].

More fundamentally, the symmetry of the current-induced switching that I observe is different from Oersted field-induced switching. Consider the field-induced vortex generation of [33] (Fig 2.7a). Since the layers have different thicknesses, they respond differently to the Oersted field. In general, the thicker layer develops a vortex domain first due to its lower coercive field, which generates a rise in resistance as the field is increased from zero. At higher magnetic field, a vortex with the same generated in the thin layer, lowering the resistance as the magnetization in the two layers become more uniformly aligned. A symmetric rise and fall in the resistance is observed for the opposite current sweep direction. By contrast, once the trilayer has switched into an antiparallel configuration in my devices, increasing the current further does not cause the resistance to drop. Figure 2.7b demonstrates this for a $(Co_2/Cu_6/Co_{100})$ trilayer device. This kind of symmetry is more consistent with

spin-transfer torques than Oersted fields.

2.4.1 Comparing Hysteresis Data to Spin-Transfer Models

We have thus established that the current-induced switching has the symmetry of spin-transfer torques, but it is important to compare the currents involved more quantitatively with the torque model. To do this, we return to the modified Landau-Lifschitz-Gilbert (LLG) equation of Chapter 1:

$$\frac{d\vec{S}_{F2}}{dt} = \gamma \vec{S}_{F2} \times \vec{H}_{eff} - \left[\gamma\alpha\hat{s}_{F2} \times \left(\vec{S}_{F2} \times \vec{H}_{eff}\right) + \frac{cI}{e}\hat{s}_{F2} \times \left(\hat{s}_{F1} \times \vec{S}_{F2}\right)\right], \quad (2.4)$$

where $\vec{S}_{F2}$ is the spin moment in the excited domain of layer $F2$, and $\hat{s}_{F1(F2)}$ a unit vector in the direction of the spin moment in layer $F1(F2)$. As detailed in Chapter 1, the first term represents the torque contributed by energy-conserving processes, which are expressed in terms of an effective field $\vec{H}_{eff}$. The second term (the first term in square brackets) represents energy dissipation processes with magnitude set by the dimensionless Gilbert damping parameter $\alpha << 1$, while the third is spin-transfer torque. It is the balance between the damping and spin-transfer torques that determines the current threshold needed to generate an excitation. Slonczewski gives an expression for the proportionality constant c in the spin-transfer term [35]:

$$c = \hbar \frac{g(\theta)}{|\vec{S}_{F2}|}, \quad (2.5)$$

$$g(\theta) = \left[-4 + (1+P)^3 \frac{(3+\cos(\theta))}{4P^{3/2}}\right]^{-1}, \quad (2.6)$$

where θ is the angle between the moments in the two layers, and P is the polarization factor of the magnet, defined as

$$P = \frac{n_\uparrow - n_\downarrow}{n_\uparrow + n_\downarrow}, \quad (2.7)$$

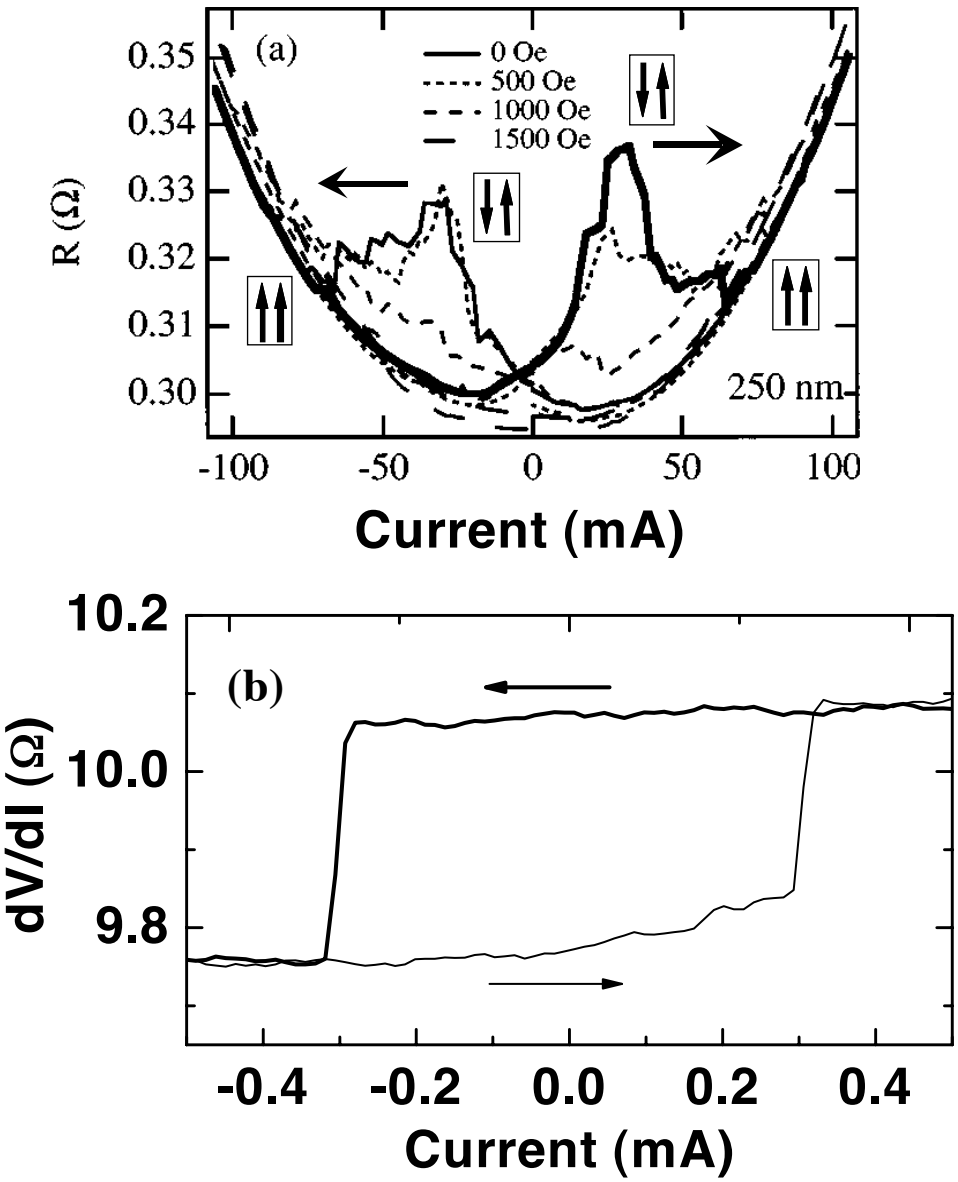


Figure 2.7: (a) A plot of differential resistance dV/dI vs. current I for a trilayer pillar device from [33], showing the signatures of Oersted field-induced vortex formation in the two layers. As the current increases, the low-coercivity film forms a vortex, raising the resistance; at higher currents, the high-coercivity film forms a vortex of the same helicity, and the resistance drops again. (b) dV/dI vs. I hysteresis loop for a $(Co_2/Cu_6/Co_{100})_{nm}$ trilayer device, demonstrating a different switching symmetry from Oersted field effects. Once the current has switched the layers into an antiparallel configuration, additional current does not cause the device to drop back into the low resistance state.

where $n_{\uparrow}, n_{downarrow}$ are the numbers of spin-up and spin-down electrons at the Fermi level that are transmitted through the magnet. These numbers can be determined from band-structure calculations [36], or from measurements of the spin polarization via Andreev reflection [20].

In order to compare the damping and spin-transfer terms of Equation (2.4) quantitatively, the total effective field $\vec{H}_{eff}$ that is felt by the domain in layer F2 must be determined. The effective field can be written in full generality as

$$\vec{H}_{eff} = -\frac{1}{\gamma}\frac{\partial E_{tot}\left(\vec{S}_{F2}\right)}{\partial \vec{S}_{F2}}, \tag{2.8}$$

where $E_{tot}\left(\vec{S}_{F2}\right)$ is the total energy of the domain and the derivative is with respect to the three components of the spin moment $\vec{S}_{F2}$. Determining the total configurational energy of the domain is a formidable task, however. In addition to any external fields we may apply (which can trivially be incorporated into $\vec{H}_{eff}$), there are a host of contributions to the energetics of a thin magnetic film. These include anisotropies from the crystal lattice and strain fields, magnetostatic (dipolar) field energy (both from within the thin layer and from the thick layer), and interlayer exchange. These can have complicated symmetries and, in some cases, are not even uniform over the extent of the domain. It is thus highly questionable whether the single-moment LLG equation can even be applied to the nanoconstriction system, much less whether an effective field can be determined for it. A rigorous application of the LLG equation to this geometry should probably be micromagnetic, in the sense that the film should be simulated as a grid of spins, each obeying the LLG equation and each coupled to one another. Such numerical calculations incorporating spin-transfer have only recently begun to be performed on small collections of spin moments [37].

I thus will not attempt an exact correspondence between these data and the

Slonczewski torque model. However, an estimated comparison between theory and experiment can provide insight into the microscopic workings of the thin-layer domain in the presence of a spin-polarized current. I will begin by assuming that $\vec{H}_{eff}$ takes the simplest possible form that can describe the data, i.e., the observation that the domain switches between two stable states. This is the form of a uniaxial anisotropy, which in terms of energy is

$$E_u = K_u \sin^2(\theta), \tag{2.9}$$

where K_u is the uniaxial anisotropy energy. θ is the angle of the moment from the direction of minimum energy, which is called the easy axis. Directions perpendicular to this are called the hard axes. Substituting Eqn. (2.9) into Eqn. (2.8) yields

$$\left|\vec{H}_u\right| = \frac{2K_u}{\gamma\left|\vec{S}_{F2}\right|}\cos(\theta) = H_u\cos(\theta), \tag{2.10}$$

where $\vec{H}_u$ points along the easy axis. The two energy minima defined by $\vec{H}_u$ will in general be at different levels due to local field couplings, so I add another degree of freedom in the form of an offset field $\vec{H}_{offset}$, pointing along the easy anisotropy axis in one particular direction. This approach neglects the easy-plane anisotropy of the thin-film geometry, from the large dipolar demagnetizing fields generated when the moment points out of the plane. The demagnetizing field is in fact crucial to a quantitative understanding of the spin-transfer effect in nanopillars, which I discuss in Chapters 4 and 5. For the more general estimate here, I assume that the effect of this and other local fields can be represented in some averaged way by the uniaxial and offset field terms alone. Also, I assume that the definition of "parallel" and "antiparallel" states is strict, so that the polarization direction of the thick layer $\hat{s}_{F1}$ is along the easy axis of the domain. This is likely not true generally, as the magnetoresistance data show that the zero-field orientation of the domains

in the two layers often lies somewhere between parallel and antiparallel. For an order-of-magnitude estimate, however, such a simplification is reasonable.

Inserting these assumptions into Eqn. (2.4), I find

$$\begin{aligned} \frac{d\vec{S}_{F2}}{dt} &= \gamma \vec{S}_{F2} \times \left(\vec{H}_u + \vec{H}_{offset} \right) \\ &- \left[-\alpha\gamma \left| \vec{S}_{F2} \right| \hat{s}_{F2} \times \left(\left(\vec{H}_u + \vec{H}_{offset} \right) \times \hat{s}_{F2} \right) \right] \\ &+ \left[\frac{cI}{e} \left| \vec{S}_{F2} \right| \vec{s}_{F2} \times \left(\hat{s}_{F1} \times \hat{s}_{F2} \right) \right]. \end{aligned} \tag{2.11}$$

Suppose that $\vec{S}_{F1}$ and $\vec{S}_{F2}$ begin nearly parallel (the low resistance state), that $\vec{H}_{offset}$ is parallel to the two spin moments, and that the current I is positive. Then the two terms in square brackets are pointed in opposite directions. If angular fluctuations are small (θ close to 0) before the switching event, we can rewrite the LLG equation in a form where there is no current and the damping constant α is replaced with an effective constant α', where

$$\alpha' = \alpha \left(1 - \frac{\hbar g(0) I}{\left(H_u + H_{offset} \right) \alpha\gamma \left| \vec{S}_{F2} \right| e} \right). \tag{2.12}$$

We immediately see that the effective damping is reduced as I is made more positive, and that it in fact becomes *negative* when I crosses the critical value

$$I_c^+ \geq \frac{\alpha \left(H_u + H_{offset} \right) \gamma \left| \vec{S}_{F2} \right| e}{\hbar g(0)}. \tag{2.13}$$

Similarly, if $\vec{S}_{F1}$ and $\vec{S}_{F2}$ begin in a nearly antiparallel configuration (high resistance state and θ near π), the effective damping α' will become negative when

$$I_c^- \leq -\frac{\alpha \left(H_u - H_{offset} \right) \gamma \left| \vec{S}_{F2} \right| e}{\hbar g(\pi)}. \tag{2.14}$$

A negative damping constant implies that, over time, the magnet spirals *away* from the energy minimum. As it approaches the other stable direction, the damping and

spin-transfer terms now are of the same sign, so that $\alpha' > \alpha$ and the magnet settles in this new direction. It is convenient to subtract out the offset field by taking the difference in critical currents:

$$g(0)\left|I_c^+\right| - g(\pi)\left|I_c^-\right| = 2\frac{\alpha H_u \gamma \left|\vec{S}_{F2}\right| e}{\hbar}. \tag{2.15}$$

We can immediately substitute numbers into Eqn. (2.17), using the nanoconstriction of Figure 2.6 as an example. The factor $g(\theta)$ depends on the polarization P of the material. From spin polarization measurements [20], I use $P = 0.35$ for Co. This yields $g(0) = 0.13$ and $g(\pi) = 0.52$. I should point out that $g(0)$ and $g(\pi)$ are really generic quantities representing the efficiency with which the current transfers angular momentum to the magnetic layers; the values given are specific to the model employed by Slonczewski [35], in which electrons travel ballistically through defect-free layers. The magnetization of the domain $M = \gamma \left|\vec{S}_{F2}\right| = mV$, where $m = 1400$ emu/cm^3 for Co and V is the volume of the domain. Substituting these numbers into Eqn. (2.17) yields

$$0.13 \times \left|I_c^+\right| - 0.52 \times \left|I_c^-\right| = I_c^+ = 4.2 \times 10^{-4}\,(\alpha H_u V) \text{ mA}, \tag{2.16}$$

where H_u is in kOe and V is in nm^3. The volume V of the domain is difficult to determine precisely, but as an order of magnitude I will take it to be a disk of the diameter of the constriction, approximately 10 nm, and of the same thickness as the thin film, 4 nm. This yields $V \approx 300\ nm^3$.

This leaves the anisotropy field H_u and the damping α. The magnetoresistance data provides us with an estimate of H_u from the saturation field field H_s, as this is the external magnetic field required to overcome the local field on the domain and align it with the field direction. From Figure 2.4, the saturation field for the device in question is approximately 4 kOe. However, this should be taken as a lower

bound on the effective H_u, as current-induced reversal involves an additional effect from the demagnetizing field that does not come into play in field-induced reversal. I explore this role more explicitly in Chapter 4. This leaves Eqn. (2.14) as

$$0.13 \times \left|I_c^+\right| - 0.52 \times \left|I_c^-\right| = \alpha \times 0.5 \text{ mA}, \tag{2.17}$$

However, if I substitute the measured values of $I_c^+ = +0.65$ mA and $I_c^- = -2.8$ mA into this equation, I run into a major problem: order-of-magnitude agreement with the Slonczewski model only occurs if I assume a damping constant $\alpha > 1$! This is an unphysical result, since the above analysis relies on the LLG equation, which assumes $\alpha << 1$. If more reasonable values of α are used, the predicted critical currents are much smaller than the ones actually observed. Results using my other nanoconstriction devices show similar discrepancies, with the critical currents far larger than predicted by this single-domain torque model.

What's going on here? The main failing of the discussion above is that it does not fully take into account the unique nature of the excited domain——namely, that it is exchange-coupled to an extended film. Slonczewski has explored this situation theoretically, by considering the case of a current of finite diameter d injected into a uniform magnetic trilayer of unbounded width [49]. A continuum version of the LLG equation was solved in this geometry, and a critical current I_{crit} for magnetic excitations was found. The current took the form

$$\begin{aligned} \left|I_{crit}\left(\theta = 0, \pi\right)\right| &= I_{damping}\left(\alpha, H_{eff}\right) + I_{exch} & (2.18) \\ &= \frac{et_{F2}}{\hbar g(\theta)}\left(c_1 \pi (d/2)^2 \alpha m H_{eff} + c_2 A\right), & (2.19) \end{aligned}$$

where $c_1 \approx 1$ and $c_2 = 23.4$ are constants, and θ depends on whether the transition is from an initially parallel or antiparallel configuration of the two magnetic layers. A is the exchange stiffness of the material, which is a kind of spring constant that

describes the strength of exchange coupling between local spin moments in the magnet. The first term $I_{damping}$ comes from the same single-domain physics as that in my initial discussion and essentially is Eqn. (2.13), with the domain size equated to the size of the constriction. The second term I_{exch} comes from the coupling of this domain to the rest of the film. When the local moments (those within the current diameter) begin to move as a result of spin-transfer, the neighboring moments coupled through exchange move in response. In this way a disturbance at the current source propagates out through the magnetic layer. We can consequently think of the extended film as a sink for angular momentum; a transient excitation caused by the current will eventually die out *even if the damping is zero*, due to this propagation, whose efficiency is governed by the exchange stiffness A.

The geometry in my devices is not precisely that which Slonczewski has described, since my films are decidedly not uniform, and the domain at the constriction may not be maximally exchange-coupled to the rest of the film due to the deformation of the film there. The local environment of a domain which can freely switch between two stable states is decidedly different from a similar-sized region that has only one stable configuration within a uniform magnet, and so the details of how angular momentum is propagated away from the domain are likely not well described by Slonczewski's model. However, the idea that the exchange coupling allows the film to act as an angular momentum sink still probably applies to my geometry. I therefore write modified versions of Eqns. (2.13) and (2.14) that incorporate both the damping and the propogation mechanisms of angular momentum dissipation from the domain [38]:

$$I_c^+ = \frac{\alpha\pi(d/2)^2 t_{F2} m e}{\hbar g(0)} (H_u + H_{offset}) + \frac{e t_{F2}}{\hbar e} c_{exch} A, \tag{2.20}$$

$$I_c^- = -\frac{\alpha\pi(d/2)^2 t_{F2} me}{\hbar g(\pi)}(H_u - H_{offset}) - \frac{et_{F2}}{\hbar e} c_{exch} A, \qquad (2.21)$$

where c_{exch} is a geometric factor that represents the degree to which the excited domain is exchange-coupled to the rest of the film Using Slonczewski's value $c_{exch} = 23.4$ as an initial estimate, and the exchange stiffness of Co $A = 1\times10^{-6}$ erg/cm, the magnitude of the exchange term is $I_{exch} \approx 11$ mA, much larger than the transition currents actually seen. This suggests that the actual contribution of the exchange coupling in my devices is smaller than that in ideal uniform films, a reasonable conclusion considering the structure of my trilayers.

It difficult to go further and determine the relative contributions of the damping and the exchange terms of Eqns. (2.20) and (2.21) in my devices from the switching data alone, since they each have a free parameter (α and c_{exch}, respectively). In Section 2.5 I present data on spin-transfer excitations induced at high magnetic field, which provides further information about the damping constant α. At the moment, though, we can still gain some insight by studying the relative magnitude of Eqns. (2.20) and (2.21). Slonczewski has argued [35, 49] that $|I_c^+| > |I_c^-|$, as expressed through the $g(\theta)$ factor. This imbalance comes from the increased scattering, and thus more efficient spin-transfer, that occurs in the trilayer in the antiparallel state, reflected in its reduced conductance. However, the case for most (but not all) of my devices is that $|I_c^+| < |I_c^-|$, which can be interpreted as an antiferromagnetic coupling between the layers generating an offset field $H_{offset} < 0$ in the above sign convention. Such a coupling can also explain the rise in resistance that is often seen in magnetoresistance sweeps (e.g., Fig 2.6) as the field is reduced to zero. As my spacer layers are too thick to mediate a significant interlayer exchange coupling, the source of the coupling is most likely dipolar. It has been shown [39] that surface roughness can generate a dipolar coupling between magnetic layers; depending on

the correlations of the roughness between the two layers, the coupling can be either ferromagnetic or antiferromagnetic.

To conclude, the equations (2.20) and (2.21) establish general bounds for the expected switching currents in the nanoconstriction geometry. The observed critical currents fall between the lower bound set by the damping mechanism alone, and the upper bound set by damping plus a maximally-efficient exchange propogation of momentum. The observations are thus generally quantitatively consistent with the predictions of the spin-transfer torque model. In Chapter 4 I explore the nanopillar geometry, where greater quantitative agreement with the torque model can be achieved.

2.4.2 Temperature Dependence of Hysteresis

All of the measurements I have discussed so far take place at liquid helium temperature, $T = 4.2$ K. In principle, spin-transfer effects should still be observable at higher temperature. However, this is not always the case in the nanoconstriction geometry. Figure 2.8 shows plots of dV/dI vs I for a $(Co_2/Cu_6/Co_{100})_{nm}$ trilayer for both current sweep directions, at $T = 4.2$ K and $T = 295$ K (room temperature). The room temperature curves were taken after warming the sample up from liquid helium temperature. The overall resistance of the device is significantly higher at $T = 295$ K than at $T = 4.2$ K, due to increased electron scattering by thermal phonons and magnons. In addition, the rise in resistance at both biases at low temperature has become more rounded at room temperature, indicating that the spectroscopic information about inelastic electron scattering provided by the nanoconstriction geometry has been smeared out by thermal broadening. The device has also become much more sensitive to the current sweeps; the two sweeps at

room temperature do not lie on top of each other because the resistance of the device jumped after it was swept to large biases. Subsequent sweeps at room temperature show additional irreversible jumps in resistance. These most likely correspond to voltage-dependent electromigration events, which can be assisted by thermal fluctuations at room temperature and therefore are far more common there. For this reason I have only studied devices at room temperature after the low-temperature data have been acquired.

The most significant change in terms of spin-transfer is that the hysteresis at low temperature is no longer present at room temperature; instead, there is a reversible peak roughly at the location of the parallel-to-antiparallel transition at low temperature. The DC resistance change associated with this peak is approximately the same as the difference in resistance levels of the hysteresis at low temperatures. This suggests that the thin layer domain still flips into roughly antiparallel alignment with the thick layer at a certain positive current, but if the current is reduced below this level, the domain immediately flips back. The obvious culprit encouraging this instability is temperature. Although both moment orientations may still be metastable at room temperature, the barrier to reversal (set by the anisotropy energy) may not be large enough to prevent thermal fluctuations from driving the moment from one stable point to the other. The fact that only the parallel configuration is stable at low current bias indicates that the barrier to switching from parallel to antiparallel is much higher than switching from antiparallel to parallel; in other words, the current can switch the domain into antiparallel alignment with the thick layer, but once the current is reduced, the moment can be driven over the relatively shallow barrier via thermal fluctuations and switch back into parallel alignment. This is borne out by the low-temperature data. The hysteresis loop

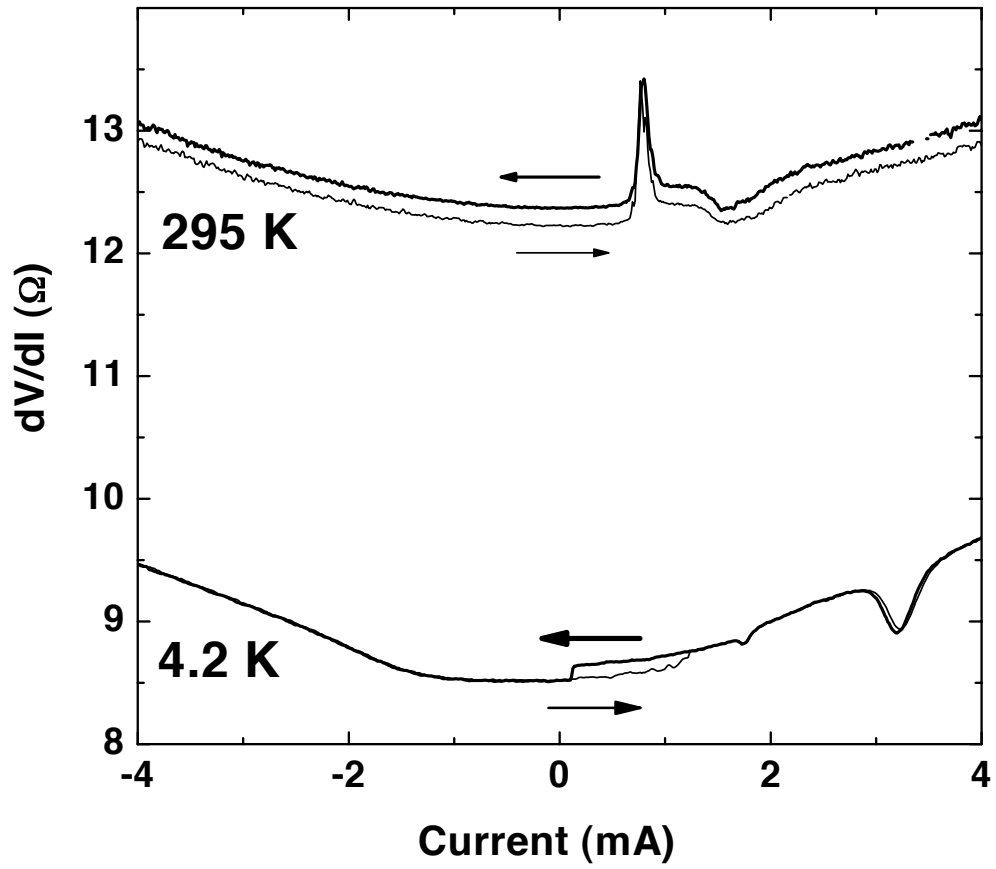


Figure 2.8: Differential resistance dV/dI vs. current for a $(Co_2/Cu_6/Co_{100})_{nm}$ device (CD05R32) at $T = 4.2$ K and $T = 295$ K (room temperature), for both sweep directions.

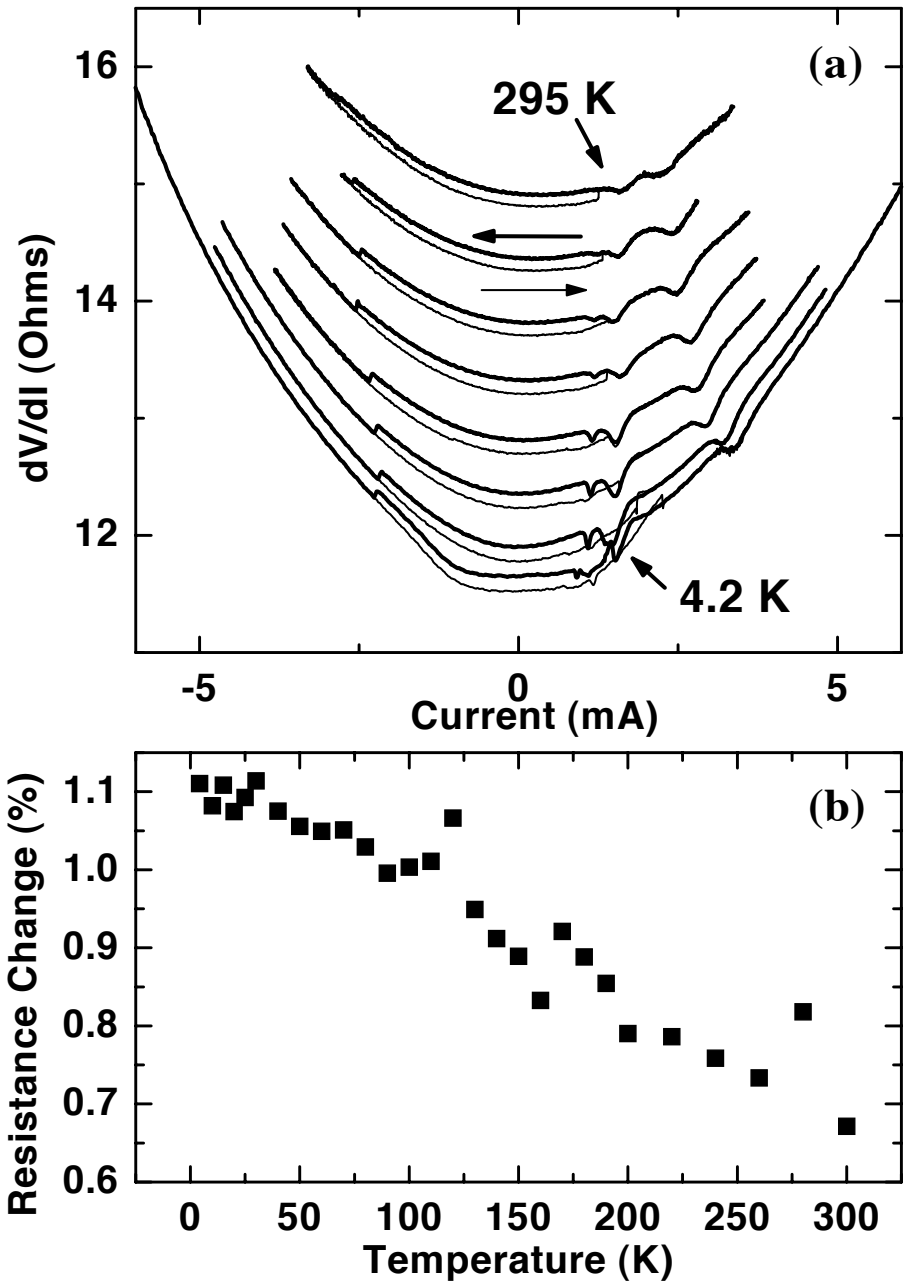


Figure 2.9: (a) Differential resistance dV/dI vs. current for a $(Py_2/Cu_4/Co_{100})_{nm}$ device (CE11R83) at temperatures ranging from $T = 4.2$ K to $T = 295$ K (room temperature), for both sweep directions. (b) Magnetoresistance ratio $(R_{AP} - R_P)/R_P$, where $R_{AP(P)}$ is the high (low) resistance state at zero current bias for this device, vs. temperature.

for this device at 4.2 K lies entirely at positive bias, which suggests that the two magnetic layers are coupled ferromagnetically−−in other words, there is an effective offset field that makes the parallel configuration more thermally stable than the antiparallel configuration. In Chapter 5, I study similar phenomena in nanopillar devices and describe the effects in terms of a more rigorous spin-transfer model, one that more formally takes into account the role of thermal fluctuations.

Not all devices show changes with temperature that can be understood merely as a thermally-fluctuating thin-layer domain. Others show abrupt modifications of the resistance, indicating that microstructural changes occur as the device is warmed. Of the several Co/Cu/Co devices I have measured at room temperature, none have hysteresis which persists at that temperature. However, I have measured a Py/Cu/Co (Py=Permalloy=81% Ni, 19% Fe) trilayer device in which hysteresis is present at temperatures up to and including room temperature. The hysteresis loop in current at various temperatures for a $(Py_4/Cu_4/Co_{100})_{nm}$ device is shown in Figure 2.9a. In Figure 2.9b I plot the ratio $(R_{AP} - R_P)/R_P$, where R_{AP}, R_P are respectively the high and low resistance states at zero current bias, as a function of temperature. This number drops as the temperature increases, showing that the difference in spin-dependent scattering for the two states decreases with increasing temperature. The magnitude of the drop is consistent with previous measurements of the temperature dependence of the GMR in Py/Cu multilayers [40]; these data were explained as a consequence of thermally-induced spin fluctuations in the magnetic films [41].

2.4.3 Suppression of Hysteresis

The data above show that, in certain cases, the hysteresis of a Co/Cu/Co trilayer can be suppressed via thermal fluctuations. Equations (2.20) and (2.21) suggest other ways that the hysteresis can be eliminated even at low temperatures. For instance, the critical currents as described by these equations scale with the thickness of the thin layer t_{F2}. A similar trend can be seen in the data; the average critical currents are smaller in devices made with thin layer thickness $t_{F2} = 2$ nm than in devices with $t_{F2} = 4$ nm, by about 50% [42]. However, if the thin layer is made thicker, a qualitatively different variation is seen, one that highlights the special nature of the domain that is excited by spin transfer.

Figure 2.10 is a plot of a $(Co_7/Cu_4/Co_{100})_{nm}$ trilayer device at zero field and $T = 4.2$ K. Hysteresis is observed with respect to the direction of current sweep, but the hysteretic region, spanning about 0.1 mA, is much smaller than that seen in devices with thinner $F2$ layers. Also, both switching transitions occur at positive current bias. If the layer is made even thicker ($\gtrsim$ 10 nm), then the hysteresis disappears entirely. This initially seems to be in conflict with Eqns. (2.20) and (2.21), which predict that the transitions move away from each other as the domain is made thicker. However, the observations are more reasonable from the point of view of the Slonczewski model if we consider the effect that an increased layer thickness has on the structure of the domain and its environment. For very thin layers (Figure 2.11a), the excited domain is a grain or small group of grains near the constriction that, due to the thickness variations of the film (and possibly the dimple at the constriction), is not strongly exchange-coupled to the rest of the film. This exchange coupling, in addition to providing the angular momentum propagation mechanism described earlier that results in higher critical currents, also affects the

offset field $\vec{H}_{offset}$, as exchange favors a particular direction——one that minimizes the angular deviation between the domain and its neighbors. As the layer is made thicker (Figure 2.11b), both the thickness of the domain, and the exchange coupling to the domain, increase. If the domains in the two layers that contribute to the GMR signal are stable at zero field in roughly parallel alignment, then this exchange field will shift both I_c^+ and I_c^- to more positive values. At a certain thickness (occuring somewhere between $t_{F2} = 7$ nm and $t_{F2} = 10$ nm in my devices), the exchange field overcomes the effective uniaxial anisotropy field, and there remains only one stable orientation of the domain, set by the competition of exchange with the other local fields. The large reduction in $I_c^+ - I_c^-$ for layers not quite thick enough to fully suppress the hysteresis is less understandable, although it may be indicative of the large offset field making the energy well associated with the antiparallel state shallow enough that it is susceptible to thermal fluctuations, even at low temperatures.

The observed current-induced hysteresis can also be suppressed by applying a magnetic field $H > H_s$. Below this field, the critical currents that make up the hysteresis loop have a field dependence that varies widely from device to device, and bears little relation to the linear dependence predicted by Eqns. (2.20) and (2.21). Figure 2.12 shows the field dependence of the critical currents I_c^+ and I_c^- for a $(Co_2/Cu_6/Co_{100})_{nm}$ device as a function of magnetic field applied in the plane of the layers. As can be seen, I_c^- varies strongly but nonmonotonically as the field varies, while I_c^+ appears to have little to no field dependence. At a field of approximately 1.1 kOe, the hysteresis abruptly disappears. Similar complex behavior is seen in the other devices that exhibit hysteresis. The field dependence of my devices in general also depends on the field history; different variations of the critical currents with field are seen if the field is increased from zero as opposed to decreased from a large

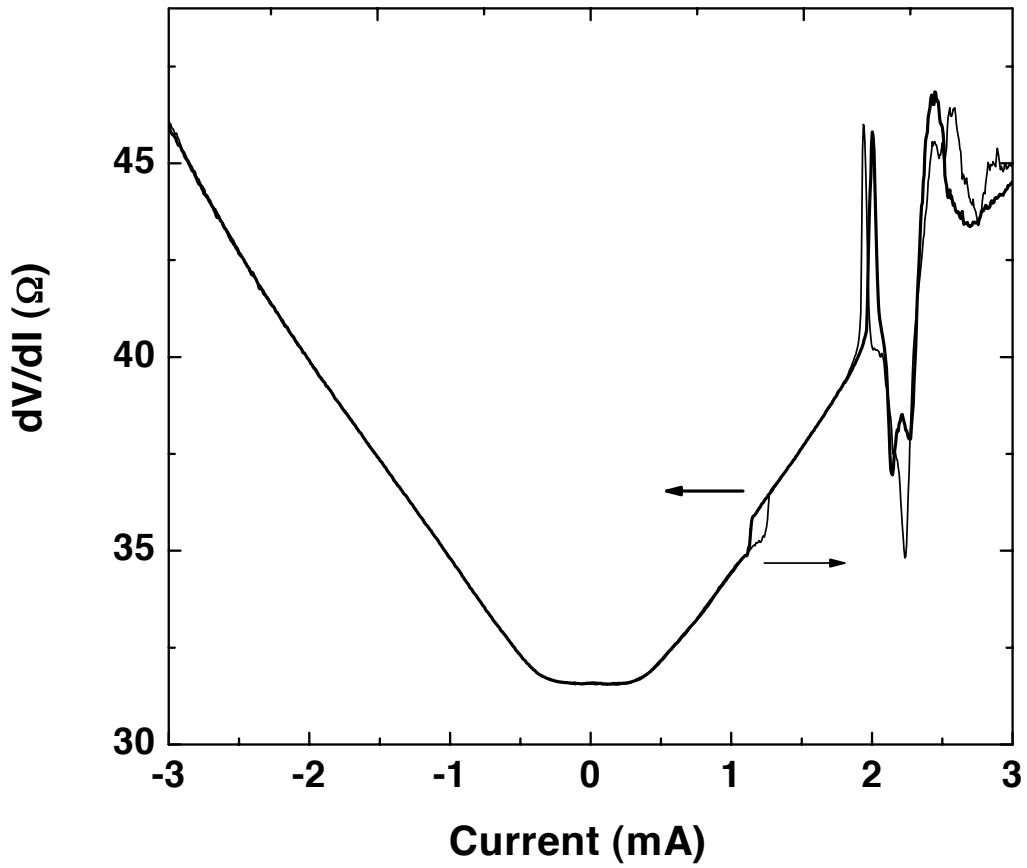


Figure 2.10: Differential resistance dV/dI vs. current for a $(Co_7/Cu_4/Co_{100})_{nm}$ device (CC09ER21) at $T = 4.2$ K and zero applied field, for both current sweep directions.

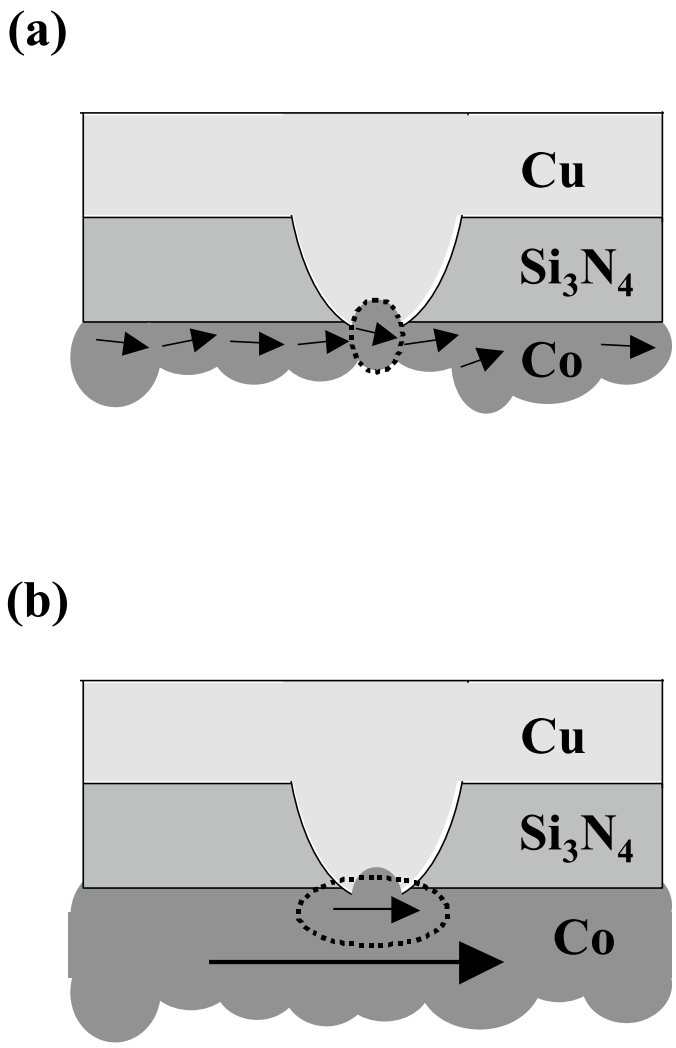


Figure 2.11: Schematic of domain evolution as the thin layer is made thicker in a nanoconstriction device. (a) For thinner layers, the domain at the constriction may be loosely bound to the rest of the layer. It is therefore more free to point in multiple directions. (b) As the layer is made thicker, the exchange coupling to the domain grows. The domain at the constriction thus feels a stronger exchange field that favors one particular direction.

field to zero. None of this is especially surprising, considering that the external field is not only applied to the excited domain, but also to all of the domains in the thin film, which will consequently reorient and change the local field $\vec{H}_{eff}$ that the excited domain feels. As a result, the local field will vary in a very complex way with the external field. In addition, the size of the domain may change with $\vec{H}_{eff}$ in a complicated manner, affecting the measured critical currents. If the field is kept below the coercive field and varied between positive and negative values, nearly all of the devices can be put into a state where features appear at *negative* current bias; Figure 2.13 shows an example for a $(Co_4/Cu_6/Co_{100})_{nm}$ device at a field of 2.8 kOe, below its saturation field of $H_s \approx 4$ kOe [43]. This indicates that the domain structure around the constriction has been rearranged so that the total local field, and thus the thin layer domain, is not aligned with the external field alone. Since the thick layer is aligned with the external field, the symmetry of spin-transfer (set by the thick-layer moment direction) favors some sort of realignment of the thin layer domain for *both* signs of current. At the field shown in Fig. 2.13, the hysteresis has largely been extinguished, and the features seen at both signs of current bias are different from what has been considered up to this point. I discuss these new kinds of excitations in the next section.

2.5 Excitations for Thick Layers and High Fields: Dynamical Excitations

A large magnetic field and a thick excited layer both have similar effects on spin-transfer, in that they both favor a single direction for the excited domain moment. This is in opposition to anisotropy forces, which, at low fields and for thin layers,

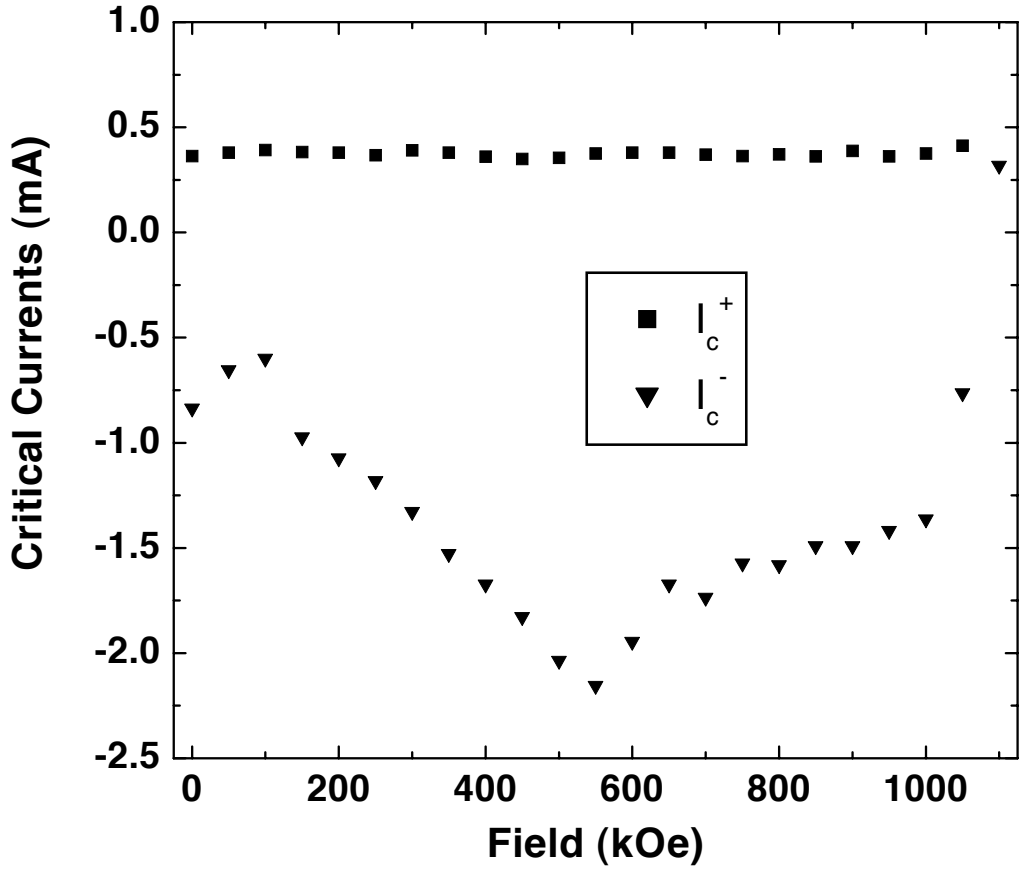


Figure 2.12: Critical currents I_c^+ (squares) and I_c^- (upside-down triangles) vs. applied field for a $(Co_2/Cu_6/Co_{100})_{nm}$ device (CD05R12) at $T = 4.2$ K. The field, less than the saturation field H_s, was varied from positive field down to zero.

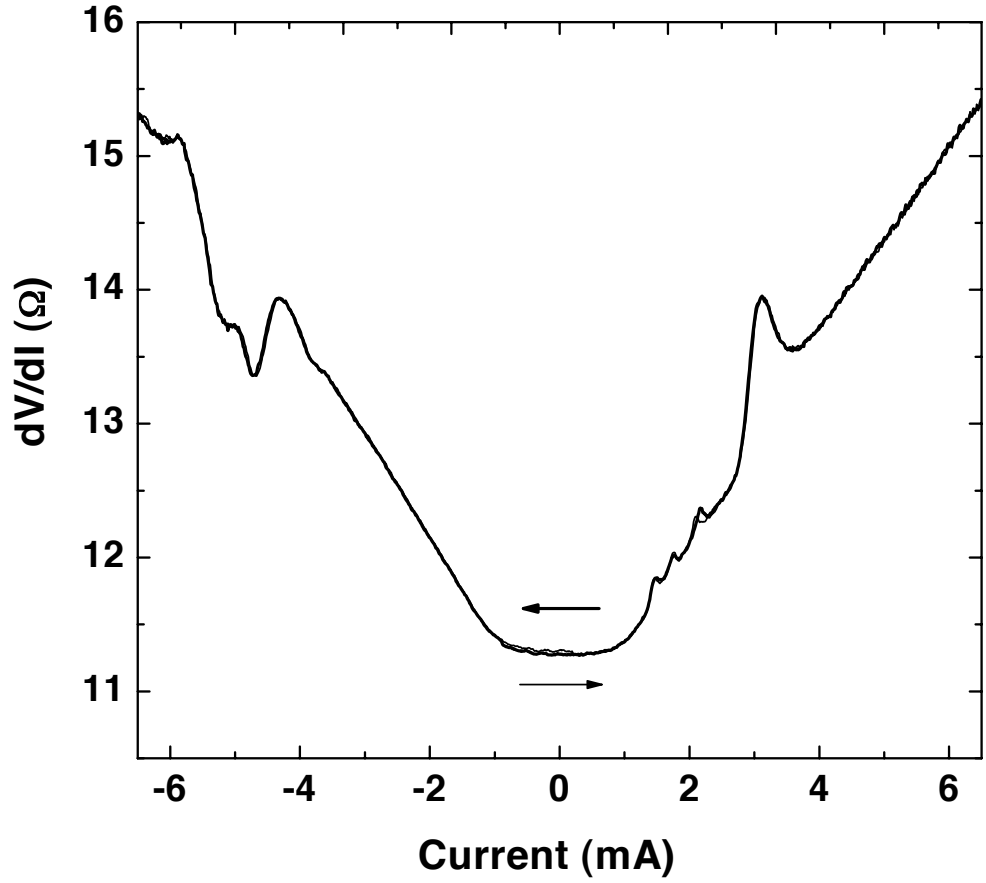


Figure 2.13: Differential resistance dV/dI vs. current for a $(Co_4/Cu_6/Co_{100})_{nm}$ device (CD05M41) at $T = 4.2$ K and a field $H = 2.8$ kOe applied in the plane of the layers, for both current sweep directions.

provide the moment with multiple stable orientations. If the field is large enough or the excited layer thick enough, the bistable state is eliminated, and hysteretic changes in the magnetization direction are no longer observed. What, then, is seen in these devices? As it turns out, I still observe features that are consistent with spin-transfer-induced magnetic excitations. However, these excitations are qualitatively different from what has been discussed so far. Unlike the switching between static states observed previously, the excitations at high fields are likely dynamic excitations.

It is far easier to explore this new regime for a given device by varying the field than by varying the thickness of the thin layer, so I will focus on the excitations observed when a large magnetic field is applied. Figure (2.14) is a plot of differential resistance dV/dI vs. current I for the same $(Cu_4/Co_6/Cu_{100})_{nm}$ trilayer device as shown in Fig. 2.6, at magnetic fields of 10 kOe, 20 kOe, and 30 kOe. The field is applied perpendicular to the layers. Both sweep directions are shown, indicating that all hysteretic features are gone. Instead, there is a series of peaks in dV/dI, all occuring at positive current bias. These peaks are continuous and reversible, in the sense that the AC excitation of the lock-in measurement follows the change in resistance with current. The peaks change with magnetic field, following a general trend of moving to larger current bias with increasing field. Peaks with similar qualitative field dependences are seen at large magnetic fields in essentially all of my devices, with the features only appearing for positive currents. This is true even for devices which do not show clear hysteretic switching at low fields.

The strong field dependence of these features suggest that they, like the low-field switching, are related to changes in the magnetic state of the trilayer. It is somewhat misleading, however, to compare these features to those at low field simply by looking

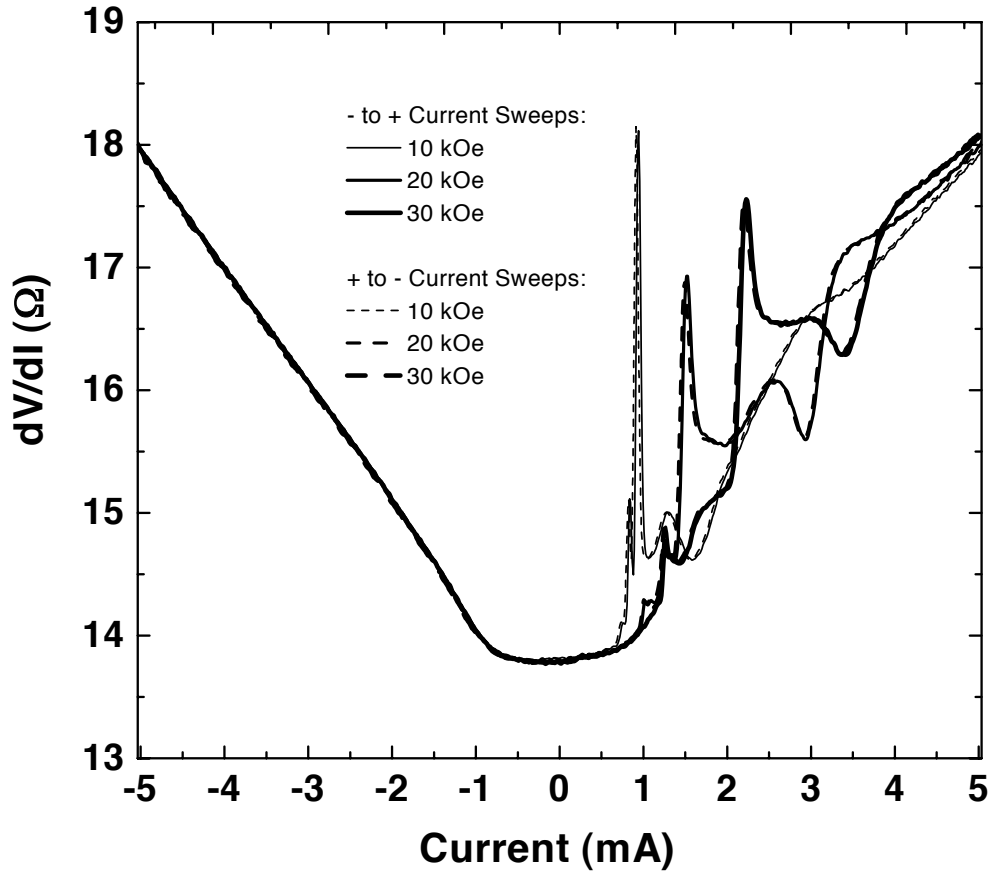


Figure 2.14: Differential resistance dV/dI vs. current for the same device depicted in Fig. 2.6 (CD05M62), at various applied magnetic fields, for both current sweep directions. The field is applied perpendicular to the layers.

at the differential resistance. My measurements of the switching data were taken using the differential lock-in signal dV/dI, because it provides a high signal-to-noise ratio. However, the phenomenon as described by the spin-transfer model really is a change in the overall DC resistance V/I of the device. A lock-in measurement in fact does not give the true resistance derivative at the switching transition points, since the AC excitation cannot follow the hysteretic switch in V/I. If it could, there would be delta-function peak at the P to AP transition, and a similar dip at the AP to P transition. However, at low bias, $dV/dI \rightarrow V/I$, and so the zero bias resistance states that I measure with the lock-in are effectively the values of these DC resistances. If the high-field excitations also correspond to GMR-like changes in the DC resistance signal, then they are more properly understood in terms of V/I rather than dV/dI.

Figure 2.15a shows the same data as in Fig. 2.14, but now integrated over current I and replotted as DC resistance V/I. The field-dependent features are somewhat obscured by the spectroscopic background, which is largely due to scattering that is symmetric in voltage. This background can be subtracted by plotting the resistance difference between the device at a current I and the device at a current $-I$, as a function of I. This is done in Figure 2.15b. For each field, the additional resistance at positive current increases in an irregular fashion as the current increases. Each of these features individually move to higher current with increasing magnetic field. The overall resistance change is approximately $300 - 400\ \mu\Omega$.

Assuming that we can read this resistance change as a GMR signal, then these measurements show that the two magnetic layers, initially both in parallel alignment with the magnetic field at low positive currents, deviate from that alignment in an irregular but continuous manner with increasing current. This sign of current is also

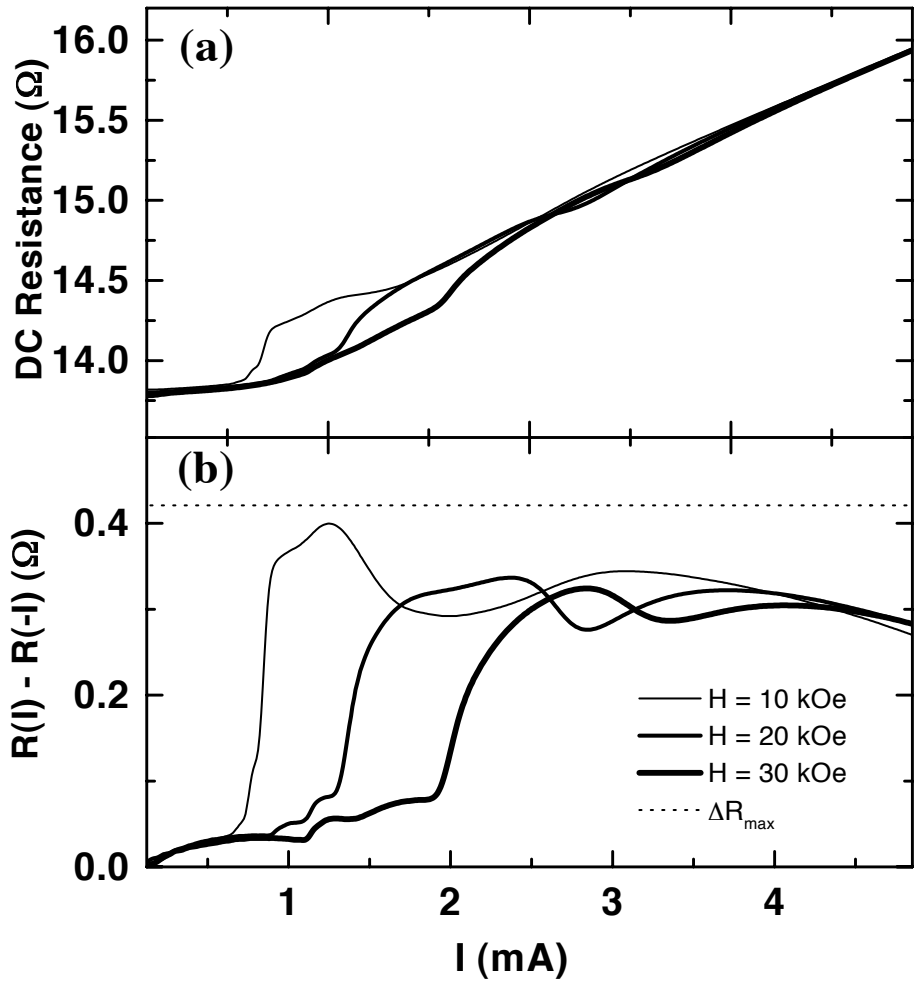


Figure 2.15: (a) DC resistance vs. current I, found by integrating the data in Fig. 2.14. (b). DC resistance with the background subtracted by taking the difference $R(I) - R(-I)$, and plotting vs. I. The horizontal dotted line is the maximum resistance difference seen in the magnetoresistance data for this device, ΔR_{max}.

the current direction for which, as described by the torque models, spin-transfer favors an antiparallel alignment of the domains in the two layers. The symmetry of these features is thus consistent with an instability in the thin layer induced by spin-transfer, although the kind of excitation allowed in a system with only one stable state at zero current needs to be developed further. For the moment, we can compare the resistance change to that seen in other measurements. From magnetoresistance measurements, the largest resistance difference observed in this device is approximately 420 $\mu\Omega$. This is plotted for comparison as the horizontal dotted line in Fig. 2.15b. Due to the complex domain motion that undoubtedly occurs in the two layers during a magnetoresistance sweep, it is difficult to say whether full antiparallel alignment is achieved at any field, so the maximum resistance difference quoted above may not be the maximum difference possible in principle. However, the comparison shows that the current-induced resistance change at high fields is close to but less than the maximum measured resistance difference. Analyses on similar devices show resistance changes that are a significant fraction of, and occasionally slightly exceed, the maximum change in resistance. This suggests that the thin-layer moment has been rotated from parallel alignment with the field by a significant fraction of 180 degrees.

I need to sound several notes of caution here in this discussion of the high-field features, as the resistance increase may not be entirely due to the GMR effect. For example, thermoelectric effects may also give asymmetries in dV/dI with respect to the sign of I; however, such models typically merely shift the resistance curve and do not predict the complicated peak structure that is observed [44]. As these features persist only at finite bias, another contribution to the changes in dV/dI may come from energy-dependent scattering (to which the nanoconstriction

geometry is uniquely sensitive). Any large spectroscopic contribution to the peaks from scattering that obeys electron-hole symmetry can be immediately ruled out, as there are no features at the corresponding negative current (or, more properly, voltage) bias. For energy-dependent inelastic scattering mechanisms that could in principle be bias-sensitive, such as magnon scattering, the spectroscopic nature of the nanoconstriction generally yields a signal in d^2V/dI^2 that is proportional to the density of states of the scatterer [45]. It is then highly implausible that such a signal would give the kind of peaks seen in dV/dI, with regions where the slope of dV/dI is negative. I can thus with some confidence rule out a large spectroscopic contribution to the measured rise in DC resistance.

Recent theoretical predictions also suggest another possible contribution to the resistance change. As mentioned earlier, the excitation predicted by most spin-transfer theories at high magnetic field is a dynamic spin-wave, in which the excited magnet precesses uniformly. In Berger's model of spin-transfer [46], these spin-waves are driven by inelastic spin-flip processes at the normal metal-ferromagnet interface. The energy for the spin-waves comes from a spin-split chemical potential in the normal metal. This results in an effective voltage ΔV across the interface, where $e\Delta V$ is proportional to the energy $\hbar\omega$ of the spin-wave. More recent theoretical work on precessing magnets in multilayers [48] also predicts an imbalance in the spin chemical potentials near the magnetic layer due to the precession, with a splitting similar in magnitude to Berger's model. The maximum voltage predicted by these models [46, 47, 48] is approximately $\hbar\omega/e$; with $\omega/2\pi \approx 10$ GHz, this is on the order of 10 μV. By contrast, the resistance change in Fig. 2.12 corresponds to an increased voltage $\Delta V \approx 300$ μV, demonstrating that Berger's voltage, if it exists at all, is a small contribution.

The preceding discussion has given us some confidence that we can interpret the high-field features as continuous and reversible deviations of the thin-layer domain away from parallel alignment with the thick layer and the field. We have also seen, though, that the angular deviation is probably less than a full 180 degrees away from the field axis. A simple look at the Landau- Lifschitz-Gilbert equation (Eqn. (2.4)) tells us that this kind of situation cannot be static; the first term of Eqn. (2.4) will generate a large precessional torque on the spin moment, causing it to rotate around the total effective field. As a result, it is natural to conclude that the excitations I observe at high field consist of a dynamical state, with the thin layer domain tilted far from its energy minimum and precessing around the applied field. The main spin-transfer models come to similar conclusions about the kind of excitation possible at high magnetic field [46, 49]. My measurements do not provide direct confirmation of a dynamical state, as they only provide a GMR signal averaged over timescales much longer than typical magnetic precession periods (sub-nanosecond). However, a group at Michigan State has seen similar asymmetric high-field peaks in the differential resistance when sending current through a mechanical point-contact into a magnetic multilayer [50], and have performed further measurements that may be interpreted as demonstrating the coherent AC nature of the excitation [51]. By bathing the device in RF radiation of the appropriate frequency, a rectifying DC voltage can be generated across the point-contact as the external radiation and the radiation from the precessing moments mix. With this technique, the frequency of the spin-waves can be measured, and was found to be in the 10's of GHz.

2.5.1 Field Dependence of Dynamical Excitations

The current threshold for dynamical excitations is determined within the torque model in exactly the same way as it is determined for the hysteretic switching, since both depend on a small-angle instability criterion. The qualitative difference between the two kinds of excitations is set by the large-angle stability properties of the magnetic system once this threshold has been reached. We can therefore apply the results derived previously for the low-field switching to the high-field dynamics. I will only apply the model to the initial threshold for excitation; the additional features at higher currents are more complicated, and will be discussed in a later section. Since at high fields the two layers begin in a parallel configuration, the appropriate current threshold expression is that for I_c^+:

$$I_c^+ = \frac{\alpha\pi(d/2)^2 t_{F2} m e}{\hbar g(0)} (H_{eff}) + \frac{e t_{F2}}{\hbar e} c_{exch} A, \tag{2.22}$$

where d is the constriction diameter and m the magnetization density. Since the external field H enters linearly into H_{eff}, the dependence of Eqn. (2.23) on H should be linear. However, as we have seen in Section 2.4.3, the other local fields also implicitly depend on H when H is less than the saturation field H_s. Although this may not strictly be true, for simplicity I will assume that for $H > H_s$ these other fields remain constant with H, as the thin film has settled into relatively uniform alignment with H. I therefore rewrite Eqn. (2.22) in a form linear in H but defined over a more restrictive range:

$$I_c^+ (H > H_s) = \frac{\alpha\pi(d/2)^2 t_{F2} m e}{\hbar g(0)} (H - H_s) + I_c^+ (H = H_s). \tag{2.23}$$

The intercept $I_c^+ (H = H_s)$ contains information about both the effect of exchange coupling and the other contributions to the local field.

Even though the peaks correspond to changes in the DC resistance, it is still easiest to track their field dependence by measuring dV/dI. Figure 2.16 shows a series of dV/dI vs. I traces for a $(Co_4/Cu_6/Co_{100})_{nm}$ device, at various constant magnetic fields applied in the plane of the layers. The initial threshold current for the dynamical excitation increases approximately linearly with increasing magnetic field. The slope of the variation is $dI_c^+/dH = 35$ μA/kOe. Using the values $g(0) = 0.13$, $d = 10$ nm, $t_{F2} = 4$ nm, and a magnetization $m = 1400$ emu/cm^3 for Co, the prefactor to the term in Eqn. (2.24) proportional to H becomes

$$\frac{dI_c^+}{dH} = \alpha \times 0.47 \text{ mA/kOe}, \tag{2.24}$$

which, for good agreement, yields $\alpha = 0.07$. Analyses on similar devices give fitted damping constants $\alpha = 0.05 - 0.2$. While these numbers are small enough that they do not grossly violate the small-α assumption implicit in the LLG equation, they are still significantly larger than damping constants measured in FMR experiments on macroscopic Co samples, $\alpha \approx 0.007$ [52].

The difference in values for the damping can be ascribed to the different natures of the excitations in the two experiments; here I provide a very hand-wavy (but hopefully suggestive) argument. In most FMR measurements, a spin-wave is excited by applying a DC magnetic field H and a smaller AC field at the frequency of a spin-wave resonance, set by the dispersion relation unique to the material and geometry. However, the wavelength of the AC radiation is many orders of magnitude larger than typical spin-wave wavelengths, so the radiation couples most strongly into the uniform (infinite-wavelength) spin-wave mode. By contrast, the excitation generated by the current coming from a narrow constriction into into an unbounded magnet is decidedly not uniform; it is made up of a continuum of spin-wave modes, from the uniform mode up to modes of wavelength of order d, where d is the current

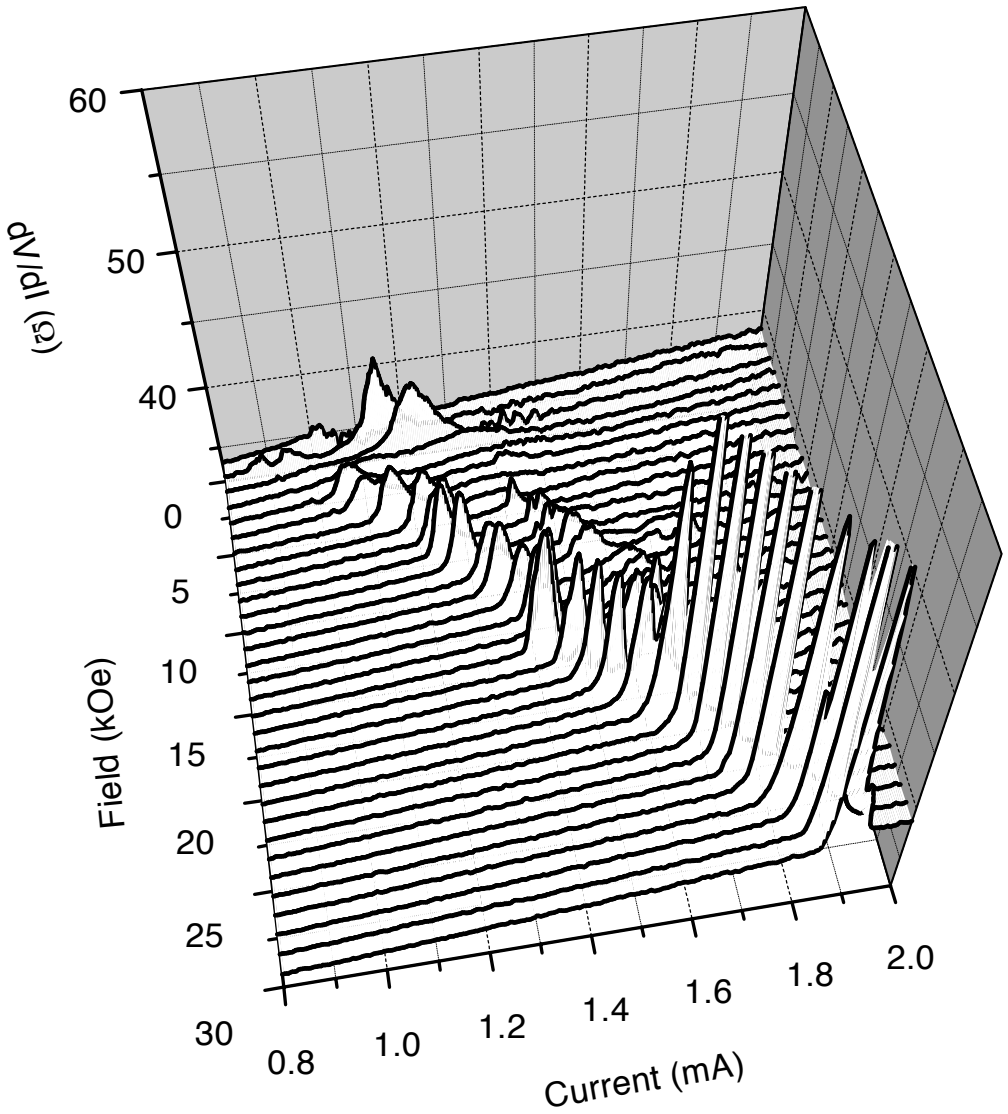


Figure 2.16: Plots of differential resistance dV/dI vs. current for a $(Co_4/Cu_6/Co_{100})_{nm}$ device (CH03EL62) at $T = 4.2$ K, at various magnetic fields applied in the plane of the layers.

diameter. Each of these modes is individually coupled to other degrees of freedom in the system, such as phonons and conduction electrons, and, in time, will dissipate energy to these degrees of freedom via scattering events. Thus there are many more channels through which this kind of excitation can give up energy than there is for a uniform mode alone (as long as the excitation power is not too large; see [53]). Some of the energy is propagated away from the constriction and no longer plays a role in local dynamics; this is the the exchange propagation term of Slonczewski, which does not make a distinction whether the energy is dissipated a certain distance away from the constriction or is carried away to infinity. The rest of the energy is dissipated right at the constriction; this portion, since it does depend on the local magnetic dynamics, is incorporated as an enhanced local damping parameter. Large damping constants similar to my own have been invoked [49] to explain the field dependence of the current-induced features seen by the Michigan State group [50]. In other experiments, magnetic reversal in small individual regions of large magnetic films has been induced via local field pulses; damping constants $\alpha \sim 0.05 - 0.2$ were required to explain the reversal dynamics [54]. In each case the highly nonuniform nature of the excitation couples to a larger manifold of spin-waves than the FMR AC excitation, resulting in a greater degree of dissipation [55].

It is a good time to perform a consistency check on how the high-field data compare to the data for the same device at low field. I use the device of Fig. 2.16 as an example. If the measured damping constant $\alpha = 0.07$ is inserted into the expression for the scaled critical current difference that comes from the damping term alone, Eqn. (2.15), the predicted value is 35μA. This is only approximately 4% of the actual measured value for this device, which is about 1 mA. Thus the vast majority of the contribution to the zero-field critical currents must come from

the exchange term. However, if an equivalent scaled critical current difference is calculated just using the ideal Slonczewski exchange term, a value of about 7.5 mA is predicted, which suggests that the efficiency of angular momentum propagation due to exchange is only about 15% of the ideal uniform film case. This finding is consistent with the picture of the thin-layer domain being loosely coupled to the rest of the film. We can also compare the intercept of the high-field data to the low-field data. The intercept I_c^+ $(H = H_s)$ is not strictly equal to the zero field critical current Eqn. (2.21), but since both are dominated by the exchange term, they should be similar in magnitude. In general this is found to be true, although the intercepts are usually slightly smaller than the zero-field critical current.

In summary, I find that the field dependence of these excitations provides us with insights into the microscopic dynamics of domains within extended films, showing that they are highly damped processes. It is a testament to the uniquely localized nature of the spin-transfer effect that individual domains can be manipulated in a (mostly) otherwise static magnetic film, and suggests that spin-transfer is a useful tool for studying and controlling the local dynamics of magnetic systems.

2.6 Other Current-Induced Features

I conclude by discussing features in the data that do not fit cleanly into the previous two categories, although they can also be understood in terms of spin-transfer. Let us first return to the low-field switching data. As I noted upon introducing Figure 2.6, there often is a dip in the differential resistance at positive currents beyond the hysteretic region at zero applied field. Occasionally there also is a companion peak at negative current bias; Figure 2.17 shows a hysteresis loop for a $(Co_2/Cu_6/Co_{100})_{nm}$ trilayer device that exhibits both features. Within the simplest

torque model, these features do not make sense as excitations in the thin layer domain, since the additional current beyond the switching transitions should merely enhance the stability of the state into which the thin layer domain has switched. Instead, they indicate that some other part of the trilayer is being excited.

The only other major suspect is the thick layer. Looking at the symmetry of the high-current features, this suspicion seems to be borne out. In my initial discussion of the torque model in Chapter 1, I noted that torques appear on both magnetic layers of the trilayer, but since the threshold for exciting the thick layer is much higher than it is for exciting the thin layer due to its much larger spin moment, the thick layer can effectively be treated as fixed. However, if we relax this assumption, then it becomes important what the symmetry of the torques are on the thick layer. This is easy to figure out; reversing the sign of current has the same effect on the system as switching the positions of the thin and thick layers. If so, then the symmetry of the torque felt by the thick layer for a given sign of current is that felt by the thin layer for the opposite sign of current. In other words, the current that tries to move the thin layer into parallel (antiparallel) alignment with the thick layer simultaneously tries to move the thick layer into antiparallel (parallel) alignment with the thin layer. The observed features are consistent with this picture. At a certain positive current beyond that which switches the thin layer domain into antiparallel alignment with the thick layer, there is an excitation which causes the thick layer to deviate from antiparallel alignment; thus there is a dip in differential resistance, corresponding to a drop in the DC resistance. Similarly at negative current, after the thin layer has switched to be parallel to the thick layer, there is an instability which drives the thick layer away from parallel alignment; this causes a rise in the resistance.

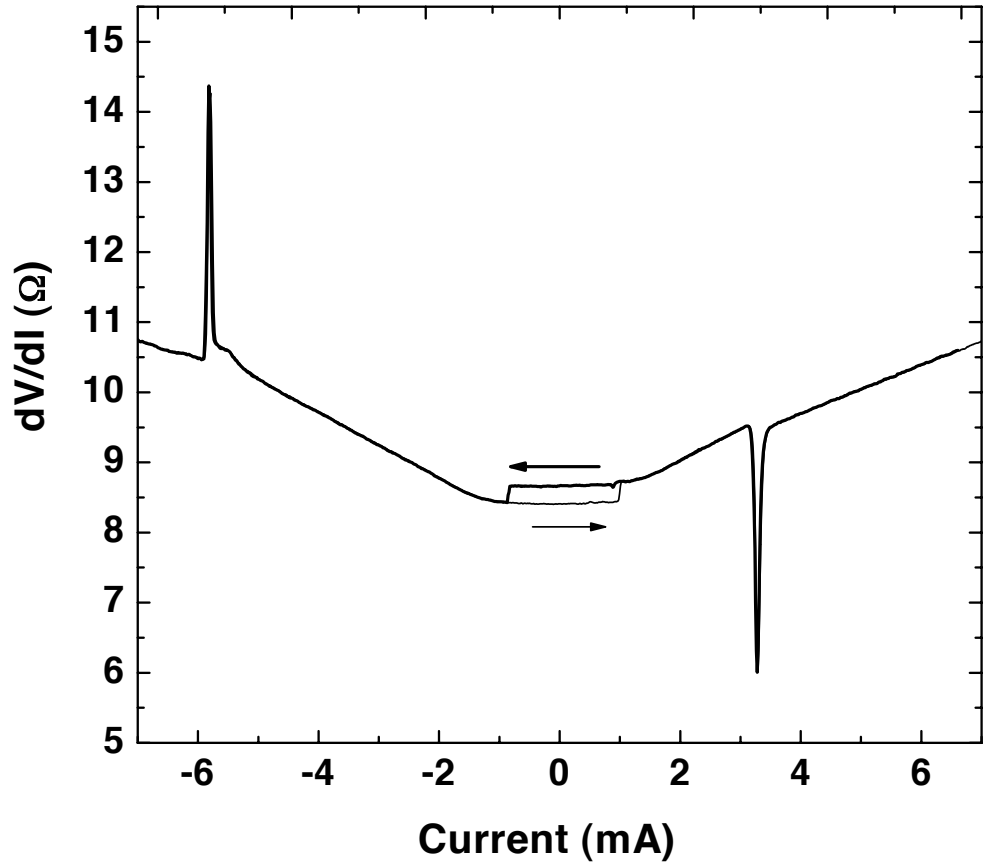


Figure 2.17: Differential resistance dV/dI vs. current for a $(Co_2/Cu_6/Co_{100})_{nm}$ device (CD05R31) at $T = 4.2$ K and zero field, for both sweep directions.

Although a thick-layer excitation is allowed by the Slonczewski model, the predicted currents at which this happens are much higher than what are actually observed. The threshold currents for excitations within the Slonczewski model typically scale with the layer thickness; thus the thick-layer threshold current should be 50 times that of the thin layer. Moreover, the current density is lower in the thick layer than the thin layer due to current spreading, raising the current threshold even higher. However, these excitations are occuring at currents only 3-5 times larger than the hysteretic switching events. One possible explanation may be that the excitations are not occuring throughout the thick layer, but only near the interface closest to the constriction. Slonczewski's approach cannot describe such excitations, as he considers only dynamics that are uniform throughout a layer's thickness. Bazaliy [56] has considered the effect of a spin-polarized current on the magnetic moments at the magnetic-nonmagnetic interface. Due to rapid precession of the spins as they enter the magnet, the layer absorbs all of the transferred angular momentum from the spins within approximately 10 nm of the interface. This will tilt the moments in this region relative to the rest of the layer. At a current density of approximately $10^8 - 10^9$ A/cm^2 for transition metal ferromagnets, the moments near the layer become unstable to spin-wave excitations. Since the effective volume of the excited region in the thick layer is much smaller than the total volume, the threshold currents are much smaller, and are within reach in my geometry.

In discussing the high-field dynamical excitations, most of the torque models only treat the initial instability, and do not discuss what happens when the current is increased further. As a result, I have only considered the first peak in differential resistance when comparing my data quantitatively to the model. However, as can be seen in Figs. 2.14-2.16, there are multiple excitations as the current is increased.

While these seem similar in nature to the initial excitation, their field dependence can be very complicated.

Figure 2.18a is a plot of dV/dI vs. I for a $(Co_4/Cu_6/Co_{100})_{nm}$ trilayer device at a field of 20 kOe applied in the plane of the layers. Four peaks can be distinguished. Although their precise nature cannot be determined from the data, it may very well be that each peak corresponds to a specific threshold for a new kind of dynamical excitation. The fact that they occur at discrete current levels is somewhat surprising, as the spin-wave spectrum is typically continuous once the lowest-order mode is excited. However, Slonczewski has found [49] that the symmetry of the geometry defines a set of discrete excitations, with the second threshold a few times larger in current than the initial one. Also, defects in the thin layer may inhibit further spin-wave generation until certain energy thresholds are reached. The complex nature of these additional excitations is made apparent when their field dependence is studied; a plot of the threshold current for the four excitations as a function of field H applied in the plane of the layers is shown in Figure 2.18b. While the first two features move roughly linearly to higher currents with increasing field, the higher-bias features move in a much more erratic fashion, even at times going to *lower* currents. In the Slonczewski model, the damping scales with the spin-wave frequency $\omega \sim \gamma H$, and so the threshold current should normally increase with field. There may be more complicated interactions occurring between the spin-waves that are not treated by the Slonczewski approach, such as direct scattering between spin-waves, or perhaps an indirect effect that arises from the spin-waves at lower currents changing the torque thresholds for the higher-current spin-waves. An AC measurement that could measure the frequency of the excitations would provide insight into their high-frequency nature and how they fit into the spin-wave

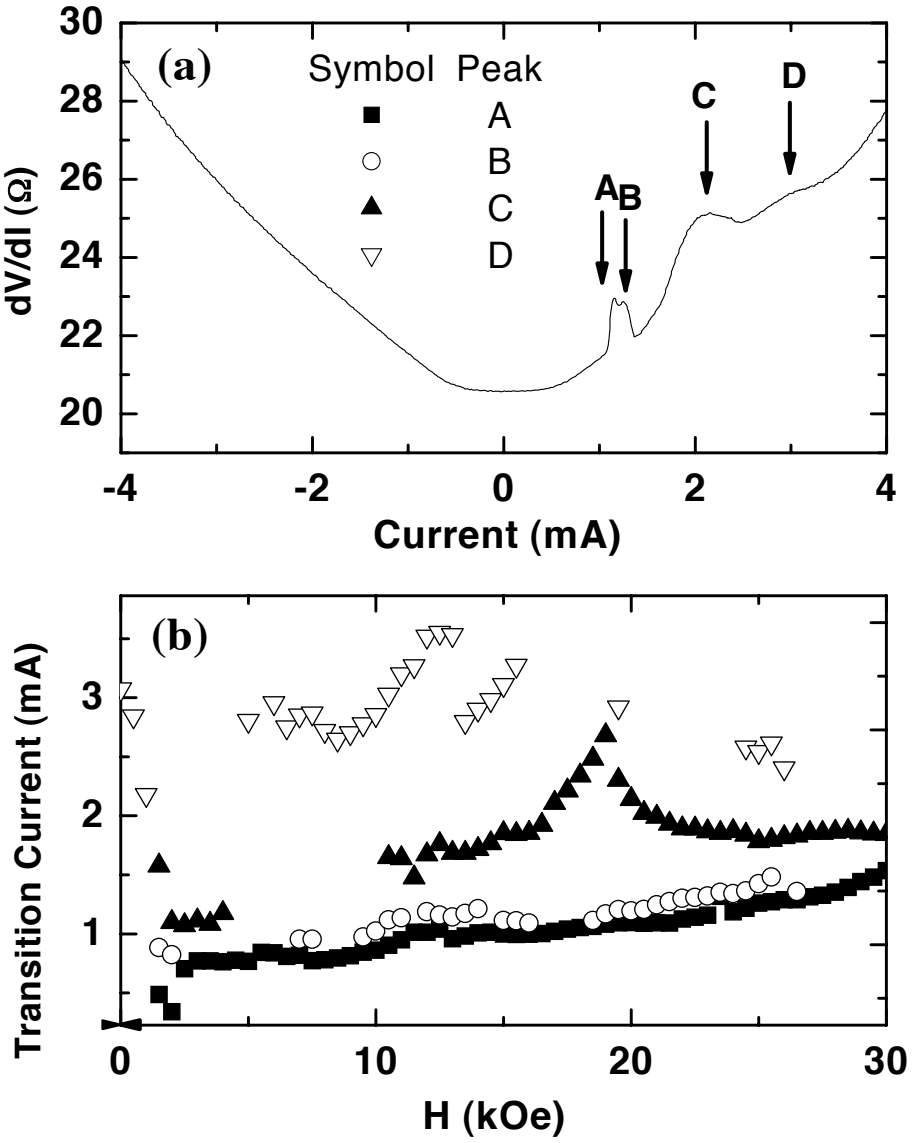


Figure 2.18: (a) Differential resistance dV/dI vs. current for a $(Co_4/Cu_6/Co_{100})_{nm}$ device (CC09R22) at $T = 4.2$ K and a field $H = 20$ kOe applied in the plane of the layers. Four distinct features are seen. (b) Field dependence of the four features in (a), with the field applied plane of the layers and varied from 30 kOe to zero.

spectrum of the thin film.

2.7 Final Thoughts

The nanoconstriction geometry has allowed me to confirm the basic prediction of spin-transfer theory: that a spin-polarized current, if large enough, can alter the magnetization state of a small ferromagnetic system due to the exchange coupling between them. At low magnetic fields, a domain with two stable directions can be controllably switched between those directions by applying a current of the appropriate magnitude and sign. If the field is large enough that only one direction is allowed, then the current will cause the moment to precess around the field. These phenomena suggest new ways of exploring and controlling the physics of magnetic systems at the nanometer size scale. However, to truly gain a quantitative understanding of spin-transfer, we need greater control over the properties of the physical system than is possible in the nanoconstriction geometry. In Chapters 4 and 5 I tackle this issue experimentally, by moving to a device geometry in which the excited domain is created with greater precision. In the next chapter, I proceed from a more theoretical perspective, by connecting spin-transfer torque to the microscopic properties of the magnetic trilayer system.

Bibliography

[1] K. S. Ralls, R. A. Buhrman, and R. C. Tiberio, App. Phys. Lett. **55**, 2459 (1989).

[2] K. S. Ralls, Dissertation, Cornell University, Ithaca, NY (1990).

[3] D. C. Ralph, Dissertation, Cornell University, Ithaca, NY (1994).

[4] R. N. Louie, Dissertation, Cornell University, Ithaca, NY (1997).

[5] S. K. Upadhyay, Dissertation, Cornell University, Ithaca, NY, (1998).

[6] M. M. Deshmukh *et al.*, App. Phys. Lett. **75**, 1631 (1999).

[7] F. J. Himpsel *et al.*, Adv. Phys. **47**, 511 (1998).

[8] S. S. P. Parkin, R. Bhadra, and K. P. Roche, Phys. Rev. Lett. **66**, 2152 (1991).

[9] I. K. Yanson, Zh. Eksp. Teor. Fiz. **66**, 1035 (1974) [Sov. Phys. JETP **39**, 506 (1974)].

[10] N. I. Bogatina and I. K. Yanson, Zh. Eksp. Teor. Fiz. **63**, 1312 (1972) [Sov. Phys. JETP **36**, 692 (1973)].

[11] A. G. M. Jansen, A. P. van Gelder, and P. Wyder, J. Phys. C: Solid St. Phys. **13**, 6073 (1980).

[12] A. M. Duif, A. G. M. Jansen, and P. Wyder, J. Phys.: Condens. Matter **1**, 3157 (1989).

[13] Yu. V. Sharvin, Zh. Eksp. Teor. Fiz. **48**, 984 (1965) [Sov. Phys. JETP **21**, 655 (1965)].

[14] K. S. Ralls, R. A. Buhrman, Phys. Rev. B. **44**, 5800 (1991).

[15] K. S. Ralls, D. C. Ralph, and R. A. Buhrman, Phys. Rev. B **47**, 10509 (1993).

[16] D. C. Ralph, R. A. Buhrman, Phys. Rev. Lett. **69**, 2118 (1992).

[17] D. C. Ralph *et al.*, Phys. Rev. Lett. **72**, 1064 (1994).

[18] D. C. Ralph, R. A. Buhrman, Phys. Rev. Lett. **72** 3401 (1994).

[19] S. K. Upadhyay *et al.*, Phys. Rev. Lett. **81**, 3247 (1998).

[20] S. K. Upadhyay, R. N. Louie, and R. A. Buhrman, App. Phys. Lett. **74**, 3881 (1999).

[21] M. V. Tsoi, A. G. M. Janes, and J. Bass, J. App. Phys. **81**, 5530 (1997).

[22] K. P. Wellock *et al.*, Phys. Rev. B **60**, 10291 (1999).

[23] S. J. C. H. Theeuwen *et al.*, App. Phys. Lett. **75**, 3677 (1999).

[24] S. J. C. H. Theeuwen *et al.*, App. Phys. Lett. **77**, 2370 (2000).

[25] Yay!

[26] W. H. Rippard and R. A. Buhrman, App. Phys. Lett. **75**, 1001 (1999).

[27] R. F. Soohoo, Magnetic Thin Films, Harper and Row, New York (1965).

[28] A. Hutten *et al.*, Phys. Status Solidi A **189**, 327 (2002).

[29] R. M. Bozorth, Ferromagnetism, IEEE Press, Piscataway, NJ (1993).

[30] H.-J. Kim, B.-I. Lee, and S.-K. Joo, J. App. Phys **81**, 3995 (1997).

[31] J. L. Vossen and W. Kern, Thin Film Processes, Academic Press, New York (1978).

[32] K. Bussmann *et al.*, App. Phys. Lett. **75**, 2476 (1999); **78**, 2029 (2001).

[33] J. A. Katine, F. J. Albert, and R. A. Buhrman, App. Phys. Lett. **76**, 354 (2000).

[34] Note that this nonuniform current also enhances the asymmetry in spin-transfer effects on the two layers, which is crucial to the current-direction asymmetry described in Chapter 1.

[35] J. C. Slonczewski, J. Magn. Magn. Mater. **159**, L1 (1996).

[36] M. D. Stiles, J. App. Phys. **79**, 5805 (1996).

[37] J. Miltat *et al.*, J. App. Phys. **89**, 6982 (2001).

[38] If I were to perform a more formal extension of my single domain analysis——which would still, I emphasize, be oversimplified relative to a full micromagnetic simulation—— I would add a phenomenological angular momentum sink term to the LLG equation, and derive the critical currents from there.

[39] P. Vargas and D. Altbir, Phys. Rev. B **62**, 6337 (2000).

[40] H. Kubota, M. Satao, and T. Miyazaki, Phys. Rev. B **52**, 343 (1995).

[41] H. Hasegawa, Phys. Rev. B. **47**, 15080 (1993); J. App. Phys **79**, 6376 (1996).

[42] Frank Albert has performed a far more systematic study of the effects of layer thickness on the critical currents in nanopillars; see F. J. Albert *et al.*, preprint (2002).

[43] At times a device can exhibit similar negative bias features at zero applied field; however, once a large field is applied and then returned to zero, most devices that exhibit simple two-state switching do not show negative-bias features at zero current.

[44] A broad asymmetry due to thermoelectric effects may be the cause of the gradual negative slope of the resistance difference at high currents in Fig. 2.12 [4]. I explore thermoelectric effects in more detail in Chapter 5.

[45] I. O. Kulik, R. I. Shekhter, and A. N. Omelyanchouk, Solid State Commun. **23**, 301 (1977).

[46] L. Berger, Phys. Rev. B. **54**, 9353 (1996).

[47] L. Berger, Phys. Rev. B. **59**, 11465 (1999).

[48] Y Tserkovnyak and A. Brataas, Phys. Rev. Lett. **88**, 117601 (2002).

[49] J. Slonczewski, J. Magn Magn. Mater. **195**, L261 (1999).

[50] M. Tsoi *et al.*, Phys. Rev. Lett. **80**, 4281 (1998).

[51] M. Tsoi *et al.*, Nature **406**, 46 (2000).

[52] F. Schreiber *et al.*, Solid St. Comm. **93**, 965 (1995).

[53] H. Suhl, J. Phys. Chem. Solids. **1**, 209 (1957).

[54] C. H. Back *et al.*, Science **285**, 864 (1999).

[55] The damping may also be enhanced due to the presence of the magnetic-nonmagnetic interface. I discuss this possibility in more detail when looking at data on nanopillars, in Chapter 4.

[56] Ya. B. Bazaliy, B. A. Jones, and Shou-Cheng Zhang, Phys. Rev. B. **57**, R3213 (1998).

Chapter 3

Deriving Spin-Transfer Torques from the Spin-Dependent Scattering Properties of Magnetic Layers

In the previous chapter, I presented data demonstrating that spin-polarized currents, at large current densities, can controllably reverse magnetic domains or generate dynamical excitations in magnetic trilayer systems. The symmetry and magnitude of the currents required to generate these excitations were consistent with predictions of models in which spin-polarized electrons exert torques on the moments of the magnetic layers through spin-dependent exchange scattering. However, the only discussion of how such scattering generates a torque was in Chapter 1, where an idealized thought experiment involving perfect spin-filters was used as a simple illustration. In this chapter, I finally roll up my sleeves (and button up my shirt, as I will be discussing theory) and discuss spin-transfer torques in more imperfect

systems. In work done with colleagues [21], I employ the Landauer-Büttiker formalism of scattering in mesoscopic systems to relate the spin-dependent scattering properties of magnetic layers to the torques that are generated within them. The formalism we develop is very general, allowing us to explore a wide range of transport regimes, from fully ballistic to diffusive scattering. Although we will find that the torques in my Co/Cu/Co devices are best described in the ballistic limit of our model, spin-transfer torques survive even if transport between magnetic layers is diffusive, so that we may treat a wide array of magnetic systems. We also find that, by choosing materials with different scattering properties, the torques on the magnetic layer can be of either sign for a given current. Finally, I apply this formalism to my experimental data to attain a deeper understanding of the microscopics of spin-transfer, and find that a rigorous treatment of the scattering properties of magnetic-nonmagnetic interfaces over the full Fermi surface is required to properly explain the data.

3.1 Spin and the Landauer-Büttiker Scattering Formalism

My initial illustration of spin-transfer in Chapter 1 treats a magnetic layer as a perfect spin-filter. This means that, in a transport experiment where electrons are sent perpendicularly through the layer, only electrons with spins aligned with the magnetic spin moment (spin-up) can pass through the film; those electrons with spins antialigned with the moment (spin-down) are completely reflected. If the electron is polarized in some direction between these two extremes, the wavefunction is split by the layer into transmitted spin-up and reflected spin-down components.

This quantum-mechanical splitting gives rise to a transfer of angular momentum from the current to the moment, which for a steady current of electrons acts as an effective torque.

The limit of perfect spin-filtering allows us to translate this transfer of angular momentum into simple visual terms as in Figure 1.4, where the torque can be read directly from the difference in directions between the spins of the incoming and outgoing electrons. However, with the possible exception of half-metallic oxides such as LSMO [1] and CrO_2 [2], most materials (e.g., transition metal ferromagnets) do not polarize currents with 100% efficiency; in other words, both spin-up and spin-down electrons can pass through a magnetic layer, albeit with different degrees of success. If quantitative comparison is to be made between the predictions of the spin-transfer model and the observed current-induced excitations, it is therefore important that the simple scattering picture of Chapter 1 can be extended to treat imperfect spin-filters.

This can be achieved by employing the Landauer-Büttiker formalism [3, 4], which connects the microscopic scattering properties of small systems to macroscopic transport properties, i.e., currents and voltages. Consider a system connected to two large electron reservoirs via narrow one-dimensional leads (Figure 3.1). The reservoirs are taken as macroscopic, so that each have well-defined chemical potentials, μ_L and μ_R. If $\mu_L \neq \mu_R$, then a current will flow through the system. The system itself can be of arbitrary shape and extent, but I will assume that it has some characteristic size $l < l_{inel}$, where l_{inel} is the inelastic scattering length of the material. The leads are assumed to be ideal, meaning that electrons pass ballistically through them without any scattering. Consequently, all of the inelastic electron scattering occurs only within the reservoirs, and we can define chemical potentials only there. Electron flow

in the leads and the system is consequently nonequilibrium, and can be thought of as a superposition of ballistic electron states, with the appropriate momentum-space Fermi distributions, injected from each reservoir.

These electrons, once they enter the system proper, will scatter elastically. As a result, only a certain portion of the entering electrons will be transmitted through the system from one reservoir to the other, while the rest will be reflected back into the original reservoir with reversed momentum. Choosing plane wave states in the lead $\sim e^{ikx}$, where x is distance along the system and k the wavenumber, we will in general have incoming and outgoing waves in both directions, with amplitudes A, A', B, and B', as defined in Fig. 3.1.

Given the incoming wave amplitudes A, A', we can calculate the outgoing wave amplitudes B', B using the reflection and transmission properties of the system. This can be written in matrix form [5, 6]:

$$\begin{bmatrix} B' \\ B \end{bmatrix} = S \begin{bmatrix} A \\ A' \end{bmatrix}, S = \begin{bmatrix} r & t' \\ t & r' \end{bmatrix}. \tag{3.1}$$

Here S is called the scattering matrix; its components, r, t, r', t' are, are, respectively, the complex reflection and transmission coefficients (to be distinguished from the *probabilities* $R = |r|^2, T = |t|^2$) for states incident from the left, and the coefficients for states incident from the right. Although the microscopic origins of the scattering in the system may be in general quite complicated, the Landauer-Büttiker formalism allows us to express the transport properties of the system entirely in terms of the scattering matrix S.

The transport formalism described above is strictly one-dimensional. It can be extended to more realistic systems by treating the leads as a superposition of one-dimensional channels, with the number of channels set by the quantization condition

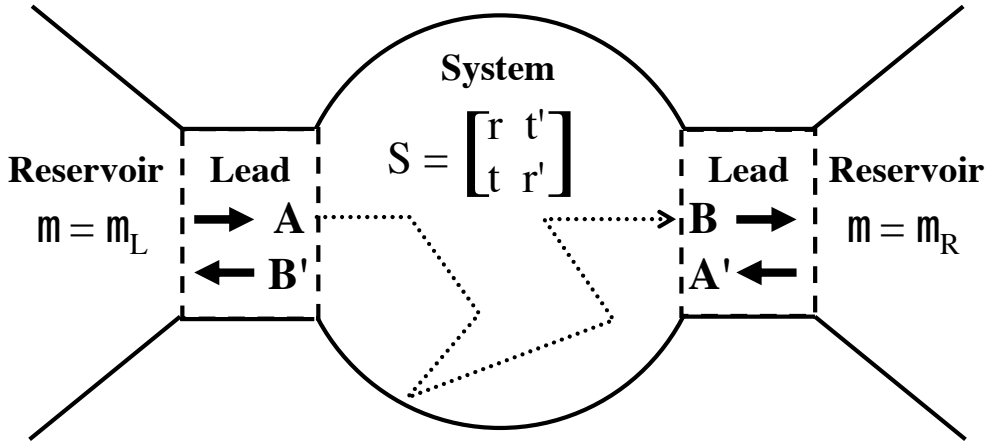


Figure 3.1: Schematic of Landauer-Büttiker scattering formalism. A system is attached to two macroscopic electron reservoirs, with chemical potentials μ_L, μ_R, via ballistic one-dimensional leads. Electrons enter the system through channels in the leads; scattering in the system causes electrons to be reflected back through the initial lead or transmitted through the other lead. The outgoing amplitudes B', B can be related to the incoming amplitudes A, A' through the scattering matrix S associated with the system. For the general case of $2N_{ch}$ channels, the amplitudes are $2N_{ch}$-long vectors and S a $4N_{ch} \times 4N_{ch}$ matrix.

transverse to the conduction direction. For example, an ideal box extended in the x-direction but restricted to a square of length $2a$ in the y and z directions would have single-electron eigenenergies

$$E(k_x, n_y, n_z,) = \frac{\hbar^2\pi^2}{8ma^2}({n_y}^2 + {n_z}^2) + \frac{\hbar^2{k_x}^2}{2m}, \tag{3.2}$$

where $n_y, n_z \geq 0$ are the quantization numbers in the y and z directions, respectively, k_x the (continuous) wavenumber in the x direction, and m the electron mass. The number of channels is determined by the number of choices of (k_x, n_y, n_z) which set the above expression equal to the Fermi energy E_f, as only Fermi-surface electrons participate in conduction at low biases. For this square geometry the number of channels is $2N_{ch} \sim \frac{8(ak_F)^2}{\pi^2}$, with N_{ch} momentum channels multiplied by a factor of 2 for spin.

For multiple channels the four elements of the scattering matrix are themselves generalized into $4N_{ch} \times 4N_{ch}$ matricies:

$$S = \begin{bmatrix} r & t' \\ t & r' \end{bmatrix}, r = \begin{bmatrix} r_{11} & \cdots & r_{1(2N_{ch})} \\ \vdots & & \vdots \\ r_{(2N_{ch})1} & \cdots & r_{(2N_{ch})(2N_{ch})} \end{bmatrix}, etc., \tag{3.3}$$

where, for example, r_{ij} is the coefficient for incident electrons in the j-th channel on the left side which are scattered into the i-th outgoing channel on the left side. Although the Landauer-Büttiker formalism can be useful in systems where quantum confinement makes the number of channels small [7], there is no formal limit to the number of channels that it may treat. As a result, we may freely apply it to both of my device geometries: the nanoconstriction, where $2N_{ch} \sim 3600$, and the nanopillar, where $2N_{ch} \sim 300,000$.

The great utility of this formalism for our purposes is that it allows us to describe spin-transfer torques in terms of the generic scattering properties of the magnetic

trilayer system. Slonczewski [8] solved a one-dimensional version of the scattering problem for the trilayer geometry by treating the magnetic layers as square spin-dependent potential barriers; the difference between the barrier heights for spin-up and spin-down electrons was set by a mean-field approximation of exchange. However, more rigorous treatments of the spin-dependent scattering that occurs when an electron crosses a magnetic-nonmagnetic interface show that exchange energy alone does not determine transport; rather, transmission across an interface depends on the specifics of how the detailed band structures of the two materials match at the interface [9, 10]. The reflection and transmission coefficients which result from the band structure calculations can be used directly as inputs into the Landauer-Büttiker formalism. This is essentially a "black box" approach to the scattering problem, which allows us to incorporate the results of full *ab initio* calculations without having to perform the calculations ourselves. In addition, the scattering coefficient approach allows us to express the scattering in a more quantum-mechanically accurate manner than Slonczewski. His barrier calculations only treated electrons as being either completely transmitted or completely reflected from the magnetic layer; the polarization of the layer was expressed in terms of the fraction of the total number of electrons that were transmitted. Our approach allows for partial reflections of *single* coherent electrons, which is likely more valid for electrons that maintain their phase across the layer.

3.2 Warmup Case: Single Magnetic Layer as Non-ideal Spin Filter

As a simple example of the Landauer-Büttiker scattering approach applied to magnetic systems, I return to the initial case of Chapter 1, where a single electron is incident perpendicularly on a magnetic layer (Figure 3.2). The layer lies in the $y-z$ plane and has its spin moment along the z-axis, while the incoming electron, traveling in the $+x$ direction, is polarized in the $z-x$ plane at some angle θ to the $z-$axis. The layer, rather than being a perfect spin-filter, now has generalized scattering coefficients associated with it. To write down the scattering matrix S, we first need to determine how many channels are involved in the problem. For an incident electron at the Fermi energy with wavevector $\vec{k}_F = (k_x, k_y, k_z\rangle$ that only undergoes elastic scattering, the channel is set by the momentum $\vec{k}_{transverse} = (0, k_y, k_z)$ transverse to current flow. If the magnetic interface is rough, electrons can be randomly scattered into a new direction $\vec{k}'_F = (k'_x, k'_y, k'_z)$, which constitutes a different channel. Thus the full number of channels $2N_{ch}$ must be considered when the interface scattering is diffuse. However, if the interfaces are very smooth and the materials are well lattice-matched, such as Cu and Co [10], then we may expect the scattering to be specular, meaning that $\vec{k}_{transverse}$ is conserved during the scattering process. In this case the channels that are each associated with a single momentum $\vec{k}_{transverse}$ can be treated separately, greatly simplifying the problem. I discuss the problem of diffuse scattering later on.

Assuming specular scattering, then, the scattering matrix S for the magnetic layer is block diagonal, with each 4×4 block consisting of 2×2 reflection and

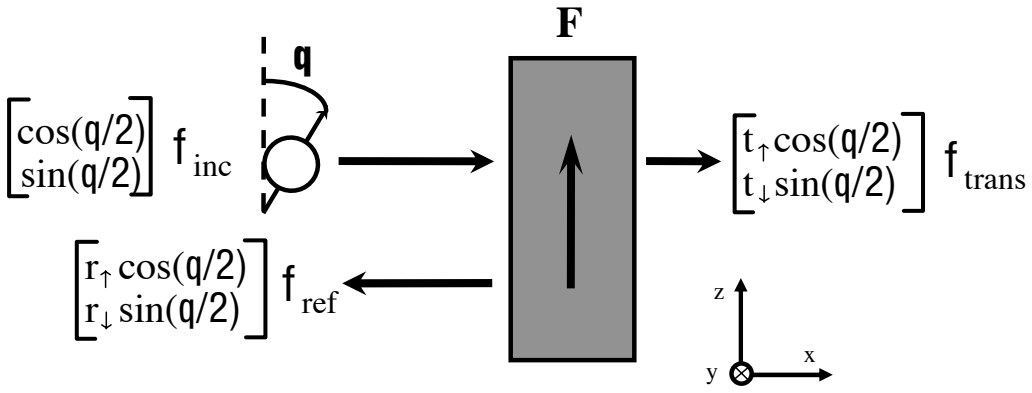


Figure 3.2: Scattering of an incident spin-polarized electron by a single magnetic layer, for the case of general spin-filtering. The total electron wavefunction is composed of a two-component spinor and a spatial wavefunction $\phi_{inc}, \phi_{trans}, \phi_{ref}$. The transmitted and reflected waves are determined by the scattering matrix of the layer.

transmission matrices, e.g.,

$$r = \begin{bmatrix} r_{\uparrow\uparrow} & r_{\uparrow\downarrow} \\ r_{\downarrow\uparrow} & r_{\downarrow\downarrow} \end{bmatrix}, etc., \tag{3.4}$$

where up ("$\uparrow$") and down ("$\downarrow$") are defined relative to the direction of the spin moment of the magnetic layer. The coefficients with $\uparrow\uparrow, \downarrow\downarrow$ subscripts are associated with transmission and reflection within each spin channel; I call these the spin-filtering coefficients. The off-diagonal elements with $\uparrow\downarrow, \downarrow\uparrow$ subscripts are the spin-flip coefficients, describing scattering processes within the layer that do not conserve spin. The coefficients themselves follow charge conservation laws, e.g., $|r_{\uparrow\uparrow}|^2 + |r_{\downarrow\uparrow}|^2 + |t_{\uparrow\uparrow}|^2 + |t_{\downarrow\uparrow}|^2 = 1$, etc.

Spin-flip processes may be important in magnetic multilayers, both with respect to the giant magnetoresistance effect [11] and with respect to spin-transfer torques [12]. However, the off-diagonal elements add a complication to the determination of spin-transfer torques beyond the increased calculational complexity. Due to spin-orbit coupling, processes that are normally independent of spin, such as electron-phonon scattering, can result in a spin-flip [13]. As a result, the total spin angular momentum of the conduction electron-plus-moment system is not conserved, making it more difficult to determine the torques on the moments. Also, these processes can often be inelastic, violating the assumption of phase coherence implicit in the Landuaer-Büttiker formalism. However, current-perpendicular-to-plane (CPP) transport measurements on magnetic multilayers [14, 15] have found that typical spin mean free paths in Co ($6 - 15$ nm) are larger than the typical thickness of the thin layer in my devices ($2 - 4$ nm), suggesting that spin-flips due to bulk scattering processes should not have a great effect on the spin-polarized current. For certain special materials combinations (e.g., Nb/Cu), there have been reports of enhanced

spin-flip interface scattering due to alloying at the interface [16], but no specifically interfacial contribution to spin-relaxation has been observed for the materials combinations discussed in this dissertation [15]. As a result, for the rest of this chapter I will neglect explicit spin-flip processes and assume that the magnetic layers scatter electrons via spin-filtering processes alone [17].

With this restriction, S becomes

$$S = \begin{bmatrix} r_\uparrow & 0 & t'_\uparrow & 0 \\ 0 & r_\downarrow & 0 & t'_\downarrow \\ t_\uparrow & 0 & r'_\uparrow & 0 \\ 0 & t_\downarrow & 0 & r'_\downarrow \end{bmatrix}, \tag{3.5}$$

where I have made the notation changes $r_\uparrow = r_{\uparrow\uparrow}$, etc. The wavefunction of the incident electron in Fig. 3.2 can be written as

$$\psi_{inc} = \begin{bmatrix} \cos(\theta/2) \\ \sin(\theta/2) \end{bmatrix} \phi_{inc}(\vec{r}), \tag{3.6}$$

where $\phi_{inc}(\vec{r})$ is the spatial part of the wavefunction and ψ_{inc} is written in two-component spinor notation. Applying S to this incident state yields the reflected wave

$$\psi_{ref} = \begin{bmatrix} r_\uparrow \cos(\theta/2) \\ r_\downarrow \sin(\theta/2) \end{bmatrix} \phi_{ref}(\vec{r}), \tag{3.7}$$

and the transmitted wave on the other side

$$\psi_{trans} = \begin{bmatrix} t_\uparrow \cos(\theta/2) \\ t_\downarrow \sin(\theta/2) \end{bmatrix} \phi_{trans}(\vec{r}). \tag{3.8}$$

How do we proceed to relate these scattered waves to the torque generated by the scattering process? As I mentioned earlier, I have restricted my focus to spin-filtering scattering events that directly involve the exchange coupling between the

conduction electrons and the spin moment of the magnetic layer. Thus any spin angular momentum that leaves the current must be taken up by the layer. As a result, we can determine the rate of angular momentum deposited in the layer – the torque – by examining how the angular momentum in the current differs on either side of the layer. The quantity that provides us with this information is the spin flux, which is a tensor that is defined in analogy with probability flux (number current density), a vector [18]. For a current in the x-direction (translational symmetry along the y and z-directions), the spin flux can be projected onto the number current direction to get a vector $\vec{\Phi} = (\Phi_x, \Phi_y, \Phi_z)$. This is the density of vector angular momentum that crosses the $y-z$ plane at a particular x-value per unit time. Given a spinor wavefunction of the form $\psi = \begin{bmatrix} \psi_\uparrow \\ \psi_\downarrow \end{bmatrix}$, the spin flux can be written as [8, 19]

$$\vec{\Phi} = \frac{\hbar^2}{2m} Im\left[\psi^\dagger \vec{\sigma} \frac{\partial}{\partial x}\psi\right], \tag{3.9}$$

where $\vec{\sigma}$ is the set of Pauli spin matrices. The torque is then simply the difference between the spin flux on the left side of the magnetic layer and that on the right side.

In general any Bloch wave could be used for the spatial components of the waves ϕ. For simplicity I choose plane wave states, so that $\phi_{inc} = \phi_{trans} = \frac{1}{\sqrt{2\pi}} e^{ik_x x} f(y,z)$, $\phi_{ref} = \frac{1}{\sqrt{2\pi}} e^{-ik_x x} f(y,z)$, where $f(y,z) = e^{ik_y y + ik_z z}$. The phases of the incoming and transmitted waves may of course be different, but this information is contained in the scattering coefficients. Combining this with Eqns. (3.6)-(3.8) and inserting into Eqn. (3.9), the torque $\vec{\tau} = (\tau_x, \tau_y, \tau_z)$ is calculated as

$$\tau_x = \frac{\hbar^2 k_x}{4\pi m} \sin\theta (1 - Re[r_\uparrow^\dagger r_\downarrow + t_\uparrow^\dagger t_\downarrow]), \tag{3.10}$$

$$\tau_y = -\frac{\hbar^2 k_x}{4\pi m} \sin\theta \, Im[r_\uparrow^\dagger r_\downarrow + t_\uparrow^\dagger t_\downarrow], \tag{3.11}$$

$$\tau_z = 0. \tag{3.12}$$

We initially note that the torque always acts perpendicular to the moment, thus conserving the magnitude of the magnetization. The $\sin\theta$ factor also shows that the magnitude of the torque is proportional to the portion of the incoming spin transverse to the spin moment of the layer. However, the direction of the torque depends on the complex scattering coefficients, and in general points anywhere in the $x - y$ plane. This differs from the classic Slonczewski result, where $\tau_y = 0$. The discrepancy arises from the different ways the two approaches treat electron scattering. As noted earlier, Slonczewski only considers electrons that are fully transmitted or reflected by the magnetic layers. This can be equivalently expressed in our formalism as assigning transmission and reflection coefficients of either 0 or 1 to the layer. Since these are purely real quantities, the y-component of the torque vanishes, and the symmetry of our results reduce to the Slonczewski result.

However, by allowing for complex scattering coefficients, the scattering formalism can capture aspects of the physics not considered by Slonczewski's simpler model. We can gain insight into this physics by peeking inside the "black box" and observing how electrons scatter within the magnetic layer. In general a scattering process will involve both direct scattering from the two magnetic-nonmagnetic interfaces and travel between these interfaces within the layer. We can associate scattering coefficients with each interface, e.g., r_{NF} for reflection from an interface when the electron is incident from the normal metal, and r_{FN} for reflection when the electron is incident from the ferromagnet. These coefficients can be derived from rigorous band-structure calculations that determine how individual electron states match up at the interface [10]; in general the scattering coefficients are complex, although *ab initio* calculations for real materials systems have shown that the imaginary

parts are typically an order of magnitude smaller than the real parts [20, 18]. The overall reflection and transmission coefficients for the full magnetic layer r, t are constructed from a combination of these interface coefficients and phase factors from the paths the electrons take within the magnetic layer. The phase factors contain terms of the form $e^{ik_\uparrow L}, e^{ik_\downarrow L}$, where $k_\uparrow, k_\downarrow$ are the transverse wavevectors for up and down spins within the magnet and L is the thickness of the magnetic layer. Since the interface scattering is specular, the components of momentum transverse to current flow are conserved as the electron enters the magnet. However, due to the different local spin-dependent potentials in the ferromagnet [10], the x-component of momentum will change to conserve energy and will depend on spin, so that $k_{\uparrow,\downarrow} \neq k_x$ in general, and $k_\uparrow \neq k_\downarrow$. Consequently, the spin-up and spin-down components of the electron wavefunction within the magnet accumulate different phases as the electron propagates away from the interface, with the phase difference between the two components being $e^{i(k_\uparrow - k_\downarrow)x}$. This quantum-mechanical "beating" can be interpreted as a precession of the electron spin around the spin moment of the magnet, with precession length set by the exchange splitting of the band structure. Note that in Slonczewski's formalism, any electrons that enter the magnetic layer are fully aligned with the spin moment of the layer, so that precession cannot be considered.

We can combine both interface scattering and propagation within the layer into a single scattering coefficient by writing, e.g., the transmission coefficient $t_\uparrow$ as the following sum of scattering processes:

$$t_\uparrow = t_{NF,\uparrow} t_{FN,\uparrow} \Psi_\uparrow \left[1 + (r_{FN,\uparrow}\Psi_\uparrow)^2 + (r_{FN,\uparrow}\Psi_\uparrow)^4 + ...\right] \tag{3.13}$$

$$= t_{NF,\uparrow} t_{FN,\uparrow} \Psi_\uparrow \frac{1}{1 - (r_{FN,\uparrow}\Psi_\uparrow)^2}, \tag{3.14}$$

where $\Psi_{\uparrow,\downarrow} = e^{ik_{\uparrow,\downarrow}L}$. A similar expression can be written for $t_\downarrow$. The first term in

Eqn. (3.13) represents the portion of spin-up electrons that transmit freely through the layer, while the successive terms correspond to electrons that are reflected multiple times within the layer before finally emerging on the other side. Similarly, the reflection coefficient $r_\downarrow$ is

$$r_\uparrow = r_{NF,\uparrow} + t_{NF,\uparrow} r_{FN,\uparrow} t_{FN,\uparrow} (\Psi_\uparrow)^2 \left[1 + (r_{FN,\uparrow}\Psi_\uparrow)^2 + ...\right] \quad (3.15)$$

$$= r_{NF,\uparrow} + t_{NF,\uparrow} r_{FN,\uparrow} t_{FN,\uparrow} \frac{(\Psi_\uparrow)^2}{1 - (r_{FN,\uparrow}\Psi_\uparrow)^2}. \quad (3.16)$$

Note that this differs from the expression for the transmission coefficient in that the first reflection involves no propagation of the electron into the magnet at all. The various transmission and reflection scatterings are shown in Figure 3.3.

The coefficients as expressed in Eqns. (3.16) and (3.18) are only valid for a single coherent incident electron, whose wavefunction is clearly sensitive to the phase accumulated during scattering. The spin-transfer effect is not generated by a single electron but by a current made up of many electrons, however; these electrons will not in general be phase-coherent with one another. We consequently need to determine the average torque generated by a spread of incident electrons. There are various ways this average can be performed; later, when considering diffusive transport, it is most convenient to perform an average over the disorder in the system. Here I assume smooth interfaces and specular scattering, so it is easiest to consider an average over the angle of electron incidence. I assume all incoming electrons lie at the Fermi surface, so $|\vec{k}| = |\vec{k}_F|$ is constant; the average then amounts to an average over the transverse wavenumber k_x. Since the wavevectors inside the magnetic layer are coupled to k_x via the conserved transverse momentum components, this is also an average over $k_\uparrow$ and $k_\downarrow$.

If we insert Eqns. (3.16) and (3.18) into Eqns. (3.10) and (3.11), we find products

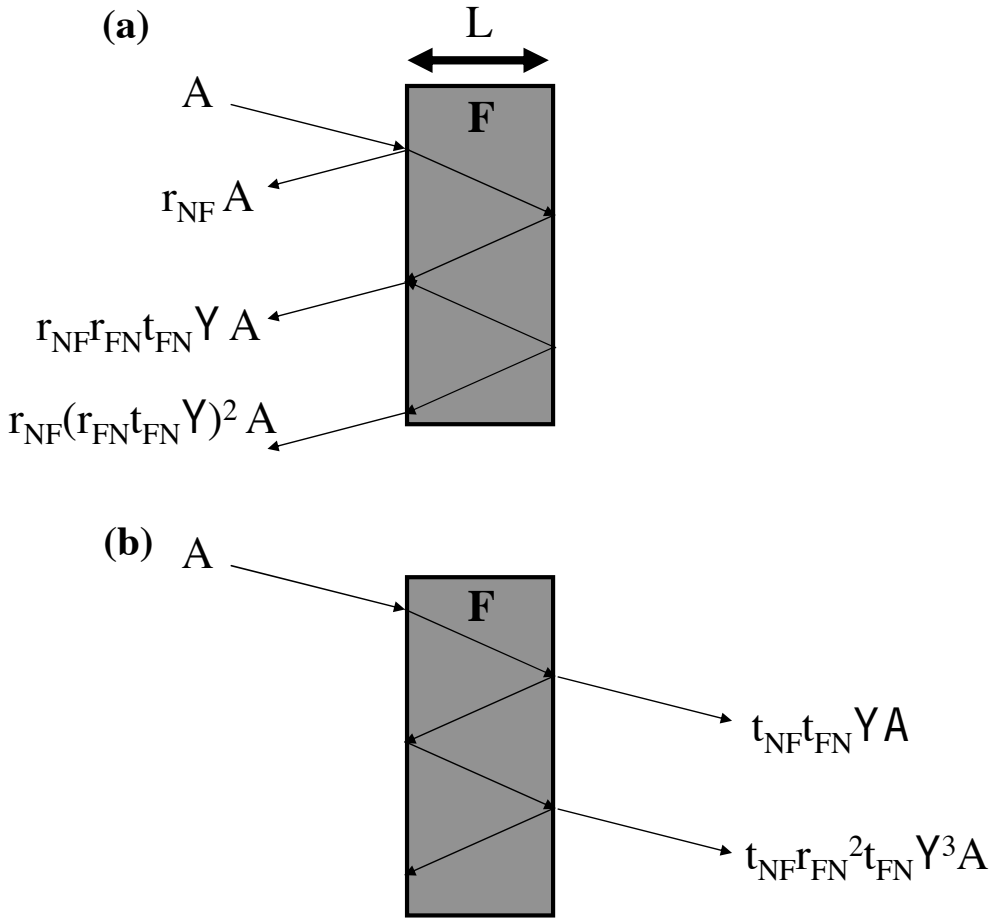


Figure 3.3: Scattering off of a magnetic layer of thickness L in the clean ballistic limit. An incident electron with amplitude A is scattered from each of the non-magnetic interfaces, with associated coefficients $r_{NF}, r_{FN}, t_{NF}, t_{FN}$. In addition, the electron picks up a phase factor $\Psi = e^{ik_{\uparrow,\downarrow}L}$ each time it traverses the layer. The full reflection and transmission coefficients can be written as a coherent sum of the various processes that can either scatter the electron backwards (a) or forwards (b).

of the form

$$t_\uparrow^\dagger t_\downarrow = t_{NF,\uparrow} t_{NF,\downarrow} t_{FN,\uparrow} t_{FN,\downarrow} \Psi_\uparrow^\dagger \Psi_\downarrow \frac{1}{(1-(r_{FN,\uparrow}\Psi_\uparrow^\dagger)^2)\,(1-(r_{FN,\downarrow}\Psi_\downarrow)^2)}, \tag{3.17}$$

and

$$r_\uparrow^\dagger r_\downarrow = r_{NF,\uparrow} r_{NF,\downarrow} + \left(\Psi_\uparrow^\dagger\right)^2 f_1 + (\Psi_\downarrow)^2 f_2 + \left(\Psi_\uparrow^\dagger \Psi_\downarrow\right)^2 f_3, \tag{3.18}$$

where I have highlighted the phase factor of each term of the product in Eqn. (3.18), hiding the rest of the symbols for brevity within the quantities f_1, f_2, f_3. An average over k_x will average both over the phase factors and the interface coefficients. The thickness of the layer L, typically a few nm, is significantly larger than typical values of k_F^{-1}, a few $\mathring{A}$. The phase factors $\Psi, \Psi^\dagger$ will consequently oscillate rapidly during computation of the average. Terms containing the product $\Psi^\dagger\Psi$ will not oscillate as rapidly, since their precession length is set by the exchange splitting $|k_\uparrow - k_\downarrow|$, which is smaller than k_F. However, for most transition-metal ferromagnetic systems of interest (e.g., Co, Fe) [18], $|k_\uparrow - k_\downarrow|^{-1}$ is still larger than typical layer thicknesses L, so that these terms also rapidly oscillate as the average is taken. In addition, the interface coefficients will vary over the average, but their variation with k_x is slower [10]. As a result, all terms that contain a phase factor $\Psi_{\uparrow,\downarrow}$ should average out to zero. This completely eliminates the contribution from the transmission coefficients, and eliminates all contributions from the reflection coefficients except that from the initial reflection. The vanishing of the contribution of transmission to the torque can be thought of in physical terms as a consequence of the incoherent summation of electrons that propogate within the magnet. Since these electrons all precess around the spin moment of the magnet with different precession lengths, their angular momentum perpendicular to the moment of the magnet sums to zero, and therefore the net torque also sums to zero.

Using these results, the torque can be written as

$$\tau_x = \frac{\hbar^2}{4\pi m} \sin\theta Re\left[\langle k_x\rangle - \left\langle k_x r^{\dagger}_{NF,\uparrow} r_{NF,\downarrow}\right\rangle\right], \tag{3.19}$$

$$\tau_y = \frac{\hbar^2}{4\pi m} \sin\theta Im\left[\langle k_x\rangle - \left\langle k_x r^{\dagger}_{NF,\uparrow} r_{NF,\downarrow}\right\rangle\right], \tag{3.20}$$

The z-component of the torque remains zero. As expressed here, this torque is not the torque per current, but the torque per incident electron; it must be divided by the number current that actually makes it through the layer to express it in a form similar to the Slonczewski term in the LLG equation. Of course, even after averaging, our torque does *not* look like the Slonczewski result; due to the complex nature of the interface reflection coefficients, it lies in the $x-y$ plane. While τ_x is the standard Slonczewski torque, τ_y can be thought of as a rotational torque [18] that drives the magnet perpendicular to the plane formed by the magnet's spin moment and the current's polarization direction. As noted earlier, though, this contribution to the total torque is typically an order of magnitude smaller than the Slonczewski torque when theoretically calculated values of the scattering coefficients are inserted [20, 18]. I have written the torque in terms of the real and imaginary parts of the quantity $\langle k_x\rangle - \left\langle k_x r^{\dagger}_{NF,\uparrow} r_{NF,\downarrow}\right\rangle$, to highlight the agreement between this calculation and the calculation of the so-called mixing conductance $G^{\uparrow\downarrow}$, derived in an alternative circuit formalism of spin-transfer that assumes diffusive transport [20, 31]. In Section 3.3.2 I compare our formalism to this circuit theory.

So what has this exercise shown us? For starters, it demonstrates that we can derive a very general expression for the torque, which in the limiting case of real scattering coefficients reduces to the Slonczewski result. The flexibility of our approach allows us to note an interesting symmetry with respect to the scattering properties of the layer. As long as $r_\uparrow \neq r_\downarrow$, a finite torque will be exerted on the spin moment of the layer. However, the sign of the torque is the same regardless of whether $r_\uparrow > r_\downarrow$

or $r_\uparrow < r_\downarrow$. As a result, the symmetry of the torque does not vary whether the magnet transmits down-spins or up-spins more easily. We can understand this by noting that the torque can be equivalently calculated using the difference in spin fluxes between incoming and outgoing waves, rather than the difference in the spin fluxes of the wavefunctions on the left and right sides of the layer. Thus the torque is not sensitive to interchanging the reflected and transmitted waves, i.e., changing the sign of spin asymmetry in the scattering coefficients. This is an important result that goes beyond the work of Slonczewski, who only considered materials for which $r_\uparrow < r_\downarrow$; as we will see, it will have important consequences when we consider the full trilayer system.

3.3 Adding a Second Magnetic Layer

The trilayer geometry is completed by adding a second magnetic layer to the above system. The presence of this second layer has the effect of allowing for multiple scattering of the electrons between the two layers, which gives rise to the asymmetry of the torque with respect to current direction. We can take into account the multiple scatterings in a manner similar to the internal scatterings of a single magnetic layer in the ballistic limit, but, as the geometry has become more complex, it is better to approach this problem in a more formal way. The formalism I outline in this section is work done in collaboration with Xavier Waintal and Piet Brouwer [21].

Figure 3.4 shows a schematic of the trilayer system. Rather than a single scattering matrix S, we now have three: S_1, S_2, and S_N, for the thick magnetic layer $F1$, the thin magnetic layer $F2$, and the normal layer N in between. We provide the normal metal spacer with its own scattering matrix so that we may incorporate either ballistic transport or diffusive scattering in the normal layer into the calculations.

When an electron in a single channel passes through this trilayer, it is scattered by each of the layers so that there are general left-going (L) and right-going (R) wave amplitudes ψ_{iL}, ψ_{iR} at the four spots $i = 0, 1, 2, 3$ shown in Fig. 3.4. The scattering matrices connect the amplitudes on either side of each layer:

$$\begin{bmatrix} \psi_{0L} \\ \psi_{1R} \end{bmatrix} = S_1 \begin{bmatrix} \psi_{0R} \\ \psi_{1L} \end{bmatrix}, \tag{3.21}$$

$$\begin{bmatrix} \psi_{1L} \\ \psi_{2R} \end{bmatrix} = S_N \begin{bmatrix} \psi_{1R} \\ \psi_{2L} \end{bmatrix}, \tag{3.22}$$

$$\begin{bmatrix} \psi_{2L} \\ \psi_{3R} \end{bmatrix} = S_2 \begin{bmatrix} \psi_{2R} \\ \psi_{3L} \end{bmatrix}. \tag{3.23}$$

With two magnetic layers in the system, we must consider the possibility that their spin moments are not aligned. For simplicity, I will take layer $F2$, the thin layer, to have its moment momentarily pointed along the $+z$ axis, and have "up" and "down" spins defined instantaneously relative to this quantization axis. If layer $F1$ has its moment at some angle θ to the z-axis, then its spin-dependent scattering properties will be different, because "up" and "down" spins no longer have the same meaning for the two layers. We can account for this by applying a rotation operation to each $2N_{ch} \times 2N_{ch}$ reflection and transmission submatrix, e.g.,:

$$r_1(\theta) = R_\theta r_1(0) R_{-\theta}, \tag{3.24}$$

$$R_\theta = \begin{bmatrix} \cos(\theta/2) & -\sin(\theta/2) \\ \sin(\theta/2) & \cos(\theta/2) \end{bmatrix} \otimes 1_{2N_{ch}}, \tag{3.25}$$

where $1_{2N_{ch}}$ is the $2N_{ch} \times 2N_{ch}$ unit matrix. This transformation effectively takes the incoming wave amplitudes, rotates them into the local spin moment frame of

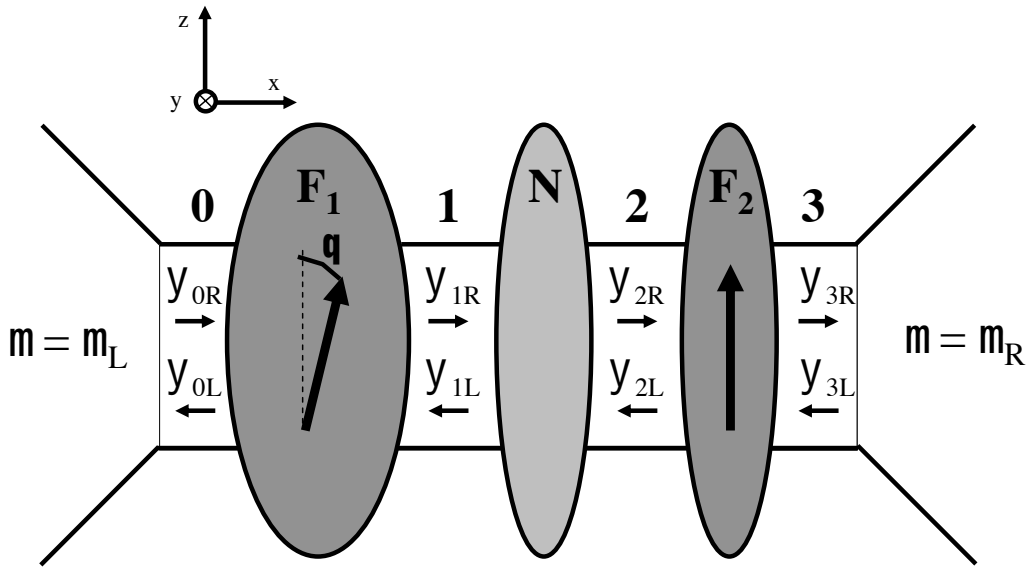


Figure 3.4: Scattering formalism applied to the trilayer system. Electrons are injected into the system from the reservoirs at chemical potentials μ_L, μ_R, and scatter off of each of the three layers $F1$, N, and $F2$. The moments in $F1$ and $F2$ are at an angle θ to one another. The calculation tracks the right- and left-going electron waves in $2N_{ch}$ channels at the four spots 0, 1, 2, and 3.

layer $F1$, applies the scattering coefficients, and rotates them back into the global frame set by layer $F2$.

The initial known quantities are these scattering matrices and the incoming wave amplitudes ψ_{3L} and ψ_{0R}; from these the rest of the amplitudes can be calculated. We can define quantities that connect the incoming amplitudes to the amplitudes at any other point in the layer:

$$\begin{bmatrix} \psi_{iR} \\ \psi_{iL} \end{bmatrix} = \begin{bmatrix} \Gamma_{iR} & \Lambda_{iR} \\ \Gamma_{iL} & \Lambda_{iL} \end{bmatrix} \begin{bmatrix} \psi_{0R} \\ \psi_{3L} \end{bmatrix}, i = 0, 1, 2, 3. \tag{3.26}$$

This defines a set of linear equations, from which the Γ's and Λ's can be solved. As these quantities have similar mathematical forms, I display the result of one calculation. If there is only a right-going electron flow (positive current), then $\psi_{3L} = 0$. After some algebra, the quantity Γ_{2R} is

$$\Gamma_{2R} \equiv \Omega = \frac{1}{1 - r_n' r_2} t_n \frac{1}{1 - r_1' t_n' r_2 (1 - r_n' r_2)^{-1} t_n - r_1' r_n} t_1, \tag{3.27}$$

where the dependence of r_2, t_2, r_2', t_2' on θ is implicit. This expression will appear again, so I define it as a matrix Ω to simplify notation.

The expression for the spin flux, Eqn. (3.9), can also be expressed in matrix form, as a trace over diagonal elements. The spin flux will depend on the occupations of incident wave amplitudes via Eqn. (3.26). These occupations can be related to more experimentally-relevant quantities, the chemical potentials of the two reservoirs μ_L and μ_R (Fig. 3.4). When one of these chemical potentials is changed by an amount $\delta\mu_L$ ($\delta\mu_R$), the number of electrons that pass through the trilayer changes. This changes the total incident flux, and thus the spin flux, by an amount proportional to $\delta\mu_L$ ($\delta\mu_R$). After substitution of Eqn. (3.26) into Eqn. (3.9), the differential change in spin flux at the points $i = 0, 1, 2, 3$ is

$$\frac{\partial \vec{\Psi}_i}{\partial \mu_L} = \frac{1}{4\pi} Re \left[Tr \left(\vec{\sigma} \Gamma_{iR} \Gamma_{iR}^\dagger \right) - Tr \left(\vec{\sigma} \Gamma_{iL} \Gamma_{iL}^\dagger \right) \right], \tag{3.28}$$

$$\frac{\partial \vec{\Psi}_i}{\partial \mu_R} = \frac{1}{4\pi} Re \left[Tr \left(\vec{\sigma} \Lambda_{iR} \Lambda_{iR}^{\dagger} \right) - Tr \left(\vec{\sigma} \Lambda_{iL} \Lambda_{iL}^{\dagger} \right) \right]. \tag{3.29}$$

The torque on layer $F2$ is simply $\vec{\tau}_2 = \vec{\Psi}_2 - \vec{\Psi}_3$. If we assume that there is no spin-flip scattering, then off-diagonal elements not related to the rotation of the spin moment of layer $F2$ disappear, and the calculation simplifies. As in the single-layer case, there are both x and y-components to the torque. However, as I have noted that the y-component (the rotational torque) is relatively small [20, 18], I will focus only on the τ_x component of the result. Suppose a voltage V_0 is applied, changing the chemical potential of reservoir 0 by $\delta_0 = -eV_0$. For $V_0 > 0$, electrons flow from right to left in Fig. 3.4. Explicit calculation of the relevant Γ and Λ matrices and substitution into Eqn. (3.28) yields

$$\frac{\partial \tau_2^x}{\partial V_0} = -\frac{e}{2\pi} Re \left[Tr_{N_{ch}} \left(\left(\Omega_{\uparrow\uparrow} \Omega_{\downarrow\uparrow}^{\dagger} + \Omega_{\uparrow\downarrow} \Omega_{\downarrow\downarrow}^{\dagger} \right) \times \left(1 - r_{2,\uparrow\uparrow} r_{2,\downarrow\downarrow}^{\dagger} - t_{2,\uparrow\uparrow} t_{2,\downarrow\downarrow}^{\dagger} \right) \right) \right], \tag{3.30}$$

where the trace is no longer over spin indices, but instead only over the N_{ch} momentum channels, and the $\uparrow\uparrow$, etc. subscripts denote a particular $N_{ch} \times N_{ch}$ momentum submatrix of the full scattering matrix, e.g., the elements of the matrix in Eqn. (3.4). Comparison of Eqn. (3.30) with Eqn. (3.10) shows that the torque in the trilayer case actually contains within it the result for the torque in the single-layer case. The effects of multiple scatterings due to the presence of the second layer is contained in the prefactor involving the Ω's. Note that the presence of the off-diagonal spin elements of Ω means that if $\theta = 0$ or $\theta = 180°$ (both layer spin moments aligned or antialigned, respectively) then the torque vanishes, as there is no mixing of spins.

Before proceeding to the next step in the calculation, I note that in general $\partial \vec{\Psi}_i / \partial \mu_R \neq -\partial \vec{\Psi}_i / \partial \mu_L$. This results in the remarkable fact that changing the chemical potentials of both reservoirs by an equal amount can result in a net torque on the layers, even though the potential difference has not changed; in particular, this can

occur even with *zero* potential difference across the trilayer. This is a consequence of the phase coherence in Eqns. (3.28) and (3.29) and gives an offset to the torque in Eqn. (3.32). The existence of a zero-bias spin flux and the associated torques is not a new idea; it is in fact a manifestation of the well-known itinerant-electron-mediated exchange interaction, also known as the RKKY interaction, between two ferromagnetic films separated by a normal-metal spacer. This interaction can be understood in a number of different formalisms, including the scattering formalism [22, 23, 24, 25]. However, the RKKY contribution to the torque is far smaller (a factor of $1/N_{ch}$ smaller) than the finite-bias torque. Also, as it depends to a certain degree on strict phase coherence, it is greatly diminished when the ensemble averaging techniques of the next section are applied to the system. As a result, we ignore the zero-bias torque contribution in our subsequent calculations, and take $\partial\vec{\Psi}_i/\partial\mu_R = -\partial\vec{\Psi}_i/\partial\mu_L$ in all cases.

3.4 Ensemble Averaging: Ballistic and Diffusive Scattering

3.4.1 Ballistic Limit

Our expression for the torque in the trilayer system, Eqn. (3.32), includes phase factors that are accumulated when electrons in each of the channels propagate through the system. The typical thicknesses of the layers are much larger than the Fermi wavelengths of the propagating electrons, so small fractional variations in the propagating pathlengths or in the angles of incidence will result in large oscillations of the phase terms. As in the single-layer case, then, we need to average over the phase in some manner. There are a couple of ways this can be done. In the case of purely

ballistic transport and specular scattering (no channel mixing), the phase can be averaged directly, as in my simple single-layer example. Of course, the expression for the torque in the trilayer system (Eqn. (3.30)) is more complicated than the single-layer expression (Eqns. (3.10)-(3.12)), and so the averaging techniques must be somewhat more sophisticated. In [21] we performed such an average by assuming that the normal metal spacer thickness $L >> k_x$, where k_x is the transverse momentum in the normal metal; thus an average over $\vec{k}_F$ vectors amounts to an average over the phase in the normal metal. Our results for the torque and the conductance are quite lengthy, and I do not reprint them here; I refer the reader to [21] for details.

3.4.2 Diffusive Limit: A Pedagogical Approach

For the rest of this section I look at averaging in the opposite limit of diffuse scattering, where electrons can be scattered from one momentum channel into another. I wish to emphasize at this point that, despite this focus, the reader should not be misled into thinking that the diffusive approach is the best way to model my devices. As mentioned in Chapter 1, the typical spacer thicknesses of my devices (a few nm) is smaller than typical mean free paths in my spacer materials ($\sim$ 20 nm in Cu at room temperature). Therefore, it is likely that, if momentum channel mixing occurs at all in my devices, it must occur at the interfaces, due to roughness or material intermixing. The degree to which interface scattering is diffusive or specular depends on the particular material combination [26], but for materials like Cu and Co, whose interfaces are typically sharp and smooth [27], specular scattering is expected to be quite important [28]. As we will find, a purely diffusive approach also results in a quantitative discrepancy between the predicted torques and the effects I observe

in Co/Cu/Co trilayers, which can only be resolved by properly taking into account ballistic transport.

However, the diffusive limit of our scattering formalism is worthy of discussion, primarily for pedagogical reasons. Diffuse scattering allows for a great mathematical simplification that is not possible in the ballistic limit, which makes it simpler to incorporate the results of rigorous band-structure calculations, the scattering coefficients, into our theory. Although we should not expect this to lead to good quantitative agreement with my device results, it allows me to present spin-transfer in a more pedagogically useful manner, showing how these scattering coefficients directly relate to the symmetry of the torque. The basic qualitative symmetries seen in the diffusive limit are unchanged if transport is instead ballistic [21]. Taking the diffusive limit also shows how our phase-coherent results reduce to those of other groups, who calculate the torques within a purely incoherent formalism. The fact that extensive channel mixing does not destroy the torque is significant, because it suggests that spin-transfer may be found experimentally in a wide array of device geometries that do not satisfy the largely ballistic conditions of my trilayers.

3.4.3 Averaging in the Diffusive Limit

The usefulness of having a scattering matrix S_N associated with the normal metal spacer now becomes apparent, since we can introduce the effects of disorder into the system via tha properties of this matrix. The primary effect of including diffusive scattering is that the N_{ch} momentum channels can be mixed by S_N, through its off-diagonal matrix elements. Although we primarily associate the mixing with nonspecular scattering from the disordered magnetic-nonmagnetic interfaces, it can also in principle include diffusive scattering in the bulk of the normal spacer. This ma-

trix can additionally account for spin relaxation, by mixing spin channels. However, as typical spacer thicknesses (a few nm) are much smaller than the spin-diffusion lengths in Cu (a few 100's nm)[15], we can simplify the calculations by restricting the mixing to amongst only momentum channels.

There are well-established techniques for treating diffuse scattering in the scattering matrix formalism [6, 29]. The general method is to decompose S_N into a product of matrices:

$$S_N = U' M_T U. \tag{3.31}$$

The two outer matrices U, U' are block diagonal, and relate how waves in right-going (left-going) channels are scattered into other right-going (left-going) channels. The middle matrix M_T contains information about the average transmission properties of the layer, so that it has off-diagonal elements which can reflect waves in right-going (left-going) channels into left-going (right-going) channels. The elements of the U, U' matrices are random, and are valid for only a particular microscopic configuration; their ensemble is the unitary group $U(N_{ch})$.

Diagrammatic techniques exist for averaging over the ensemble of configurations [30]; the particular calculation for the trilayer system appears in our work [21]. I do not discuss the details here, but instead jump right to the results. The major insight drawn from these calculations was that the fully diffusive channel mixing allows the replacement of the $2N_{ch} \times 2N_{ch}$ matrices with far simpler 4×4 matrices that in some sense represent ensemble averages over the larger matrices. The effects of each of the three layers reduce to "hat" matrices, e.g., $r_1 \rightarrow \hat{r}_1$, etc. This hat matrix, expressed in terms of a general $2N_{ch} \times 2N_{ch}$ matrix A, takes the form

$$\hat{A} = \frac{1}{N_{ch}} Tr_{Nch} A \otimes A^{\dagger}, \tag{3.32}$$

where "$\otimes$" denotes a tensor product. The trace over the N_{ch} momentum channels

leaves only spin as the indices of the 4×4 matrix $\hat{A}$. Since there is no explicit spin-flip scattering, only those matrices associated with layer $F2$ will have off-diagonal elements, due to a rotation of the spin-filtering coefficients. Since the normal spacer is independent of spin entirely, its scattering matrices can be expressed in terms of the 4×4 identity matrix 1_4:

$$\hat{t}_n = g_N 1_4, \tag{3.33}$$

$$\hat{t}_n = (1 - g_N)\, 1_4. \tag{3.34}$$

The proportionality constant g_N is the average conductance per channel. The result for the average torque ends up looking like this:

$$\begin{aligned} \left\langle \frac{\partial \tau_2^x}{\partial V_0} \right\rangle &= -\frac{e}{2\pi N_{ch}} Re\Big[(Tr_{N_{ch}}\left(\Omega_{\uparrow\uparrow}\Omega_{\downarrow\uparrow}^{\dagger}\right) + Tr_{N_{ch}}\left(\Omega_{\uparrow\downarrow}\Omega_{\downarrow\downarrow}^{\dagger}\right) \\ &\quad \times \left(1 - Tr_{N_{ch}}(r_{2,\uparrow\uparrow} r_{2,\downarrow\downarrow}^{\dagger} - t_{2,\uparrow\uparrow} t_{2,\downarrow\downarrow}^{\dagger})\right)\Big]. \end{aligned} \tag{3.35}$$

The average conductance $\langle g \rangle$ for the trilayer can be calculated in a similar fashion. Remarkably, averaging over diffuse disorder in the normal layer is equivalent to taking the form of the fully phase-coherent solution, Eqn. (3.10), and replacing the terms with their far simpler "hat" counterparts, where a trace has been taken over the N_{ch} momentum channels. This means that the scattering coefficient products (e.g., $r_{2,\uparrow\uparrow} r_{2,\downarrow\downarrow}^{\dagger}$) only enter into the result through their average value. This makes the incorporation of band-structure information into the result much simpler, since only average properties of the scattering coefficients need to be known, rather than their full momentum dependence. A further simplification to Eqn. (3.35) can be made by averaging over phase or disorder in the magnet itself; as it stands, our diffusive result holds even in the limit of magnets of thicknesses comparable to k_F^{-1}, where phase coherence becomes important. Although we will find that a purely diffusive approach leads to results that are not quantitatively consistent with my

experimental data, the dramatic reduction in the complexity of the result allows us to more easily illuminate the important qualitative symmetries of spin-transfer.

3.4.4 Spin-Transfer and Phase Coherence

Before I explore the form of the torque found in the formalism in the diffusive limit, I must say a few words about the formalism itself. The results of the diffusive calculation make clear that the preservation of phase coherence is not crucial for the generation of spin-transfer torque as electrons scatter between the layers. The two most important ingredients in the creation of the torque are the spin-dependence of the scattering combined with the rotation of the quantization axis of the conduction electron spin states that occurs when the moments are not collinear. This is an important insight, because it shows that spin-transfer can occur generally in normal metal-ferromagnet hybrid systems, even when the scattering is inelastic. The inelastic scattering can occur between the current and the moments or any other part of the system, e.g., phonons; the only restriction is that spin can only be transferred between the current and the moments——in other words, the spin-diffusion length set by processes such as spin-orbit scattering must be larger than the system dimensions. This not only opens up the spin-transfer effect to a much wider variety of physical systems than the initially phase-coherent picture would suggest, it allows for simpler and more flexible formalisms to describe the torque.

The most prominent of these is the finite-element circuit theory developed by, among others, Brataas, Nazarov, and Bauer (BNB) [31]. In this approach systems are constructed out of generalized reservoirs, nodes, and resistive contacts connecting them. With regard to the trilayer system, the interior of each of the three layers in the BNB approach would be designated as nodes, and the inter-

faces between the layers, where the scattering properties of the system arise, being the contacts. Phase information is irrelevant in this formalism, as transport both between nodes and within the nodes is incoherent and can involve non-spin-flip energy relaxation. Transport can thusly be described in terms of well-defined Fermi distribution functions. However, the presence of spin-polarized currents, and the resulting possibility of rotated spin reference frames due to noncollinear magnetizations in different nodes, requires that the distribution functions be defined in a more sophisticated way. BNB do this by generalizing all quantities——e.g., distribution functions, currents, and chemical potentials——into 2×2 matrices, in which the off-diagonal elements contain information about rotations between spin channels. The spin and charge currents can then be calculated at any point in a system by summing the contributions from all adjacent nodes in a manner analogous to a Kirchoff sum rule for ordinary transport. Application of this formalism to magnetic-nonmagnetic systems yields a quantity $G^{\uparrow\downarrow}$, called the spin-mixing conductance [20]:

$$G^{\uparrow\downarrow} = \frac{e^2}{h}\left[N_{ch} - \sum_{ij} r_{\uparrow}^{ij}(r_{\downarrow}^{ij})^{\dagger}\right], \tag{3.36}$$

where $r_{\uparrow,\downarrow}^{ij}$ are the elements of the reflection matrix in the contact between two nodes. The real and imaginary parts of this quantity are related to, respectively, the Slonczewski and rotational torques exerted on the spin moment of a magnet by the current. This result is quite similar to our results in Eqns. (3.19), (3.20), and (3.30) [32]. It can be rigorously shown that the general result for spin-transfer torques in the circuit formalism is equivalent to our phase-coherent formalism, in the limit that the number of channels is large [33].

The circuit formalism has several advantages over our approach. For one thing, it allows one to construct complicated structures out of the bare elements of reservoirs, nodes, and contacts. Since the transport is described in terms of incoherent

superpositions of charge and spin currents, the calculational complexity scales only linearly with the number of components of the system. This has allowed theorists to consider exotic configurations such as three-terminal transistor-like systems [34] and systems that combine normal metals, ferromagnets, and superconductors [35]. In our fully coherent and nonlocal formalism, the complete structure must be considered all at once, making more complicated structures far more difficult to study. Also, the effect of spin-flip processes can be incorporated into the circuit formalism very simply, by adding a spin-relaxation term to the Kirchoff sum rule for spin currents entering and leaving a node. To treat spin-flip processes with our calculations, explicit values must be added to the off-diagonal elements at the start of the calculation, complicating the mathematics considerably. This is not to say, however, that the simpler incoherent approach is preferable to our phase-coherent approach in all respects; for example, Tserkovnyak and Brataas [36] found it more convenient to perform a random-matrix average similar to our own [21] when calculating the shot noise in ferromagnetic-normal metal systems. Our formalism is more general in that it can be applied even when quantum confinement is important and the number of channels N_{ch} is small. When $N_{ch} >> 1$, our results reduce to the BNB results.

3.4.5 Results for Diffusive Scattering

Symmetry and Limiting Cases

As mentioned earlier, the torque has both x and y-components, as in my single-layer example, although the y-component (proportional to the imaginary part of the BNB mixing conductance) is relatively small. It can be shown that $\langle \partial \tau_2^x / \partial V_0 \rangle = -\langle \partial \tau_2^x / \partial V_3 \rangle$, so that the torque changes sign when the current bias changes. This result is equivalent to having no zero-bias torque, which demands that changing

the chemical potential of each reservoir by the same amount generates equal and opposite torques on the layer. Recall that the equilibrium RKKY torque is smaller than the average current-induced torque by $\sim \frac{1}{N_{ch}}$, so that it is neglected here (see page 114).

Our formalism thus describes a torque with the same general symmetry as the results of Slonczewski. The compact form of Eqn. (3.35) provides little further intuition, however; it is therefore useful to look at it in limiting cases. In the limit that both layers are perfect spin filters, then the torque reduces to

$$\left\langle \frac{\partial \tau_2^x}{\partial V_0} \right\rangle = -\frac{e}{4\pi} \frac{g_N \sin\theta}{3+\cos\theta} = -\frac{h}{4\pi e} \langle g \rangle \frac{\sin\theta}{2(1+\cos\theta)}, \tag{3.37}$$

where $\langle g \rangle = \frac{e^2}{h} g_N (4\cos^2\theta/2)/(3+\cos\theta)$ is the average conductance per channel of the system. If we take the torque per unit current as

$$\frac{\tau_2^x}{I} = \left\langle \frac{1}{g} \frac{\partial \tau_2^x}{\partial V_0} \right\rangle, \tag{3.38}$$

then we can immediately see that this agrees with the Slonczewski result $g(\theta)\sin\theta$ [8] (See Eqn. (2.6) of this dissertation) for a polarization $P = 1$.

We can take the opposite limit of spin-dependent scattering and consider what form the torque takes when the scattering coefficients are are very weakly spin-dependent. We define g_1 and g_2 as the conductance of layers $F1$ and $F2$, respectively, averaged over momentum and spin. The average conductance for spin-up electrons and spin-down electrons can be written as

$$g_{1\uparrow} = g_1 + \delta g_1, g_{1\downarrow} = g_1 - \delta g_1, etc. \tag{3.39}$$

The conductance difference $\delta g_{1,2}$ can be positive or negative. The torque can be expanded in powers of $\delta g_{1,2}$; the lowest-order term has the form

$$\left\langle \frac{\partial \tau_2^x}{\partial V_0} \right\rangle = -\frac{e}{2\pi} g_N^2 \delta g_1 \delta g_2^2 \sin\theta F(g_1, g_N, g_2, N_{ch}). \tag{3.40}$$

From this expression we can see the consequences of spin-transfer's insensitivity to the sign of the spin-dependent properties of the magnet, first remarked upon at the end of Section 3.2. Because δg_2 appears through its square, the sign of the torque does not depend on whether spin-up electrons are transmitted more easily ($\delta g_2 > 0$) or spin-down electrons are transmitted more easilty ($\delta g_2 < 0$). It is in fact only the sign of the spin-polarization coming from the *other* layer (δg_1) that determines the sign of the torque. This basic symmetry has also been verified in the general case [21].

General Results

It is difficult to explore the general result in great analytical detail, as the matrices in Eqn. (3.35) make for long and tedious expressions. It is far easier to study the dependence of the torque on the scattering coefficients by calculating the traces in Eqn. (3.35) via a software algorithm and plotting out the results. For simplicity we assume that the scattering coefficients are independent of momentum. In Section 3.5 I will show that, although this approximation may be reasonable in the diffusive limit for systems such as Co/Cu/Co, due to the mathematical simplification shown earlier in this section, in the ballistic limit such a simplification cannot in any way be justified. Using the scattering coefficients, along with the angle θ between the spin moments of the two layers and the average conductance of the normal layer, the torque $\langle \partial \tau_2^x / \partial V_0 \rangle$ and the average conductance $\langle g \rangle$ can be calculated. A useful quantity to parametrize the results is the polarization of each magnetic layer, which is defined as

$$P_{1,2} \equiv \frac{|t_{1,2\uparrow}|^2 - |t_{1,2\downarrow}|^2}{|t_{1,2\uparrow}|^2 + |t_{1,2\downarrow}|^2}. \tag{3.41}$$

Figure 3.5 is a plot of torque per unit current, in units of $h/2\pi e$, vs. angle θ for a trilayer system in which $|P_1| = |P_2| = 0.98$, for the four possible sign combinations of the polarization. The normal layer conductance is perfect, $g_N = 1$. The torque is highly asymmetric upon reflection around $\theta = 90°$, with the slope $d\tau/d\theta$ much larger near $\theta = 180°$ than near $\theta = 0$. This is a consequence of the smaller conductance near $\theta = 180°$, which increases the torque per transmitted electron. The four-fold symmetry seen in the analytical case of small spin asymmetry ($P << 1$) can be seen here as well; changing the sign of the polarization of layer $F1$ alone changes the sign of the torque. The magnitude of the torque changes, however, when the sign of the polarization of layer $F2$ is changed.

For systems where P is not quite so close to 1, the torque per unit current in the diffusive model is drastically reduced. Figure 3.6 shows the torque per unit current vs. θ for various choices of $P = P_1 = P_2$. The normal layer conductance $g_N = 1$, as before. Reducing the polarization from $P = +0.98$ to $P = +0.35$ reduces the torque by nearly two orders of magnitude, and makes the shape of the torque curve far more symmetric about $\theta = 90°$. This is an important departure from Slonczewski's results. Figure 3.7, taken from [21], shows the torque per current vs. θ found using both our calculations and Slonczewski's calculations for a polarization of $P_{1,2} = +0.67$ for both layers. The torque predicted in the diffusive limit is significantly smaller than that predicted by Slonczewski. The inset to Fig. 3.7 shows the derivative of $\tau_2^x(\theta)$ per current vs. $\langle T_\downarrow \rangle = \langle |t_{1,2,\downarrow}|^2 \rangle$ for both models. $\langle T_\uparrow \rangle = 1$ for both layers, so increasing $\langle T_\downarrow \rangle$ implies decreasing P. As can be seen, the torque in the diffusive model falls off much more rapidly than in the Slonczewski model, dropping to nearly an order of magnitude below the Slonczewski result for $\langle T_\downarrow \rangle = 0.6$ ($P = 0.25$). Thus disorder which gives rise to diffusive scattering strongly reduces, but does not fully eliminate,

spin-transfer torque. The small size of the torque in the diffusive model relative to the Slonczewski model also strongly suggests that transport in my devices does not involve a great deal of diffusive scattering; I will address this point further in Section 3.5.

3.5 Applying Band Structure Calculations to the Scattering Formalism

One of the intriguing results of our calculation is that the sign of spin-transfer torque depends on the sign of polarization of the scattering coefficients of the magnetic layers. Throughout this dissertation, and particularly in the interpretation of my experimental data for Co/Cu/Co trilayers in Chapters 2, 4, and 5, I have assumed a positive polarization within the torque model, which gives a torque with the same symmetry as observed. A negative polarization for both layers, however, would imply that the torque favors parallel alignment of the layers at positive currents in my sign convention (see Chapter 2), and favors antiparallel alignment at negative currents. Since the conductance $\langle g \rangle$, unlike the torque, does not vary when the polarization of both layers changes sign, the parallel configuration remains the low resistance state, and the hysteresis loop should be flipped about $I = 0$ relative to the observed loops for the Co/Cu/Co trilayers. Spin transfer thus provides a clear experimental signature of the asymmetry of the spin-dependence of the magnetic layers' scattering properties, and it is important to explore how this spin-dependence is established microscopically.

Stiles [10] has performed first-principles calculations to determine the transmission and reflection probabilities of the interface formed between a magnetic and

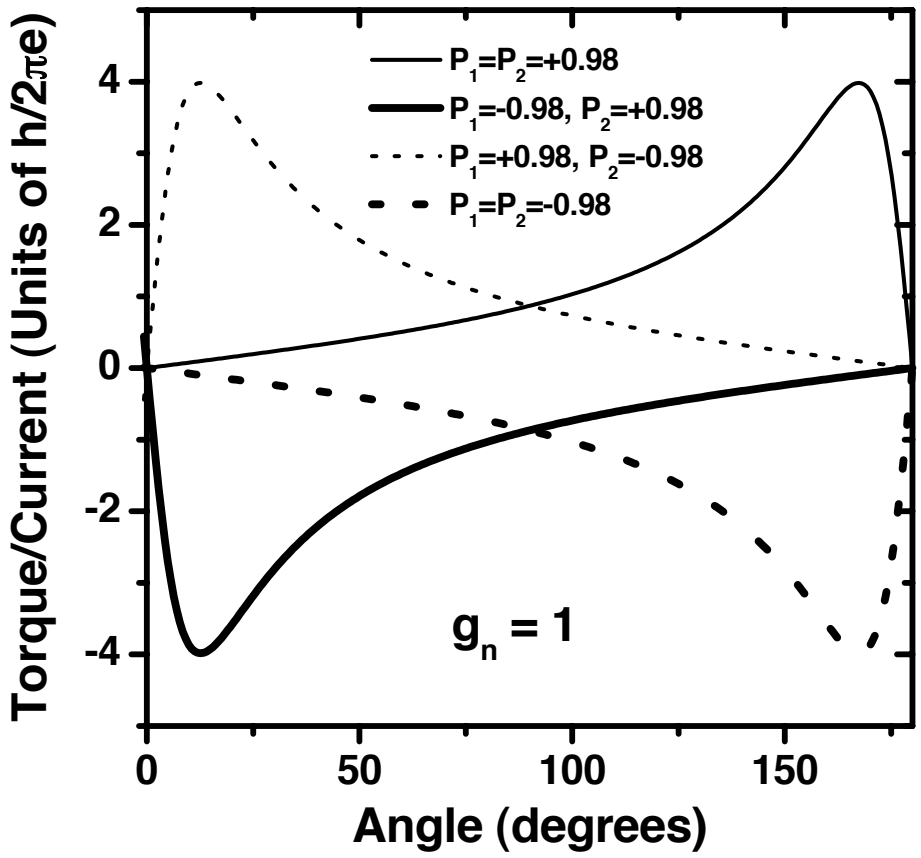


Figure 3.5: Torque per current, in units of $h/2\pi e$, vs. angle θ in the diffusive limit, in the case where the polarization of both magnetic layers (defined in the text) is $|P| = 0.98$, for the four possible sign combinations.

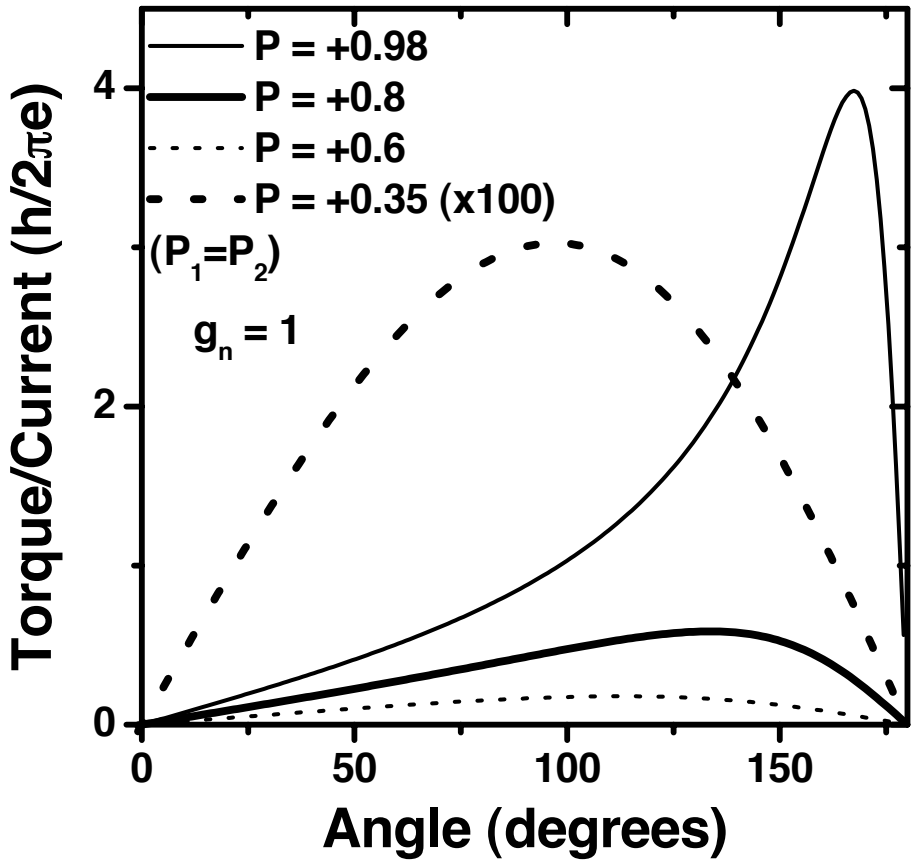


Figure 3.6: Torque per current, in units of $h/2\pi e$, vs. angle θ in the diffusive limit, for various values of the polarization P (defined in the text). The curve for $P = +0.35$ is multiplied by 100 for visibility.

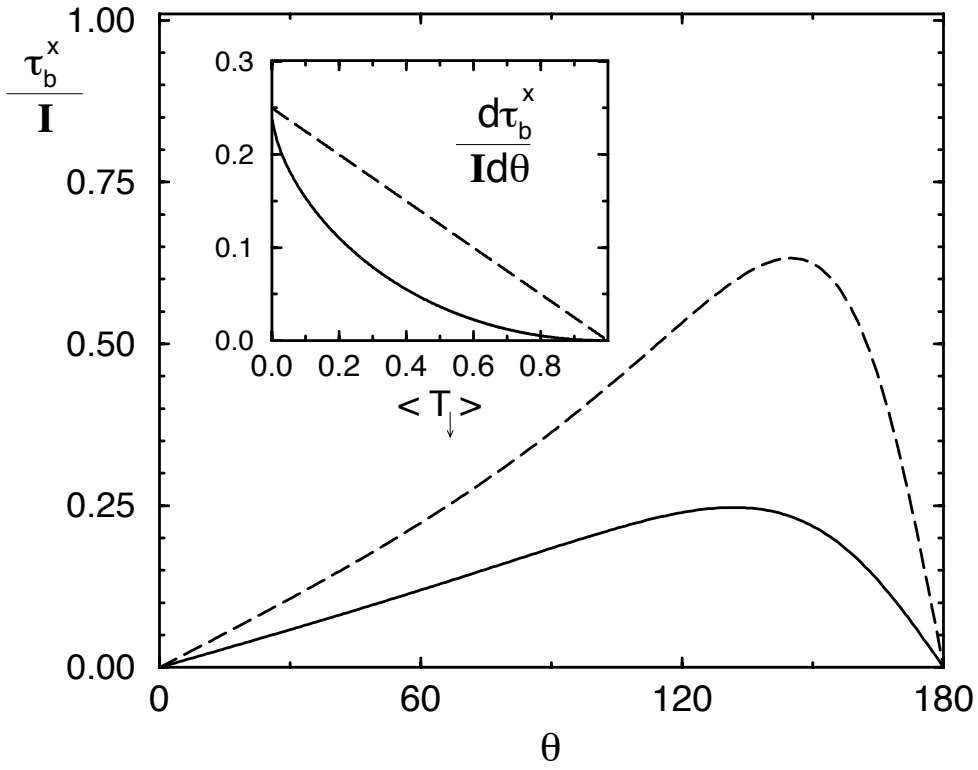


Figure 3.7: Torque per current, in units of $h/2\pi e$, vs. angle θ, using our formalism in the diffusive limit (solid line) and Slonczewski's result (dotted line) [8], from [21]. For our formalism, the coefficients $\langle |t_\downarrow|^2 \rangle = \langle T_\downarrow \rangle = 0.2$ for all channels. In Slonczewski's case, $\langle T_\downarrow \rangle = 1$ for 20% of the channels, and is set to zero for the remainder; $\langle T_\uparrow \rangle = 1$ for all channels in both cases. Inset: torque derivative per current $d\tau/Id\theta$ near $\theta = 0$ as a function of $\langle T_\downarrow \rangle$.

nonmagnetic metal, for various materials combinations. A mean-field potential at every point in space was determined using the local spin-density approximation, from which Bloch states and Fermi surfaces in both materials could be determined. A perfect interface was assumed, so that only specular scattering occured at the interface; in other words, the components of the momentum transverse to the current direction (parallel to the plane of the interface) were conserved during transmission and reflection. The scattering probabilities were determined by matching the Bloch states at the interface. Although exchange is an important factor in determining the scattering properties of the interface, the ultimate criterion for determining transmission and reflection is how individual states match up at the interface. Sometimes total reflection occurs if a state on one side of the interface has no corresponding state with the same transverse momentum on the other side. The symmetry of the particular band in which each state resides is also important, e.g., *sp*-orbital states match well with dz^2-orbital states, but not other *d*-orbital states. This symmetry requirement also can result in reflection of electrons.

Figure 3.8 shows calculations from [10], where the (real) transmission probabilities for electrons crossing a Cu/Co (001) interface is shown as a function of transverse momentum. As can be seen, the probability is very anisotropic. For spin-up (majority) electrons, the transmission is nearly perfect for a large range of incident angles, from normal incidence up to a certain critical angle. Beyond this angle, the transmission rapidly drops to zero. For spin-down (minority) electrons, the transmission is much lower, but also is inhomogeneous−−certain momentum directions are still favorable, due to a strong degree of band-matching at those angles. Table 3.1 gives the transmission probabilities for this interface averaged over the Fermi surface, along with average transmission probabilities for other crystal

orientations. The table also includes calculations for the Cr/Fe interface. As can be seen, the two materials combinations give qualitatively different scattering probabilities. With Cu and Co, the up-spin bands match more closely than the down-spin bands in the two materials, giving a higher up-spin than down-spin transmissions. The opposite is true for Cr and Fe, where the better-matched down-spin bands give a higher transmission than the up spins. It is important to note that these transmission probabilities are a property of the specific interface between two materials, and not of the magnetic material alone. For example, Stiles [10] finds that a Ag/Fe interface transmits up-spin electrons far more easily than down-spins, the opposite symmetry to that seen for the Cr/Fe interface.

Table 3.1: Average transmission probabilities for real materials interfaces, calculated by Stiles in [10].

Material(orientation)	$T_{NF,\downarrow}$	$T_{NF,\uparrow}$	$T_{FN,\downarrow}$	$T_{FN,\uparrow}$
Cu/Co(001)	0.49	0.79	0.27	0.95
Cu/Co(111)	0.54	0.73	0.33	0.94
Cu/Co(110)	0.44	0.66	0.29	0.92
Cr/Fe(001)	0.58	0.36	0.82	0.41
Cr/Fe(110)	0.59	0.48	0.84	0.39
Cr/Fe(211)	0.59	0.59	0.82	0.39

3.5.1 Torque Predictions in Diffusive Limit

As noted earlier, the presence of extensive diffusive scattering mixes the momentum channels, effectively averaging over the momentum dependence of the scattering coeffients. The diffusive result Eqn. (3.35) includes traces over products of coeffi-

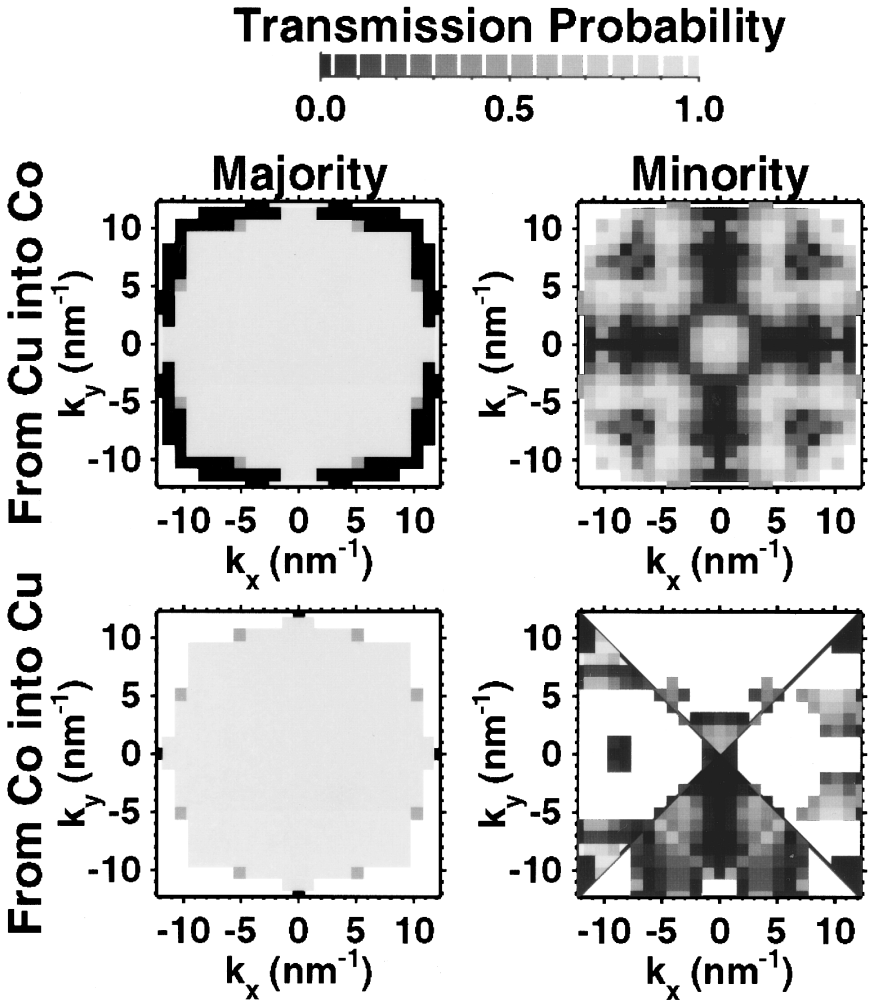


Figure 3.8: Plots of transmission coefficient vs. transverse momentum, for majority (spin-up) and minority (spin-down) electrons crossing a Cu/Co (001) interface, from [10]. The coordinate system varies from my own; here the interface lies in the $x-y$, rather than the $y-z$, plane.

cients such as $\frac{1}{N_{ch}} Tr_{N_{ch}}(t_{2,\uparrow\uparrow} t^{\dagger}_{2,\downarrow\downarrow})$. We note that for the Cu/Co interface, the spin-up transmission is essentially either 1 or 0 for nearly all momentum directions; thus, to a good approximation, $\frac{1}{N_{ch}} Tr_{N_{ch}}(t_{2,\uparrow\uparrow} t^{\dagger}_{2,\downarrow\downarrow}) \approx \langle t_{2,\uparrow\uparrow} \rangle \frac{1}{N_{ch}} Tr_{N_{ch}}(t^{\dagger}_{2,\downarrow\downarrow}) = \langle t_{2,\uparrow\uparrow} \rangle \langle t^{\dagger}_{2,\downarrow\downarrow} \rangle$, and we can replace the individual coefficients with their averages from Table 3.1. This is how the simplification in Section 3.4 of taking the scattering coefficients to be independent of momentum turns out to give roughly accurate results for the Co/Cu/Co system in the diffusive limit, since in the end, only the average values matter. Such a simplification is far less justified for the Fe/Cr/Fe system, where the transmission coefficients lie between 0 and 1 over significant portions of the Fermi surface [10]. However, I will apply this simplification to the Fe/Cr/Fe system anyway, just to get a qualitative idea of the torques in this system in the diffusive limit; a more rigorous application of the scattering coefficients would likely give a larger torque. Taking an average over crystal orientations, and approximating the full scattering probability for each layer as the scattering probability associated with the normal metal-to-ferromagnet transport direction (first two columns of Table 3.1), I find $\sqrt{T_{\downarrow}} = t_{\downarrow} = 0.7$, $t_{\uparrow} = 0.85$ for the Co/Cu/Co trilayer, and $t_{\downarrow} = 0.77$, $t_{\uparrow} = 0.69$ for the Fe/Cr/Fe trilayer. Figure 3.9 shows the calculated torques for both systems using these parameters. As expected, the torque in the Fe/Cr/Fe system is of opposite sign to that in the Co/Cu/Co system. As we also saw in Section 3.4.5, though, the predicted torque in the diffusive model is quite small. The inset to Fig. 3.9 shows the prediction in the Slonczewski model for the torque in the Co/Cu/Co system, using a polarization parameter $P = (|t_{\uparrow}|^2 - |t_{\downarrow}|^2)/(|t_{\uparrow}|^2 + |t_{\downarrow}|^2) = 0.2$. The Slonczewski torque is more than an order of magnitude larger than the predicted torque in the diffusive limit of our formalism; this difference will be discussed further in Section 3.5.3.

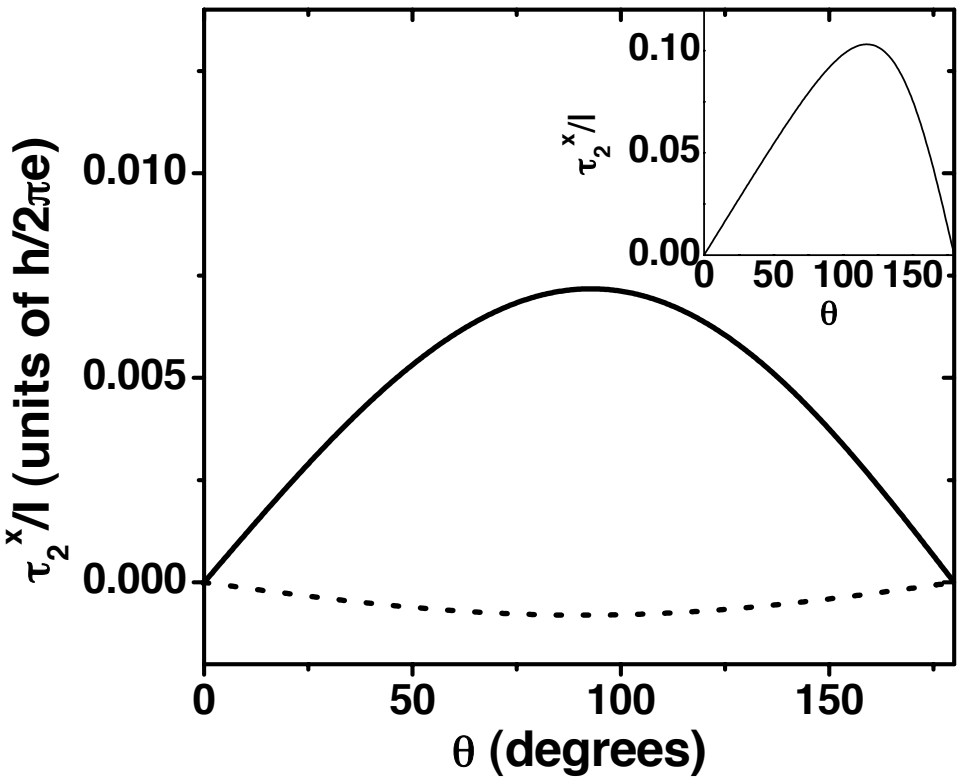


Figure 3.9: Torques per current τ_2^x/I, in units of $h/2\pi e$, vs. angle θ in the diffusive limit for two trilayer systems, Co/Cu/Co (solid line) and Fe/Cr/Fe (dotted line), using the average scattering coefficients of [10]. Inset: Torque per current vs. angle in the Slonczewski model for the Co/Cu/Co system. Note the different scales.

3.5.2 Aside: Experimental Evidence for Opposite Torques?

In light of these results, it is natural to seek experimental confirmation of the different polarizations in the Co/Cu/Co and Fe/Cr/Fe systems. I have already shown ample evidence of the symmetry in the Co/Cu/Co trilayer system. Exploring the effect in Fe/Cr/Fe trilayers is a somewhat more difficult business, as the bulk resistivity of Cr ($\rho_{Cr} = 12.7 \times 10^{-8}\ \Omega m$ at room temperature) is far higher than that of Co ($\rho_{Co} = 1.7 \times 10^{-8}\ \Omega m$ at room temperature). Although bulk properties are not as important for the nanoconstriction geometry, a higher bulk resistivity implies a lower mean free path, which will raise the quasiballistic device resistance; this limits the currents that can be reached without damaging the device. Also, Cr oxidizes extremely easily, increasing the likelihood of adsorbate impurities being incorporated into layered devices. As a result, most of the devices I have attempted to make do not show the rise in differential resistance with increasing bias that is characteristic of good quasiballistic transport (see Section 2.2.1), and instead show anomalies more typical of low-resistance tunneling transport. Device resistances are typically in the $100 - 200\ \Omega$ range, compared with $5 - 20\ \Omega$ for Co/Cu/Co devices.

I have fabricated Fe/Cr/Fe devices in the Buhrman group sputtering chamber, however, that do show lower resistances ($\sim 50\ \Omega$). These exhibit characteristics consistent with spin-transfer, although the symmetry of the features is ambiguous. Hysteretic switching has been observed with a symmetry opposite to that of Co/Cu/Co; however, when a large field is applied to the devices, peaks in the differential resistance appear, but only at positive current biaas. bias. For negatively-polarized materials, the high-field features would be expected to occur at negative bias. Frank Albert has made sputtered Fe/Cr/Fe nanopillar devices, and has observed features that similarly do not show a clear symmetry [37]. Part of the ambiguity may stem

from the lower coercive fields of Fe films as compared with Co films of similar thickness [38]; this may make self-field effects, which have a different symmetry than spin-transfer (see Chapter 2), more important [39, 40]. Also, Cr is not merely an inert paramagnetic spacer like Cu; it has a transition to an antiferromagnetic phase below $T = 200$ K [41]. The antiferromagnetic phase is believed to play some sort of role in the oscillatory exchange coupling that is the zero-bias limit of the torque in our formalism [42]. At high fields this antiferromagnetic order may be disrupted, altering the scattering properties of the interface. At the moment, the data do not fully resolve these issues.

3.5.3 More Realistic Torques in the Ballistic Limit

While the diffusive model has been of pedagogical use due to its relative mathematical simplicity, we have found that the torques it predicts are significantly lower than in the Slonczewski model. A smaller torque implies a larger predicted critical current; while this might still find agreement with some of my results for nanoconstrictions and nanopillars, it would require neglecting the enhanced damping processes that undoubtedly occur in these devices (see Chapters 2 and 4). In addition, a much smaller torque would result in an important discrepancy between the torque model and the field dependence of high-field dynamic excitations observed in nanopillars [43]. It thus appears that the diffusive model does not accurately describe the magnitudes of the torques observed in my experimental geometries.

As discussed in Section 3.4.2, however, this should not be a great shock, as transport in my devices is likely to be largely ballistic anyway. How, then, does the ballistic limit of our scattering formalism fare with respect to the data? To answer this question, we must first acknowledge the greater degree of complexity

involved in applying *ab initio* scattering coefficients to our formalism in the ballistic limit. In the diffusive picture of spin-transfer torque, the mixing of momentum channels allowed us straightforwardly take an average over the various electron paths in the system, and reduce the complexity of the mathematical machinery to the 4×4 "hat" matrices that contained the values of the scattering coefficients averaged over the momentum channels. One important consequence of this simplification for the Co/Cu/Co system was that the dependence of the scattering coefficients on momentum could be folded into a single parameter, the average. However, the ballistic calculation does not lead to the simple form of Eqn. (3.35); there is no channel mixing, and the N_{ch} momentum degrees of freedom remain in the final averaged result. The effects of each channel enter into the result in a complicated way, which means that the scattering coefficients for each channel *cannot* all be replaced by an average over all momentum channels; in other words, different sets of scattering coefficients with the same average value can result in vastly different torques in the ballistic limit. In particular, replacing all scattering coefficients with an average underemphasizes the role of channels with transmission near 1, as the high-transmission channels provide a disproportionate amount of the torque [21].

Unfortunately, we have not yet attempted to incorporate the full momentum-dependence of the scattering coefficients into our ballistic results. However, for systems such as Co/Cu/Co, we can directly see that the result will in fact be quite close to Slonczewski's. If, as shown in Fig. 3.8, the transmission coefficients are all nearly 1 or 0, then electrons are, for the most part, either completely reflected or completely transmitted by the magnetic layer. If we calculate the polarization P using the average transmission coefficients in Fig. 3.1 and the expression for P in Eqn. (3.41), then there should thus be little difference between the torque predicted

by our ballistic calculation and that from Slonczewski's calculation, shown for the Co/Cu/Co system in the inset to Fig. 3.9. Slonczewski himself makes this important point in a recent paper [44]. In other words, when ballistic (specular) effects are a significant part of transport, as is likely true in my devices, the Slonczewski result is a valid quantitative expression of the spin-transfer torque; this justifies my use of his term when discussing my data in the other chapters of this dissertation.

3.6 Final Thoughts

It is somewhat amusing that, after all of the time spent in this chapter on a formal scattering model for the trilayer system, the true magnitude of the spin-transfer torque in the Co/Cu/Co system is found to be roughly the same as that in Slonczewski's far simpler one-dimensional ballistic model. However, the work presented here is still time well spent, as our scattering approach can describe systems for which Slonczewski's model is not valid. For example, as noted earlier, similar *ab initio* transmission calculations for Fe/Cr interfaces [10] show that the values of the transmission coefficients deviate significantly from 0 or 1. The assumptions of Slonczewski's approach consequently break down, and our scattering approach is the preferred method of determining the torques. To do so, though, it is again necessary to consider the role of specular scattering, and to incorporate the full momentum dependence of the scattering coefficients. A fully specular calculation of the torque at a Cr/Fe interface was recently performed by Stiles and Zangwill [18]. The torque is opposite in sign to the Co/Cu torque, as in our diffusive results (Fig. 3.9), but is significantly larger, arising from the more rigorous treatment of the scattering coefficients and the assumption of specular scattering. Such calculations demonstrate that our scattering formalism can capture the physics of spin-transfer, but must

be combined with the correct microscopic scattering coefficients to provide a true quantitative picture of the torques generated in the magnetic layers.

Bibliography

[1] R. J. Soulen *et al.*, Science **282**, 85 (1998).

[2] Y. Ji *et al.*, Phys. Rev. Lett.**86**, 5585 (2001).

[3] R. Landauer, IBM J. Res. Dev. **1**, 223 (1957); **32**, 306 (1988).

[4] M. Büttiker, IBM J. Res. Dev. **32**, 317 (1988).

[5] Y. Imry, from Directions in Condensed Matter Physics edited by G. Grinstein and G. Mazenko **1**, World Scientific, pp. 120-145 (1986).

[6] C. W. J. Beenakker, Rev. Mod. Phys. **69**, 731 (1997).

[7] B. J. van Wees *et al.*, Phys. Rev. Lett. **60**, 848 (1988).

[8] J. Slonczewski, J. Magn. Magn. Mater. **159**, L1 (1996).

[9] K. M. Schep, P. J. Kelly, and G. E. W. Bauer, Phys. Rev. Lett. **74**, 586 (1995); K. M. Schep *et al.*, Phys. Rev. B **56**, 10805 (1997).

[10] M. D. Stiles, J. App. Phys. **79**, 5805 (1996); Phys. Rev. B **54**, 14679 (1996).

[11] T. Valet and A. Fert, Phys. Rev. B. **48**, 7099 (1993).

[12] L. Berger, Phys. Rev. B **54**, 9353 (1996).

[13] V. Kambersky, Can. J. Phys. **48**, 2906 (1970).

[14] P. Holody, Dissertation, Michigan State University (1996).

[15] J. Bass and W. P. Pratt, J. Magn. Magn. Mater. **200**, 274 (1999).

[16] D. Baxter *et al.*, J. App. Phys. **85**, 4545 (1999).

[17] This approach does ignore the possible importance of spin-flip scattering processes which involve direct couplings between the conduction electrons and the moments, such as those in Berger's model [12].

[18] M. D. Stiles and A. Zangwill, J. App. Phys. **91**, 6812 (2002); Phys. Rev. B **66**, 014407 (2002).

[19] J. Slonczewski, Phys. Rev. B **39**, 6885 (1989).

[20] K. Xia *et al.*, Phys. Rev. B. **65**, 220401 (2002).

[21] X. Waintal *et al.*, Phys. Rev. B **62**, 12317 (2000).

[22] K. B. Hathaway and J. R. Cullen, J. Magn. Magn. Mater. **104-107**, 1840 (1992).

[23] J. C. Slonczewski, J. Magn. Magn. Mater. **126**, 374 (1993).

[24] P. Bruno, Phys. Rev. B **52**, 411 (1995).

[25] D. M. Edwards, A. M. Robinson, and J. Mathon, J. Magn. Magn. Mater. **140-144**, 517 (1995).

[26] D. J. Keavney *et al.*, J. App. Phys **86**, 476 (1999).

[27] F. J. Himpsel *et al.*, Adv. Phys. **47**, 511 (1998).

[28] W. F. Egelhoff, Jr. *et al.*, J. Vac. Sci. Technol. B **17**, 1702 (1999).

[29] A. D. Stone *et al*, in Mesoscopic Phenomena in Solids, North Holland, Amsterdam (1991).

[30] P. W. Brouwer and C. W. J. Beenakker, J. Math. Phys. **37**, 4904 (1996).

[31] A. Brataas, Y. V. Nazarov, and G. E. W. Bauer, Phys. Rev. Lett. **84**, 2481 (2000); Eur. Phys. J. B **22**, 99 (2001).

[32] Close inspection reveals that our rigorous result, Eqn. (3.30), contains transmission coefficients that are not present in either the BNB result (Eqn. (3.36)) or my single-layer result (Eqns. (3.19) and (3.20)). This is because Eqn. (3.36) is a more general result, valid even when the magnetic layer thickness is comparable to k_F^{-1} and the averaging techinques of Section 3.2 do not eliminate the contribution to the torque from the transmitted electron wave. The incoherent BNB formalism implicitly assumes that the layer is thick enough that there is no transmission contribution to the torque.

[33] G. E. W. Bauer *et al.*, Mat. Sci. Eng. B **84**, 31 (2001).

[34] G. E. W. Bauer, Y. V. Nazarov, and A. Brataas, Physica E **11**, 137 (2001).

[35] D. Huertas-Hernando, Y. V. Nazarov, and W. Belzig, Phys. Rev. Lett. **88**, 047003 (2002).

[36] Y. Tserkovnyak and A. Brataas, Phys. Rev. B **64**, 214402 (2001).

[37] F. J. Albert, personal communication.

[38] B. D. Cullity, Introduction to Magnetic Materials, Addison-Wesley, California (1972).

[39] K. Bussmann *et al.*, App. Phys. Lett. **75**, 2476 (1999); **78**, 2029 (2001).

[40] J. A. Katine, F. J. Albert, and R. A. Buhrman, App. Phys. Lett. **76**, 354 (2000).

[41] E. E. Fullerton *et al.*, Phys. Rev. Lett. **75**, 330 (1995).

[42] A. Fert *et al.*, J. Man. Magn. Mater. **140-144**, 1 (1995).

[43] J. A. Katine *et al.*, Phys. Rev. Lett. **84**, 3149 (2000).

[44] J. C. Slonczewski, J. Magn. Magn. Mater **247**, 324 (2002).

Chapter 4

Current-Induced Excitations in Magnetic Trilayers using Nanostructured Pillars

Up to this point, all of the experimental evidence I have presented for spin-polarized current-induced excitations in magnets, so-called spin-transfer, has come from measurements on nanoconstriction devices. In these devices a small hole is drilled through an insulating membrane, and metal layers are deposited on either side; very large current densities can be generated by driving a current through the hole. Although we have seen clear signatures of magnetic excitations having the symmetry of the spin-transfer torque models, we have also seen that making *quantitative* connections to theory is a very difficult proposition. The excited magnet in the nanoconstriction geometry is a domain located at the hole which, although deformed by the hole itself, is still exchange-coupled to the rest of the extended film. In this chapter I turn to a simpler geometry, in which a magnetic domain is created without a large number of extraneous couplings and then be excited via spin-transfer.

Simplifying the magnetic structure is our best hope to quantitatively describe our observations in terms of spin-transfer models. This chapter will describe a geometry in which this hope is largely achieved, by incorporating an isolated magnetic domain into a vertical pillar geometry; this is called the nanopillar geometry. The control over the magnetic structure afforded by this technique allows us to create systems that can be modeled by spin-transfer in a more straightforward manner than in the nanoconstriction geometry.

4.1 Fabrication of Nanopillars and Measurement Set-Up

4.1.1 Nanopillar Fabrication

Pillar geometries have long been employed as a means of probing giant magnetoresistance in magnetic multilayers in the current-perpendicular-to-plane (CPP) geometry. The initial CPP experiments were performed by fabricating large pillars (up to 1 mm in diameter), whose small resistances could be detected by using superconducting niobium leads that provide little contact resistance [1, 11]. The use of superconductors, however, limits the field and temperature range over which the multilayer can be studied. In more recent years, other groups have developed techniques for making pillars in the micron and submicron diameter range, increasing the GMR resistance signal relative to the contact resistance and thus eliminating the need for superconducting leads [2, 3, 4, 5]. The method I have utilized for making pillars was developed by colleagues of mine at Cornell, primarily Jordan Katine and Frank Albert [6, 7, 8]. Using this method, pillars as narrow as 50 nm can be formed regularly, far smaller than what has been achieved previously. The small

size of the pillar provides us with three advantages over previous techniques: (1) it improves the ratio of device resistance to lead resistance, giving a larger signal; (2) the reduced domain size simplifies the reversal mechanics; and (3) the smaller cross-sectional area allows us to drive current densities through the magnet large enough to generate spin-transfer-induced excitations. This last fact also assures that the effects of the self-field of the current, which can dominate in larger nanopillar devices (see [7, 32], and the discussion in Chapter 2), is minimized.

As with the nanoconstriction fabrication section of Chapter 2, I devote an appendix (Appendix B) to a detailed fabrication recipe, while here I provide a more schematic description of the process. We begin by depositing the magnetic trilayer on an insulating substrate, usually silicon oxide. A typical sequence of layers is shown in Figure 4.1a. A thick Cu layer is grown below the trilayer; this will later serve as the bottom electrode for the nanopillar. The thick magnetic layer is typically grown first, so that positive current, which in our sign convention is current flow from the thick layer to the thin layer, flows from the bottom to the top electrode. On top of the thin magnetic layer a thin capping gold layer is grown. I have made devices using both sputtered and thermally evaporated layers, and have not seen systematic differences between them. After the layers are grown, electron beam lithography and liftoff techniques are used to deposit a metallic mill mask (Fig. 4.1b). The size and shape of this mask are determined by the lithography and sets the size of the eventual pillar; typically the mask size is 50-250 nm. For most of my devices I have used either chrome or gold as the mill mask material.

The next step is to create the pillar by performing a precision ion mill. In the ion mill machine, a beam of ionized Ar atoms is accelerated at the layers and the metal is sputtered ("milled") off. The mill mask protects the metal underneath

by getting milled off first, so that the result is a pillar approximately in the shape of the mill mask (Fig 4.1c). The mill rates for each material are well determined through previous testing; as a result, the mill depth, if timed correctly, can be controlled to within a few nm. Typically I time the mill so that it stops before it removes a significant amount of the thicker layer. In this way the thin layer is sculpted into a small confined magnet (the "nanomagnet"), while the thicker layer is left as an extended film. This enhances the differences in coercive fields of the two layers, making it easier to separate the behavior of the thick layer from that of the nanomagnet. Since it is important to catalog the typical height and size of the pillars on a particular wafer, at this point an atomic force microscope (AFM) and a scanning electron microscope (SEM) are used to characterize the pillars by imaging an array that is fabricated in parallel on the wafer with the device pillars. AFM and SEM images of arrays are shown in Figures 4.2 and 4.3, respectively.

We still need to make separate contact to the top and bottom of the pillar, so the bottom electrode must be isolated from what will eventually be the top electrode. This is done by depositing polyimide, an insulating polymer similar to PMMA, onto the pillar structure (Fig. 4.1d). The pillar is now submerged in the polyimide, so a precision reactive ion etch must be performed to expose only the top of the pillar prior to deposition of the top lead. Successful execution of this step requires precision timing and knowledge of the pillar height and the thickness of the polyimide. Typically a range of etch times are used to find the "sweet spot" of ideal pillar exposure, where a sufficient amount of the Au cap is exposed for good contact, but the magnetic layers underneath remain submerged in the insulator. A short ion mill is performed to clean the surface of the pillar, and a top lead is then deposited (Fig. 4.1e).

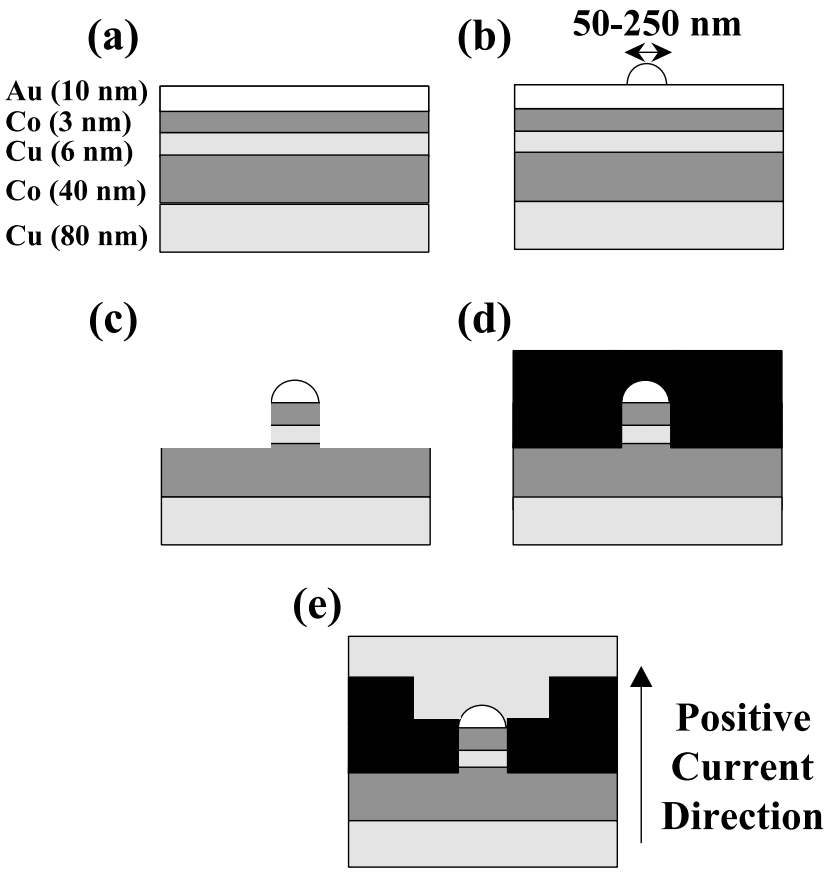


Figure 4.1: Schematic of nanopillar fabrication. (a) Metal layers are deposited on an insulating substrate. (b) Electron beam lithography and liftoff are performed to deposit a mill mask that will define the pillar size. (c) A timed ion mill forms the pillar; the mill is usually timed so that the thicker magnetic layer is left as an extended film, while the thin layer forms a confined nanomagnet. (d) A polyimide insulator (black color) is deposited. (e) The top of the pillar is exposed through reactive ion etching, and a top lead is deposited.

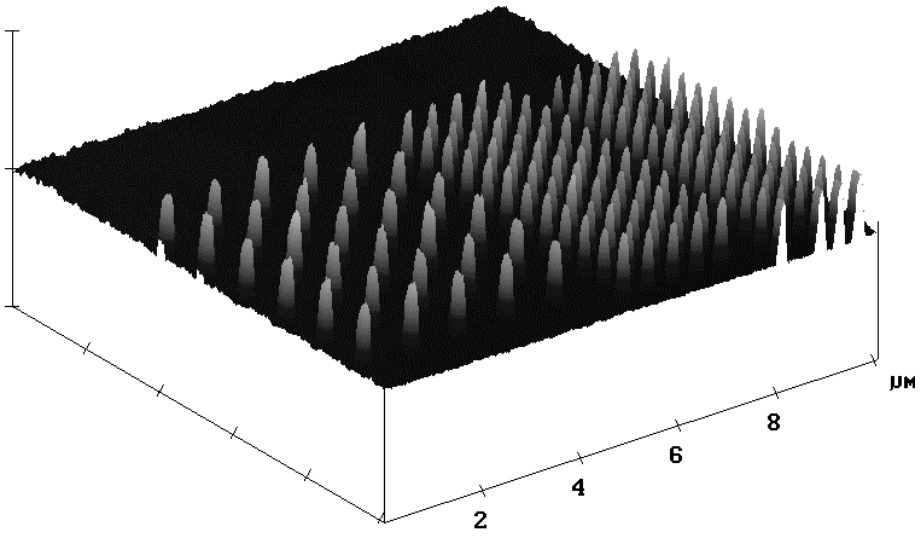


Figure 4.2: Atomic force microscope image of an array of pillars. The pillar heights here are approximately 140 nm.

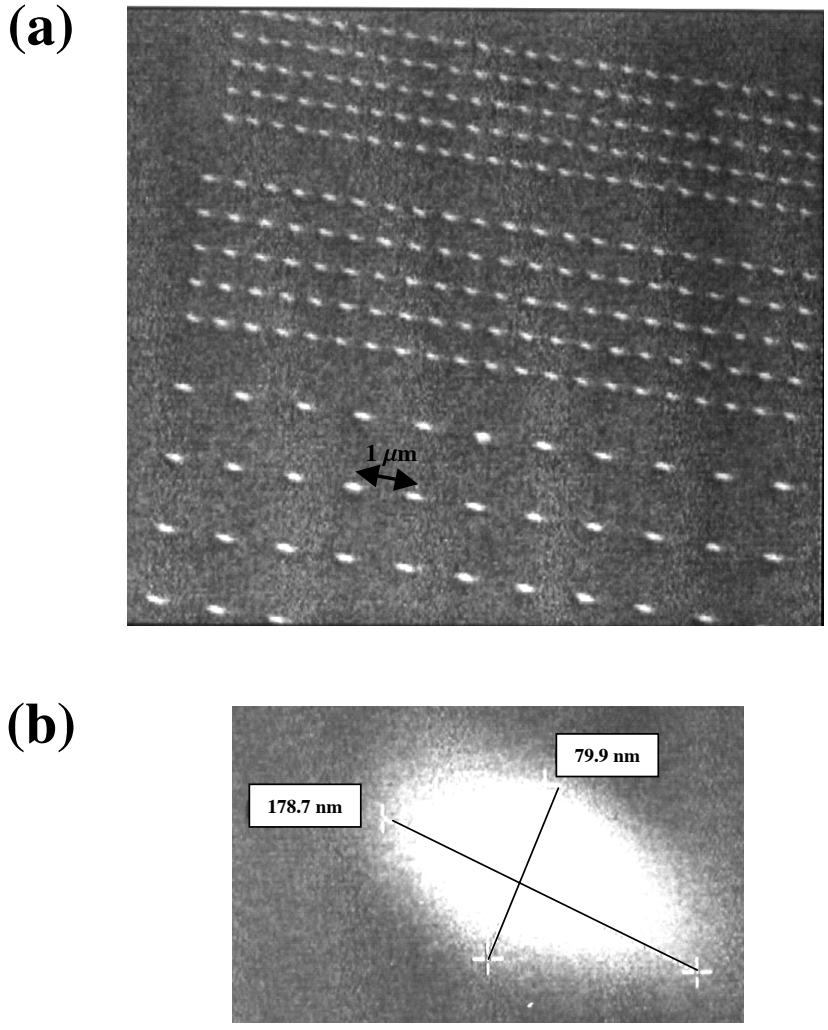


Figure 4.3: (a) Top-down scanning electron microscope image of the array pictured in Figure 4.2. The different subsets of the array are pillars of different sizes. (b) Closeup of one pillar, showing the dimensions (approximately 180×80 nm).

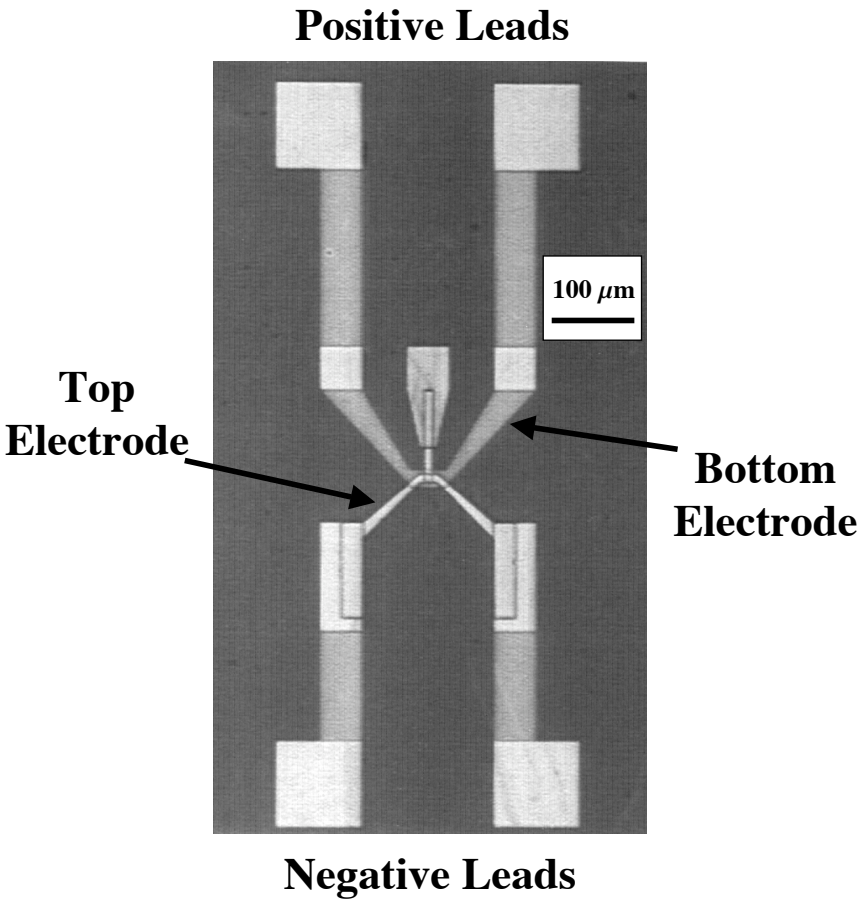


Figure 4.4: Optical image of a finished pillar device. The pillar sits at the center of the image, directly between the top and bottom electrodes. Wirebonds are formed to the larger pads at the top and bottom of the image for a 4-probe measurement.

Interspersed among these steps are layers of photolithography (5 in all), which, among other things, define the leads to which we make contact to the top and bottom electrodes. A completed device is shown in Figure 4.4, with pads connected to the top and bottom electrodes so that 4-probe measurements can be made. Small groups of devices are mounted onto chip carriers and the device leads are connected to the carrier via wirebonds. This allows the nanopillar device to be mounted into any standard carrier socket for room temperature measurements, or measurements on a dipper down to liquid helium temperature.

4.1.2 Measurement Set-Up

The same lock-in techniques as described in Chapter 2 for measurements on nanoconstrictions were used for nanopillar measurements. Unlike nanoconstrictions, however, the full range of spin-transfer effects discussed in this dissertation are observable in nanopillars at room temperature, and so the bulk of my measurements (except for those where temperature is an important parameter, such as in Chapter 5) are performed at ambient temperature. The reason for this difference in the two geometries arises from the reduced effects of magnetic coupling in nanopillars as compared to nanoconstrictions. I will discuss how this reduced coupling leads to simpler interpretations of spin-transfer excitations in nanopillars in the next section.

Typically, electromagnets are used to generate a field at room temperature. I have utilized two measurement geometries for applying magnetic fields to nanopillars at room temperature, both of which allow me to control both the magnitude and direction of the field in a 2-D plane. In one magnet provided to us by Yu Lu at I.B.M. (Figure 4.5a), two pairs of finite solenoids are wrapped around a copper ring; the fringe fields generated by the solenoids at the center of the magnet can

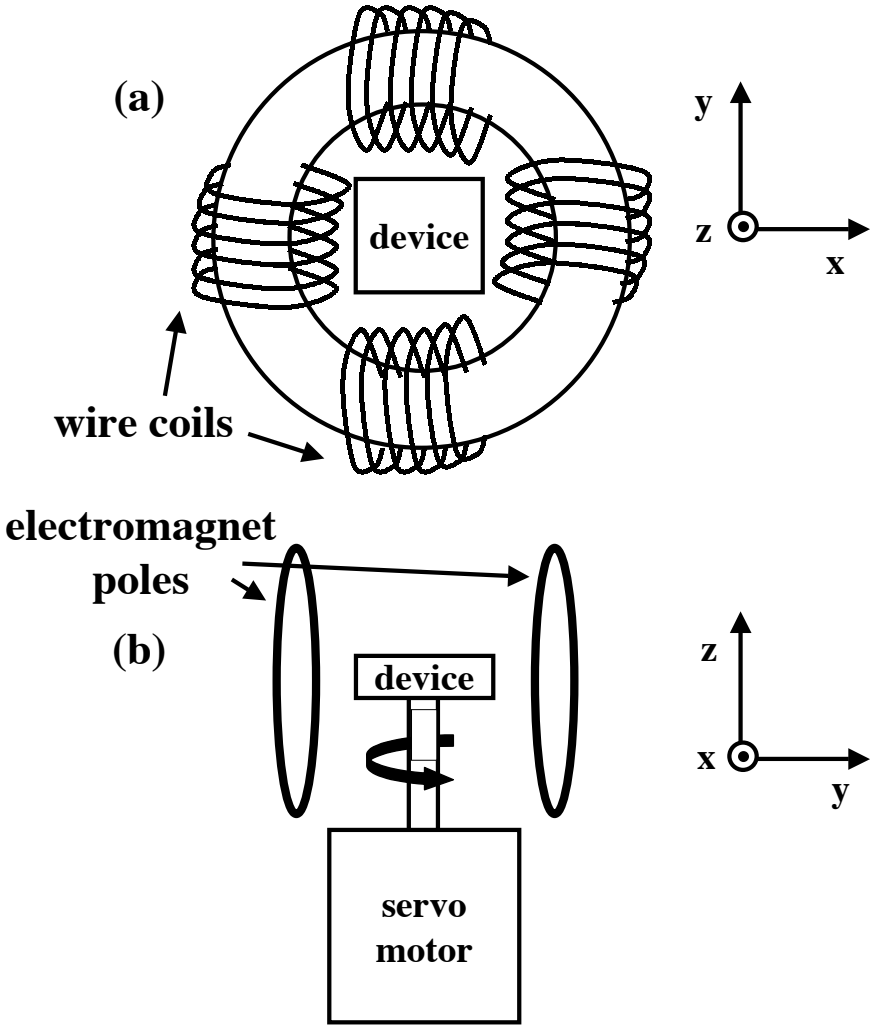


Figure 4.5: Two methods in which a magnetic field is applied to nanopillar devices in a 2-dimensional plane. In both case the field is applied in the plane of the magnetic layers, which is the x-y plane here. (a) For small fields (< 300 Oe), two pairs of solenoid coils around a copper ring generate a field in the center of the ring whose direction can be controlled by varying the currents within each coil pair. (b) For larger fields (up to 10 kOe), the device is mounted on the shaft of a servo motor with fine angular control, and placed between the poles of a commercial electromagnet. The device is then rotated to change the relative field angle.

be made as large as 300 Oe, and the direction can be controlled by varying the currents in each coil pair independently. This setup is most useful for fine control of small fields, which is important when using materials with very low coercivities such as Permalloy. The other magnet setup varies the direction of the field relative to the device not by rotating the field, but by rotating the device itself. A sample holder is mounted onto the end of a servo motor, and is placed between the poles of an electromagnet (Fig. 4.5b). The servo allows control of the angle of the device relative to the field to high precision. Fields as high as nearly 10 kOe can be applied to the device in this setup. There is a slight remanent field in the poles of 50 Oe which needs to be compensated for when taking the data; as a result, the solenoid setup is preferred when working at small fields.

4.2 Nanopillars vs. Nanoconstrictions

As I mentioned at the start of this chapter, the nanopillar technique allows us to create magnetic domains with well-controlled sizes, shapes, and magnetic environments. This allows us to make quantitative comparisons to spin-transfer models to a degree that is simply not possible in the nanoconstriction geometry. As much of the fundamental nanopillar work was done by colleagues prior to my use of the technique, I briefly summarize their results in this section.

4.2.1 Current-Induced Reversal of Nanopillar Magnets

At low magnetic field, Katine [6] observed in Co/Cu/Co pillars a hysteretic switching of the two layers, similar to what is observed in the nanoconstrictions. Figure 4.6a shows switching in a $(Co_{2.5}/Cu_6/Co_{10})_{nm}$ nanopillar device of lateral dimensions

130×130 nm. Note that the formal device name is shown in parenthesis in the figure caption for identification. As can be seen, the switch from the low resistance state (parallel alignment of the two layers) to high resistance state (antiparallel alignment of the layers) occurs at positive current bias, and the opposite switch at negative bias. This has the same symmetry as predicted by spin-transfer torque models. Moreover, the critical current densities needed to switch the nanomagnet in this geometry is on the order of $10^8 A/cm^2$, significantly lower than those needed in nanoconstrictions. In this work the Slonczewski model was applied to these transitions, and it was found that the values of the zero-field critical currents were consistent with the Slonczewski model when a damping parameter α close to that found in FMR studies of bulk Co [15] was used. This is in stark contrast to the nanoconstriction results of Chapter 2, where the small-α assumption necessary to the analysis breaks down completely. The absence of an extended disordered film exchange-coupled to the nanomagnet means that the loss of angular momentum due to propagation away from the current source is minimized; therefore the measured damping is more characteristic of that for uniform motion in an isolated bulk sample, which is the dominant mode probed in FMR experiments. As an illustrative example, I apply the Slonczewski model quantitatively to switching transitions in my own Co/Cu/Co devices in section 4.3.

The data from the initial nanopillar work [6], while demonstrating switching behavior more easily understood by theory than that from nanoconstrictions, still had some complexity. In circular nanopillars multiple jumps in the resistance are often observed as the current is swept (as in Fig. 4.6a), indicating that the reversal is not simple. The multiple resistance states suggest either that a domain wall nucleates and propagates through the nanomagnet as the current increases, or that the nanomagnet's moment gets pinned in some direction intermediate between full

parallel and antiparallel alignment with the thicker magnet as it reverses. These kinds of behaviors may be energetically favorable in circular polycrystalline nanomagnets, where there is no preferred magnetization axis. To resolve these issues, shape anisotropy was introduced into the pillar fabrication design [8]. By making the nanomagnet elongated in one direction, domain walls are made energetically less favorable at zero field, due to the in-plane demagnetizing field; thus the magnet will tend to act as a simple uniaxial magnet, magnetized along the long axis in either direction [10]. This axis is typically called the easy axis, and the direction perpendicular to it in the plane of the magnet is the (in-plane) hard axis. Figure 4.6b shows a current-induced hysteresis loop for a $(Co_{2.5}/Cu_6/Co_{40})_{nm}$ nanopillar of dimensions 130×60 nm, at room temperature and zero field, from [8]. This device shows only two stable resistance states, indicating that spin- transfer switches the magnet cleanly between its two stable orientations along the easy axis.

4.2.2 Dynamical Excitations at Higher Fields

When the field significantly exceeds the coercive field of the nanomagnet, the hysteresis is suppressed and a peak appears in the differential resistance, corresponding to a dynamical excitation in the nanomagnet (Figure 4.6c) [7]. These peaks are similar to those observed in nanoconstrictions (Chapter 2). If the dependence of these peaks on the applied magnetic field is measured and the slope fit to the Slonczewski model, a good fit can be achieved by assuming a damping parameter α 1-2 orders of magnitude smaller than the damping constant for high-field excitations in the nanoconstriction geometry, and close to that for bulk Co. Again, the absence of a large film exchange coupled to the domain here simplifies the physics, as the spin-waves do not couple to a continuum of nonuniform modes; therefore the damping

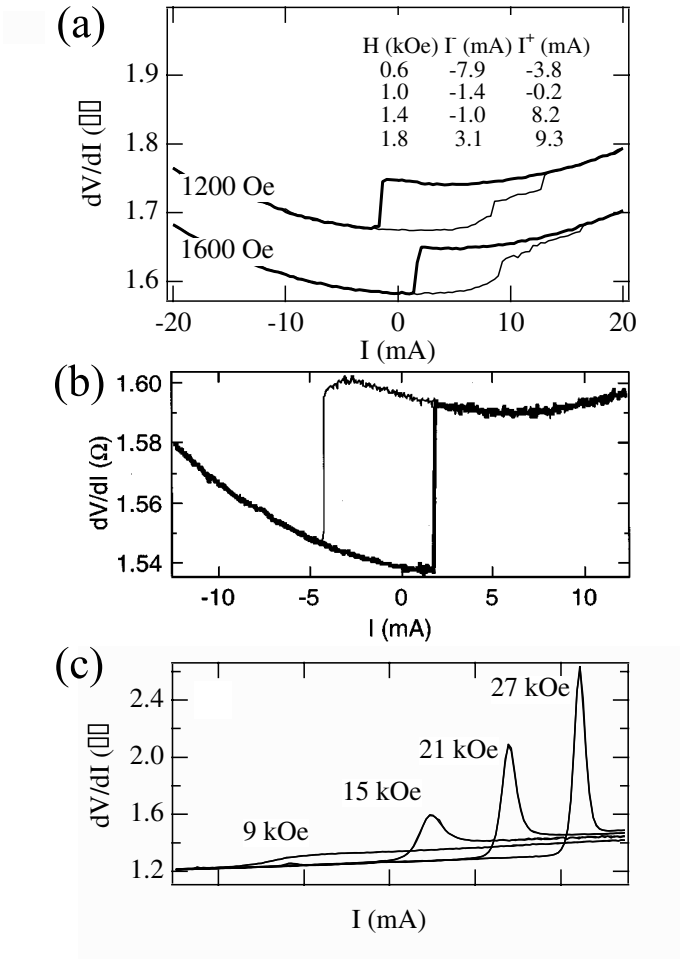


Figure 4.6: Central nanopillar results previous to this work. (a) Current-induced hysteresis seen in a circular 130 × 130 nm nanopillar, with the same asymmetry with respect to current direction as seen in nanopillars. When shape anisotropy is introduced into the pillar (b), the switching characteristics consistently simplify to two resistance states, representative of the magnet's two stable states along its long axis. (c) At higher magnetic fields, peaks are seen in the differential resistance, corresponding to dynamical excitations.

constant is essentially that for a bulk excitation.

4.3 My Nanopillar Devices

A significant amount of the time I have spent on nanopillars has gone towards mastering the technique and reproducing the basic results of Katine and Albert. Although I have not extensively studied these pillars in the high-field regime, I have made devices which show clean switching behavior similar to that in [8]. For the remainder of this chapter, I summarize my basic observations. However, becuase much of this simply confirms the previous studies, I will not dwell too long on measurements that have been performed before, except to illustrate specifics of the data not discussed in the brief summary above. Instead, I focus on a subset of the devices I have made that have particularly simple switching characteristics, which make them highly favorable systems for studying spin-transfer. These devices feature prominently in Chapter 5, which is a study of the role that temperature plays in current-induced excitations.

4.3.1 Magnetoresistance

Figure 4.7a shows a magnetoresistance loop at zero applied current bias for a $(Co_{2.5}/Cu_6/Co_{40})_{nm}$ pillar device of dimensions 130×70 nm. From SEM images of arrays formed in parallel with this device, the dimensions are accurate to within ± 10 nm. The field H is applied along the long axis of the pillar. There are two distinct jumps in the differential resistance dV/dI as the field is swept: a jump to high resistance at about 70 Oe, and a jump back to low resistance at about 570 Oe. A similar shape to the magnetoresistance curve was seen in Albert's work[8]. Due to

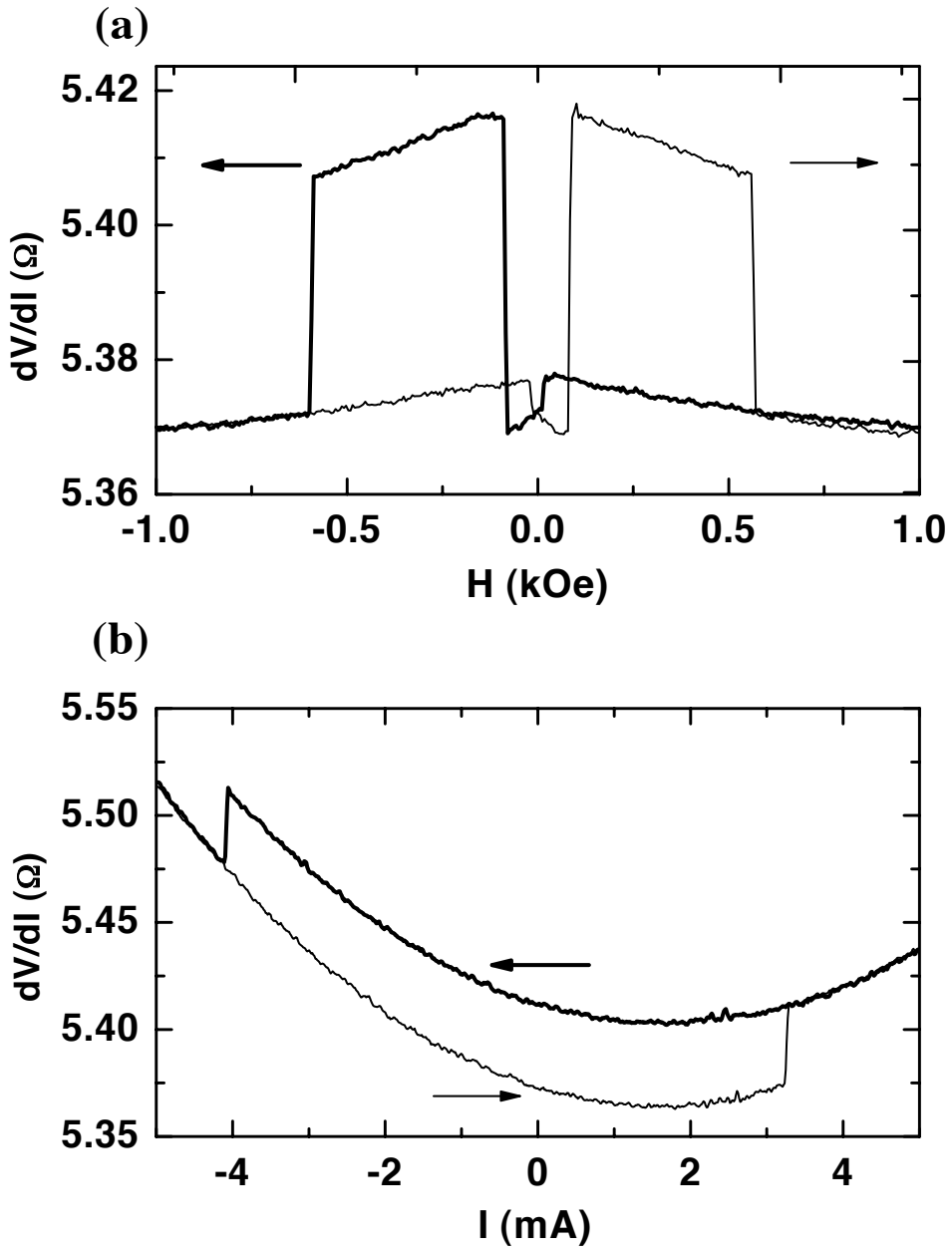


Figure 4.7: (a) Magnetoresistance loop for a $(Co_{2.5}/Cu_6/Co_{40})_{nm}$ pillar device (SC1744) of dimensions 130 $\times$ 70 nm. The field is applied along the long axis of the pillar. (b) Current-induced reversal hysteresis loop for the same device.

the simplicity of the nanopillar system, we can clearly distinguish these two jumps as corresponding to the different coercive fields of the nanomagnet and the thick film. As established in Chapter 2, Co films in this thickness range (several 10's of nm) have coercive fields on the order of 50 Oe; therefore the thick film reverses first. The nanomagnet cannot reverse as easily, since it must generate high-energy dipolar fields during the reversal process, due to its small size. Although the coercive field for nanomagnets is set by a large number of parameters, such as size, thickness, and edge roughness, and cannot be easily predicted, a coercive field of 570 Oe is consistent with measurements on nanomagnets with similar dimensions [10]. There are additional features at fields smaller than 50 Oe; these are likely due to nonuniform motion of the thick layer below its coercive field.

The typical magnetoresistance ratio, defined as $MR = (R_{AP}(I = 0) - R_{low}(I = 0))/R_P(I = 0) \times 100\%$, where R_{AP} and R_P are the resistance states of the antiparallel and parallel configurations, respectively, ranges from 1-5% for my devices. This is similar to the MR ratios measured in the nanoconstrictions, and, as noted in the discussion in Chapter 2, is smaller than expected for a pure Co/Cu/Co spin-valve geometry. While in the nanoconstrictions the smaller MR ratio is due to the large spin-independent ballistic Sharvin resistance intrinsic to the point-contact geometry, in nanopillars the ratio is likely reduced due to a large contact resistance at the top of the pillar. The nanopillars, after their creation, are exposed to air for a considerable amount of time, and may develop oxides or adsorbates. The gold cap should minimize oxidation at the top of the pillar, but some contaminants may still form there. Even though I perform an ion mill clean immediately prior to deposition of the top lead, the top of the pillar is exposed to air briefly as the sample is moved from the ion mill to the thermal evaporator. Frank Albert performs an *in situ* ion

mill prior to deposition of the top lead in an evaporator mounted with an internal ion mill; in general his devices with similar cross-sectional areas have a resistance lower than my own by roughly a factor of two [12]. I have utilized this system occasionally, but with little success in reducing the contact resistance in my own devices; in any case, the size of the contact resistance does not appear, except in extreme cases, to correlate with the quality of the magnetic characteristics of my devices.

To estimate the importance of contact resistance, we need to determine the relative contributions of all other sources of resistance in the pillar. The trilayer itself makes a certain contribution, of course; otherwise, we wouldn't be able to measure a GMR signal. Previous CPP studies have determined values for the interface and bulk resistance contributions in Co/Cu multilayers, using the two-channel series resistor model [11]. With the (significant) caveat that these values may not scale down accurately to only two magnetic layers, these results can be used to get an estimate of the resistance of the trilayer in the parallel and antiparallel configurations. The quantities in [11] are in the form of RA, where R is the resistance and A the cross-sectional area of the multilayer. Adding together the interface resistance contributions for each spin channel (two interfaces for the nanomagnet, and the single closer interface for the thicker film), along with the bulk resistance contributions (proportional to thickness) from the Co nanomagnet and the Cu spacer, I estimate roughly that the trilayer depicted in Figure 4.7 contributes in the parallel state a resistance-times-area $R_P A \approx 910$ Ω-nm^2, while in the antiparallel state it contributes $R_{AP} A \approx 1550$ Ω-nm^2. Given that the device has a cross-sectional area $A = 130\ nm \times 70\ nm = 9100\ nm^2$, the expected resistances in the two states are $R_P \approx 100\ m\Omega$ and $R_{AP} \approx 170\ m\Omega$. This is only about 2-3% of the total resistance

measured. There are other contributions from the bulk resistivity of the top Au cap and the Cu top lead, as well as from the so-called spreading resistance, which arises when a narrow channel (the nanopillar) is connected to a macroscopic lead. However, this cannot fully account for the remainder of the resistance. Given Frank Albert's pillars with significantly lower resistance, I estimate that a minimum of 50% of the total resistance derives from the contact formed between the Au cap and the Cu top lead. This contribution varies greatly from sample to sample, giving total resistances from $1.5\Omega - 15\Omega$ for devices with the same nominal dimensions. It is interesting to note, though, that the absolute resistance-times-area difference between the two states, $(R_{AP} - R_P)A = 600 \pm 200$ Ω-nm^2 for most of my devices. devices. This is in reasonable agreement with the above estimation for the intrinsic trilayer resistances, and is also consistent with the resistance levels observed in Frank Albert's devices of similar sizes ,where $(R_{AP} - R_P)A = 480 \pm 20$ Ω-nm^2 [13].

4.3.2 Current-Induced Switching

Figure 4.7b is a plot of differential resistance dV/dI vs. current I for the same device shown in Fig. 4.7a, in a small field of 50 Oe applied along the long axis, and at room temperature. A clear hysteresis in the signal as a function of current can be observed, corresponding to a switching of the nanomagnet between parallel and antiparallel alignment with the thick layer. The symmetry of this hysteresis is the same as that seen in previous nanopillar studies, as well as the nanoconstriction studies. In addition to this hysteresis, there is an asymmetric rise in differential resistance with increasing current bias of both signs. This rise may come about from a combination of Joule heating of the sample by the current, and thermopower voltages generated by the dissimilar metals in the pillar [14]. The two resistance

levels measured by sweeping the current are the same levels seen in the magnetoresistance (Fig. 4.7a), confirming that in both cases the nanomagnet is cleanly switched between its two stable configurations along the long axis. The consistency of the magnetic behavior between application of current and field again highlights the simplicity of this geometry in comparison to nanoconstrictions, where the current and magnetic field can affect different parts of the thin extended magnetic layer and thus result in resistance signals that are hard to correlate.

The measured critical currents can be compared quantitatively to the Slonczewski torque model, using the Landau-Lifschitz-Gilbert (LLG) equation:

$$\frac{d\vec{S}_{F2}}{dt} = \gamma \vec{S}_{F2} \times \vec{H}_{eff} - \left[\gamma\alpha\hat{s}_{F2} \times \left(\vec{S}_{F2} \times \vec{H}_{eff}\right) + \frac{cI}{e}\hat{s}_{F2} \times \left(\hat{s}_{F1} \times \vec{S}_{F2}\right)\right], \quad (4.1)$$

where $\vec{S}_{F2}$ is the spin moment in the excited domain of layer $F2$, and $\hat{s}_{F1(F2)}$ a unit vector in the direction of the spin moment in layer $F1(F2)$. The constant c is defined in Chapter 2 and contains Slonczewski's factor $g(\theta)$, which depends on the polarization properties of the materials and the angle θ between $\vec{S}_{F1}$ and $\vec{S}_{F2}$. As before, the critical quantity needed to determine the instability threshold is the effective field $\vec{H}_{eff}$. For the nanoconstrictions, quantitative analysis necessitated replacing the complex local field $\vec{H}_{eff}$ with an oversimplified average. In the simpler geometry of nanopillars, however, the main contributions to $\vec{H}_{eff}$ can be included directly into the calculation. I write the total effective field as

$$\vec{H}_{eff} = \vec{H}_u + \vec{H}_{demag} + \vec{H}_{offset}. \quad (4.2)$$

The first field $\vec{H}_u$ lies along the long axis of the pillar and represents the effects of shape (magnetostatic) anisotropy. There may be other contributions to the anisotropy from the crystalline structure of the Co, but the existence of the two stable magnetization states along the long axis demonstrate that the dominant part

of the in-plane anisotropy is due to shape. The second term $\vec{H}_{demag}$ represents the large demagnetizing field felt by the moment when it points out of plane, also due to magnetostatics. This has the form

$$\vec{H}_{demag} = -4\pi\gamma \left(\vec{S}_{F2} \cdot \hat{n}\right) \hat{n}, \tag{4.3}$$

where $\hat{n}$ is a unit vector normal to the nanomagnet plane, pointing outwards. The quantity $4\pi\gamma \left|\vec{S}_{F2}\right|$ is the magnetization in field units, which for Co is 17 kOe. The last field term, $\vec{H}_{offset}$, contains all other possible local field couplings, including dipolar couplings between the layers and interlayer exchange. To simplify the analysis, I make the following two assumptions: that $\vec{H}_{offset} || \vec{H}_u$; and that $\vec{S}_{F1} || \vec{H}_u$. The second of these assumptions can be achieved experimentally by applying a small field greater than the coercive field of the thick magnetic layer (50 Oe) approximately along the easy axis of the nanomagnet, as in Figure 4.7. We cannot be as sure of the validity of the first assumption, but, as there are fewer extraneous couplings involved, it is likely a far less egregious simplification than it is for the nanoconstriction geometry.

Returning to Eqn. 4.1, we find that the effective field $\vec{H}_{eff}$ described above results in a precession around the easy axis that is not circular, but compressed into an ellipse due to the demagnetizing field (Figure 4.8). While in the plane of the film, the moment orbits according to the uniaxial anisotropy. This bring the moment out of the plane, which generates a large demagnetizing field and induces a much faster precession along the long axis of the ellipse. Since the damping is proportional to the rate of change of the moment, it is therefore not constant over the orbit, and does not always point radially in towards the easy axis. As a result, the damping and spin-transfer torques do not lie along the same direction at all points on the orbit, and we cannot easily compare their magnitudes at any particular time, as

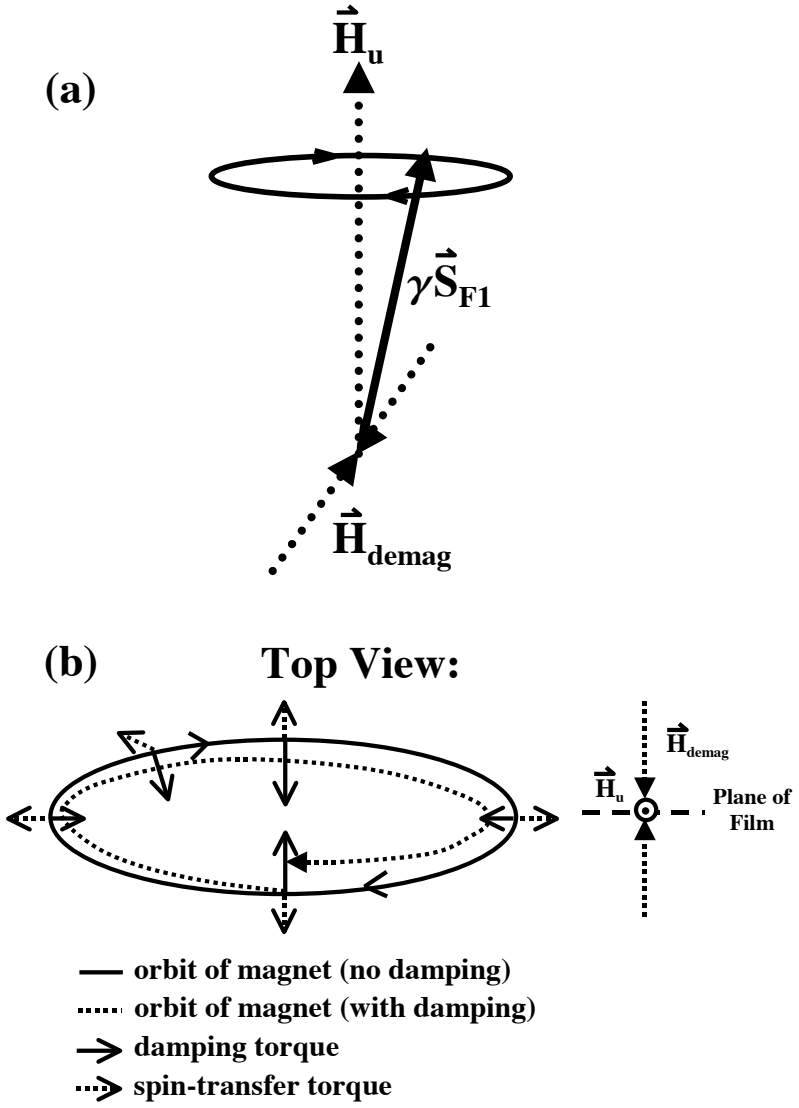


Figure 4.8: (a) Motion of spin moment $\vec{S}_{F2}$ in the presence of a uniaxial anisotropy $\vec{H}_u$ and a large perpendicular demagnetizing field $\vec{H}_{demag}$. (b) Top view of the moment motion. The precession orbit is elliptical in the absence of damping (solid line); with damping it spirals inwards (dotted line), with its largest damping torque (solid arrow) occurring when the moment moves out of the film plane. The damping is not necessarily opposite in direction to spin-transfer (dotted arrow); thus an average over a complete orbit is necessary to compare the relative effects of damping and spin-transfer.

we could for the simple uniaxial anisotropy model in Chapter 2. However, if we assume that the damping is small ($\alpha << 1$), then we can compare the effects of the damping and spin transfer *averaged* over a complete orbit, since it will take many such orbits before either the damping or the spin-transfer has a significant effect on the moment. This was done in [6] by calculating the average rate of change in the energy of the magnet over one orbit, for a small elliptical orbit about one of the energy minima with average angle amplitude A:

$$\left\langle \frac{dE}{dt} \right\rangle_{orbit} \sim A^2 \frac{(H_u \pm H_{offset})}{\gamma \left| \vec{S}_{F2} \right|} \times \left(-\alpha\gamma \left[H_u \pm H_{offset} + 2\pi M \right] + \frac{Ig(\theta)}{e \left| \vec{S}_{F2} \right|} \right), \quad (4.4)$$

where $E = \gamma \left| \vec{S}_{F2} \right| \cdot \vec{H}_{eff}$, $g(\theta)$ is the Slonzcewski factor, and the sign of H_{offset} depends on whether the offset field favors or opposes the energy minimum of interest. With $I = 0$ or very small, $\langle dE/dt \rangle_{orbit} < 0$, and the moment decays to the energy minimum. If the average energy change is positive, however, the moment is driven away from the minimum and switching occurs. Let us assume that $\vec{H}_{offset}$ is in the same direction as $\vec{S}_{F1}$, so that it favors a parallel alignment of the moments. If the moments $\vec{S}_{F1}$ and $\vec{S}_{F2}$ begin nearly parallel ($\theta \approx 0$), and the current I is positive, then the magnet will switch at currents greater than the critical current

$$I_c^+ = \frac{\alpha e \left(H_u + H_{offset} + 2\pi M \right) \gamma \left| \vec{S}_{F2} \right|}{\hbar g(0)}. \quad (4.5)$$

If the moments in the two layers are nearly antiparallel ($\theta \approx 180°$), then a negative current is required to switch the layers; the critical current is

$$I_c^- = -\frac{\alpha e \left(H_u - H_{offset} + 2\pi M \right) \gamma \left| \vec{S}_{F2} \right|}{\hbar g(\pi)}. \quad (4.6)$$

The effect of the offset field can be subtracted out, as was done in Chapter 2, by combining the equations above:

$$g(0) I_c^+ - g(\pi) I_c^- = 2 \frac{\alpha e \left(H_u + 2\pi M \right) \gamma \left| \vec{S}_{F2} \right|}{\hbar}. \quad (4.7)$$

The value of the uniaxial field H_u can be approximated as the coercive field H_c, taken from the magnetoresistance data. For the device of Fig. 4.7, $H_c = 560$ Oe. Note, however, how this is dwarfed by the term in Equation (4.7) that comes from the demagnetizing field, $2\pi M = 8.5$ kOe. This illustrates the starkly different thresholds for reversal induced by a current within the torque model as opposed to reversal induced by a magnetic field. At fields greater than the in-plane anisotropy H_u, one of the stability points is no longer a stable energy minimum (formally, it becomes a saddle point), and natural dissipative processes will drive the magnet to align with the other stable point, which is a global energy minimum. In the case of the current, however, even when spin-transfer torque overcomes the damping associated with H_u, the moment will still rotate out of plane during its precession and generate the much larger demagnetizing field, which creates a correspondingly larger damping that drives the moment back towards the energy minimum. It is only when spin-transfer can overcome the damping associated with *both* H_u and H_{demag} over a complete orbit that the magnet will be driven away from its stability point over time. I will explore the distinct mechanisms of field and current-induced reversal in more detail in Chapter 5, when I consider a more complete nanomagnet stability diagram.

For the moment, we can substitute numbers into Equation (4.7) and compare with the measured critical currents. The Slonzczewski factors are $g(0) = 0.13$ and $g(\pi) = 0.52$, and $\gamma \left|\vec{S}_{F2}\right| = (1400\ emu/cm^3)\, V$ for Co, where V is the volume of the nanomagnet. This volume for the device of Fig. 4.7 is $(130 \pm 10)\ nm \times (70 \pm 10)\ nm \times 2.5\ nm = 23{,}000 \pm 5000\ nm^3$. The resulting expression is

$$0.13 \times \left|I_c^+\right| - 0.52 \times \left|I_c^-\right| = \alpha \times (80 \pm 20)\ mA, \tag{4.8}$$

which for the device in question yields good correspondance when $\alpha = 0.02 - 0.03$.

An average of similar calculations for my my other devices also gives typical damping constants of $\alpha = 0.01 - 0.03$. In Chapter 5, I show that reversal is a thermally-activated process, so that the measured switching currents are likely smaller than the $T = 0$ values, typically by 30-40%; this suggests that the estimated values of α should be adjusted upward slightly, to about $\alpha = 0.015 - 0.045$. A damping constant in this range is in general agreement with the previous studies [6, 8], and are several times smaller than the values extracted from the nanoconstriction measurements of Chapter 2 ($\alpha = 0.05 - 0.2$). This can be understood as a consequence of the relative isolation of the nanomagnet in the pillar as opposed to the domain in the constriction. The nanomagnet is not exchange-coupled to an extended film, and so there do not exist a large set of spin-wave modes which couple to the moment and can channel energy away from it. Thus the damping processes associated with current-induced reversal of the nanomagnet should be significantly smaller than for the domain in the nanoconstriction geometry.

However, it should be pointed out that the nanopillar damping determined from the switching currents is 2-3 times larger than than the damping extracted from FMR measurements on macroscopic samples, $\alpha = 0.007$ [15]. Moreover, in the measurements performed by Katine and Albert on the high-field dynamical excitations in nanopillars [6], the fitted damping constant is $\alpha \approx 0.005$, lower than seen for switching and much closer to the FMR measurements. One explanation for the discrepancy is that, unlike the high-field precession, the magnetic reversal induced by spin-transfer might involve nonuniform motion of the moment; there may be more complex modes which couple to finite-wavelength spin-waves in the magnet. This would increase the effective damping, but, unlike the nanoconstriction case, these modes are bounded by the finite size of the nanomagnet and so cannot draw energy

away from the region of excitation. Thus the enhancement is relatively small. By contrast, the lower damping for the high-field excitations might indicate that they are more uniform excitations, and so correspond better to the damping measured in uniform-mode FMR measurements. Recently, it has been observed that the presence of an interface between a ferromagnetic thin film and a paramagnetic film can also significantly enhance the FMR linewidth of the ferromagnet [16]. This has been explained as an increased damping due to parametric pumping of conduction electron spins into the normal metal by the precessing spin moment [17]. Alternatively, Berger has predicted an increased damping at normal-ferromagnetic interfaces due to an enhanced spin-flip scattering rate of conduction electrons there [18].

Of all the Co/Cu/Co devices I have made, roughly 5-10% of them show clean two-level switching [21]. The remainder still show effects that can largely be attributed to spin-transfer, but the signals often include multiple switching events and peaks in the differential resistance. This indicates that there can be large sample-to-sample structural variations, which can give rise to complex magnetic behavior. Such variations are not always correlated to the structural variations of the pillar shape as measured on the test arrays by AFM and SEM, as devices made from wafers with regular arrays can have a wide variety of magnetic behaviors. One additional factor that could contribute to this variation, and something that is not easily measured via either SEM or AFM, is the microscopic variation in the mill depth from sample to sample. If the mill grinds down significantly into the thicker magnetic film, it could create a partially-isolated domain below the nanomagnet that might contribute to additional complexity in the signal. In addition, the material that is sputtered off of the layers by the mill does not just disappear, but is redeposited elsewhere. Most of it lands far from the pillar, but a small portion of sputtered material may

redeposit on the sides of the pillar. If this includes a significant amount of Co, the nanomagnet may feel additional couplings which would complicate the reversal mechanism. Both the AFM and the SEM are sensitive only to the shape of the pillar, not the material composition, so such structural irregularities can not be observed before measurements on a finished device are made.

4.3.3 Anomalously-Small Devices

Although the structural variations limit the yield of quality devices, it can also have positive results. A small subset (about 10%) of the two-level switching devices, produced during one particular fabrication run, showed unusually good switching properties. The pillars on this wafer were all fabricated to have lateral dimensions of 130 $\times$ 70 nm. While the average difference between critical currents $I_c^+ - I_c^-$ for all of the devices was about 10 mA, several devices had switching current differences $I_c^+ - I_c^- < 2$ mA, with both $|I_c^+|, |I_c^-| <1$ mA. The magnetoresistance ratio of these devices was also relatively large, about 5%, and the resistance difference between the two states $(R_{AP} - R_P) \approx 150 - 300\ m\Omega$, higher than the vast majority of the devices, and significantly higher than that estimated in section 4.3.2 for a device with the same cross-sectional area. Figure 4.9 shows the current-induced hysteresis loop for one of these devices.

The large $R_{AP} - R_P$ suggests that these devices have a smaller cross-sectional area than expected; further measurements reveal that their shapes are also likely different from the other devices. Figure 4.10a is a magnetoresistance plot for the device pictured in Fig. 4.9, with the field applied along the pillar's long axis, which I will define as an angle of $\phi_{exp} = 0$. Although two jumps can be distinguished, there is also significant continuous variation of the resistance with field, indicating that the

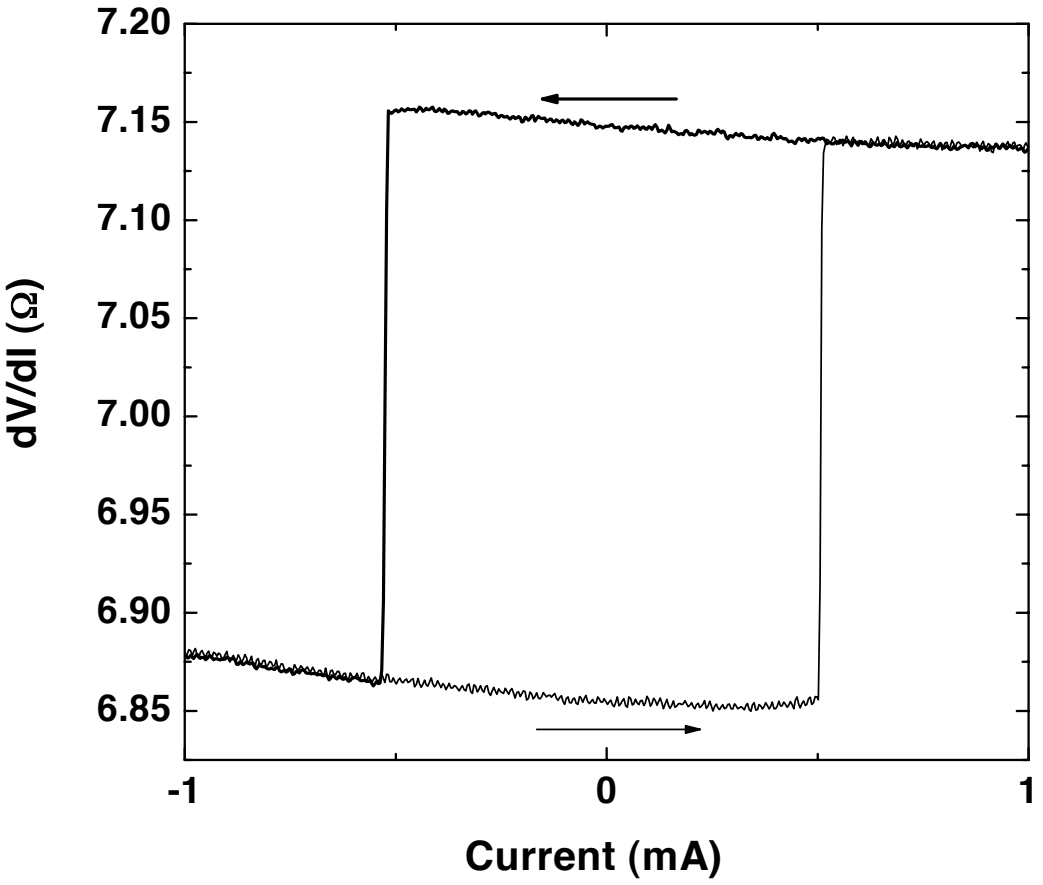


Figure 4.9: Current-induced hysteresis loop for a $(Co_{2.5}/Cu_6/Co_{40})_{nm}$ device (SC3434) of nominal dimensions 130×70 nm. The switching currents for this and a select few other devices are considerably lower than devices of the same supposed size made in parallel on the same wafer.

average magnetization direction of the nanomagnet does not remain fixed as the field is swept. If we rotate the field angle by 90°, however, the magnetoresistance curve changes dramatically (Figure 4.10b). Now the resistance is nearly constant, other than the two abrupt jumps due to reversal of the thick layer and the nanomagnet. The difference in the two resistance states is also increased, which suggests that full antiparallel and parallel alignment is more closely achieved for this field angle. Other devices in this subset show this same dependence on field angle.

These results are completely contrary (one might even say "orthogonal") to what one would expect for the device. Since the pillar is engineered to have its easy axis along the $\phi_{exp} = 0$ direction, the stable magnetization directions should be aligned here. The magnetoresistance data, however, indicates that the nanomagnet's easy axis is much closer to *perpendicular* to this long axis. There can be no other conclusion than that the structure of this device is not what think it is; somewhow it has been deformed enough to make the easy axis roughly perpendicular to what was intended. Moreover, from the large difference in resistance levels and the low currents needed to switch the device, we can surmise that these nanomagnets are significantly smaller in cross-sectional area than intended. For the device in Fig. 4.9, the resistance difference of $(R_{AP} - R_P) \approx 280\ m\Omega$ is 4 times larger than the calculated estimate for a 130×70 nm pillar, suggesting that the cross-sectional area is 4 times smaller. This is consistent with the observation that the critical currents are 4-5 times smaller than average. Similar analyses on the other devices which display large values of $R_{AP} - R_P$ indicate that they are 2-4 times smaller than originally engineered. The anomalously-small pillar size may have come about due to a glitch in the electron-beam exposure, which made a significantly smaller dot, or an inhomogeneity in the mill mask which resulted in a partially-destroyed pillar.

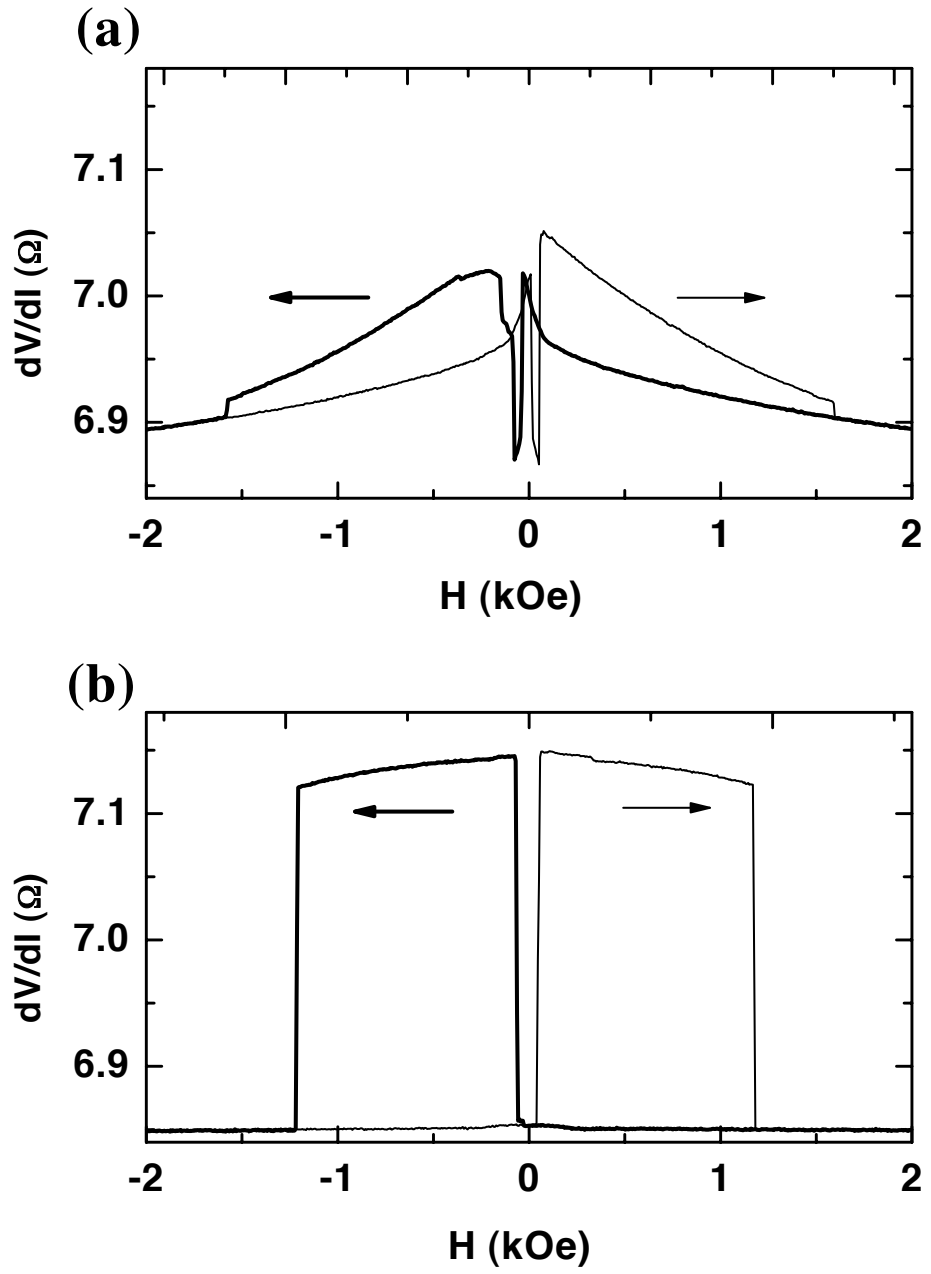


Figure 4.10: Magnetoresistance loops for the device of Figure 4.9 (SC3434), with the field applied (a) along and (b) perpendicular to the engineered long axis of the device.

The associated arrays for these devices show pillars of the approximate engineered size and elongated along the correct axis, so there was little prior evidence that could have predicted such occurrences. I can also estimate the shape of the device depicted in Fig. 4.9 in the following manner: if I assume that the crystal's contribution to the total anisotropy averages out over the polycrystalline nanomagnet, and if we neglect any contribution from surface anisotropy or strain fields, then the anisotropy is entirely determined by its shape via magnetostatic fields, and we can estimate the aspect ratio from the coercive field. Approximating the nanomagnet as an ellipsoid [22], taking the coercive field along the easy axis $H_c \approx 1.5$ kOe, and using the magnetization for Co $4\pi M = 17$ kOe, I find that this nanopillar behaves like a magnet of rough dimensions 30×80 nm, with long axis approximately perpendicular to the engineered hard axis. The similarity of the long axis for this device to the short axes of more typical devices suggests that this pillar may have formed as a narrow slice of a normally-engineered pillar due to an inhomogeneous mill mask.

If we look at the data in more detail, we find that these deformed magnets are not merely small, but extremely well-behaved as well, as their behavior with the direction of applied magnetic field can largely be understood by the very simplest of magnetic models. Figure 4.12a displays a series of magnetoresistance traces over a 90° field range in 4.5° increments, taken from $\phi_{exp} = 81°$ to $\phi_{exp} = -9°$. The field is swept from negative to positive values. Although I have looked at the angular dependence of the field on the magnetoresistance for other devices of similar quality, this is the only device for which I have done such a detailed study. As the field direction is varied, the shape of the curve changes from a near-rectangle to a much more sloped line with smaller height. At the same time, the coercive field of the nanomagnet, corresponding to the jump down in resistance at higher field, changes

non-monotonically, first decreasing, then increasing.

We can capture the shape and behavior of these curves by employing the Stoner-Wohlfarth model of uniform magnetization reversal [23, 24]. In this model, exchange forces are assumed to be strong enough that the magnetization is completely uniform throughout the magnet, so that it can be treated as a single vector $\vec{M}$. The magnet has a uniaxial anisotropy with anisotropy energy K_u, and an external magnetic field $\vec{H}$ is applied. The simplest version of the model assumes that the anisotropy axis, $\vec{H}$, and $\vec{M}$ all lie in the same plane, which can be reasonably applied to my experimental geometry, where the strong demagnetizing field inhibits moment motion out of the plane of the nanomagnet. The total energy can be written as

$$E(H,\theta,\phi) = K_u \sin^2(\theta) - \vec{M}\cdot\vec{H}, \tag{4.9}$$

$$= K_u \sin^2(\theta) - MH\left(\sin(\theta)\sin(\phi) + \cos(\theta)\cos(\phi)\right), \tag{4.10}$$

where θ is the angle between the easy axis and $\vec{M}$, and ϕ is the angle between the easy axis and $\vec{H}$.

It is the competition between the anisotropy and the field energy terms that gives rise to magnetic hysteresis. The case for a particular field angle ($\phi = 45°$) is illustrated in Figure 11. The model assumes the magnetization $\vec{M}$ always resides at a local minimum of the energy. Consider a field sweep from negative to positive H. If $H << -K_u/M$ (Figure 4.10a), then $\vec{M}$ will be approximately aligned with H, in the direction of $\theta = 225°$. As H is reduced to zero (Figure 4.11b), $\vec{M}$ rotates away from 45° until it points along one of the energy minima of the anisotropy term $\theta = 180°$. When H changes sign (Figure 4.11c), $\vec{M}$ will continue to rotate, staying in the local (no longer global) energy minimum. It is only when this minimum disappears, which, for $\phi = 45°$ occurs at a field $H_c = K_u/M$, that the magnet switches to the global energy minimum (Figure 4.11d).

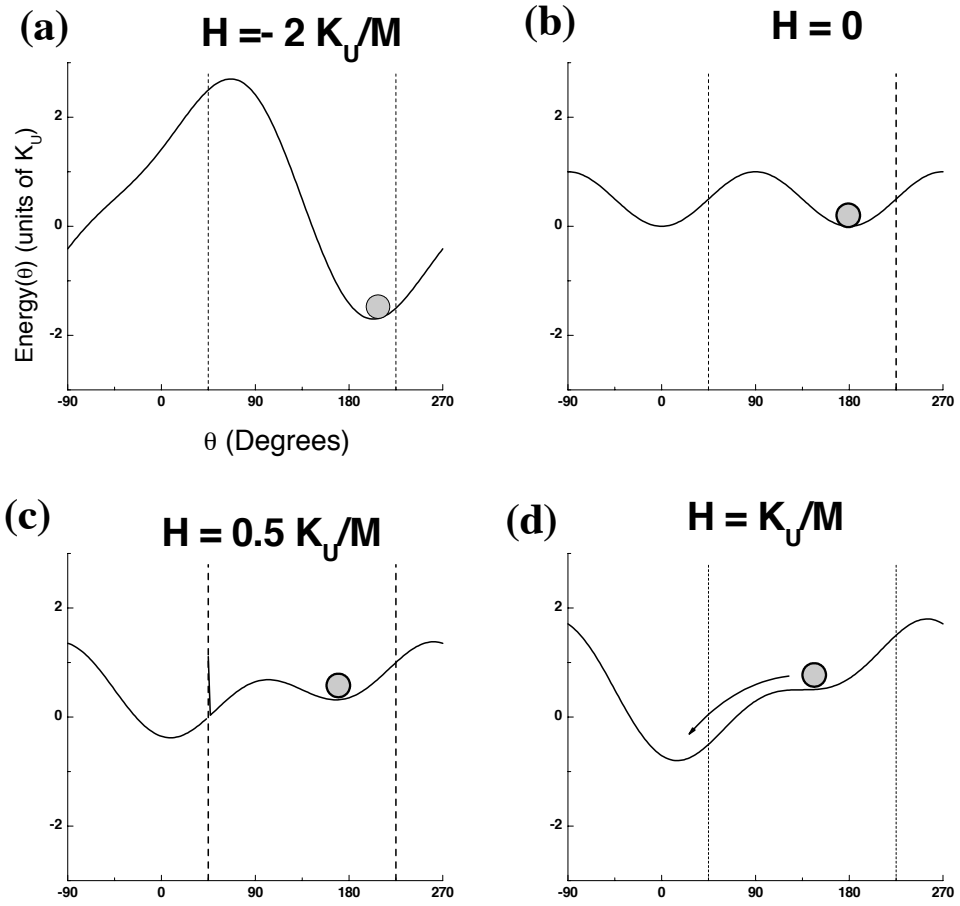


Figure 4.11: Schematic of total energy vs. angle for a magnet in the Stoner-Wohlfarth model, for a sequence of magnetic fields applied at an angle $\phi = 45°$ to the easy axis. The two vertical dashed lines represent the directions of the field for both field signs. (a) At large (negative) fields, the magnet lies near the direction of the field. (b), (c) The magnet rotates as the field is reduced and changes sign, until the local minimum disappears (d). For this field angle, this occurs at the coercive field $H_c = K_u/M$, where K_u is the anisotropy energy and M the magnetic moment.

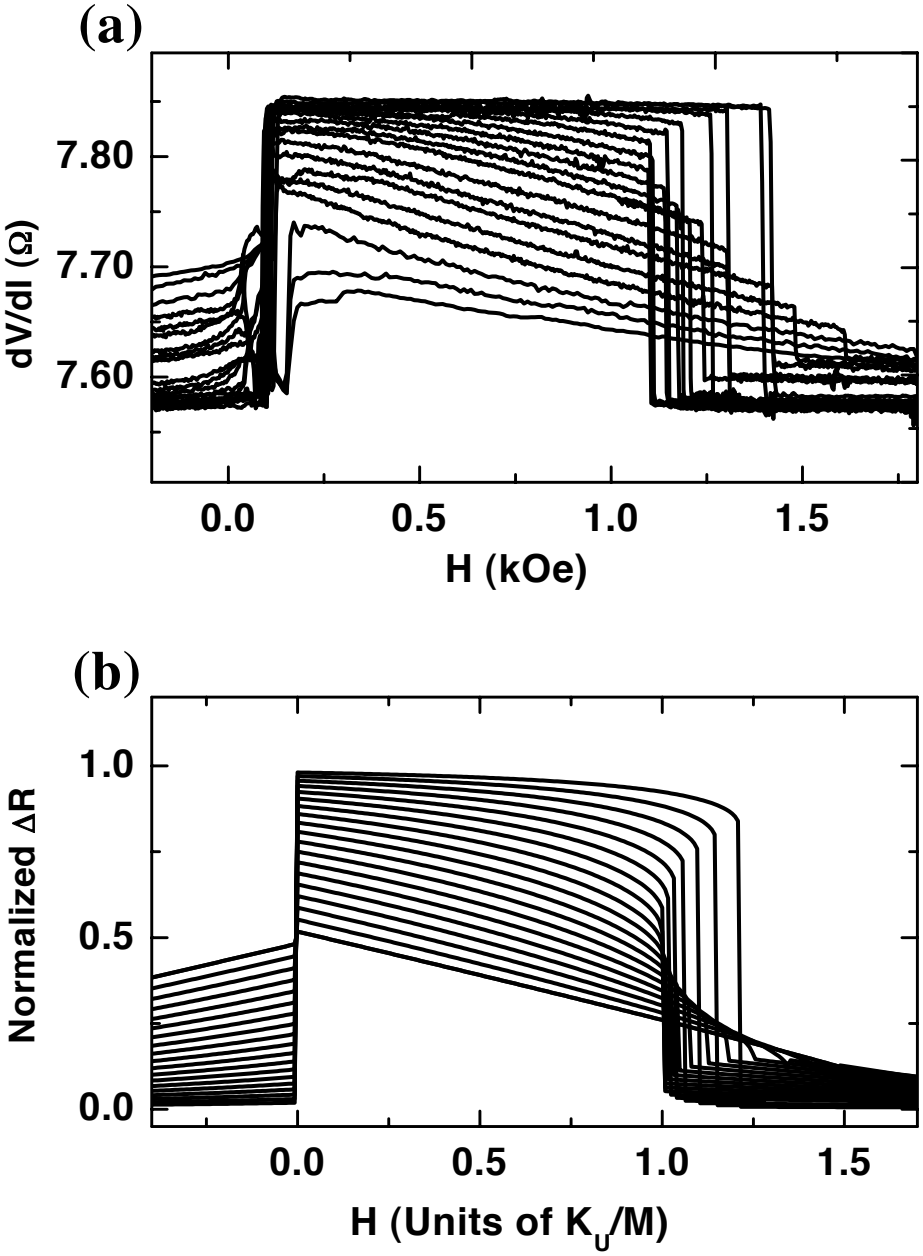


Figure 4.12: (a) Magnetoresistance at various angles of applied magnetic field for the device of Fig. 4.9 (SC3434), with the field swept from negative to positive values, over a 90° angle range. (b) Theoretical magnetoresistance curves, calculated within the Stoner-Wohlfarth model as described in the text. The curves are calculated from $\phi = 16°$ (top curve) to $\phi = 92°$ (bottom curve), where ϕ is the angle between the field and the anisotropy easy axis.

The degree of rotation of $\vec{M}$ and the field at which it switches depends on the angle ϕ. By calculating the minima of Eqn. (4.9) as a function of magnetic field amplitude and direction, we can determine the magnet's direction within this simple model. However, in my experiment I read the magnetization direction indirectly, as a resistance level in the device via the GMR effect. To a good approximation (within a few percent), the GMR effect for two layers is expected to give a resistance of the form

$$R(\vec{M}_1, \vec{M}_2) = A + B\vec{M}_1 \cdot \vec{M}_2, \tag{4.11}$$

where $\vec{M}_1, \vec{M}_2$ are the magnetic moments in the two layers, and A and B are constants [25]. If we assume that the magnetization of the thick extended film follows the direction of the magnetic field, which is reasonably valid as long as H is larger than the coercive field of the film (50 Oe), then we can use Equation (4.10) to translate the Stoner-Wohlfarth model into an expected magnetoresistance curve.

The results of those calculations are shown in Figure 4.12b. The field angles used in the figure range from $\phi = 16°$ to $\phi = 92°$. Note that ϕ and ϕ_{exp} refer to different quantities, as ϕ_{exp} is defined independent of the magnet's easy axis. As in Fig. 4.12a, the field is swept from negative to positive. The model captures the qualitative behavior of the magnet's motion. Near $\phi = 0°$ ($\phi_{exp} \approx 81°$), the field is nearly aligned with the easy axis, so that the energy minimum stays essentially fixed in one direction along the easy axis until the coercive field is reached. As the magnetic field direction deviates from $\phi = 0°$, the equilibrium magnetization direction will not be along the easy axis but at some angle between the easy axis and the field. Since this angle is less than 180° but greater than 0°, it will result in a resistance larger than that for full parallel alignment for negative field, and a resistance smaller than that for full antiparallel alignment for positive field. Also,

this equilibrium angle moves as the magnitude of the field changes, giving a slope to the resistance, until the local minimum disappears and the nanomagnet switches.

The striking agreement of this nanopillar's behavior with the Stoner-Wohlfarth model is noteworthy, because it demonstrates that the dominant mode of reversal is simple uniform rotation of the moment, and does not involve formation of domains or pinning directions, even when the field is pointed along the hard axis. This is not true of most of my nanopillars; for example, the simple magnetoresistance for the device in Fig. 4.7 breaks up into multiple jumps when the field direction is moved significantly off the easy axis. Thus, even though these other pillars appear to exhibit simple current-induced switching behavior when the field is aligned with the easy axis, the actual reversal mechanisms may not be simple, likely involving nonuniform motion of the nanomagnet moment. This limits the extent to which we can quantitatively compare the current-induced reversal properties to the simplest Slonczewski model, in which the magnet acts as a single giant spin. By contrast, the device of Fig. 4.9 may be a more ideal system in which to study spin-transfer, as the magnet conforms to the uniaxial anisotropy model over a wide range of magnetization angles.

Unfortunately, if we press further and try to make more quantitative comparisons between the Stoner-Wohlfarth model and this nanopillar device, we find that our hopes for ideality only take us so far. One specific prediction that comes out of the Stoner-Wohlfarth model is the dependence of the magnitude of the coercive field, H_c, on the field angle ϕ. The coercive field is maximized both when the field is pointed along the hard axis, and (less intuitively) along the easy axis. The dependence can be expressed analytically as

$$\left(H_c(\phi)\cos(\phi)\right)^{2/3} + \left(H_c(\phi)\sin(\phi)\right)^{2/3} = \left(H_c(\phi=0)\right)^{2/3}. \tag{4.12}$$

This is called the switching astroid. Figure 4.13 shows a plot of Eqn. (4.9), along with the measured coercive fields as a function of the experimental field angle ϕ_{exp} for the nanomagnet of Fig. 4.9. The theoretical curve has been plotted using a fit parameter of $H_c(\phi = 0) = 2.24$ kOe, and has been shifted by $-85.5°$ to provide a good fit to the data. The fit is close over the range $\phi_{exp} = 0 - 81°$ and its mirror image $\phi_{exp} = 180 - 261°$, but there is significant deviation over the rest of the data. In particular, the minimum and maximum H_c are not 45 degrees apart, as predicted by the model, and the peak around $\phi_{exp} = 180°$ (the hard axis direction) is not symmetric.

It is disappointing, but not surprising, that perfect agreement with the extremely simple Stoner-Wohlfarth model is not achieved here. In previous studies of lithographically-defined Co ellipses 50-150 nm in size [26], agreement with the Stoner-Wohlfarth model was observed over certain angle ranges for small (80×50 nm) magnets. However, deviations from Stoner-Wohlfarth behavior, similar to the ones observed here, were found that could be explained as a consequence of shape irregularities that modified the effective uniaxial anisotropy field as a function of angle. For magnets closer to the typical sizes of my nanopillars (130×70 nm), and as is found generally for even larger nanomagnets (e.g., [10]), the switching deviates strongly from Stoner-Wohlfarth reversal and usually consists of multiple switching events when the field is near the hard axis. One might thus think that making the magnet even smaller would bring us closer to uniaxial reversal. However, measurements on nanomagnets as small as 3 nm have shown that crystalline and surface anisotropy contributions dominate the total anisotropy as the magnet size is reduced, and in general give significant higher order terms above the uniaxial term [27, 28]. The ideal Stoner-Wohlfarth model system thus appears to be an ill fit to

real nanomagnets; it is fortunate that the model applies to some of my devices as well as it does.

Unfortunately, the event which created these devices seems to have been a double-edged sword, as they are also unusually fragile. The reader will notice that the full range of angles are not represented in Figure 4.13. This is because an irreversible change in the sample occurred part of the way through the angular study. At approximately $\phi = 130°$ on the graph, the resistance of the device suddenly doubled and the magnetoresistance disappeared. In short, the sample was no more. As the deviations from the Stoner-Wohlfarth astroid are most prominent immediately prior to this event, they could have been a precursor of a structural change in the device. However, the resistance of the device in this region did not change significantly before the sudden jump. This device, and the others like it, had a prior history of instability and fragility. As the astute reader will note, the resistance levels shown in Figure 4.9 do not match those in Fig. 4.10. This is because the resistance jumped by approximately 0.7 Ω between the measurements. The qualitative characteristics of the device did not change, but the critical currents increased by about 50%, and the critical fields by about 30%, after the jump. These jumps in general occurred spontaneously, and to the best of my knowledge were not triggered by voltage spikes or other overtly-damaging influences. This fragility is in contrast to typical nanopillar devices made by my colleagues, some of which lasted for years, and are usually only destroyed by very large currents. This may indicate that the devices were experiencing significant stresses——perhaps induced by ion-mill damage, perhaps magnetoelastic——and eventually (and unfortunately) relaxed.

In concluding this chapter, I note that, for the device I have been using as illustration, the final, fatal magnetic field measurements were taken only after a

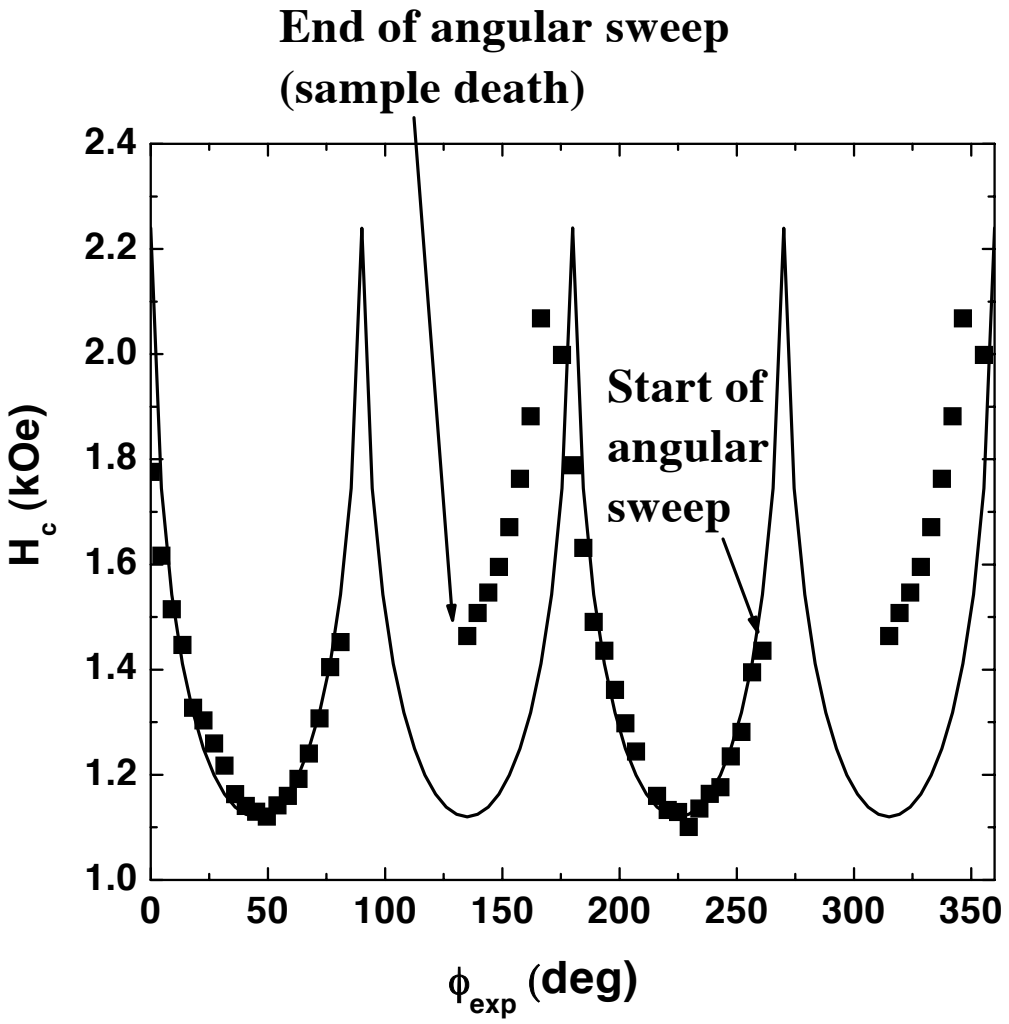


Figure 4.13: Plot of coercive field H_c vs. field angle ϕ_{exp} for the device of Figure. 4.9 (SC3434) (squares), compared with the predictions of Stoner-Wohlfarth theory (line). A complete angular survey was not completed due to device fatality.

large amount of data had been previously accumulated. This device is in fact the centerpiece of the next chapter, which is the study of the role thermal fluctuations play in current-induced reversal. To perform this study, the statistics of current-induced reversal must be measured, and to that end this magnet was successfully reversed, using either a current or a magnetic field, over 100,000 times. As we will see, the accumulated statistics not only give insight into the finite-temperature stochastic nature of the reversal, but they can be used to understand the switching behavior at zero temperature.

Bibliography

[1] W. P. Pratt *et al.*, Phys. Rev. Lett. **66**, 3060 (1991).

[2] M. A. M. Gijs, S. K. J. Lenczowski, and J. B. Giesbers, Phys. Rev. Lett. **70**, 3343 (1993); M. A. M. Gijs *et al.*, App. Phys. Lett. **63**, 111 (1993).

[3] W. Vavra *et al.*, App. Phys. Lett. **66**, 2579 (1995).

[4] J. P. Spallas *et al.*, IEEE Trans. Magn. **33**, 3391 (1997).

[5] K. Bussmann *et al.*, IEEE Trans. Magn. **34**, 924 (1998).

[6] J. A. Katine *et al.*, Phys. Rev. Lett. **84**, 3149 (2000).

[7] J. A. Katine, F. J. Albert, and R. A. Buhrman, App. Phys. Lett. **76**, 354 (2000).

[8] F. J. Albert *et al.*, App. Phys. Lett. **77**, 3809 (2000).

[9] F. Schreiber *et al.*, Solid State Comm. **93**, 965 (1995).

[10] R. P. Cowburn, J. Phys. D **33**, R1 (2000).

[11] J. Bass and W. P. Pratt, J. Magn. Magn. Mater. **200**, 274 (1999).

[12] F. J. Albert, personal communication.

[13] F. J. Albert *et al.*, preprint (2002).

[14] R. N. Louie, Dissertation, Cornell University, Ithaca, NY (1997).

[15] F. Schreiber *et al.*, Solid St. Comm. **93**, 965 (1995).

[16] R. Urban, G. Woltersdorf, and B. Heinrich, Phys. Rev. Lett. **87**, 217204 (2001).

[17] Y Tserkovnyak and A. Brataas, Phys. Rev. Lett. **88**, 117601 (2002).

[18] L. Berger, J. App. Phys **90**, 4632 (2001).

[19] M. V. Tsoi *et al.*, Phys. Rev. Lett. **80**, 4281 (1998); M. Tsoi *et al.*, Nature **406**, 46 (2000).

[20] H. Suhl, J. Phys. Chem. Solids. **1**, 209 (1957); IEEE Trans. Magn. **34**, 1834 (1998).

[21] This percentage only includes devices in which good contact has been made to the top of the pillar due to a well-timed polyimide etch. A certain fraction of the devices will either have very large ($> 1k\Omega$) resistances, indicating that the top of the pillar has not been exposed, or very small ($<< 1\Omega$) resistances, indicating that the polyimide has been overetched and the device is shorting around the pillar.

[22] J. A. Osborn, Phys. Rev. **67**, 351 (1945).

[23] E. C. Stoner and E. P. Wohlfarth, Philos. Trans. R. Soc. London Ser. A. **240**, 599 (1948) [reprinted in IEEE Trans. Magn. **27**, 3475 (1991)].

[24] L. Neel, Ann. Geofis. **5**, 99 (1949).

[25] J. Barnas, O. Baskalary, and A. Fert, Phys. Rev. B **56**, 6079 (1997).

[26] W. Wernsdorfer *et al.*, J. Magn. Magn. Mater. **151** 38, (1995).

[27] E. Bonet *et al.*, Phys. Rev. Lett. **83**, 4188 (1999).

[28] M. Jamet *et al.*, Phys. Rev. Lett. **86**, 4676 (2001).

Chapter 5

The Role of Temperature in Excitations Induced by a Spin-Polarized Current

The data I have presented in this dissertation on the spin-transfer effect have for the most part been interpreted using the Slonczewski torque model. This model uses as its primary mathematical tool the Landau-Lifschitz-Gilbert (LLG) equation, a partial differential equation that connects the dynamics of a spin moment to the torques exerted on it, which come from the couplings of this moment to the external world. The couplings discussed so far are the effective field, which defines the potential energy landscape for the moment; the damping, which describes how the moment gives up energy to its environment; and, of course, spin transfer. As described by the LLG equation, magnetic excitations occur in a nominally stable magnet when spin transfer pumps energy into the system faster than the damping can remove it. However, this simple balance is only strictly valid at zero temperature, a restriction which has been implicit in all of the analysis I have used up to

this point. At finite temperature, the environment will not merely absorb energy from the magnet, but also send energy back into the magnet in a stochastic, fluctuating manner. Understanding the effect of spin-transfer in the presence of such fluctuations is a complicated task, but its importance is undeniable, particularly since the effect is most often studied in nanopillar devices at room temperature. I devote this chapter to an exploration of the role that thermal fluctuations play in magnetic reversal induced by a spin-polarized current. By studying the statistics of reversal using both a current and an external magnetic field, I observe phenomena that highlight the distinct and novel role played by spin-transfer in manipulating small magnetic systems.

5.1 Current-Induced Switching: a Thermally Activated Process?

Figure 5.1a shows a hysteresis loop in differential resistance dV/dI vs. current for the Co/Cu/Co trilayer nanopillar featured at the end of the previous chapter, at an applied field of $H = 50$ Oe, and $T = 295$ K (room temperature). For clarity I will refer to this device as Device 1. I also display the formal device name in parenthesis in the figure caption for identification purposes. Table 5.1, at the end of this chapter, gives the details of the three devices that are primarily discussed in this chapter. The transition is abrupt as predicted by the torque model, which describes an instability to rapid reversal occuring at a specific current threshold. However, if this hysteresis loop is measured again, the reversals do not occur at exactly the same current. Figure 5.1b is a histogram of the switching currents I_c^+ for the parallel-to-antiparallel ($P \rightarrow AP$) transition, for many hundreds of such loops. As can be seen,

the switching occurs over a broad distribution of currents; the antiparallel-to-parallel ($AP \rightarrow P$) transition current I_c^- shows a similar distribution. I primarily use data from this device and a few others as the basis for the arguments in this chapter. However, the statistical distributions I observe here are seen in all of my nanopillar devices when I measure the hysteresis loops many times near room temperature.

The statistical spread in switching currents directly demonstrates that there is a stochastic character to the current-induced magnetic reversal. Several mechanisms could contribute to the randomness of the switching transition; for example, the nanomagnet might be randomly placed into a slightly different micromagnetic state each time it is reversed, thus changing slightly the current threshold for the next reversal. However, the randomness of the current-induced switching is also explicitly time-dependent. This can be seen by performing a different kind of measurement, one in which the device is biased at a constant current and the resistance is monitored. If the bias is near (but below) the bulk of the distribution of switching currents, the device will spontaneously switch after a period of time that varies between measurements. From the statistics of these so-called "waiting times" [1], we can determine the probability $P(t, I)$ of the magnet not switching after a current I has been applied for a time t. Plots of $P(t, I)$ vs. t are shown in Figure 5.2a for the $P \rightarrow AP$ transition of a $(Co_{2.5}/Cu_6/Co_{40})_{nm}$ trilayer of lateral dimensions 50×70 nm (Device 2) at room temperature and $H = 50$ Oe, for several values of current I. The curves can be well-fit to $P(t) = e^{(-t/\tau)}$, where the characteristic switching time τ is the sole fitting parameter. τ decreases rapidly as I is made larger, showing that the random spontaneous switching is highly sensitive to the size of the current. The switching time τ also depends strongly on temperature. Figure 5.2b shows the probability $P(t, I)$ with $I = 0.85$ mA for this same device, both at $T = 295$ K and

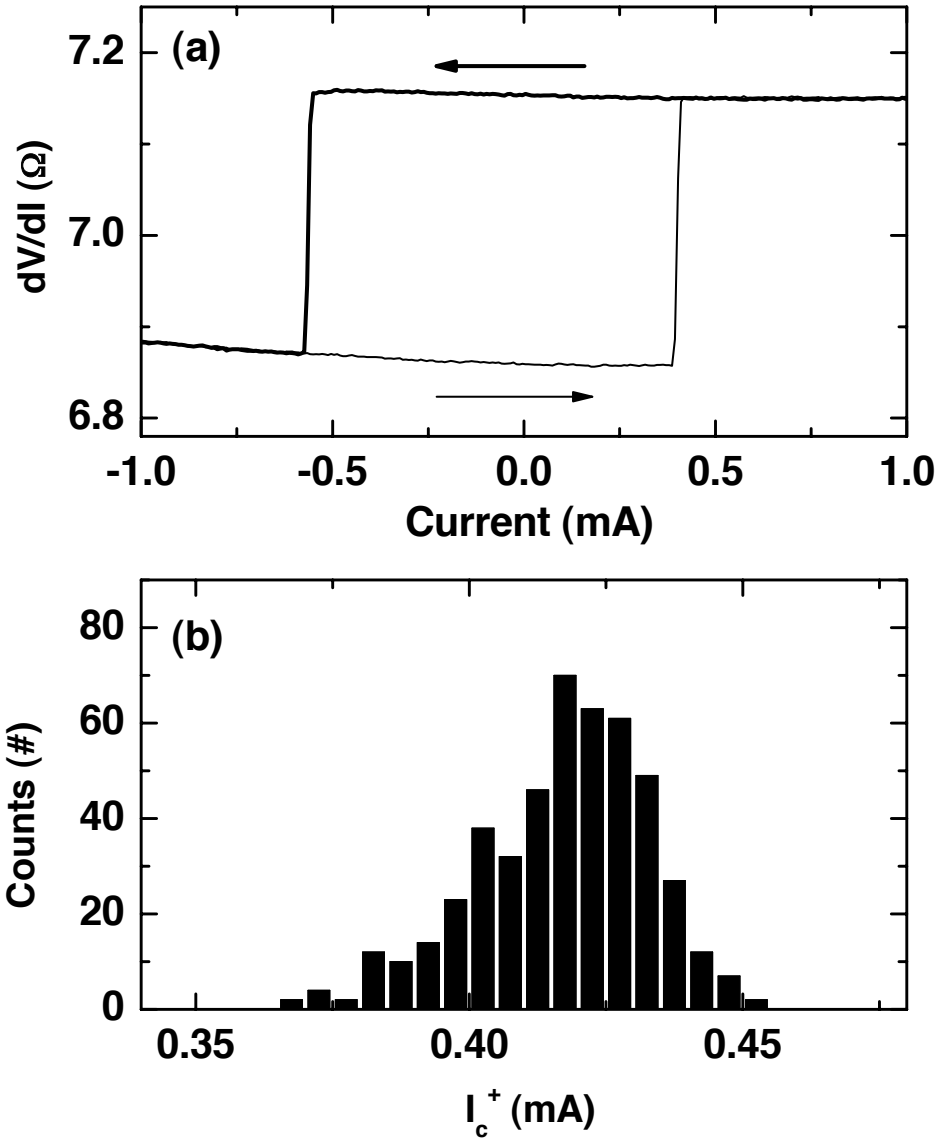


Figure 5.1: (a) Differential resistance dV/dI vs. current for a $(Co_{2.5}/Cu_6/Co_{40})_{nm}$ nanopillar device (Device 1,SC3434), at $T = 295$ K and $H = 50$ Oe, for both current sweep directions (b) Histogram of switching currents for the $P \rightarrow AP$ transition shown in part (a), when the current is swept back and forth many times.

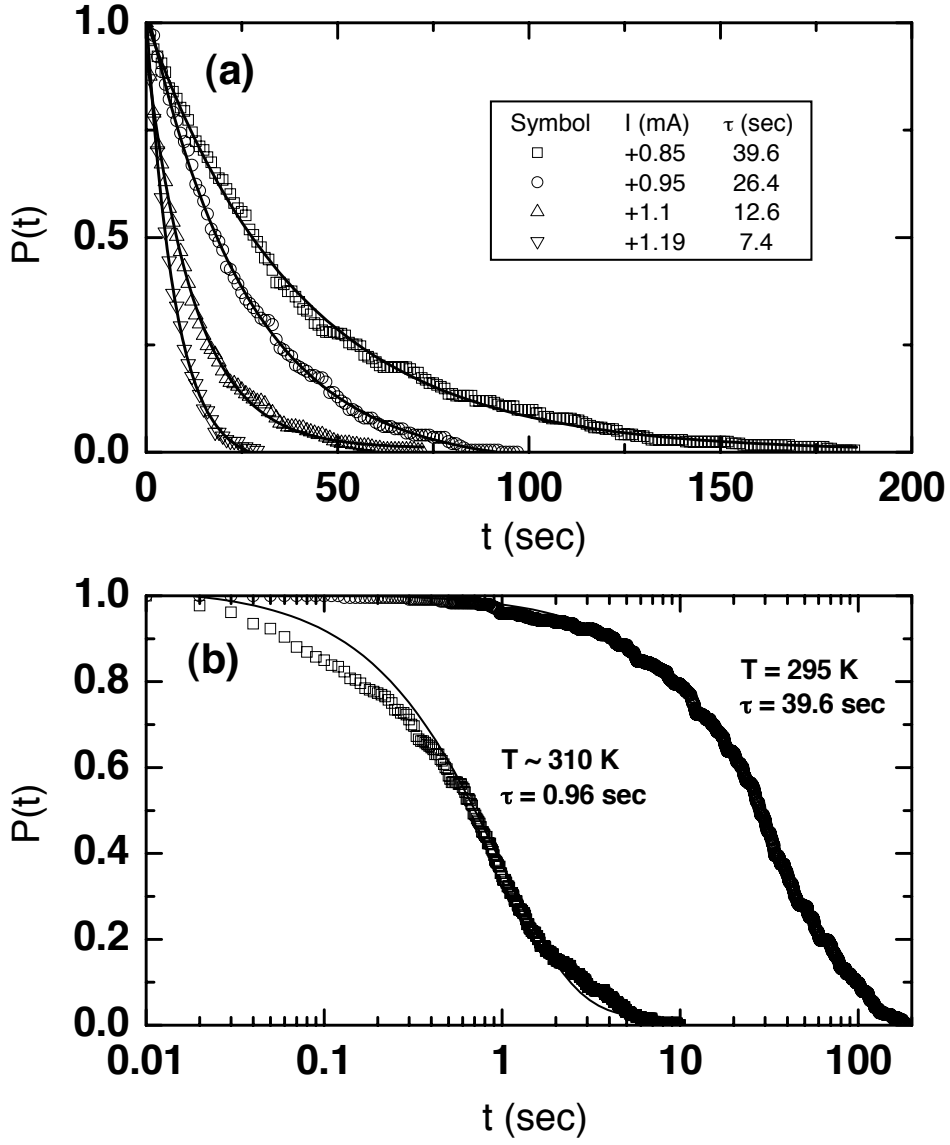


Figure 5.2: Waiting-time measurements. (a) Probability of the magnet not switching out of the P state into the AP state $P(t)$ (symbols) vs. time t, at a given constant current bias I, for a $(Co_{2.5}/Cu_6/Co_{40})_{nm}$ nanopillar device of lateral dimensions 50×70 nm (Device 2, SC3291) at $T = 295$ K and $H = 50$ Oe. The lines are fits of the data to the function $P(t) = e^{-t/\tau}$, with τ a fitting parameter. The box shows the fitted τ for each current I. (b) Measurement of $P(t)$ at a fixed current $I = +0.85$ mA, at room temperature $T = 295$ K and $T \sim 310$ K.

$T \approx 310$ K. The temperature variation in this case was done rather crudely: a heat lamp was used to warm the device, with temperature monitored by a thermometer mounted on the sample holder. As a result, the temperature may have fluctuated slightly over time, worsening the fit of the data to a simple exponential. In any case, we can see that the effect of heating the device is dramatic; increasing T by approximately 5% has decreased τ by nearly a factor of 40. After the heat lamp was switched off and the waiting-time measurement performed again, the timescale τ increased to within 25% of its initial room-temperature value.

5.1.1 Model of Thermal Activation

The data lead us to believe that thermal fluctuations play a central role in triggering the reversal. This should not come as shocking news. The role of random thermal agitations in driving physical systems out of metastable equilibrium is ubiquitous in nature [2], and has been a long-discussed topic in the study of magnetic reversal at finite temperature [7, 8, 17]. The basic concept is depicted in Figure 5.3. A classical system in a particular state x has a global potential energy $U(x)$. $U(x)$ has the functional form of two wells, one much higher in energy than the other, with a barrier of height U_b in between. Say that the system is initially placed in the higher-energy, metastable well. Classical statistics says that at $T > 0$ the system will not sit precisely at the energy minimum, but will fluctuate around that minimum, with probability of being found at any time with energy U of $P_{boltzmann}(U) \sim e^{(-U/k_BT)}$. Thus there is a finite probability in time $P_{switch}(t)$ that the system will be found at the top of the barrier; if so, it can naturally switch into the other well. The switching probability is $P_{switch}(t)$, with $P(t) = 1 - P_{switch}(t)$ the probability that the system will remain in the inital well. Once the system has escaped, we can assume that it

never returns to the metastable state, since the barrier to this transition is much larger. A general expression for the transition probability was first determined by Arrhenius in 1889 [3], and later developed further by Kramers [4], among others. This model states that the probability $P(t)$ of the system can be found from the differential equation

$$\frac{dP}{dt}(t) = -\frac{1}{\tau}P(t), \tag{5.1}$$

$$\tau = \tau_0 e^{(-U_b/k_B T)}. \tag{5.2}$$

The attempt time prefactor τ_0 depends on the microscopic details of the fluctuations within the potential well. Equation (5.3) is an extremely general expression and can be applied to a wide variety of physical and chemical processes, including processes that involve nonconservative forces, where the energy barrier is defined as an effective barrier [5, 6]. The details of the physics come into the determination of the barrier height U_b and τ_0. If U_b, τ_0, and T are constant, Equation (5.2) describes simple exponential decay of the state out of the metastable well.

In the case of magnetic reversal, Néel [7] and Brown [8] explicitly derived the Arrhenius form of reversal probability for a single-domain uniaxial magnet; more recently, the model has been extended to magnets with higher-order anisotropy terms [9]. We can extend the discussion from the previous chapter of a uniaxial magnet by considering how temperature affects field-induced reversal. At zero applied magnetic field, both potential wells are at the same level and the barrier $U_b = K_u$, where K_u is the anisotropy energy. The magnet sits in one of these wells. If a field H is applied roughly in opposition to this magnetization direction, then the energy of the magnet will increase, and the potential barrier will decrease, $U_b \to U_b(H) < U_b$. At $T = 0$ the magnet will only reverse when $U_b \to 0$; at finite temperature, the magnet will reverse before then, on a timescale $\tau = \tau(U_b(H))$ set by the field. When the

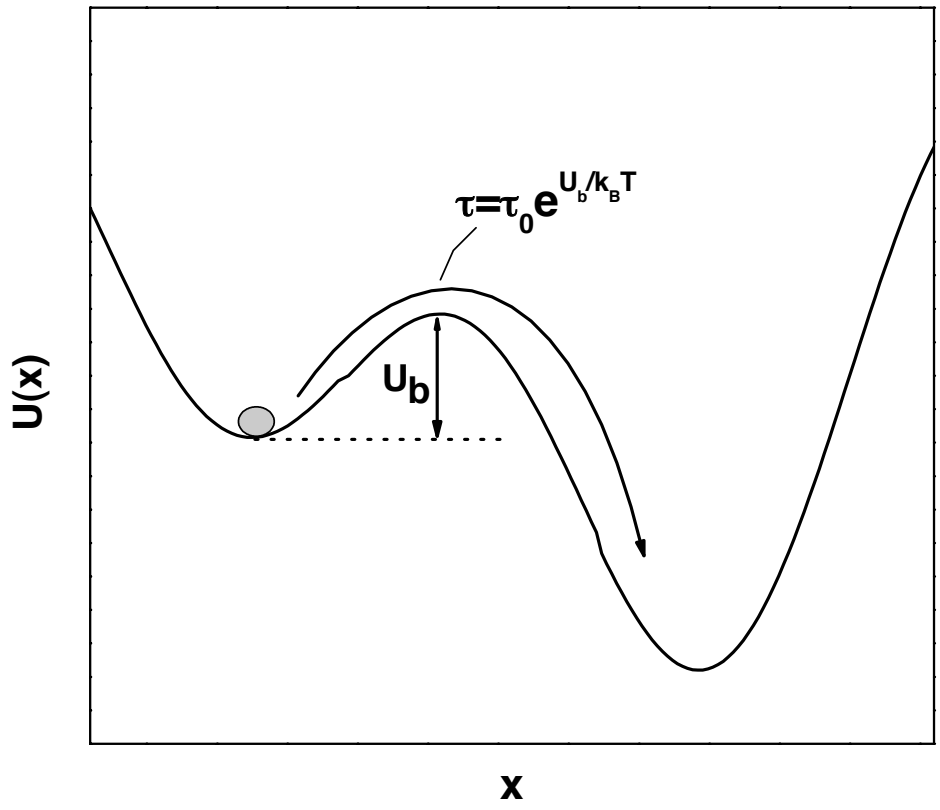


Figure 5.3: Thermally-activated reversal process. A system has a state x with energy $U(x)$. If the system is initially in a metastable energy configuration separated from the global energy minimum by an energy barrier of height U_b, random thermal fluctuations will drive the system over the barrier on an average timescale $\tau \propto e^{U_b/k_BT}$.

barrier height $U_b(H)$ is close to zero, it can be approximated by a power law:

$$U_b(H) = U_0 \left(1 - \frac{H}{H_{c0}}\right)^{a_H}, \tag{5.3}$$

where H_{c0} is the $T = 0$ coercive field, U_0 the barrier height at $H = 0$, and a_H a scaling exponent. The scaling exponent depends on the symmetry properties of the total potential energy. When the field is perfectly aligned with the anisotropy axis, $a_H = 2$; otherwise it is closer to $a_H = 3/2$ [18]. For more realistic forms of the anisotropy, the 3/2 scaling exponent still holds as long as H is close to H_{c0}. The attempt rate τ_0 also depends on the anisotropy and the applied field, as well as the magnetic damping in the system [9]; however, as the dependence of τ on the exponential factor is much stronger than it is on τ_0, most experimental data is interpreted assuming $\tau_0 \approx$ constant. Extensive recent experiments by Wernsdorfer's group [16, 17] have found that the finite-temperature reversal statistics of sufficiently small single-domain magnets in the presence of a magnetic field are well described by this model.

5.1.2 Statistical Switching Distributions: The Kurkijärvi Approach

My waiting time data suggest that this model of thermal activation can also be applied to current-induced reversal. However, the bulk of the data I have taken is not of the waiting times, but of the distributions in switching currents. This is because waiting time measurements are in general more time-consuming and more prone to experimental error. Therefore to better compare the thermal activation model to the statistics I observe, the model needs to be re-expressed in terms of switching distributions. This was first done by Kurkijärvi [20], who considered

thermal activation using a barrier of the form of Eqn. (5.3), but with H a linear function of time, $H = \dot{H}t$, where $\dot{H}$ is the sweep rate. Note that this barrier need not be explicitly derived from a potential energy, so that the Kurkijärvi approach can be applied to situations where nonconservative forces are present [5, 6]. When τ varies in time, Eqn. (5.1) becomes

$$\frac{dP}{dt}(t) = -\frac{1}{\tau(t)}P(t) \tag{5.4}$$

$$\rightarrow P(t) = e^{\int_0^t \frac{1}{\tau(t')}dt'} \tag{5.5}$$

$$= \exp\left(\int_0^t \frac{1}{\tau_0} e^{\left[U_0\left(1-\frac{\dot{H}t'}{H_{c0}}\right)^{a_H}\right]/k_BT} dt'\right). \tag{5.6}$$

The switching distributions can be related to this expression, in that the shape of the histogram of switching fields should be proportional to $dP_{switch}/dH = -dP/dH = -\dot{H}dP/dt$. Theoretical curves of $-dP/dH$ as a function of H from Kurkijärvi's paper [20] are shown in Figure 5.4 for various values of sweep rate $\dot{H}$. These distributions can be characterized by their two primary statistical properties, the mean and the standard deviation. The following two expressions will be central to my subsequent analysis; in anticipation of applying them to both field and current-induced reversal, I write them not in terms of a field H, but a more generic parameter D. The mean $\langle D_c \rangle$ and standard deviation σ_{D_c} are, to leading order, [19]

$$\langle D_c \rangle = D_{c0}\left[1 - \left(\frac{k_BT}{U_0}A(T,\dot{D})\right)^{1/a_D}\right], \tag{5.7}$$

$$\sigma_{D_c} = \frac{|D_{c0}|}{a_D}\left(\frac{k_BT}{U_0}\right)^{1/a_D}\left[A(T,\dot{D})\right]^{(1-a_D)/a_D}, \tag{5.8}$$

$$A(T,\dot{D}) = \ln\left[\frac{1}{\tau_0 a_D}\frac{k_BT}{U_0}\frac{|D_{c0}|}{|\dot{D}|}\left(\frac{|D_{c0}|}{|D_{c0} - \langle D_c \rangle|}\right)^{a_D-1}\right]. \tag{5.9}$$

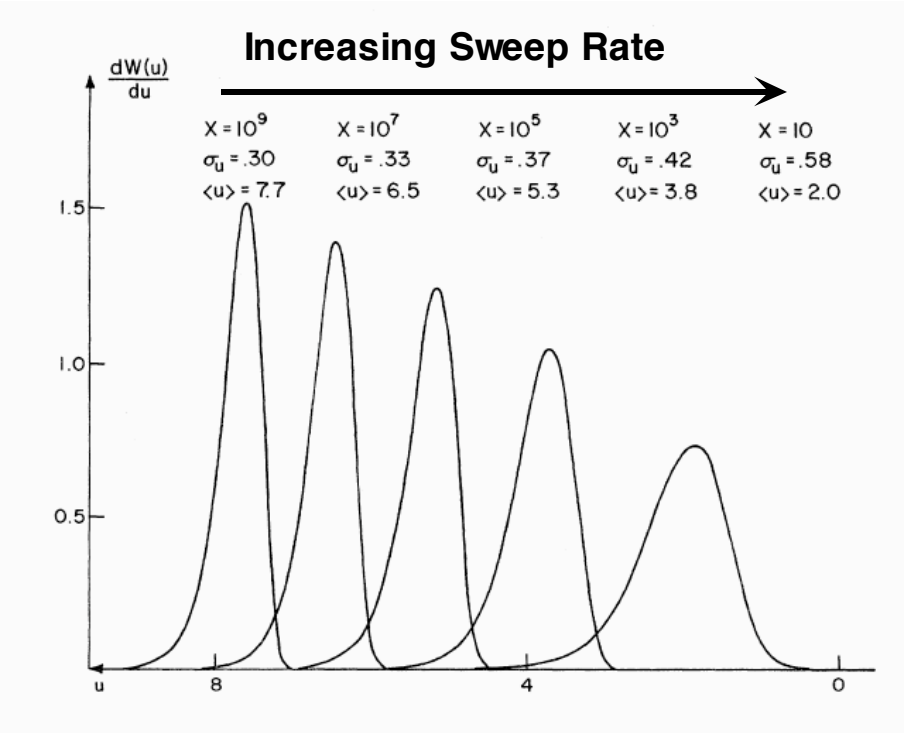


Figure 5.4: Kurkijärvi's switching distribution at various sweep rates, from [20].

5.1.3 Current-Switching Data and Kurkijärvi Equations

Equations (5.7) and (5.8) make specific predictions for how the distributions should vary with the system parameters; this allows me to test whether or not current-induced reversal is well described by the model of thermal activation. For example, as the temperature is decreased, the mean of the switching current distribution should increase towards its $T = 0$ value I_{c0}. Similarly, an increase in the sweep rate $\dot{I}$ should increase the mean; since the sweep rate dependence is contained in the logarithmic term $A(T, \dot{I})$, this dependence should be much weaker than the temperature dependence. Figure 5.5 shows plots of $\langle I_c \rangle$ as a function of T (Fig. 5.5a) and $\dot{I}$ (Fig. 5.5b), for a $(Co_{2.5}/Cu_6/Co_{40})_{nm}$ nanopillar (Device 3) of lateral dimensions 130×60 nm, for the $P \rightarrow AP$ transition. The sweep rate measurements were all taken at $T = 295$ K, while the temperature measurements were taken using $\dot{I} \approx 0.3$ mA/s. As predicted by the Kurkijärvi equations, the mean increases with both decreasing temperature and increasing sweep rate, with the sweep rate dependence much weaker. The error bars give the width $2\sigma_{I_c}$, which has no systematic dependence on sweep rate or temperature (between 150 and 220 K) for this particular transition. However, the error in the standard deviations is intrinsically larger than the error in the means, since individual data points enter into the calculation through their square rather than linearly. Studies by the Wernsdorfer group on field-induced reversal of magnetic nanoparticles [16] has found agreement between the temperature dependence of the width of the switching distributions and the Kurkijärvi model, but only by averaging the results from an ensemble of nearly-identical particles. For a single magnetic device, trends in the widths may not be visible above the noise.

There is an additional effect that the current may have on the magnet which is not covered by the Kurkijärvi equations: the current might heat the sample. The heating

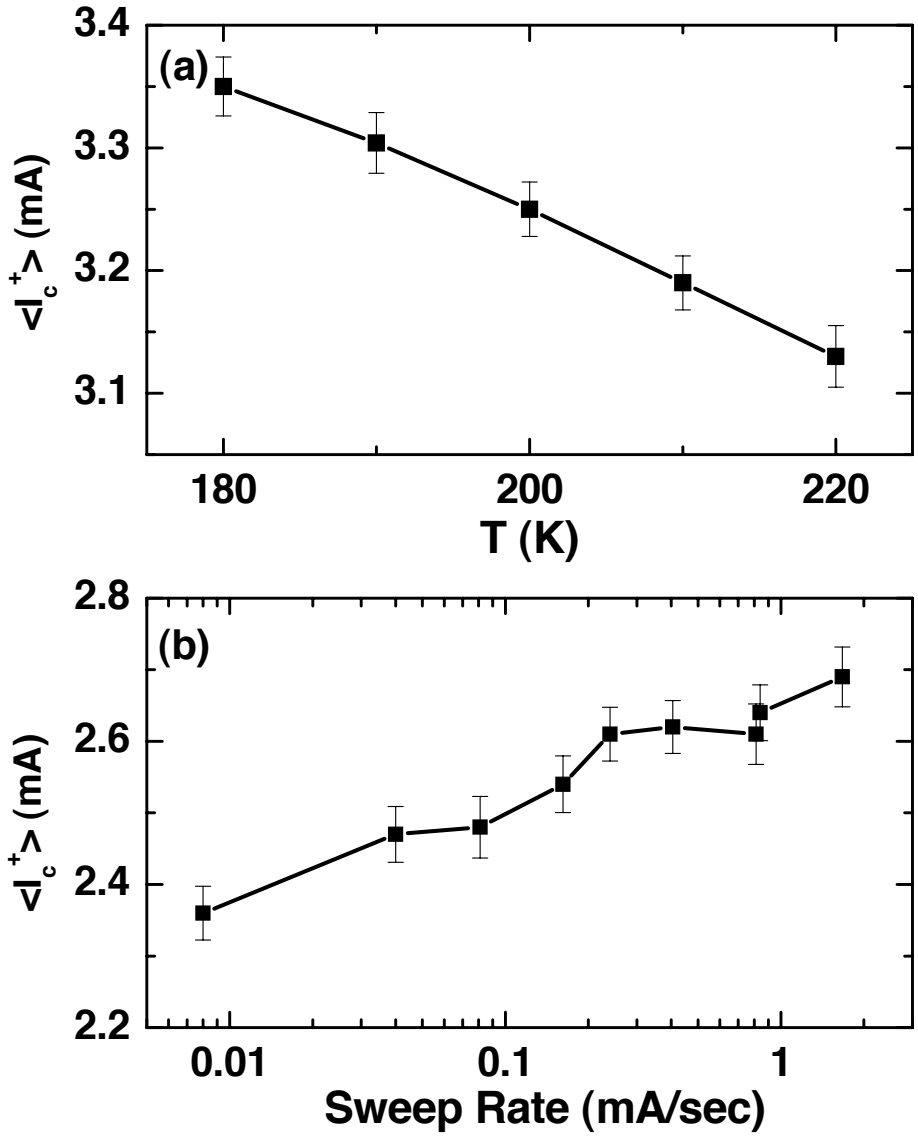


Figure 5.5: Statistical distributions vs. (a) temperature and (b) sweep rate, for a $(Co_{2.5}/Cu_6/Co_{40})_{nm}$ nanopillar device (Device 3, SMILEY2) at zero field, using the $P \rightarrow AP$ transition. The black squares represent the mean switching currents $\langle I_c^+ \rangle$, while the error bars span the width $2\sigma_{I_c}^+$. The sweep rate data was taken at $T = 295$ K, while the temperature data was taken using a sweep rate of $\dot{I} \approx 0.3$ mA/s.

effect of the current can be estimated by comparing the temperature dependence of the low-bias resistance with the increase in DC resistance when a current sufficient to switch the device is applied. For example, for Device 3, the low-bias resistance varied approximately linearly with temperature for temperatures near room temperature, with a fractional slope $\frac{1}{R_{RT}} dR/dT \approx 1.4\%/K$, where $R_{RT} = 1.86\ \Omega$ is the room temperature low-bias resistance of the device. For comparison, the DC resistance of this device increases by at most 5% above its room-temperature low-bias value when a current large enough to switch the nanomagnet (~ 4 mA) is applied. I can thus estimate the heating for this device to be no greater than ~ 3 K above room temperature, which corresponds to a 1% effect on $\langle I_c \rangle$, negligible in my analysis. I should note that heating effects can in general be quite significant in my devices, especially if the required critical currents are large; I have measured other devices that, according to the above analysis, are heated by nearly 30 K when currents sufficient to reverse the magnet are applied. In order to properly study the role that a spin-polarized current plays in thermally-activated reversal, I therefore limit my analysis in this chapter to devices where heating effects do not raise the device temperature more than a few Kelvin.

The switching current distributions, together with the waiting time data, provide compelling evidence that the process of current-induced switching at finite temperature is a thermally-activated process. In particular, the data imply that the presence of the current reduces the barrier to reversal in a manner mathematically similar to the effect of an external magnetic field. The waiting time data support this notion, as they show that, even at fixed finite current, magnetic reversal remains a thermally-activated process over a barrier. Conceptually, this is a very different way of thinking about current-induced reversal than what I have discussed so far in this

dissertation, and it may initially even seem incompatible with the previous results. After all, the $T = 0$ torque model describes the threshold of reversal in terms of the competition between damping and spin-transfer torques; it is not clear how a potential energy barrier can arise from these nonconservative influences. The role played by nonconservative forces in the stochastic dynamics of nonlinear systems is not a new problem in physics; in cases considered previously, it has been shown that these nonconservative effects can be expressed in terms of an effective energy barrier [5, 6]. Later in this chapter I will discuss intuitive approaches towards the problem of the spin-transfer model at finite temperature, and propose ideas of how we may think of the effective barrier. At this point, though, we can take the experimental evidence that current-induced reversal is thermally-activated at face value, independent of any detailed microscopic explanation of the mechanism.

5.1.4 Limitations on Statistical Measurements

Since the fluctuations at issue in this discussion are thermal in nature, it of course would be desirable to measure the distributions over as wide a temperature range as possible. Unfortunately, the range available for these nanopillar devices is in general limited. Although device performance usually does not qualitatively change upon thermal cycling, there can be random irreversible shifts in the mean $\langle I_c \rangle$ as the temperature is varied, corresponding to microstructural changes induced by thermal stresses. These changes can far exceed σ_{I_c} in magnitude, limiting the extent to which quantitative changes with temperature can be monitored. In addition, at temperatures below 100-150 K, the switching events generally consist of multiple jumps in resistance rather than a single jump (Figure 5.6). I offer a possible explanation of these multiple jumps in terms of a potential energy function with multiple minima

(Figure 5.7). As the magnet reverses, it passes through intermediate configurations that are local energy minima; these may arise due to pinning defects at the edge of the nanomagnet [10, 11]. If the escape barriers for these intermediate states are small, then at high temperatures the magnet, once it has overcome the initial large barrier, will rapidly escape from these other states (Fig. 5.7a). Only the longest "bottleneck" time scale, that for escape over the initial barrier, will be measured. At lower temperatures, higher currents will be required to thermally-activate the magnet over the barrier; this modifies the rest of the potential landscape, and may create a situation where the magnet gets "stuck" in an intermediate state until additional current allows it to escape and complete the reversal (Figure 5.7b). I only present a simple depiction of the local minima in Figure 5.7; a more generalized approach to the potential energy landscape has been developed and applied to the reversal statistics of submicron thin-film magnets [11]. In these magnets (roughly 300×800 nm), reversal occurs by domain nucleation at the ends of the magnet and eventual propagation across the film. Since the resistance measurement for my devices gives only the average magnetization direction of the nanomagnet, I cannot say whether these intermediate configurations involve domain walls or instead consist of the moment pointing uniformly in a direction between parallel and antiparallel. Due to exchange, full domain walls are energetically unfavorable for nanomagnets in my size range (< 100 nm) [14]; however, reversal involving partial texturing of the magnetization has been seen for similarly-sized nanomagnets in micromagnetic simulations, the character of which depends sensitively on the edge shape [15].

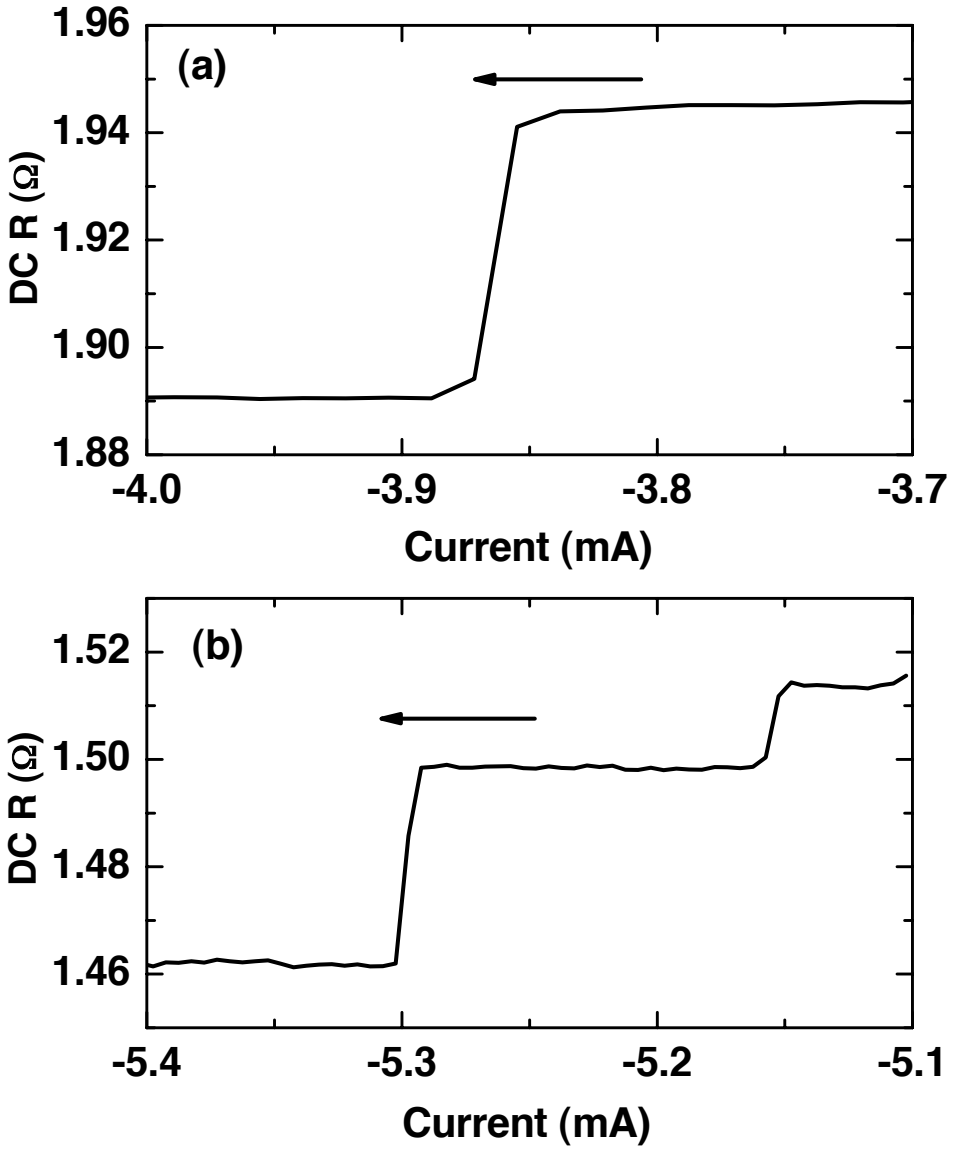


Figure 5.6: DC resistance R vs. current showing the $AP \rightarrow P$ transition of Device 3 (SMILEY2), at (a) $T = 295$ K and (b) $T = 160$ K. Note the different current and resistance levels.

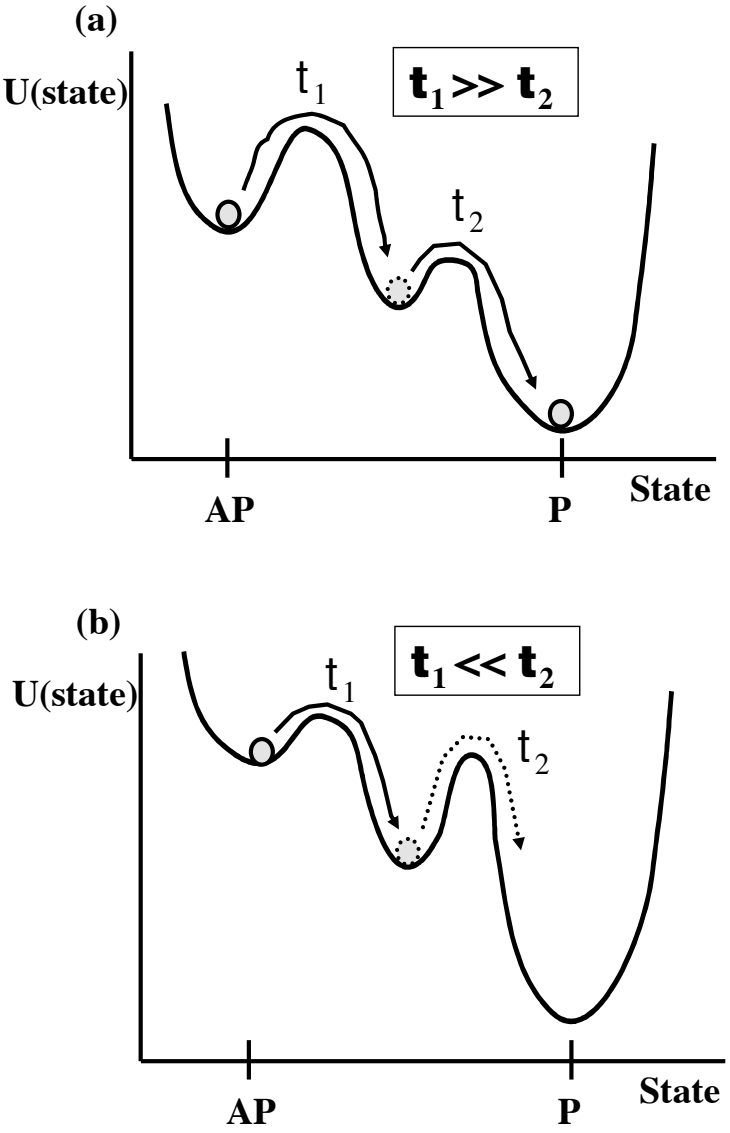


Figure 5.7: Generalized energy U as a function of state in configuration space. Due to disorder and nonuniform magnetization, the potential energy function does not merely consist of two wells, but rather has local minima for states between parallel and antiparallel alignment. Here the magnet is assumed to start in the AP state. (a) At high enough temperature, once the magnet overcomes the largest barrier via thermal fluctuations, it will rapidly pass through the intermediate states. If the temperature is lower (b), higher currents will be required for reversal, which may make the intermediate states sit in deeper wells. Once the magnet switches into these states, it does not have enough thermal energy to escape.

5.1.5 Statistics and Barrier Height: Nonuniform Reversal?

The Kurkijärvi equations can shed further light on the nature of the reversal process. There are four unknown parameters in the Kurkijärvi equations that can in principle be extracted from statistical measurements of the switching currents: I_{c0}, a_I, τ_0, and U_0. While an accurate determination of all four parameters requires a larger set of data than I have accumulated for any one device, dependencies among some of the parameters can be established using the data in Fig. 5.5. Rewriting Eqn. (5.7) in a slightly simpler format, we have

$$\epsilon^{a_I} = \frac{k_B T}{U_0} \ln\left(\frac{k_B T}{U_0} \frac{I_{c0}}{\epsilon^{a_I - 1} a_I \dot{I} \tau_0}\right), \tag{5.10}$$

where $\epsilon = |I_{c0} - \langle I_c \rangle| \,/\, |I_{c0}|$. Taking the logarithm of both sides, we have

$$a_I \ln\epsilon = \ln\left(\frac{k_B T}{U_0}\right) + ..., \tag{5.11}$$

where the term after the ellipsis on the RHS varies weakly with either T or $\langle I_c \rangle$, as long as neither T nor ϵ is close to zero. For a given I_{c0}, a plot of $\ln\epsilon$ vs. $\ln T$ should give a straight line with slope $1/a_I$. In this way a relationship can be established between two of the unknowns, the scaling exponent a_I and the $T = 0$ critical current I_{c0}. The sweep rate data can be used to extend this relationship to the barrier height U_0. Rearranging the terms in Eqn. 5.10, I can write

$$\epsilon^{a_I} = -\frac{k_B T}{U_0} \ln\dot{I} + ... \tag{5.12}$$

where, again, the term beyond the ellipsis on the RHS can be treated as constant as long as ϵ is not close to zero. The slope of ϵ^{a_I} vs. $\ln\dot{I}$ connects the barrier height U_0 to a_I and I_{c0}. The data thus provide two equations to determine three unknowns; by picking reasonable values for one of the unknowns, a range for the

other unknowns can be determined. Using Device 3 as an example, I find that, for a range of $a_I \sim 1-3$, $I_{c0} \sim 4.5-6.5$ mA, and $U_0 \sim 1.8-2.4$ eV.

Of course, the value of the barrier height has little meaning unless it can be understood in context. Wernsdorfer [16] has utilized the notion of an "activation volume" V_{act} when analyzing the statistics of field-induced reversal in small magnetic particles. This volume is defined as

$$V_{act} = \frac{U_0}{mH_c}, \tag{5.13}$$

where m is the magnetization density and H_c the coercive field. The denominator is an experimental measure of the anisotropy energy of the magnet, which would be the total energy barrier for field-induced reversal if the reversal followed Stoner-Wohlfarth single-domain rotation. If V is less than the total magnet volume, then only part of the magnet is involved in the initial threshold to reversal, and the reversal mechanism likely involves multidomain behavior. It is far from clear what should be used as an equivalent energy scale to compare to the U_0 derived from the current-induced reversal statistics, since the threshold current does not depend only on the in-plane anisotropy but also the demagnetizing field, as discussed in Chapter 4. If we compare the energy to simply the in-plane anisotropy, then, using the magnetization of Co, $m = 1400$ emu/cm^3, and a measured coercive field $H_c \approx 800$ Oe, the activation volume of Device 3 is 2500-3400 nm^3. This is $\sim 10-20\%$ of the actual nanomagnet volume, $130 \times 60 \times 2.5$ nm $= 19,500$ nm^3 (See Table 5.1 at the end of this chapter). If the demagnetizing field is in fact an important contribution to the energy barrier, then the fractional volume contributing to reversal is even smaller. Thus the switching statistics seem to support the notion of a nonuniform character to the current-induced reversal process.

Should this be surprising? As I mentioned earlier, exchange makes it energeti-

cally unfavorable for a full domain wall to form in a magnets smaller than $\sim 100-200$ nm [10]. However, partially nonuniform magnetic configurations are still allowed, due to the importance of edge structure at these small size scales [15]. In addition, disorder in my devices may further complicate the reversal process and encourage nonuniform magnetization states. However, nonuniform motion of the magnet may be intrinsic to the nature of spin transfer, and occur even in simple defect-free extended magnets. Micromagnetic simulations of rectangular nanomagnets in the presence of spin-transfer torques [21] have shown that the reversal does not follow simple uniform precession. The out of plane motion of the moments generates large fields within the film that create even more complicated motions, and nonlinear spin-waves can be generated during reversal to an extent that the dynamics become quasichaotic. Such instability occurs despite the high energy cost for exciting nonuniform spin-waves in the confined structure. This raises the compelling possibility that field-induced reversal, in which the magnet can stay essentially in the plane at all times, might be far simpler in general for these nanomagnets, and as such have a far larger activation volume. Unfortunately I do not have detailed sweep-rate data for magnetic field-induced reversal, so I cannot explore this notion further here.

5.2 Current-Induced Reversal Models and Thermal Fluctuations

As I remarked above, a microscopic understanding of thermal fluctuations within the spin-transfer torque model is not required to validate my evidence that reversal is a thermally-activated process. Of course, such an understanding is of intrinsic physical

interest and is necessary for a complete description of spin transfer; I address the issue later on. For the moment we may proceed simply from the conclusion that current-induced reversal is consistent with the Kurkijärvi equations, Eqns. (5.7) and (5.8). We thus do not need to consider the full microscopics of the torque model, but only how the torque model affects the parameters that enter into the Kurkijärvi approach. This more universal way of looking at current-induced reversal is quite useful, because it allows me to consider alternative explanations of current-induced reversal, and determine their predictions for the switching statistics.

The model of Slonczewski and Berger [22, 23] were initially developed prior to observation of the effect. As interest has grown over the excitations in the past several years, alternative theoretical approaches have been developed that take a fundamentally different point of view. Heide [25, 26] has proposed an interaction between the current and the magnetic moments in a magnetic trilayer system that does not look like a torque, but instead like an effective magnetic field; I will henceforth call this the field model [24]. The origin of the proposed effective field, the nonequilibrium exchange interaction (NEXI), comes from a coupling between the moments and the spin accumulation of the current (derived from a diffusive model of transport) that resides in the bulk of the magnet. Since the spin accumulation is set by the magnetization direction of the other magnetic layer, Heide describes this interaction in terms of a coupling energy E_{NEXI} [25]

$$E_{NEXI} \propto I\vec{M}_{F1}\cdot\vec{M}_{F2} \tag{5.14}$$

$$= -\vec{M}_{F2}\cdot\vec{H}_{NEXI},\ \vec{H}_{NEXI}\propto I\vec{M}_{F1}, \tag{5.15}$$

where I is the current and $\vec{M}_{F1}, \vec{M}_{F2}$ correspond in my geometry to the magnetic moments of the thick and thin magnetic layers, respectively. The instability to reversal comes when this energy overcomes the anisotropy energy, exactly in analogy

to magnetic field-induced reversal. When I is positive, the NEXI field tries to align the moments of the two layers antiparallel with one another, while parallel alignment is favored for $I < 0$. The critical current density associated with these transitions is in the range of $10^6 - 10^7$ A/cm^2. Heide also includes in this theory [26] a torque similar to Slonczewski's, which he uses to explain the high-field spin-wave data; however, he says the effect of this torque is small compared with the NEXI field at low magnetic field.

The reader may be wondering why I have not discussed the NEXI model in detail until now, and have instead focused exclusively on the torque model when analyzing my data. The field model relies on applying a diffusion equation to perpendicular transport through magnetic multilayers. Since the mean free paths between the layers are typically larger than the layer thicknesses, the emphasis on diffusive transport may be questionable when considering my spin-transfer devices; see Chapters 1 and 3 of this dissertation. Also, the NEXI model assumes an extended buildup of transverse spin accumulation inside the magnets, which appears to be unphysical; our scattering formalism (Chapter 3) can demonstrate this rather explicitly. However, as I am in a better position to make judgements from an experimental rather than a theoretical point of view, it is better to critique the model based on predictions it makes with respect to specific measurements. In terms of the symmetry and low-field behavior of the switching, the predictions of the torque and field models are quite similar. Moreover, with particular reference to this chapter, the switching statistics as described by the field model are naturally identical to magnetic field-induced switching statistics, so that current-induced switching follows the model of thermal activation. Yet the idea that the magnetic moment reverses via relaxation in an effective field is very different from that of a spin-torque driving the magnet out of

one stable equilibrium and into another; they are decidedly *not* equivalent pictures. It is thus important to find measurements for which the predictions of the two models can be clearly distinguished. As it turns out, the finite-temperature statistics of reversal can provide just such a measurement. As the reader may easily guess, the torque model will explain the results of this measurement much better than the field model, justifying my focus on the torque model throughout this dissertation. Recent work by Frank Albert on the scaling dependence of the critical current on the thickness of the nanomagnet layer [32] has demonstrated that current-induced reversal is an interface, rather than a bulk effect, which is further evidence that the NEXI model does not properly explain the physics of reversal.

5.2.1 Reversal Using Both a Current and a Field

A distinction between the torque and field models can be found by considering magnetic reversal in the presence of both a current *and* a magnetic field. Suppose a field H below the coercive field is applied in the plane of nanopillar device. In the field model, this can be thought of two parallel fields acting on the magnet, H and H_{NEXI}, to give a total field H_{tot}

$$H_{tot} = H + H_{NEXI} = H + cI, \tag{5.16}$$

where c is a proportionality constant relating the current to the NEXI field. The effects of H and H_{NEXI} are completely symmetric; reversal is determined only by their sum H_{tot}. The statistics of reversal are also determined by H_{tot}; thus if we measure the distribution of switching currents at a particular magnetic field H, then the field model predicts that the mean $\langle I_c(H)\rangle$

$$\langle I_c(H)\rangle = \left\langle \frac{1}{c}\left(H_{tot} - H\right)\right\rangle = \frac{1}{c}\left(\langle H_{tot}\rangle - H\right) = \langle I_c(H=0)\rangle - \frac{1}{c}H, \tag{5.17}$$

and the standard deviation $\sigma_{I_c}(H)$

$$\sigma_{I_c}(H) = \sigma_{I_c}(H = 0). \tag{5.18}$$

In other words, the presence of an external magnetic field should simply produce a linear shift in the means of the distributions, without changing their widths. It is less immediately obvious what to expect when a magnetic field is applied within the torque model. However, we have seen that in the pancake geometry of the nanopillars, the thresholds for current-induced and field-induced reversal are set by different field scales; field-induced reversal depends only on the in-plane anisotropy, while current-induced reversal also includes a contribution from the out-of-plane demagnetizing field. The effects of current and field cannot merely be added together, but must be considered in the full context of the LLG equation. I explore this issue further in Section 5.3; for the moment, we can simply anticipate that a dependence of the statistical properties of current-induced switching on magnetic field might be less trivial than what is predicted in the field model.

Figure 5.8 displays the mean switching currents $\langle I_c^+ \rangle$ and $\langle I_c^- \rangle$ for Device 1, as a function of magnetic field H applied within 5° of the easy axis of the nanomagnet. At low field, both currents move towards more positive I with increasing field. As H is increased further, $\langle I_c^+ \rangle$ begins to increase nonlinearly until it crosses the $I = 0$ axis and merges with $\langle I_c^+ \rangle$, at about $H = 1.4$ kOe. This field is very close to the room-temperature coercive field $H_c \approx 1.4$ kOe. determined by a magnetoresistance measurement taken near zero current. The data are qualitatively similar to what has been seen before in elongated nanopillar devices [27], where $\langle I_c^- \rangle$ moves rapidly towards $\langle I_c^+ \rangle$ as $H \to H_c$. If we look at the standard deviations of the two transitions, $\sigma_{I_c}^+$ and $\sigma_{I_c}^-$, even more dramatic variations with magnetic field are seen. Figure 5.9 shows $\sigma_{I_c}^+$ and $\sigma_{I_c}^-$ vs. field for these same distributions. At low fields, $\sigma_{I_c}^+$

and $\sigma_{I_c}^-$ are roughly equal to one another. However, as $H \to H_c$, $\sigma_{I_c}^-$ increases by more than threefold, while $\sigma_{I_c}^-$ decreases slightly.

These data show behaviors qualitatively different from the predictions of the effective field model. We can understand the variations to a certain extent quantitatively by employing a very simple model. We begin with the Kurkijärvi expression for the standard deviation,

$$\sigma_{I_c}^{\pm} = \frac{|I_{c0}^{\pm}|}{a_I} \left(\frac{k_B T}{U_0} \right)^{1/a_I} A^{(1-a_I)/a_I}, \tag{5.19}$$

where A (Equation (5.9)) has a logarithmic dependence on the system parameters. An applied magnetic field H has two effects on this equation. First, a magnetic field changes the potential energy landscape, so that the barrier to reversal U_0 changes. In other words, the barrier to the $AP \to P$ transition is reduced (since the P configuration is aligned with the thick layer and, consequently, H), to a value

$$U_0 \to U^-(H) = U_0 \left(1 - \frac{H}{H_{c0}} \right)^{a_H}, \tag{5.20}$$

while the barrier to the $P \to AP$ transition increases to

$$U_0 \to U^+(H) = U_0 \left(1 + \frac{H}{H_{c0}} \right)^{a_H}. \tag{5.21}$$

I also make the assumption that H_{c0} depends weakly, if at all, on the current I, so that $U^{\pm}(H)$ can be inserted directly into Eqn. (5.19). This assumption is later justified from a more complete analysis of the stability boundaries of the nanomagnet.

The other quantity that changes when a field is applied is the zero-temperature critical current, $I_{c0}^{\pm}$. This is where information about the competing models can be introduced. Both the torque and the field models predict a linear dependence of the critical current on magnetic field, so we can write this dependence as

$$I_{c0}^{\pm}(H) = I_{c0}^{\pm}(H=0) \left(1 - \frac{H}{H_s^{\pm}} \right), \tag{5.22}$$

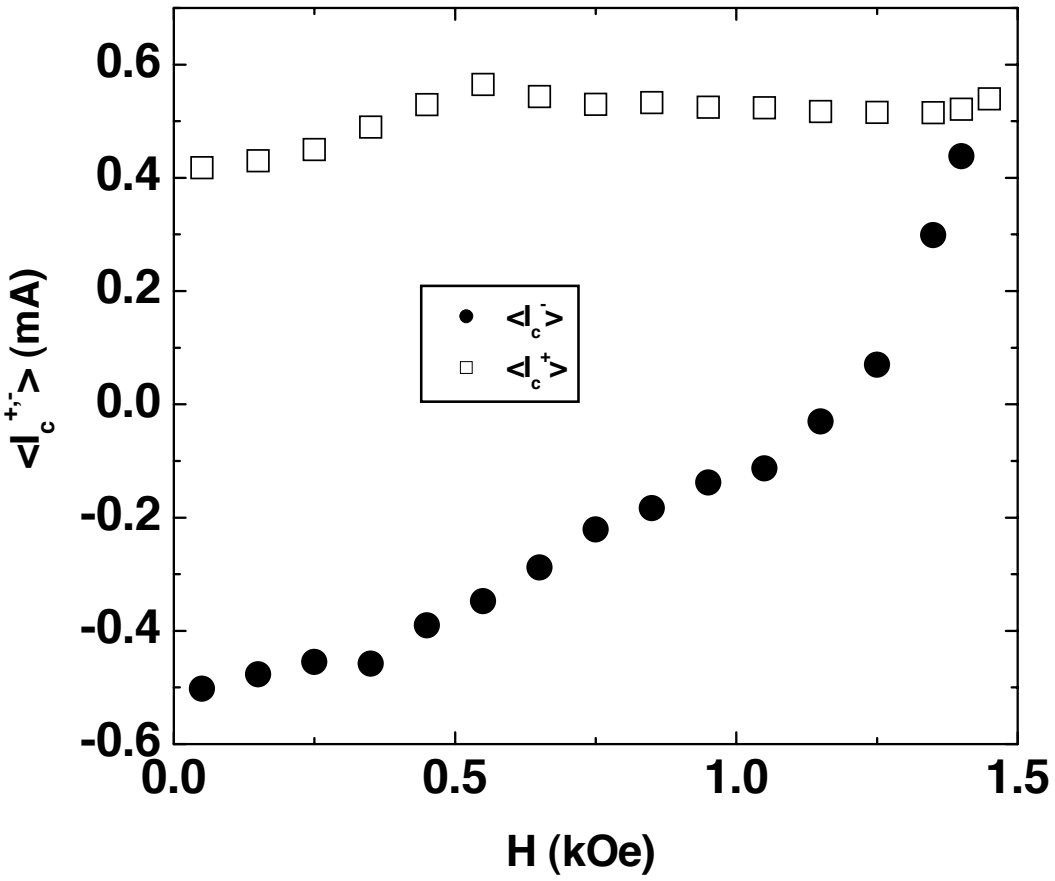


Figure 5.8: Mean switching currents $\langle I_c^{\pm} \rangle$ vs. field H for Device 1 (SC3434), at $T = 295$ K. The field is applied along the easy axis of the nanomagnet.

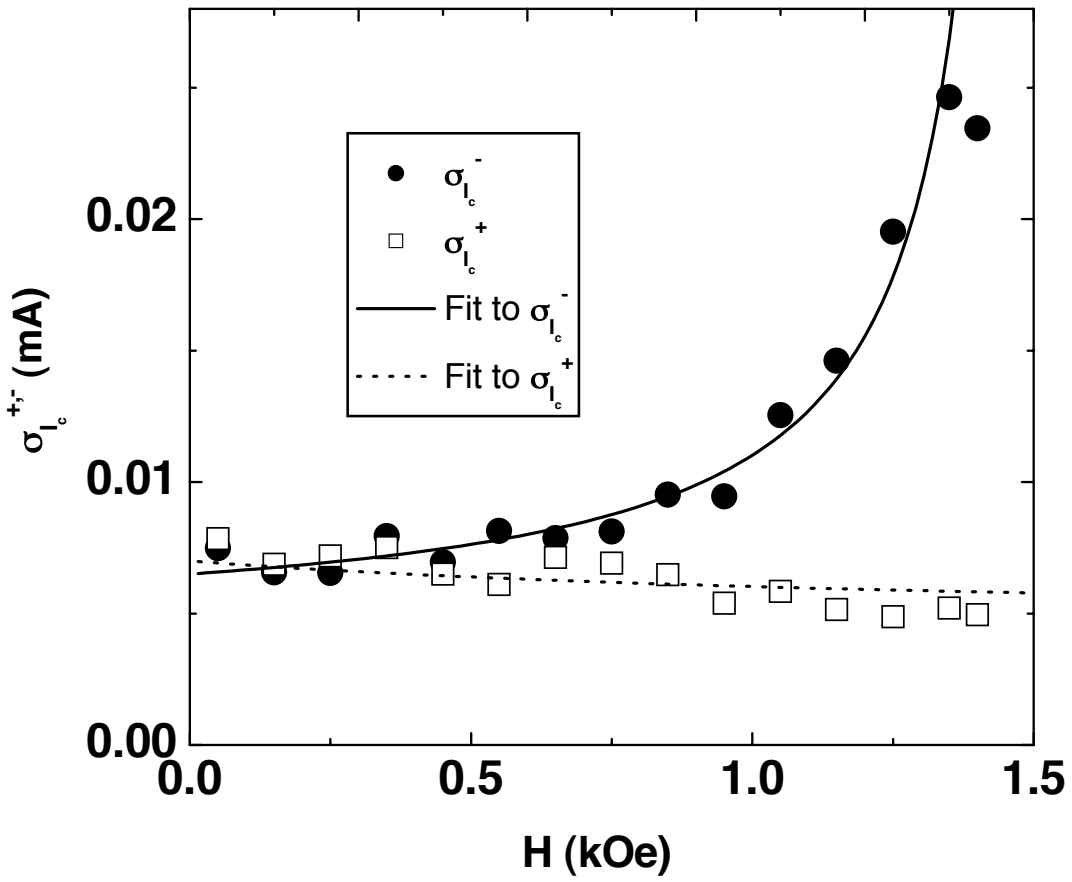


Figure 5.9: Standard deviations $\sigma_{I_c}^{\pm}$ of the switching current distributions (symbols) vs. field H for Device 1 (SC3434), at $T = 295$ K. The lines are fits of the data to Eqn. (5.23) using the parameters detailed in the text.

where $H_s^{\pm}$ is a model-dependent intercept. Using these expressions for $U_0^{\pm}(H)$ and $I_{c0}^{\pm}(H)$, Equation (5.19) becomes

$$\sigma_{I_c}^{\pm}(H) = F\left(\frac{k_B T}{U_0}\right)^{1/a_I} A^{(1-a_I)/a_I} \approx F\sigma_{I_c}^{\pm}(H=0), \tag{5.23}$$

$$F = \frac{(1 - H/H_s^{\pm})}{(1 \pm H/H_{c0})^{a_H/a_I}}. \tag{5.24}$$

Although there is an additional factor of F within the logarithm term A, I can approximate A as independent of H as long as H is not too close to H_{c0}. In the field model, $a_H = a_I$ and $H_s^{\pm} = \mp H_{c0}$, since current and field add symmetrically. Thus $F = 1$ in the effective field model and the widths are independent of H, as expected. In the torque model, H_s can be found from Equation (4.7) of Chapter 4. In that chapter a single-domain model of magnetization reversal was applied to my devices, and it was found that the torque must overcome a threshold set by a combination of the in-plane anisotropy and the out-of-plane demagnetizing field. The resulting predicted intercept is $|H_s^{\pm}| = H_{c0} + 2\pi M$, where $2\pi M \approx 850$ Oe for Co. Since $H_s > H_{c0}$ in the torque model, $\sigma_{I_c}^{\pm}(H)$ is *not* independent of H; $\sigma_{I_c}^{+}$ decreases slightly as $H \to H_{c0}$, while $\sigma_{I_c}^{-}$ in fact diverges. This is in excellent agreement with the behavior shown in the data.

Equation (5.24) can be fitted quantitatively to the data. However, there are quite a few fitting parameters: H_s, H_{c0}, a_I, and $\sigma_{I_c}^{\pm}(H=0)$, which itself depends on various other parameters. Thus we should not take the results of any fit as unique. However, assuming reasonable values for the parameters leads to some insights. The lines in Figure 5.9 show a fit to the standard deviation data using the values $H_{c0} =$ 1.5 kOe, $H_s = 2.3$ kOe, $a_I = a_H = 1.5$, and the scale factors $\sigma_{I_c}^{+}(H=0) = 0.007$ mA and $\sigma_{I_c}^{-}(H=0) = 0.0065$ mA. The fit is quite good, although similar fits can be found using different values of a_I, H_{c0} and H_s. However, in all combinations of

values that I have found to provide good fits, $H_s < H_{c0} + 2\pi M \approx 10$ kOe. This is further evidence that current-induced reversal in my nanopillar devices is not the uniform rotation of a single domain magnet. If only a small part of the nanomagnet has to precess out of plane to initiate the reversal, then the effective demagnetizing field will be smaller, and $I_{c0}^{\pm}$ will be reduced.

Note that we have been able to use the finite-temperature statistics to gain insight into $I_{c0}^{\pm}(H)$, which is a zero-temperature property of the magnet. This is a particularly useful consequence of the Kurkijärvi formulas, as it is not possible to directly measure the low-temperature switching thresholds due to the complications discussed previously. The distributions in switching currents, however, sheds light on only part of the story. To get a more complete picture of nanomagnet reversal in the presence of both a current and field, the measurement above must be repeated, but with the roles of current and field reversed.

5.2.2 Zero-Temperature Stability Boundaries

Figure 5.10a is a plot of differential resistance dV/dI vs. field H for both sweep directions is shown for Device 1, near zero current bias and at $T = 295$ K. H is applied in the same direction as in the previous measurements. The curve consists of two jumps; the one at low field corresponds to the thick layer reversing, and the one at high field to the reversal of the nanomagnet. By measuring the switching statistics of this second reversal as a function of constant current bias, I can take the complementary measurements to the ones shown in Figs. 5.8 and 5.9. However, since the coercive field of the thick layer is smaller than that of the nanomagnet, the spin moment of the thick layer will always be parallel to the field when the nanomagnet switches. Thus only the $AP \rightarrow P$ transitions in field can be measured for most

currents. Figure 5.10b shows the mean switching field $\langle H_c \rangle$ and standard deviation σ_{H_c} as a function of current bias I. As the current goes from negative to positive values, $\langle H_c \rangle$ increases nonlinearly, while σ_{H_c} actually changes nonmonotonically, increasing to a peak at about $I = -0.2$ mA, then decreasing at more positive currents. Similar peaks have been seen in other devices, always occuring at negative current bias.

The data in Fig. 5.10b certainly have more structure than the complementary measurement of Figs. 5.8 and 5.9, and a quantitative expression analogous to Eqn. (5.24) to describe these data is not as simple to obtain. However, we can get a more direct idea of what these statistics tell us about the low-temperature properties of the magnet by performing a simple addition trick. We first note that the mean of the distribution (Eqn. (5.7)) is the zero temperature parameter D_{c0} minus a temperature-dependent quantity. By inspection, we can see that the distribution's standard deviation (Eqn. (5.8)) is approximately proportional to this temperature-dependent quantity. Thus if we combine the equations like so:

$$\left\langle I_c^{\pm} \right\rangle \pm a_I A \sigma_{I_c}^{\pm} = I_{c0}^{\pm}, \tag{5.25}$$

and

$$\langle H_c \rangle + a_H A \sigma_{H_c} = H_{c0}, \tag{5.26}$$

then we can effectively extrapolate to the zero temperature quantities $I_{c0}^{\pm}$ and H_{c0}, or, more generally, $I_{c0}(H)$ and $H_{c0}(I)$. Again, this is done without reference to any specific microscopic model of reversal, and is entirely a property of the more general model of thermal activation.

The difficulty in this extrapolation comes in the determination of the proportionality constant. A more thorough analysis of the statistical distributions with sweep rate and temperature can give more insight into the microscopic parameters

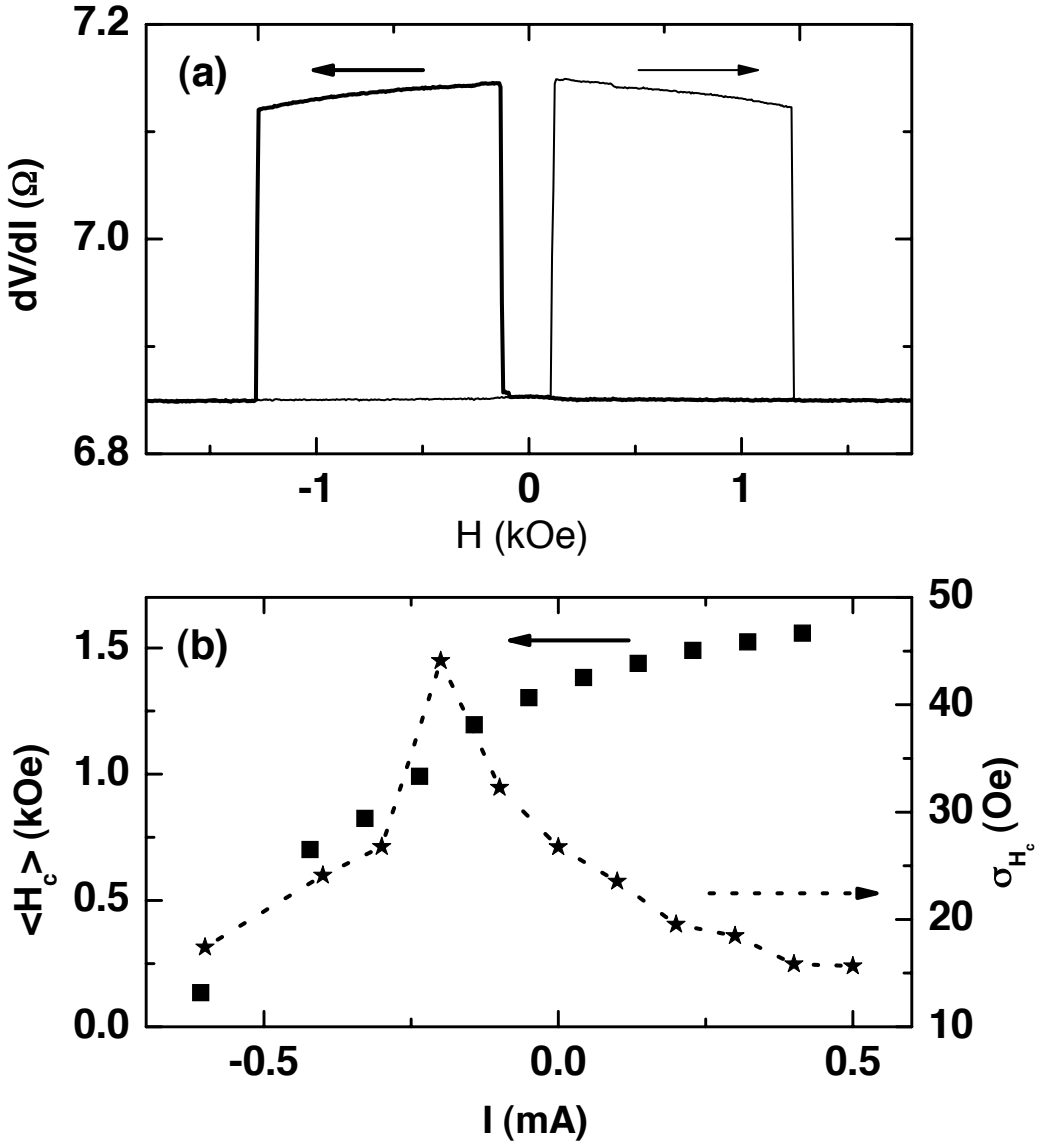


Figure 5.10: (a) Magnetoresistance loop of differential resistance dV/dI vs. field (H) for the nanopillar used in the previous figure (SC3434), near zero current bias and $T = 295$ K. The field is applied along the easy axis of the nanomagnet. (b) Mean $\langle H_c \rangle$ and standard deviation σ_{H_c} of the switching field distributions vs. current I for the same device and at the same temperature.

that go into A, but for reasons I mentioned previously, my range of available data is limited. Nevertheless, reasonable estimates can be made for the parameters to give us a rough idea of what the stability boundaries of this nanomagnet look like. Once again I assume $a_I = a_H = 1.5$. Using this and the variation of the current switching distributions with sweep rate for Device 1 (not shown), I estimate a barrier height of $U_0 \sim 1.5 - 2$ eV, for a range of $I_{c0}^{\pm} \sim 0.5 - 0.8$ mA. For both the current sweeps and the field sweeps, I take $\left|\dot{D}\right| / |D_{c0}| \sim 0.05 - 0.1$ s^{-1}. The attempt time τ_0 is a rather tricky quantity, as its value varies by several orders of magnitude in the literature; as a consequence, this quantity, despite being within the logarithm term, has the largest effect on the proportionality constant. I have found the most consistent results in the extrapolation occur when I choose $\tau_0 \sim 100$ nsec. This is far larger than the $\tau_0 \sim 1$ nsec seen in Co nanoparticles that obey the Stoner-Wohlfarth model of reversal [16]. However, my choice for τ_0 is similar to the attempt times found for larger nanomagnets [11], where the reversal mechanism is domain nucleation and propagation, and τ_0 is set not by a single coherent spin-flip time, but by the diffusion of the domain wall between pinning sites.

Some of the quantities mentioned above depend on one another, so my choices were adjusted in a self-consistent manner. Excepting τ_0 and a_D, the estimated proportionality constant is not very sensitive to any possible errors in this analysis. Choosing a maximally self-consistent set of parameters, I find a proportionality constant $a_I ln A \sim 10$. The results of an extrapolation using this constant are shown in Figure 5.11. Here the statistical data of both current I and field H sweeps for Device 1 are plotted on the same two-dimensional I-H plane. The means are shown as the squares and circles, while the horizontal and vertical lines extending from these points have lengths of the standard deviations multiplied by the proportionality

constant. The resulting extrapolated stability boundaries are represented by the crosses, with lines through them as guides for the eye. Within these boundaries, at low H and I, the magnet is bistable, with both P and AP configurations allowed. At large H or large negative I, only the P configuration is allowed, while at reasonably low H and large positive I, only the AP state is stable. At large H and large positive I, dynamical excitations begin to be excited in the magnet; I do not show this region for clarity. As can clearly be seen, the boundary to go from the bistable to the P-stable region consists of two lines with different slopes, that join to form a knee at negative current. These lines are none other than $I_{c0}^{-}(H)$ and $H_{c0}(I)$, and the fact that they have different slopes is a graphic illustration that the current-induced reversal process is qualitatively different from the field-induced reversal process. The field and current statistics each make an independent estimate of $I_{c0}^{-}(H)$; their estimates roughly overlap. Meanwhile, $H_{c0}(I)$, established soley by the field-switching statistics, apparently varies weakly with I, in agreement with the earlier assumption of $H_{c0} \approx$ constant in my analysis of the current switching statistics alone. In the region close to the knee, the magnet is maximally subject to thermally-activated reversal through the combined effects of the current and the field, and therefore σ_{H_c} has a peak here, and falls off on either side.

The idea that the current and field have qualitatively different effects on the stability of the magnet is clearly far more in the spirit of the torque model than of the effective field model. However, it is still important to qualitatively compare these experimentally-determined stability boundaries to the $T = 0$ predictions of each model. In Figure 5.12 the boundaries from both models are plotted in the I-H plane. The field model stability boundaries are simple straight lines, since current and field add symmetrically. The torque model boundaries were calculated

by numerically integrating the LLG equation with Slonczewski torque term for a single domain magnet with easy-plane and uniaxial in-plane anisotropies. The out-of-plane demagnetizing field was chosen in this case to be roughly 11 times the in-plane anisotropy field. Similar calculations have been performed previously, in various device geometries [12, 13]. As the reversal mechanism in my devices may not be single-domain, we should not expect this model to be quantitatively accurate. Even so, the torque model does appear to capture the general shape of the measured stability boundaries. There are indeed two lines with different slopes separating the bistable region from the P-stable region which join at a knee at negative current. The prediction for $I_{c0}^{+}(H)$ is not as close to the measured dependence, which may be due to non-single-domain behavior in the nanomagnet.

5.2.3 Field and Current in Opposition: Telegraph-Noise

The current-field stability diagram is thus a more interesting beast than that predicted by an effective field model. Although I have so far focused on the $H > 0, I < 0$ quadrant of the plane, even more intriguing physics occurs when $H > 0$ and $I > 0$, because in this quadrant current and field have opposite effects on the magnet. At $T = 0$, after H and I become large enough to eliminate both stable static directions, the tension between their effects results in a dynamical excitation. At finite temperature, fluctuations will make each of these directions unstable before the dynamical region is reached, so we might expect to see thermally-induced dynamics at lower H and I. Figure 5.13 shows what is observed when Device 1 is biased at $H = 1.4$ kOe and $I = +0.5$ mA, and the DC resistance is monitored in time. The resistance does not stay constant, but jumps randomly between two levels. These levels are the same as those seen for P and AP alignment at zero current bias. The escape times

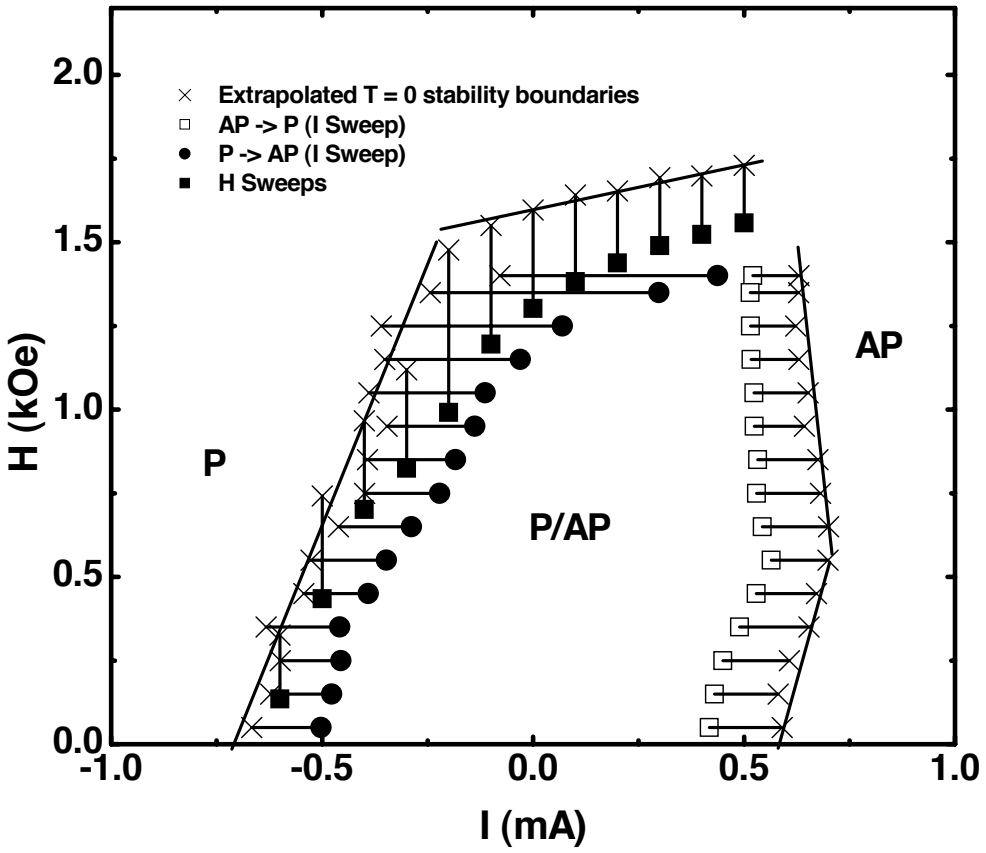


Figure 5.11: Extrapolation of room-temperature switching data to the $T = 0$ stability boundaries of Device 1 (SC3434). The mean switching currents $\langle I_c^{\pm} \rangle$ (black circles and white squares) and mean switching field $\langle H_c \rangle$ (black squares) from the previous figures are plotted on the $I-H$ plane. The horizontal and vertical lines are the corresponding standard deviations $\sigma_{I_c}^{\pm}, \sigma_{H_c}$ multiplied by a proportionality constant 10, derived in the text. The resulting zero-temperature stability boundaries are the X's, separating the P-stable, AP stable, and the P/AP (bistable) states for the magnet. The lines are guides for the eye.

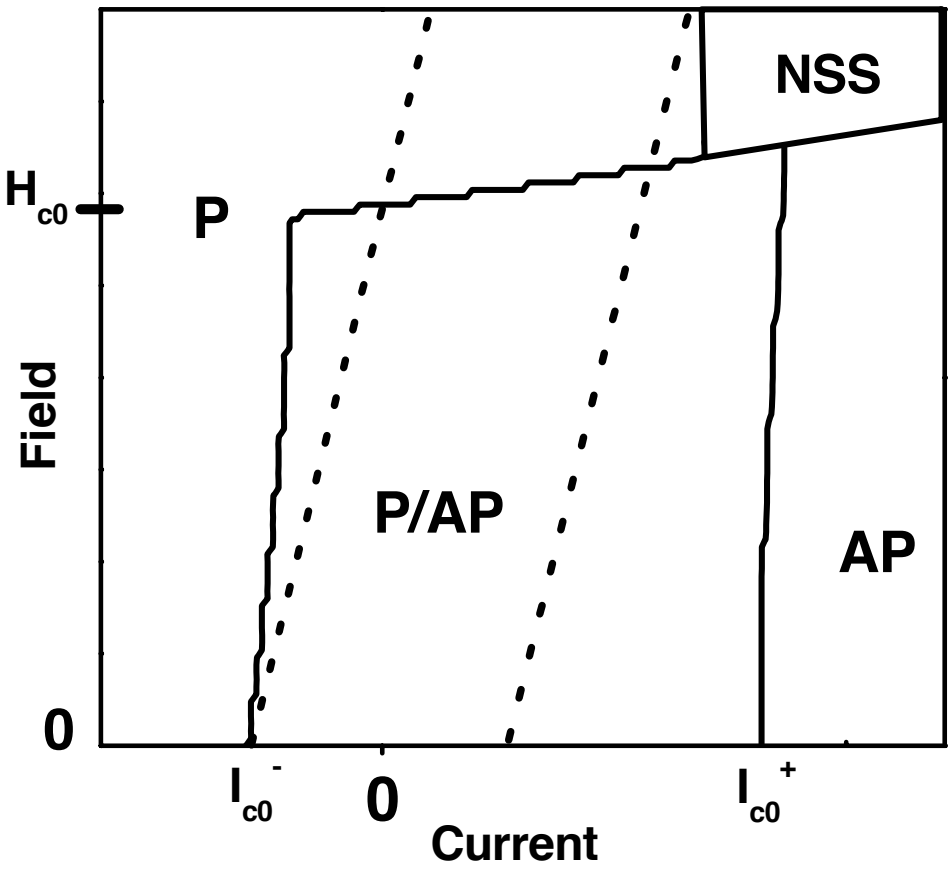


Figure 5.12: Predictions of the torque (solid lines) and the effective field (dotted lines) models for the stability diagram for a single-domain nanomagnet. The regimes of P-,AP-, and P/AP-stability are shown. The torque model also predicts a region of nonstatic (dynamical) states (NSS).

for each state follow very well exponential statistics of the form $P(t) = e^{t/\tau}$, where $\tau = \tau_{P\to AP}, \tau_{AP\to P}$ are defined for each resistance level. This is telegraph-noise switching, induced by the combination of current and field making both moment directions unstable to thermal activation [28]. Telegraph noise switching has been induced previously in magnetic nanoparticles using a magnetic field alone, by applying the field along the hard axis; the switching occurs between two angles on either side of, but close to, the hard axis [16]. This kind of switching can also be seen in my device at low current bias by applying a field perpendicular to the field applied in this measurement. However, the telegraph switching induced by a perpendicular field is clearly different from the switching induced by a parallel field plus current, as the transitions in the latter case are not between two closely-separated angles, but between full P and full AP alignment. This is a rather remarkable dynamical state, as it is about as large a fluctuation of the spin-moment degree of freedom of the nanomagnet as is physically possible.

Equally remarkable, but not surprising in the context of the torque model, is that the mean escape times $\tau_{P\to AP}, \tau_{AP\to P}$ can be controllably and *independently* tuned by varying H and I (Figure 5.14). If H is held fixed and I is increased (Fig. 5.14a), $\tau_{P\to AP}$ decreases roughly exponentially, as expected for a thermal activation timescale that obeys Eqn. (5.2). Over this same region, $\tau_{AP\to P}$ increases, but much more slowly. A similar asymmetry can be seen by holding I fixed and increasing H (Fig. 5.14b); $\tau_{AP\to P}$ decreases exponentially, while $\tau_{P\to AP}$ increases at a much slower rate. The data demonstrate that that H, and not I, is largely determining the thermal stability of the AP state, while I alone is determining the same for the P state. This is another indication of the independent means by which field and current affect magnetic reversal. The timescales in the two plots do not match

up precisely because, between the measurements, a small discrete change in $\tau_{P\rightarrow AP}$ and $\tau_{AP\rightarrow P}$ occured. This may be due to a micromagnetic shift in the device that modified the $T = 0$ switching currents and field, thus changing the timescales. Such shifts are occasionally seen in my devices. They do not usually coincide with a change in the device resistance, indicating that a large change in the physical microstructure has not accompanied the micromagnetic shift.

The Limits of Telegraph Noise: Incoherence to Coherence

It seems that, micromagnetic shifts notwithstanding, if H and I are both slowly increased within the telegraph-noise region, the timescales $\tau_{P\rightarrow AP}$ and $\tau_{AP\rightarrow P}$ should shorten until they reach the attempt time τ_0, at the point that the barrier height $U \rightarrow 0$. I can certainly drive the nanomagnet to a region where the fluctuation is faster than I can resolve using my standard measurement-setup, which has an acquisition time on the order of ~ 100 μsec. To look at fluctuations on shorter timescales, it is easier to work in the frequency rather than in the time domain; this implies use of a spectrum analyzer to determine the characteristic timescales of the telegraph noise [30]. I have not performed extensive spectral analysis of my devices to determine the limits to which the fluctuation timescales can be shortened. It is interesting to ponder this limit, though, as the crossover to where both barriers are reduced to zero is just where dynamical states emerge in the $T = 0$ stability diagram of the torque model. Dynamic instabilities are qualitatively different from hysteretic reversal, as they require a constant influx of spin-torque to sustain themselves. Thermal fluctuations will certainly populate a distribution of incoherent spin-waves (magnons); this essentially how thermal fluctuations alter the magnetization direction in the first place. The predicted spin-torque-induced exci-

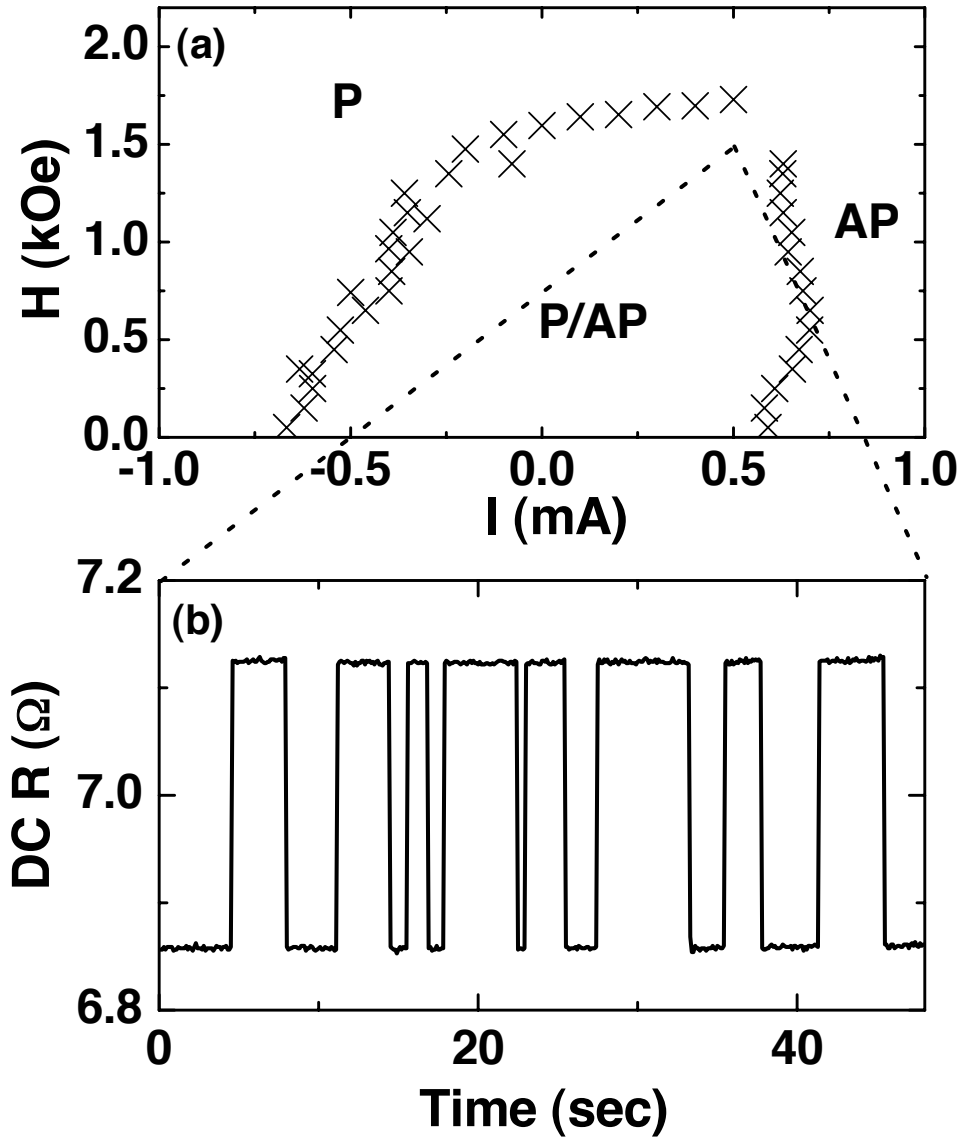


Figure 5.13: (a) Experimentally-determined $T = 0$ stability diagram of Device 1 (SC3434). (b) DC resistance R measured vs. time when the device is biased at $H = 1.4$ kOe and $I = +0.5$ mA.

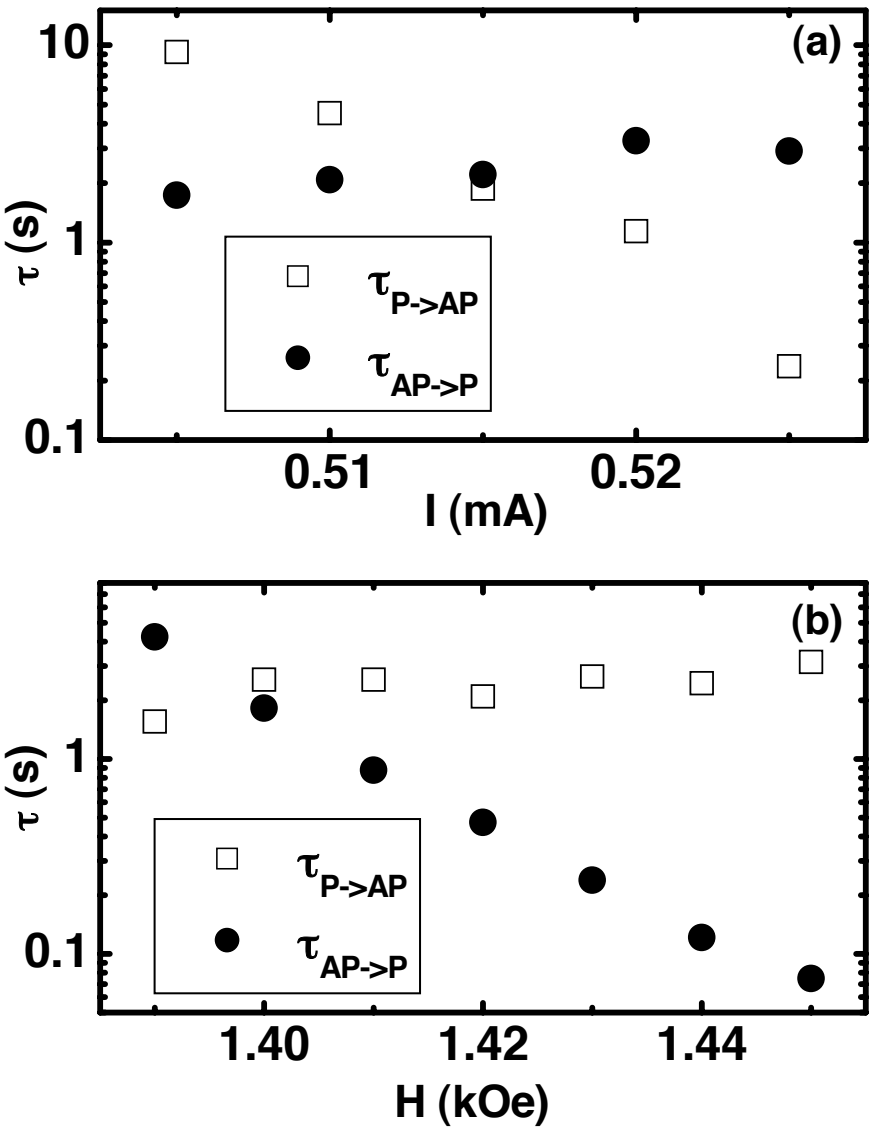


Figure 5.14: Mean switching times $\tau_{P\to AP}, \tau_{AP\to P}$ from the telegraph noise data of the device of the previous figure (SC3434). (a) Switching times vs. current I at constant field $H = 1.4$ kOe. (b) Switching times vs. field H at constant current $I = +0.51$ mA.

tations in the single-domain model, however, are coherent, so it is not clear whether fluctuations greatly affect them. It is a fascinating question how the crossover from telegraph-noise to coherent excitation occurs, or even if it occurs at all. Is there a discontinuous change in the sensitivity of the magnet to thermal fluctuations, or is there a broader crossover region that moves from incoherent magnons to coherent precession at higher fields? Or, is there instead no coherence in the high-field excitations, so that the discrete fluctuations of the telegraph noise give way to the continuous fluctuations of current-generated magnons? I cannot answer these questions, but I offer them as intriguing puzzles that extensions of this work could address.

5.2.4 Current-Induced Reversal as Both a Torque and a Field?

This section has shown through a number of different measurements that treating the effect of a spin-polarized current on a magnetic moment simply as an effective exchange field does not correctly predict the statistical properties of magnetic reversal. The torque model, which assigns separate and qualitatively different thresholds to current and field-induced reversal, more accurately describes the data. However, a recent model by Zhang, Levy, and Fert (ZLF) [31] has suggested that spin-transfer torque works in conjunction with an effective field to reverse the magnet. torque and an effective field. A diffusive linear-response theory similar to Heide's [25, 26] is applied to the magnetic trilayer system to derive an expression for the spin accumulation in the thin layer. Through some vector manipulations, this is shown to act both as an effective field and as a torque pointed in the same direction as Slonczewski's term and of similar magnitude. Unlike Heide's model, the effective field

here is proportional to the component of the spin accumulation perpendicular to the spin moment of the magnet, and so decays with distance from the interface over a length scale set by the exchange splitting as the electrons precess around the moment. Although both spin-transfer torques and precessional torques (which can be expressed in terms of an effective field) have been described previously, both in our own scattering formalism [35] and in the circuit theory of the Delft group [33], ZLF suggest that the effective field contribution is comparable in size to the spin-transfer torque contribution. A somewhat oversimplified reading of the ZLF model suggests that its stability diagram can be mapped from the spin-transfer torque diagram by replacing the field H with $H + H_{ZLF} = H + C_{ZLF} I$, where $H_{ZLF} = C_{ZLF} I$ is the effective field contribution of the model, proportional to the current. Such a mapping, depending on the proportionality constant C_{ZLF}, can give stability boundaries with qualitatively similar shapes to the torque-alone approach. A quantitative comparison requires knowledge of the microscopic parameters that establish the magnitudes of the torques and field. In the absence of such knowledge, it is not possible to rule out the possibility of a small effective-field contribution to the nanomagnet reversal. However, I once again note that it is somewhat doubtful whether a diffusive model can be applied to the systems I study in the first place, because the mean free paths for perpendicular transport through magnetic multilayers are typically larger than the layer thicknesses. Also, Frank Albert [32] has studied the dependence of the critical switching currents on the thickness of the thin layer; he has been able to put an upper bound of ≤ 1 nm on the length scale over which any effective field may operate. This is much smaller than the length scale described by ZLF (a few nm), and indicates that current-induced reversal is triggered largely by scattering at the magnetic interfaces. The previous theoretical work, including our own (see

Chapter 3, and [33, 34, 35]) confirms this notion, as the transverse component of the spin current is shown to disappear within a few monolayers after entering the magnet, due to averaging over electron momentum directions. It thus appears unlikely that any spin accumulation-based effective-field interactions as described by ZLF are central to the reversal observed in nanopillar devices.

5.3 Intuitive Picture of Spin-Transfer at Finite Temperature

This chapter has demonstrated that the effect of a spin-polarized current on a magnet at finite temperature is to reduce a barrier, over which thermal fluctuations can drive the magnet to reversal. At the same time, I have shown that the predictions of spin-transfer torque are consistent with the observed structure in the reversal statistics of my nanomagnets. What has been missing from this argument is how to think about the barrier microscopically within the torque model. For as I discussed earlier, there is no explicit energy barrier height that is involved in the $T = 0$ threshold for current-induced reversal; rather it is a balance between *rates of energy change* that arise from spin-transfer and damping that determines when the magnet switches. In this section I consider the torque model at finite temperature. A rigorous treatment of such is a project in itself and will not be attempted here; general formalisms for thermally-activated escape in the presence of nonconservative forces already exist in the literature [5, 6]. Here I will instead attempt to just give an inutitive physical picture of how thermal fluctuations fit naturally into the stability properties of a magnet under the influence of spin-transfer torque.

5.3.1 The Langevin and Fokker-Planck Equations

To begin, I once again write down the LLG equation for the trilayer geometry with the spin-transfer torque term:

$$\frac{d\vec{S}_{F2}}{dt} = \gamma \vec{S}_{F2} \times \vec{H}_{eff} - \left[\gamma \alpha \hat{s}_{F2} \times \left(\vec{S}_{F2} \times \vec{H}_{eff} \right) + \frac{cI}{e} \hat{s}_{F2} \times \left(\hat{s}_{F1} \times \vec{S}_{F2} \right) \right]. \quad (5.27)$$

The first term describes precession of the thin layer $F2$ around the effective field H_{eff}, while the second and third describe the competing influences of damping (with amplitude α) and spin-transfer. This equation, as I noted at the start of the chapter, is strictly only valid at $T = 0$. At finite temperature, the spin moment $\vec{S}_{F2}$ will move in response to both these torques and random thermal fluctuations. This can be described in a very general sense by adding a random torque term $\vec{T}(t)$ to the above:

$$\frac{d\vec{S}_{F2}}{dt} = \gamma \vec{S}_{F2} \times \vec{H}_{eff} - \left[\gamma \alpha \hat{s}_{F2} \times \left(\vec{S}_{F2} \times \vec{H}_{eff} \right) + \frac{cI}{e} \hat{s}_{F2} \times \left(\hat{s}_{F1} \times \vec{S}_{F2} \right) \right] + \vec{T}(t). \quad (5.28)$$

This is known as a Langevin equation [36], as it relates both the deterministic and fluctuation forces to the dynamics of a macroscopic variable of a system−− in our case, the total moment $\vec{S}_{F2}$. Given the correct torque term $\vec{T}(t)$, the problem is, to a good approximation, fully determined by the Langevin equation.

Of course, the devil is in the details, and the details here are in determining the "correct" form for $\vec{T}(t)$. Since thermal fluctuations are random, $\vec{T}(t)$ cannot be expressed analytically; rather, it is defined in terms of its statistical properties. The presence of a random torque in the LLG equation also makes the variable $\vec{S}_{F2}(t)$ an ill-defined quantity; the spin moment must be considered not in terms of a single direction, but a statistical distribution of directions $P\left(\vec{S}_{F2}, t\right)$, where $P\left(\vec{S}_{F2}, t\right) d\vec{S}_{F2}$ is the probability of finding the moment in a volume $d\vec{S}_{F2}$ in configuration space. P can be determined from the Fokker-Planck equation, a partial differential equation

that relates the time development of P to the statistical properties of the forces acting on the system. The Fokker-Planck equation takes the general form [8]

$$\frac{\partial P}{\partial t} = -\frac{\partial}{\partial x_i}\left(A_i P\right) + \frac{1}{2}\frac{\partial^2}{\partial x_i \partial x_j}\left(B_{ij} P\right), \tag{5.29}$$

$$A_i = \lim_{\Delta t \to 0} \frac{1}{\Delta t}\left\langle \Delta x_i \right\rangle, \tag{5.30}$$

$$B_{ij} = \lim_{\Delta t \to 0} \frac{1}{\Delta t}\left\langle \Delta x_i \Delta x_j \right\rangle, \tag{5.31}$$

where x_i are the coordinates of configuration space, and summation over repeated indices is implied. A_i and B_{ij} are quantities derived from the statistically-averaged behavior of the system. The Langevin equation may be inserted into Eqn. (5.29) to determine A_i and B_{ij}. The random torque term $\vec{T}(t)$ can be fixed at this point by setting $\partial P/\partial t = 0$; the resulting solution is the equilibrium probability distribution. In the absence of a current, this is simply the Boltzmann distribution,

$$P(\vec{S}_{F2}) = e^{-E(\vec{S}_{F2})/k_B T}, \tag{5.32}$$

where $E(\vec{S}_{F2})$ is the effective energy of the system with spin moment $\vec{S}_{F2}$. Once the parameters that enter into the Fokker-Planck equation are determined, a nonequilibrium initial condition $P(\vec{S}_{F2}, t = 0)$ can be inserted into the equation and the time evolution of the probability distribution can be calculated.

The above prescription is formally identical to the methods of Néel [7] and Brown [8] in deriving expressions for the reversal of a single domain uniaxial magnet at finite temperature with a magnetic field applied. Of course, the effect of spin-transfer torque in Eqn. (5.28) is qualitatively different from that of any effective field, so the specifics of solving Eqn. (5.29) will be very different. The Langevin and Fokker-Planck equations, though, let us take a more general view of thermal fluctuations and define the problem in terms of the probability distribution P, which is a well-defined entity regardless of whether a current or a field is affecting reversal.

5.3.2 Uniaxial Case

Let us first consider the simplest possible magnetic geometry: a single-domain magnet with a uniaxial anisotropy H_u, and a magnetic field H applied along this axis. I will also assume, as I have before, that the thick layer polarization direction $\hat{s}_{F1}$ is parallel to the field. In this case we may rewrite Eqn. (5.28) in spherical coordinates:

$$\frac{d\vec{S}_{F2}}{dt} = \left[\gamma S_{F2}\left(H + H_u\cos\theta\right)\sin\theta + T_\phi(\phi,\theta,t)\right]\hat{\phi}$$
$$-\left[\gamma\alpha S_{F2}\left(H + H_u\cos\theta\right)\sin\theta - \frac{cI}{e}S_{F2}\sin\theta + T_\theta(\phi,\theta,t)\right]\hat{\theta}, \tag{5.33}$$

where $T_{\phi,\theta}$ are the components of the random torque, which in general depend on angle. In principle there is also a T_ρ which changes the magnitude of the magnetization. Due to exchange, though, the energy changes associated with this kind of fluctuations will be very large compared to the temperature, provided the temperature is well below the Curie temperature. As a result, these fluctuations are comparatively small, and we will neglect them.

The next step is to insert this equation into the Fokker-Planck equation, using $x_I = \phi, \theta$ as the coordinates. However, the symmetry of the geometry allows us to make a great simplification. Without the presence of spin-transfer, the energy of the system depends only on the angle θ: $E = -\gamma S_{F2}\left(H + H_u\cos\theta\right)\cos\theta$. The addition of spin-transfer should not change this invariance with respect to ϕ, as this additional torque only induces changes in the angle θ. Since the statistical distributions are set by the energy, we thus can expect the solution for the probability distribution to be separable, with the component that depends on ϕ constant in time:

$$P(\phi,\theta,t) = P(\phi)P(\theta,t). \tag{5.34}$$

This means we need to focus only on the θ-component of the Langevin equation.

Writing out this component, we have

$$\frac{1}{S_{F2}}\frac{d\vec{S}_{F2}}{dt}_{\theta} = \frac{d\theta}{dt} = \frac{cI}{e}\sin\theta - \gamma\alpha\left(H + H_u\cos\theta\right)\sin\theta + T_\theta(\theta,t). \tag{5.35}$$

Even with only one coordinate, the calculation of $P(\theta,t)$ is still formidable. Neglecting the dependence of the proportionality constant c on θ, Equation (5.35) looks very similar mathematically to the case where there is no current, and and H is replaced by

$$H \rightarrow H_I = H - \frac{c}{e\gamma\alpha}I. \tag{5.36}$$

Note that the θ-dependence of c will make H_I angle-dependent. While this affects the rigorous result, it does not qualitatively change the intuitive arguments presented here.

If we continue and substitute the Langevin equation into the Fokker-Planck equation, the mathematical derivation of P is quite similar to the derivations of Néel and Brown for field-driven reversal, up until the point where an equilibrium ($\partial P/\partial t = 0$) solution is imposed to determine $\vec{T}(t)$. For field reversal, the total energy is known and the equilibrium solution is simply the Boltzmann term. In the presence of the nonconservative spin-transfer torque, it is not immediately clear what the equilibrium solution should be, so it is unclear whether $\vec{T}(t)$ is the same in the case when a current is applied. I contend, admittedly without derivation, that the equilibrium solution is still the Boltzmann term, with H replaced by H_I. This conclusion is supported by the idea of treating spin-transfer torque as a modification of the effective damping of the system, as I have done throughout this dissertation. Thermal equilibrium is established through the competition between the damping torque and the fluctuation torque $\vec{T}(t)$. The fluctuation-dissipation theorem [36], in its most general conception, connects the magnitudes of the damping and fluctuation terms via the temperature T. If the damping, for all mathematical intents and

purposes, is effectively larger or smaller due to spin-transfer, then the fluctuations will change accordingly. Thus it is reasonable to conclude that $\vec{T}(t)$ will look the same whether a current and a field H is applied, or there is no current and a field H_I is applied, since the effective damping is the same in both cases.

Given the contentions above, the dynamics of the magnet in the θ-direction is mathematically similar to that when only a field is applied, with the field having the form of H_I. A rigorous derivation will of course require that H_I be angle-dependent, due to the θ-dependence of c. However, such a modification does not qualitatively affect the intuitive argument presented here. In any case, the problem becomes quite similar to that solved by Néel and Brown, and their solution——in particular, Eqn. (5.2) and (5.3)——can be straightforwardly applied to this case. Does this mean that the effective field model has risen again? Not quite, because while the probability distributions $P(\theta, t)$ may be similar, the full dynamics of reversal are *not* the same. In particular, the ϕ-component of the torque, which drives the precession of the moment, is, in the presence of both a field H and a current I,

$$\left.\frac{d\vec{S}_{F2}}{dt}\right|_{\phi} = \gamma \vec{S}_{F2} \left(H + H_u \cos\theta\right) \sin\theta + T_\phi(\phi, \theta, t). \tag{5.37}$$

Thus a magnetic field alters the precessional dynamics of the moment, while a current, which only acts along the θ-direction in the Slonczewski model, does not. In other words, although the switching probability will be similar for field-induced reversal and current-induced reversal, the precise motion of the moment during reversal in each case will be quite different.

The discussion above points out that, even though current-induced reversal in the uniaxial case can be fully interpreted as reducing an energy barrier in a manner mathematically similar to that when a field is applied, we must be cautious about interpreting the energy associated with this barrier as real. For example, according

to the LLG equation, if at $T = 0$ we were to excite uniform spin-waves in the magnet via an applied AC field, their frequency (and thus their energy) would vary with an applied DC magnetic field; however, according to the Slonczewski model, only the damping, and not the energy dispersion, of the spin waves is affected by current. In the torque model, the current does not modify the $T = 0$ energy configuration of the magnet, but, rather, shifts the finite-temperature statistical distribution of moment directions away from the equilibrium Boltzmann form. This shift, depending on the sign of the current, is either towards larger or smaller energies, which has the overall effect of decreasing or increasing the effective barrier to reversal.

5.3.3 Uniaxial Plus Easy-Plane Case

In the end, spin-transfer at finite temperature in the uniaxial geometry has a surprisingly simple solution, as a mathematical correspondence can be made to magnetic field-induced reversal. This is possible due to the high symmetry of the geometry, which gave spin-transfer the precise form of an effective damping. However, we lose the advantages of such symmetry when we take a step closer to the actual geometry of my devices and add an easy-plane demagnetizing anisotropy to the uniaxial term. In this case the problem becomes much more difficult.

The central difficulty in solving the Langevin and Fokker-Planck equations when a demagnetizing field is added comes from the fact that $P(\phi, \theta, t)$ is no longer separable. We saw in Chapter 4 that the precessional orbits of a magnet in the presence of both uniaxial and easy-plane anisotropy fields are not circular, but elliptical, with the long axis in the plane of the magnet. Thus the precession in general has both ϕ and θ components, and we cannot separate out the coordinates to simplify the problem. Moreover, the damping is always perpendicular to the precession direc-

tion, so it will not point in the same direction as spin-transfer at all points along the orbit——see Fig. 4.8. This prevents us from folding spin-transfer directly into a renormalized damping.

Clearly the tricks I performed earlier to show that the current modifies the probability distribution like an effective field will not work here. This is no surprise, of course, as I have spent much of this chapter demonstrating that spin transfer in the nanopillar geometry has a qualitatively different reversal threshold than a magnetic field. Still, we should not expect thermally-activated reversal to radically change when an easy-plane anisotropy is added, as it should reduce to the effective-field case when the demagnetizing field goes to zero. In fact, the radical change occurs in the field-induced reversal, as the stable point undergoes a topological change at $H = H_c$ from a local minimum to a saddle point; without the demagnetizing field, the change is from a local minimum to a global maximum. This change is a consequence of the field contributing to the precessional torque, which is larger than either the damping or spin-transfer torques (for reasonable currents) by a factor of $1/\alpha$. Since spin-transfer does not significantly contribute to precession, such radical alterations in the moment dynamics do not occur when a current is applied. I should point out that, to the best of my knowledge, no rigorous derivations exist of thermally-activated reversal in this geometry when a field is applied; most people simply jump directly to the Néel-Brown equations, using the in-plane anisotropy for the barrier height. However, a rigorous derivation might be simpler for current-induced reversal, because the precessional orbits around the energy minimum are not significantly altered as $I \to I_c$.

Although I will not attempt such a derivation here, I offer some speculation as to how the solution might look. A correspondence between spin-transfer and

damping cannot be made at every point on the elliptical orbit. However, if an average over the orbit is performed, similar to that done in Chapter 4 to determine the $T = 0$ switching current, an average effective damping can be defined. It thus may still be possible to equate current to a field in the resulting Langevin equation, but the correspondence would have to include the demagnetizing factor, e.g., $H \rightarrow H_I = H - \left(\frac{c}{e\gamma\alpha} I - 2\pi M\right)$, in describing the average dynamics of the θ variable. This would maintain the notion of a field-like effective energy barrier, but would shift the switching currents to larger values. The demagnetizing term would not appear in an expression for thermally-activated field-induced reversal, as only the smallest barrier height, the in-plane anisotropy, matters. The barrier for current-induced reversal is in some sense spread out over a full orbit, and so both the in-plane and easy-plane anisotropies must be taken into account.

5.3.4 Nonuniform Reversal

The model cases above, however illuminating they may be, are in all likelihood oversimplified with respect to actual nanopillar devices, since current-induced reversal appears to involve nonuniform motion of the magnet. Nonuniform reversal of course greatly complicates the problem, as the two degrees of freedom of configuration space for a uniform magnet expand to as many as $2N$ degrees of freedom, where N is the number of atoms in the magnet. However, if the nonuniform reversal is analogous to the domain nucleation-annihilation transitions seen in field-induced reversals of larger magnets [1, 10, 11], then the above procedure could still be applied in principle to the fraction of the magnet where the nucleation is initiated, as this portion still remains roughly uniform during reversal. In that case, the initial motion of the nucleation region in the presence of spin-transfer would likely determine the size of

the energy barrier that thermal fluctuations must overcome.

5.4 Final Thoughts

I have tried in this chapter to demonstrate the important role of thermal fluctuations in magnetic reversal induced by spin-transfer torque. A rigorous approach to the fluctuation-driven reversal may be quite complicated, and exact solutions may be impossible. However, regardless of the complexity, the following general argument most likely still holds: Thermal fluctuations in magnets consist of a delicate balance between magnetic damping and fluctuational torques. Spin-transfer alters this balance, and induces a deterministic change in the probability distributions. This change, by all appearances, can be fully described by the well-established formalism of stochastic dynamics; no fundamentally new approach need be taken [5, 6]. However, with respect to small magnetic systems, a spin-polarized current alters the magnetization direction in a fundamentally different way than a magnetic field, and the established results for field-induced reversal do not necessarily apply to the case of current-induced reversal. The solutions to the Fokker-Planck equation will reflect this new physics, which arises from the unique interplay between temperature, damping, and spin-transfer torque.

Table 5.1: Summary of parameters for the three devices used in this chapter. The lateral dimensions were determined by comparing the measured current-induced hysteresis resistance difference ($R_{AP} - R_P$) to other devices of known lateral dimensions; see Chapter 4.

Device #	Device Name	Composition	Lateral Dimensions
1	SC3434	$(Co_{2.5}/Cu_6/Co_{40})_{nm}$	30 $\times$ 80 nm
2	SC3291	$(Co_{2.5}/Cu_6/Co_{40})_{nm}$	50 $\times$ 70 nm
3	SMILEY2	$(Co_{2.5}/Cu_6/Co_{40})_{nm}$	130 $\times$ 60 nm

Bibliography

[1] W. Wernsdorfer *et al.*, Phys. Rev. B **53**, 3341 (1996); Phys. Rev. B **55**, 11552 (1997).

[2] P. Hänggi, P. Talkner, and M. Borkovec, Rev. Mod. Phys. **62**, 251 (1990).

[3] S. Arrhenius, Z. Phys. Chem. (Leipzig) **4**, 226 (1889).

[4] H. A. Kramers, Physica (Utrecht) **7**, 284 (1940).

[5] M. I Friedlin and A. D. Wentzell, Random Perturbations of Dynamical Systems, Springer-Verlag, Berlin (1984).

[6] R. S. Maier and D. L. Stein, Phys. Rev. Lett. **69**, 3691 (1992); Phys. Rev. E **48**, 931 (1993).

[7] L. Néel, Ann. Geophys. **5**, 99, (1949).

[8] W. F. Brown, Phys. Rev. **130**, 1677 (1963).

[9] W. T. Coffey *et al.*, Phys. Rev. B **52**, 15951 (1995); Phys. Rev. Lett. **80**, 5655 (1998).

[10] R. H. Koch *et al.*, Phys. Rev. Lett. **81**, 4512 (1998).

[11] R. H. Koch *et al.*, Phys. Rev. Lett. **84**, 5419 (2000).

[12] J. Z. Sun, Phys. Rev. B **62**, 570 (2000).

[13] Ya. B. Bazaliy, B. A. Jones, and S. C. Zhang, J. App. Phys. **89**, 6793 (2001).

[14] R. P. Cowburn *et al.*, Phys. Rev. Lett. **83**, 1042 (1999).

[15] T. Schrefl, J. Fidler, Comp. Mat. Sci. **17**, 490 (2000).

[16] W. Wernsdorfer *et al.*, Phys. Rev. Lett. **78**, 1791 (1997).

[17] W. Wernsdorfer, Adv. Chem. Phys. **118**, 99 (2001).

[18] R. H. Victora, Phys. Rev. Lett. **63**, 457 (1989).

[19] A. Garg, Phys. Rev. B **51**, 15592 (1995).

[20] J. Kurkjärvi, Phys. Rev. B **6**, 832 (1972).

[21] J. Miltat *et al.*, J. App. Phys. **89**, 6982 (2001).

[22] J. Slonczewski, J. Magn. Magn. Mater. **159**, L1 (1996).

[23] L. Berger, Phys. Rev. B **54**, 9353 (1996).

[24] Of course, an effective field also generates a (precessional) torque. To clarify, I only use the term "torque model" to refer to the standard spin-transfer approach of Slonczewski and Berger [13, 23], where the torque is primarily in the plane defined by the spin moment vectors of the two magnetic layers. The precessional torque in effective-field models is mostly perpendicular to this plane. Note that our scattering formalism (Chapter 3) can describe both kinds of torques.

[25] C. Heide, P. E. Zilberman, and R. J. Elliott, Phys. Rev. B. **63**, 064424 (2001).

[26] C. Heide, Phys. Rev. Lett. **87**, 197201 (2001); Phys. Rev. B **65**, 054401 (2002).

[27] F. J. Albert *et al.*, App. Phys. Lett. **77**, 3809 (2000).

[28] Similar random switching has been seen in previous spin-transfer experiments [29], including in my own nanoconstrictions, but in those cases the magnetization states were not as clearly-defined as in the nanopillar geometry.

[29] M. Tsoi *et al.*, Phys. Rev. Lett. **80**, 4281 (1998); **81**, 493 (E) 1998).

[30] S. Machlup, J. App. Phys. **25**, 341 (1954).

[31] S. Zhang, P. M. Levy, and A. Fert, Phys. Rev. Lett. **88**, 236601 (2002).

[32] F. J. Albert *et al.*, preprint (2002).

[33] A. Brataas, Y. V. Nazarov, and G. E. W. Bauer, Phys. Rev. Lett. **84**, 2481 (2000).

[34] M. D. Stiles and A. Zangwill, Phys. Rev. B **66**, 014407 (2002).

[35] X. Waintal *et al.*, Phys. Rev. B **62**, 12317 (2000).

[36] N. G. van Kampen, Stochastic Processes in Physics and Chemistry, North-Holland, Amsterdam (1992).

Chapter 6

Concluding Remarks and Future Directions

Even though a considerable number of words have been expended in the preceding chapters, the work in this dissertation can really be expressed within a single familiar idea: Newton's Third Law. When a spin-polarized current passes through a ferromagnetic metal, exchange interactions between the current and the spin moment of the magnet scatter the current in a spin-dependent manner. Motivated by the discovery of the giant magnetoresistance effect 14 years ago, extensive thought and effort has been devoted to understanding one half of this interaction, which is the effect that spin-dependent scattering has on the current. My work simply demonstrates that the other half of the exchange interaction is important as well: spin-dependent scattering can effect the magnetic moments themselves, to the extent that the moments can be wrenched into a new stable position, or even sent into continuous dynamical motion. As I have hopefully also made clear in this dissertation, though, from simple ideas can spring quite subtle and complex challenges for physicists. I have only answered a few of the most basic questions about the spin-

transfer effect in this work. My colleague Frank Albert has answered others in his own dissertation [1]. In this chapter I suggest a few future directions for research involving spin transfer that should further illuminate the fundamental physics behind the effect.

Let me begin with the nanoconstriction geometry. Although I have shown that quantitative analysis of spin-transfer is difficult in this geometry, there are still a number of interesting experiments yet to be performed, for which nanconstrictions are advantageous over the nanopillar geometry. The central utility of nanoconstrictions is the speed by which different materials combinations may be tested; while a full nanopillar fabrication run may take the better part of a week, magnetic heterostructures can be formed in the nanoconstriction geometry in a matter of hours, as the layers only need to be grown on preexisting constrictions. This makes nanoconstrictions a highly desirable technique for exploring spin-transfer in the phase space of exotic materials. Two interesting material types to explore may be f-electron ferromagnets such as gadolinium, and half-metallic magnets such as CrO_2.

Nanopillars, though, will remain for the time being the geometry of choice for a controlled quantitative study of spin-transfer. There remain a number of questions to resolve about the spin-transfer effect here, perhaps most foremost the nature of the nanomagnet dynamics. For example, at low magnetic fields, single-domain spin-transfer models predict a coherent reversal of the magnet. My low-field switching statistics data (Chapter 5), however, suggest that the reversal is not single-domain in nanopillar nanomagnets. A more complete study of the statistics of current-induced reversal would shed more light on the parameters governing thermally-activated reversal, and the nature of the reversal. It would also be extremely useful to perform

the same set of statistical measurements when a magnetic field is applied. As I mentioned in Chapter 5, comparing the effective activation energies for field-induced and current-induced reversal may yield insights into the effect of spin-transfer in a nanomagnet, e.g., whether current-induced reversal is intrinsically more unstable to nonuniform dynamics than field-induced reversal. Also, measurements in which the magnetization state can be time-resolved at the nanosecond scale [3] would give insight into the degree of coherence of reversal.

At high fields, the spin-transfer models also predict coherence in the form of uniform precession of the nanomagnet. However, the DC measurements presented in this dissertation do not provide any direct evidence of the AC nature of the excitation. Frequency-resolved measurements, perhaps in analogy with the experiments of the Michigan State group on point contacts [2], must be performed to resolve this question. It may very well be that the nonuniform instabilities at low field also occur in some form at high field, preventing full spin-wave coherence in these confined nanomagnets. There is no need for me to oversell the need for high-frequency measurements, though; even as I write this, efforts are underway in the Ralph and Buhrman groups to begin performing such kinds of experiments.

I should not neglect the contribution of theory to the effort of understanding spin transfer. Out of our own scattering formalism, as well as the circuit theory of the Delft group (see [4], and the discussion in Chapter 3) has come a host of intriguing geometry ideas. One important notion that comes out of the scattering approach to spin-transfer is that the presence of spin-dependent scattering in some sense decouples the spin current from the charge current. This suggests multiterminal geometries where, for example, a spin-transfer torque is exerted on a magnet with *zero* charge current sent through the magnet [5]. Of course, the theorists leave the

highly nontrivial question of how to realize such geometries to the experimentalists, but such work certainly gives a sense of the broad range of new and interesting physical phenomena that may be possible with spin-transfer. As these current-induced torques are a basic consequence of the interaction between spin-polarized currents and ferromagnetic metals, their physical importance should certainly not be limited merely to the simple trilayer geometries featured in this dissertation.

Bibliography

[1] F. J. Albert, Dissertation, Cornell University, Ithaca, NY (2002).

[2] M. Tsoi *et al.*, Nature **406**, 46 (2000).

[3] S. E. Russek and S. Kaka, IEEE Trans. Magn. **36**, 2560 (2000); S. Kaka and S. E. Russek, App. Phys. Lett. **80**, 2958 (2002).

[4] A. Brataas, Y. V. Nazarov, and G. E. W. Bauer, Phys. Rev. Lett. **84**, 2481 (2000).

[5] G. E. W. Bauer, Y. V. Nazarov, and A. Brataas, Physica E **11**, 137 (2001).

Appendix A

Fabrication of Nanoconstrictions

This Appendix describes in detail the procedure for fabricating nanoconstrictions, which are used in Chapter 2 to inject large current densities into magnetic trilayers in order to study the spin-transfer effect. This appendix is expanded from a standard Ralph group recipe, with some supplementary details, asides, and warnings for the reader who may wish to make these devices. As nanoconstrictions are useful for a wide array of experiments not limited to the ones described in this thesis, I will only give instructions up to and including the creation of the hole; discussion of the metal deposition steps for my devices is contained in Chapter 2. All steps, except those explicitly noted, are performed at the Cornell Nanofabrication Facility (CNF).

Begin with double-side-polished $\langle 100 \rangle$ 3" Si wafers, available from a variety of vendors. Larger wafers may be used, of course, but currently-available equipment in the Ralph group for this process (such as photolithography masks and holders for KOH etching) are designed for 3" wafers, so plan all the steps in advance if the process is to be scaled up. On these wafers, after a MOS cleaning, 100 nm of silicon nitride should be grown on both sides, through low pressure chemical vapor deposition (LPCVD). The growth recipe for low-stress nitride should be followed,

as one of the nitride layers will eventally become a freely suspended membrane.

Next comes photolithography. It saves time to perform these steps on multiple wafers in parallel, typically 6-12 at a time. First clean the top of the spinner chuck with acetone, isopropyl alcohol, and blow dry; as we are processing both sides of the wafer, it's very important the chuck be clean. The wafers should be cleaned in a similar manner. Next, spin photoresist on one side of the wafer; this side will eventually be the membrane through which the nanoconstriction is formed, and the resist will protect the nitride from accidental scratches during subsequent steps. We will call this side of the wafer the membrane side, while the opposite side will be called the patterned side. Any photoresist will do, but typically I use Shipley 1813, as it is the same resist used for the photolithography. Spinning the resist at 2000 RPM for 30 seconds leaves a roughly 2 μm-thick protective layer. After spinning the resist, bake the wafer on clean aluminium foil in a 90° C oven for 10 minutes, which drives off the resist solvent and hardens the resist. It is very important to treat the exposed patterned side delicately, so that no scratches are made through the nitride. Then, flip the wafer over, and spin S-1813 resist on the patterned side for 1 minute at 4000 RPM. Bake in the 90° C oven on aluminium foil for 30 minutes.

Expose the patterned side on the HTG contact aligner, using the usual settings (405 nm, channel B), for 6 seconds. The typical mask pattern is shown in Fig. A.1, where a 9×9 array of devices are defined. The squares define where the silicon will be etched down to the suspended membranes on the other side, while the lines define break lines in the silicon that will facilitate dicing the wafer for individual sample measurement. The four squares adjacent to the four sides of this 9×9 array will serve as alignment marks for the electron-beam lithography step later on. It is crucial to choose the correct sizes for the squares and the break lines, as the

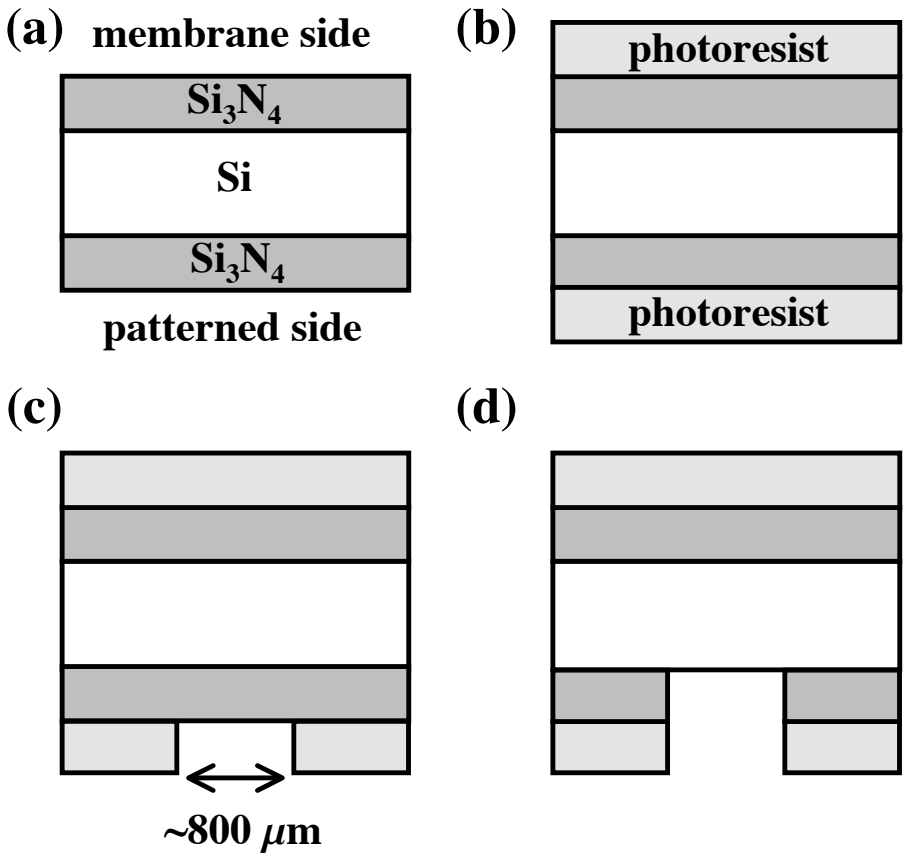


Figure A.1: Schematic depiction of first steps in nanoconstriction fabrication process (not to scale). (a) Silicon nitride films are grown on both sides of a silicon wafer. (b) Photoresist is spun on both sides. (c) Photolithography is performed on one side, using the mask depicted in Fig. A.2. This pattern is transferred to the nitride (d) by a reactive ion etch.

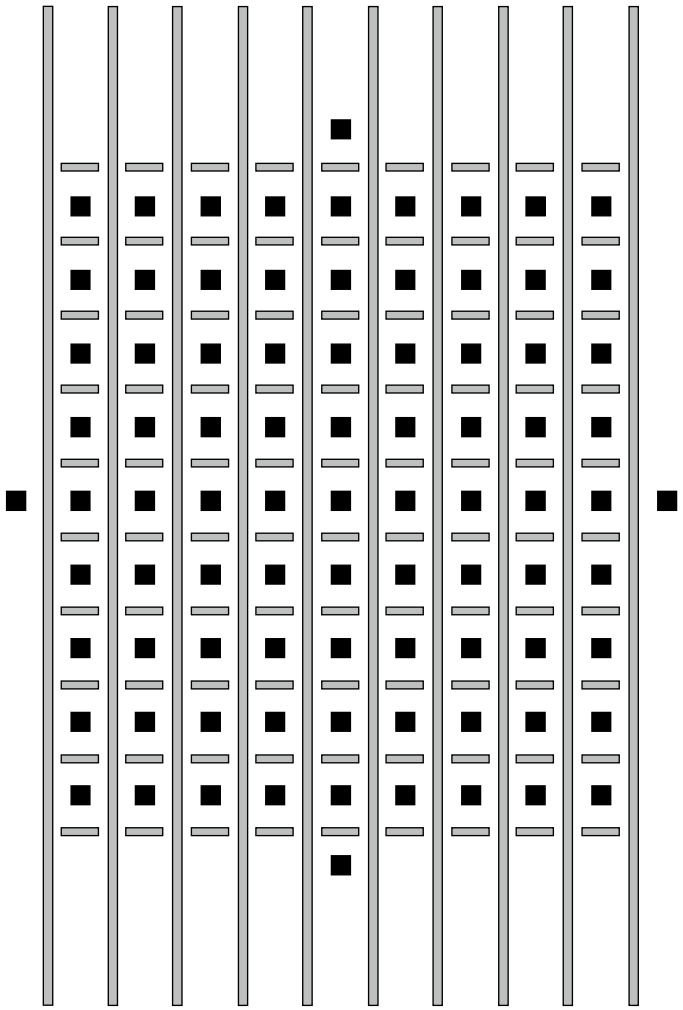


Figure A.2: Photolithography pattern applied to the patterned side of the wafer. After the KOH etch, the black squares will define the location of the suspended silicon nitride membranes, and the gray lines will define the break lines for cutting the wafer into individual devices.

optimal values depend on the thickness of the Si wafer. This can be calculated by noting that the KOH will etch the Si along its $\langle 111 \rangle$ planes, which lie at an angle of 35.26° to the wafer normal (due to its diamond crystal structure). In addition, the etch will undercut the photolithography pattern by roughly 10-20 μm on each side (Fig A.2a). So, for example, if the Si wafer is 500 μm thick, and we desired a suspended membrane size of 50 μm, then the optimal size of the window in the photolithography mask is calculated as

$$\text{mask window size} = 50\ \mu m + 2 * (500\ \mu m) * \tan(35.26°) - 40\ \mu m \quad \text{(A.1)}$$

$$= 717\ \mu m, \quad \text{(A.2)}$$

where the 40 μm is the total estimated undercut amount. The break line widths should be calculated in a similar way so that the KOH etches roughly halfway through the wafer.

After the HTG exposure, develop the wafer in 300 MIF developer for 60 seconds, rinse in DI water, and blow dry. After all this tweezer handling there are likely to be scratches in the resist, so carefully inspect and repair any scratches by manually applying photoresist with a Q-tip. It is also important to coat the edge of the wafer with resist even if it is unmarked, because the nitride is likely very thin or even nonexistent on the edges. Bake the wafer in the 90° C oven for 20 minutes.

The photoresist will not survive in the KOH Si etching solution, so we must transfer this pattern to the silicon nitride, which is KOH-resistant. This is done by etching through the exposed nitride on the patterned side in a reactive ion etcher, usually the Applied Materials at the CNF. First preclean the etcher by running an O_2 plasma for 5 minutes, with a gas flow of 30 SCCM at 30 mTorr and RF power of 100 Watts. If the chamber contains residue from a previous fluoride gas plasma, the plasma will be blue in color, while if the chamber is relatively clean, it will be

yellowish-purple. Load the wafer (up to 3 wafers can be loaded at a time) on small Si chips to prevent it from sliding when the chamber is pumped to vacuum. Etch using a mixture of CHF_3 and O_2 in the SCCM ratio 30/0.7, with a total pressure of 30 mTorr and power of 100 W. One wafer takes 12 minutes, while three will require 15 minutes. Without breaking vacuum, run an oxygen plasma (40 SCCM, 40 mTorr, 100 W) for 10 minutes to strip the resist from the wafer.

Next comes the KOH wet etch, which can be performed within Clark Hall. First make sure all residual resist has been removed from the wafers by cleaning with acetone and isopropanol, and rinsing in DI water. The KOH etch solution is made by mixing dry KOH pellets with DI water in the ratio 500 mL H_20/ 125 g KOH. Usually 1500 mL of solution is mixed in a 2500 mL or 3000 mL Pyrex glass beaker, so that the solution covers the wafers entirely. This solution is heated to $95-100°$ C for etching−−use a hotplate with a thermometer probe so the solution temperature can be regulated. The hotter the solution is, the faster the etch, but the etch also becomes less anisotropic. The boiling point of the solution is roughly 120° C. The beaker should also contain a spin magnet so that the solution can be constantly mixed, and a teflon ring so that the rack that holds the wafers can sit above the spin magnet. Place the wafers in the solution. Ideally the etch should take a little over 3 hours, but this can vary quite a bit. For the first two hours or so, monitor only to ensure that the solution covers the wafers; if it gets too low, refill with DI H_20. After this, check on the wafers every 15 minutes or so by removing one and carefully holding the wafer up to the light to see if the silicon has been etched through to the membranes. Check multiple wafers to get a sense of uniformity−−the etch is probably more uniform than the wafers themselves. BE CAREFUL about handling the wafers, as the KOH solution is quite slippery. Once light is seen through the

wafer, etch for 10-15 more minutes. Timing is not essential, as the etch slows down considerably after the 10-20 μm of underetch, but it's not advisable to keep the wafers in any longer than necessary, since residual scratches or weak spots in the nitride will eventually be converted into large holes in the silicon, and the wafer will fall apart in solution (it happens!).

When finished with etching, it is vitally important that the wafers be thoroughly cleaned of KOH residue, or else the silicon (and, to a lesser extent, the silcon nitride) will continue to be etched. To clean the wafers, move them to a boiling beaker of DI water after the etch; start this boiling about 30 minutes before the wafers are taken from the KOH. Boil them for about 10-15 minutes, then transfer them to a second (clean) boiling beaker of DI water. Boil for 10-15 minutes further, then take this beaker and run cold DI water through it until the runoff is cool. Then remove the wafers, rinse in DI water, and let drip dry. No blow drying is allowed once the membranes are suspended, as they are quite fragile. Try to keep tweezer runoff from flowing across the windows. This cleaning procedure may sound arduous (it is), but if any KOH remains on the wafer, it is effectively ruined for the later steps.

Once the wafers have been cleaned, inspect them under an optical microscope and log the window sizes and qualitative cleanliness features. They should now be stored in individual 3" wafer holders. A cross-section of the wafer at this stage looks like Fig. A.2a, with the overhanging nitride on the patterned side. That overhang will be problematic if metal is to be deposited on the patterned side, because the metal at the membrane may not be continuous with that on the nitride. To ensure easy contact to the final device, the overhang must be removed. This is accomplished by using a physical Cu mask, placed over the wafer on the patterned side, that protects the suspended membrane but leaves at least one edge of the overhanging nitride

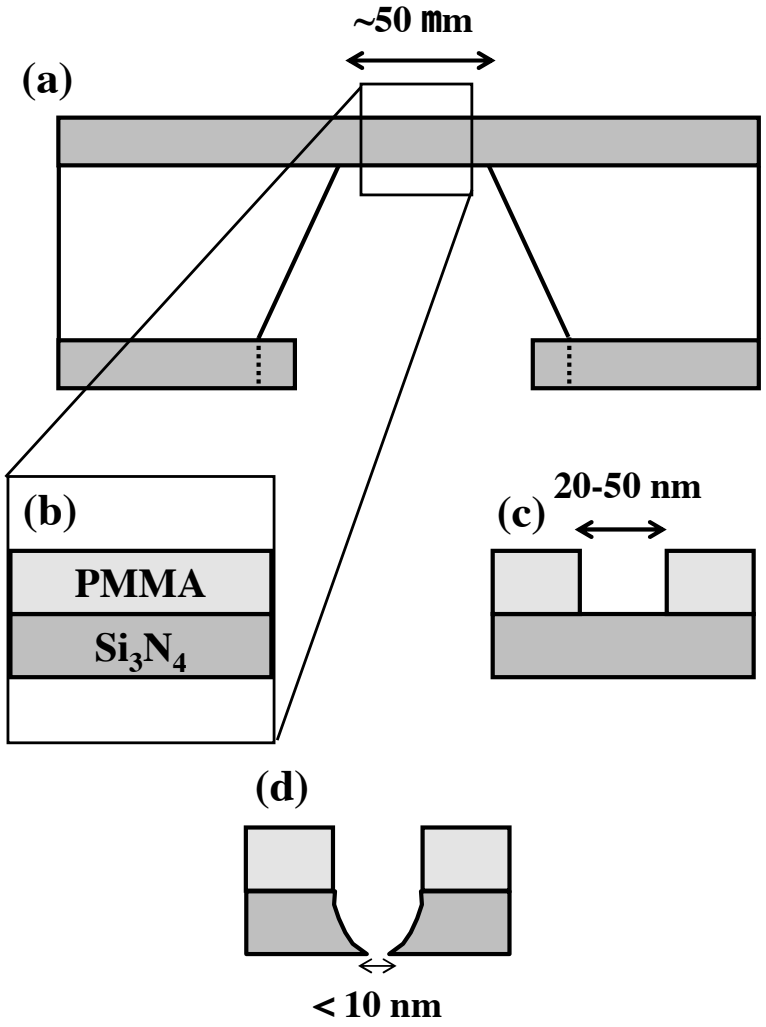


Figure A.3: Post-KOH etch steps in nanoconstriction process. (a) To allow for continuous metallic contact to the suspended membrane, the nitride overhang on the patterned side is removed (dotted line). (b) Closeup of membrane (not to scale). After the membrane is thinned (not shown), PMMA is spun on the membrane, and (c) electron beam lithography is performed to open a dot above the membrane. (d) An isotropic RIE etch forms a bowl-shaped hole through the membrane which, if timed correctly, just breaks through the bottom of the membrane.

exposed. Ralph group has the mask and a holder that clamps the mask over the wafer. Place the wafer and mask in the Applied Materials etcher, and etch using the CHF_3/O_2 30/0.7 SCCM mixture, 30 mTorr, 100 W, for 7 minutes. Only one wafer can be etched at a time here. After the etch, look at the wafer in the optical microscope from the patterned side——the overhang should be visible, and a portion of it should be etched away.

Silicon nitride etches slightly in KOH, so at this point the nitride on the membrane side won't be the original 100 nm that was grown, but something closer to 85-95 nm. The final bowl etch that creates the nanoconstriction is optimized for a nitride thickness of 50 nm, so the nitride now needs to be thinned. This is also done in the Applied Materials etcher. First measure the nitride thickness using the Leitz microscope with the attached computer. There are standard parameters for silicon nitride on silicon that are stored in the computer, but make sure that the label for the data file correspond to the correct parameters. From this measured thickness, etch the membrane side about halfway to 50 nm, assuming a standard etch rate of 1 nm/sec for the standard etch parameters (such as those for the overhang removal step). The etch rate will be close to this, but day-to-day variations are about 20%. Then measure the thickness again, and from that calculate the actual etch rate. Using this, calculate how many seconds are needed to etch to 50 nm, and perform a final etch. Measure and record the final thickness; it's usually easy to get 50 ± 2 nm.

Now comes electron-beam lithography. Spin on 5.5% PolyMethyl MethAcrylate (PMMA) in anisole solvent on the membrane side of the wafer. The typical vacuum chuck cannot be used since the vacuum will break the membranes; instead, a special vacuumless chuck with clips for the wafer is available. One minute at 3500 RPM

yields an approximately 250 nm-thick film. Bake on aluminium foil in the 170 deg C oven for 1 hour. I will assume the reader is using the Leica VB6 at the CNF for this step (you poor soul). After loading the wafer into the 3" wafer holder for the VB6, note the positions of the four alignment windows using the optical microscope in the VB6 room, relative to a stage alignment mark. Typically I use "circle1", which is the set of concentric circles in the upper right corner of the set of alignment patterns.

For the lithography, I assume the reader has some familiarity with the electron beam system and the basic software commmands. Typically an exposure pattern of a single pixel or a 2×2 pixel square is used. The standard jobfiles put a 9×9 array of this pattern on the wafer, one in (hopefully) the center of each window. Usually a range of doses are used across each column, to ensure that at least some of the devices are optimal. A typical total dose is in the range of 50,000 $\mu C/cm^2$, although it is important to know what the "going rate" is, due to the sometime variability of the VB6. After the wafer has been loaded into the machine and the standard calibration routines have been run, center on the alignment mark (e.g., circle1) and set the relative coordinate system origin to that point. Then, move to one of the alignment marks (using the information taken from the optical microscope). There is a useful script called "align_ralph_new" which will guide the reader through the rest of the alignment steps. Basically the numbers taken from the optical microscope serve as a coarse guess for the locations of the alignment windows, and typically one will have to search for the actual locations using the SEM feature of the VB6. Do not despair——they usually are very near the coarse locations. Once the alignment has been completed, run the exposure, which typically takes around 8 minutes. After exposure, develop the wafer in 1:1 MIBK:IPA for 90 seconds. Others have tried

using 1:3 MIBK:IPA with some success. Rinse in isopropanol and drip dry.

Now is the final, most important step, the bowl etch. The optimal parameters vary over time, so I cannot provide unimpeachable numbers for the etch times. The etch is performed on the Applied Materials RIE, but it is put in the so-called "non-linear" configuration. This involves changing the gas inputs and outputs and is described on an instruction sheet by the etcher. Changing the gas flow so that it is not as directed down onto the wafer changes the etching profile from one with flat sidewalls (preferred by most who use the machine) to a more isotropic bowl-shaped profile (preferred by Ralph group and, well, not many others). This is the crucial element to making a constriction hole smaller than that defined by lithography. Usually after a wafer has been exposed in the VB6, a test etch is performed by breaking a wafer into multiple parts and etching each part by a different amount. Then the wafers are made into homogeneous Cu point contacts, and from the resistance of the devices (see Chapter 2) the size of the holes (and thus the optimal etch time) can be inferred. Alternatively, an array of holes can be exposed on a window, and after etching this array can be imaged in the TEM or STEM to determine the optimal dose/etch time combination. If a partial wafer is to be etched, a dummy wafer consisting of bare silicon with PMMA spun on it should be placed under the partial wafer so that the local environment seen by the nanoconstriction is similar to that for a full wafer. It may seem a little like voodoo, but anecdotal evidence indicates that otherwise, samples on the edge of a partial wafer do not turn out well.

Preclean the chamber, as always. A total etch time in the range of 3-5 minutes is usual, broken up into 2 minute segments. Load one wafer at a time, and place on the so-called "2 o'clock" position of the electrode as viewed from the front; this position appears to give the fastest and most consistent etch times. Etch parameters

are CHF_3/O_2 30/0.7 SCCM, 30 mTorr, 100 W. After each 2 minute segment, the wafer should be removed and an oxygen clean (30 SCCM, 30 mTorr, 100 W) for 3 minutes should be performed because polymer residue in the chamber slows the etch rate. Also run a dummy etch using the CHF_3/O_2 parameters before putting the wafer back into the chamber, while checking the RF balance on the etcher. This ensures that the first few seconds of the actual etch will not be unbalanced, since consistency with every second of the etch is important. Also, rotate the sample between etches, for a more uniform overall etch. After the final etch, run an O_2 plasma (40 SCCM, 40 mTorr, 100 W) for 3 minutes with the wafer still inside to remove the PMMA.

That's it!

Appendix B

Fabrication of Nanopillars

This Appendix describes the procedure for fabrication of nanopillar devices, where large current densities can be sent through small (< 100 nm) nanomagnets of controlled size and shape, in order to study the spin-transfer effect. My experimental results on these pillars are detailed in Chapters 4 and 5. The fabrication recipe I describe here largely derives from work established by colleagues of mine in Robert Burhrman's group in the Applied and Engineering Physics Department at Cornell, in particular Jordan Katine and Frank Albert. Although this recipe if followed carefully will result in useful devices, my colleagues have been developing improvements in the procedure to reduce the contact resistance and increase the device yield. This document should therefore in no way be considered the last or latest word in nanopillar fabrication, but rather a description of a specific procedure that works. For the reader wishing to make pillars using the latest recipe, it is worth consulting Frank Albert's thesis [1] or checking with senior researchers in the Buhrman group, e.g., at the time of this writing (summer 2002), Nathan Emley. All steps except for the metal film depositions are performed at the Cornell Nanofabrication Facility.

Begin with an oxidized polished silicon wafer. Silicon oxide is not crucial; it is

just important that the substrate be insulating. This procedure describes a process using 3" wafers, but it can be straightforwardly be scaled up to larger wafers as well, without needing to remake any photolithography masks. The layers can be deposited via sputtering or thermal evaporation, although sputtering is preferred, as it tends to yield more uniform films. First deposit a thin layer (2.5 nm) of Co; this serves as a sticking layer for the layers that follow. Ti or Cr could also be used. Next, deposit a thick (80-120 nm) Cu layer; this serves as the bottom electrode for the device. Then, deposit the layers for the magnetic trilayer. For the procedure I describe here, the thick layer should be deposited first. On top of this, a capping layer of Au 15-20 nm thick is deposited. This will serve as a protective layer for the top of the pillar throughout the process.

Next, spin a bilayer of electron-beam resist on top of the layers (Figure B.1a). The bilayer technique I employ involves first depositing a thick layer of one kind of resist, and then a thinner layer of a resist that is less dose- and developer-sensitive then the first. After exposure and development, the resulting shape in the bilayer should look like Figure B.1b, with a wider hole in the bottom layer than the top. This enhances the liftoff quality when the mill mask is deposited, as the lithographically-defined feature will form separated from the rest of the deposited film (Fig. B.1c). There are a variety of resist combinations that can be used. For the thick layer, I typically use 11% 1:1 MAA. Spinning this at 3000 RPM for 40 seconds leaves an approximately 190 nm-thick film. Bake the wafer on the 170° C hotplate in the e-beam resist room at CNF for 15 minutes after spinning, then deposit the thin layer. I typically use 2% 495 PMMA for this layer. Spinning at 4000 RPM for 40 seconds yields a thickness of about 50 nm. Bake again for 15 minutes on the 170° C hotplate.

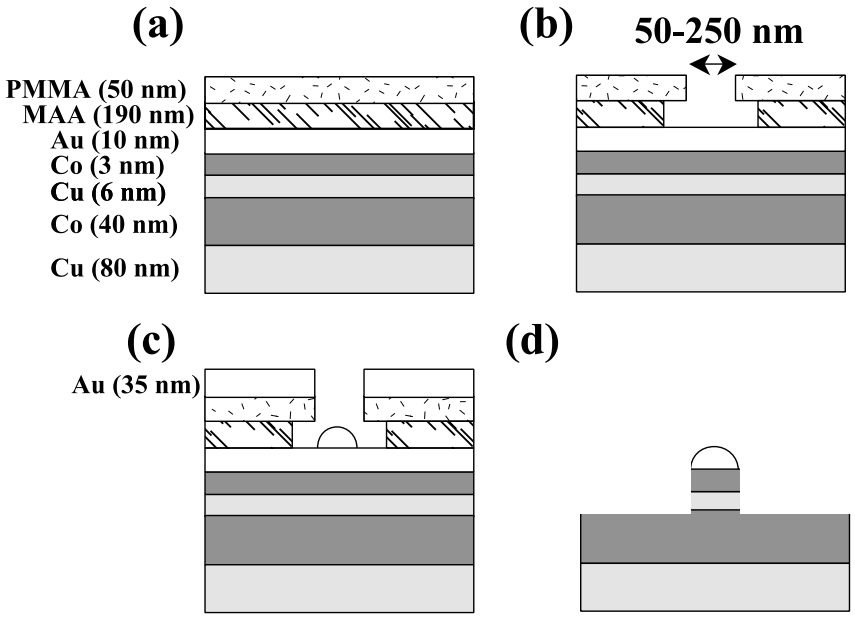


Figure B.1: Schematic of initial steps of nanopillar process (not to scale). The materials and thicknesses noted on the figure are representative. (a) The trilayer is initially deposited, with a thick Cu electrode below, and a thin Au cap above. A PMMA/MAA bilayer is spun on top of the layers. (b) After electron-beam lithography and development, a hole is opened in the bilayer. (c) An Au ion mill mask is deposited. (d) After liftoff (not shown), a timed ion mill creates the nanopillar.

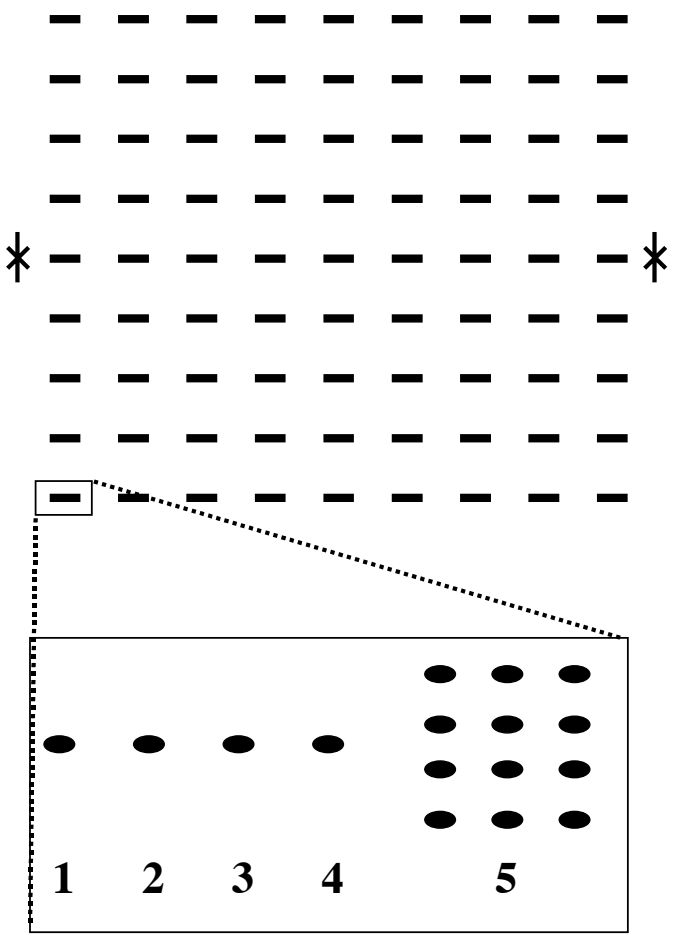


Figure B.2: Layout of the electron-beam lithography pattern (not to scale) , showing a 9×9 array with two alignment marks on either side of the array. The zoom shows each element of the 9×9 array, which consists of four individual device pillars, and, in the fifth slot, an array of pillars. The pillar array is used for imaging and characterization.

For the e-beam lithography, performed on the VB6 at CNF, I typically make 364 devices per wafer; by "device" I mean a single shape which will eventually define the shape of the pillar in the device. The 364 devices are divided into a 9×9 array of four devices each (Figure B.2). The elements of the 9×9 array are separated by 5 mm, while the four subelements are arranged on a line spaced 0.5 mm apart. There is a fifth slot for each array element, on which a subarray of pillars are exposed; this subarray will be used to characterize the pillars during the procedure. On symmetric sides of the 9×9 array large alignment marks are placed; these are typically put 2.3 mm to the left of the fifth element of the first column and 2.3 mm to the right of the fifth element of the ninth column, as shown in Figure B.2. The numbers I use here are entirely customizeable; they are chosen simply to align with the photolithography masks I use later to define the leads to the devices. Centering the pattern is not crucial, although it makes alignment easier if the array is parallel to the bottom flat of the wafer.

Of course, I should emphasize at this point that getting the desired shape out of the VB6 is something of a black art; the optimal pattern and dose for a particular desired shape will vary over time. Therefore it is imperative that a dose test be performed prior to exposing a device wafer, in order to determine the appropriate parameters. Also note that the ion mill, which creates the pillars, will not leave the pillars with perfectly vertical walls; thus the pillars will be larger than the exposed pattern. How much larger depends on the mill depth and angle of milling, but this could add as many as 10-20 nm to the pillar size.

After exposure, develop in 1:3 MIBK:IPA for 60 seconds, rinse in isopropyl alcohol (IPA), and blow dry. Descum the wafer by running a short, low-power oxygen plasma using either the Applied Materials or the PT72 reactive ion etchers (RIE).

Typically I use the PT72, running process #1 (resist strip) for 6 seconds. This tends to improve the liftoff characteristics.

Now is the time to deposit the mill mask. The purpose of the mask is to protect the region under the mask during the ion mill, so that it will leave that area as a freestanding pillar. The mill mask material type and thickness should be chosen so that it is entirely milled away at the same time that the pillar is fully milled. To do this, one needs to know the mill rates for each material used in the device. The mill rate depends on the beam current of the ion mill, the angle of incidence between the beam and the substrate, as well as the manner in which the material was originally deposited (i.e., sputtering vs. thermal evaporation). Table B.1 displays mill rates I have found for thermally-evaporated materials, using a beam current on the VEECO ion mill of 50 mA, perpendicular beam incidence, and an Argon ion pressure of 1.2×10^{-4} Torr. All values are to within $\pm 10\%$. Using these numbers, if, for example, the plan is to mill down through 20 nm of Au, 3 nm of Co, and 6 nm of Cu, then the total time that the mill mask must survive is the following:

$$\text{Total Time} = \frac{20\ nm}{0.92\ nm/sec} + \frac{3}{0.31\ nm/sec} + \frac{6}{.84\ nm/sec} = 38.6 \text{ sec.} \qquad \text{(B.1)}$$

Appropriate mill masks would then be, for example, $38.6 * .92 = 35.5$ nm Au, or $38.6 * .11 = 4.2$ nm Cr. I typically use Au as a mill mask, as it will not provide significant oxidation problems if I do not manage to completely eliminate it during the mill.

Once this calculation is completed, deposit the mill mask using thermal evaporation, as this method provides the smallest features for a liftoff process. After deposition, place the wafer in acetone and let sit for a minimum of 8 hours. If the liftoff is good there should be metal peeling off of the wafer rather quickly (within 15 minutes or so), but the resist may take considerably longer to dissolve completely.

Table B.1: Ion mill rates for various materials used in nanopillar process, using the CNF VEECO ion mill. The beam current used was 50 mA, the Ar pressure 1.2×10^{-4} Torr, and the beam was oriented at normal incidence.

Material	Mill Rate (nm/sec)
Co	0.31
Au	0.92
Cu	0.84
Cr	0.11
Py	0.38

Agitate the acetone by shaking gently every hour or so. I usually let the wafer sit overnight. If metal is not cleanly coming off by the end of the period, it is possible to sonicate the wafer to finish the job. This is a risky endeavour, and the sonicator should not be run more than a few seconds, or the mill mask may be ripped off. Rinse the wafer with acetone and IPA, and blow dry. The quality of liftoff can be checked by inspecting the wafer under an optical microscope. The pillar patterns will be invisible at this point, but the two alignment marks should be visible optically. It will take some searching to find them, but a careful survey should catch them; they are visible even if they are gold on gold.

Now comes the first of five photolithography steps. The procedure is roughly the same for all five steps, with the fifth differing only in that the lithography is performed on a small chip rather than a full wafer. Each step requires a different mill mask. The pattern on each mask represents the pattern (die) transferred to one element of the 9×9 array. I provide drawings of the patterns for each mask, along with a description of the mask I typically use, in Figure B.3. There is a set of masks in the Ralph group drawers, but I have typically used the set that resides in the Buhrman group drawers; it is to these masks that I specifically refer. For the purposes of this recipe, however, it is really the function of each of these masks and

not their specific patterns that is important, so I will describe them more generally here in the text.

The first mask is designed to protect the contact pads for each lead of each device from the first ion mill (Figure B.3a). As the wafer will eventually be covered in a polyimide insulator roughly 220 nm thick, it is important that the pads through which the outside world contacts the device remain as high above the wafer as possible. In addition, wirebonds can more consistently be formed on the top Au layer than the materials underneath. Therefore the result of this step will leave small squares of photoresist that serve as mill masks for all the contact pads of the device. The appropriate Buhrman group mask is labeled "Protect Au".

Clean the surface of the wafer with acetone and IPA on a photolithography spinner. Spin on 1813 Shipley resist for 30 seconds at 2000 RPM; this should put roughly 2 microns of resist on the wafer. Bake this resist on the 115° C hotplate for 1-2 minutes. Use the 5X stepper for photolithography. A process on the 5X will have to be written that steps the pattern onto each element of the 9×9 array. The alignment marks, located as described earlier, are nonstandard, and their positions relative to the array will have to be entered into the process file. A pre-existing process for the first four photolithography steps exist in my directory (EMDX0), with process name "myers", run name "ed". A typical exposure time is 1 second, and, for the focus, the default number is acceptable. After exposure, develop in 300 MIF for 60 seconds. It is better to err on the side of overdeveloping rather than underdeveloping, as the features are large and their exact size is not important. Rinse in water and blow dry. The pattern can be imaged optically after developing, to check on shape and consistency.

Next is a standard descum, which removes the residue from photoresist and

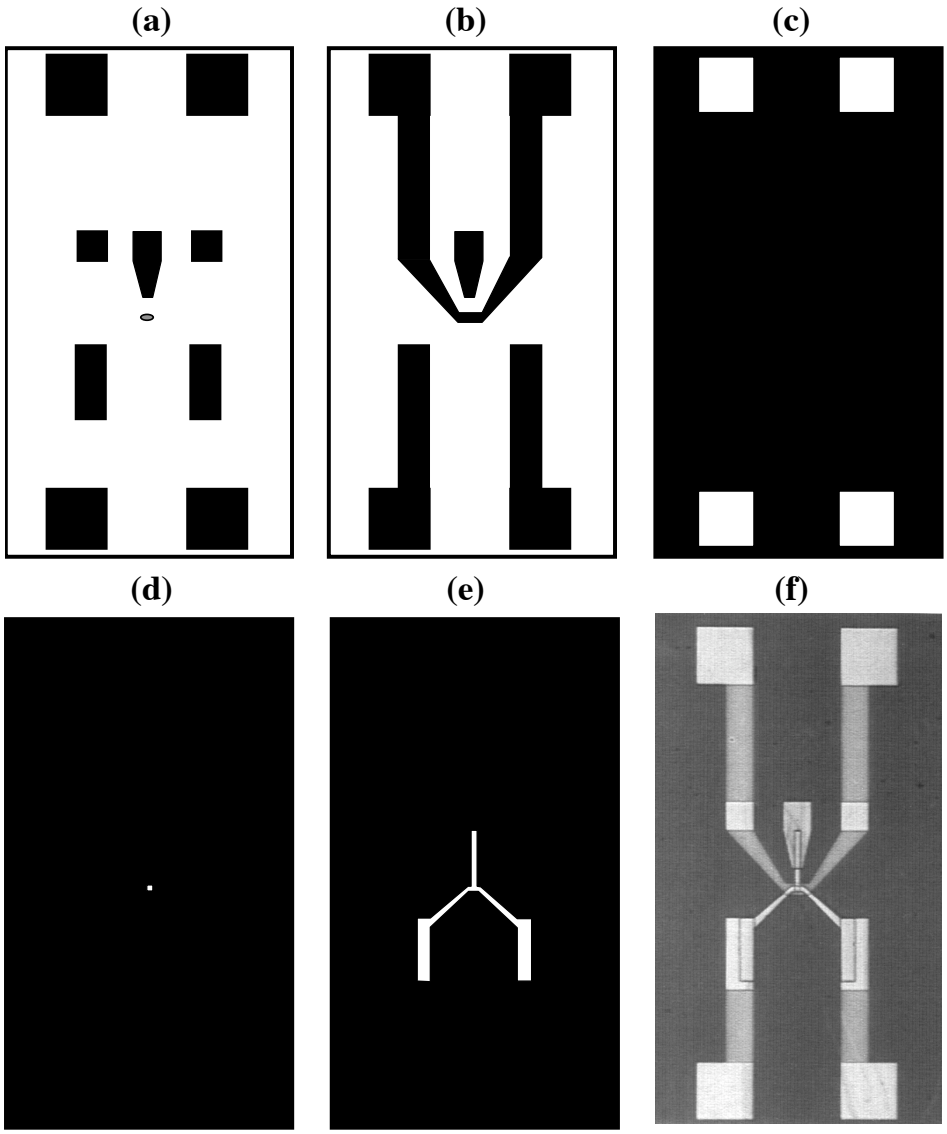


Figure B.3: Schematic of the five photolithography masks used during the nanopillar process, for a single device. For each mask, the black color is the patterned photoresist left on the wafer after development. The grey oval in the first image shows the location of the pillar. (a) The first mask defines the contact pads for the four leads. (b) The second mask defines the bottom leads and a portion of the top leads. In addition, a test mesa and alignment marks (neither shown) are defined at this step. (c) After the polyimide is spun, the third mask is leaves only the contact pads exposed so that they can be cleared of polyimide. This mask also leaves a window on the test mesa exposed so that the polyimide thickness can be measured. (d) The fourth masks opens up a small window above the pillar, through which a precision etch exposes the top of the pillar for the top electrode. (e) The fifth and final mask defines the top electrode. (f) Optical image of a completed nanopillar device.

developer in the cleared areas. I have usually used the Applied Materials etcher for this. Preclean the chamber with oxygen first, as is standard. For the descum, standard parameters are 12 seconds at 30 Watts, 40 mTorr of oxygen at 30 standard cubic centimeters per minute (SCCM).

Following this is the first ion mill step, using the VEECO ion mill. From the earlier calculations for the mill mask, the total etch time should be known. The wafer is very quickly heated by the sputtering process of the ion mill, so the full etch time should not be done in one continuous go; otherwise, the photoresist will be burned onto the wafer and impossible to remove, and the mill rates will increase from heating. I typically follow a duty cycle of 20 seconds with the shutter open (beam hitting the wafer), and 40 seconds with the shutter closed. Use the Dow Corning grease provided to heat sink the wafer to the chuck. As mentioned earlier, use 50 mA of beam current an Argon ion pressure of 1.2×10^{-4} Torr, and perpendicular beam incidence to achieve the previously-cited mill rates. I usually wait until the ion mill pressure dips below 1×10^{-5} torr before letting the Ar gas in. Keep the wafer rotating during the mill, so that the mill is even across the wafer. The pillar formed at the end of this step is schematically shown in Figure B.1d.

Soak the wafer in acetone for several hours. Often I let it sit overnight. Even after extended soaking, the photoresist rather stubbornly stays onto the wafer, so a short sonication is usually necessary. In some cases it is impossible to remove all of the resist from the wafer. This is a very annoying consequence of the ion mill, and if a more reliable method for removing the resist without risking damage to the pillars can be found, more power to the reader.

Next is the second photolithography step. This step defines the bottom leads and eliminates electrical contact between the pillars (Figure B.3b). In addition, an

additional shape called a test mesa is formed next to the fifth slot in each array element, where the pillar array resides. The thickness of the polyimide is measured on this mesa in a later step. The purpose of the test mesa is essentially to mimic the environment around the pillars so that a more accurate determination of the polyimide thickness can be made without having to measure the locations around the pillars directly. The second photolithography step also defines alignment marks for each element of the 9×9 array; these alignment marks will make it possible to perform the final aligned photolithography step on individual elements of the 9×9 array. The alignment marks are placed ± 2.3 mm horizontally from the center of each element of the 9×9 array. The appropriate Buhrman group mask for this step is labeled "Layer 1".

The procedures for photolithography and a subsequent descum are the same as those for photolithography step #1. After this is a second ion mill, which transfers the photolith pattern to the metal layers. The goal as described here is to mill through the rest of the layers down to the insulating substrate; the total time needed to accomplish this can be calculated the same way as in the earlier ion mill step. Remove the photoresist as before–it will be just as difficult to get off as the first time.

This is a convenient point to stop and characterize the pillars via imaging tools. This can just as easily be done after the first ion mill, but it is easier to locate the pillars for imaging after the second mill step. Image the subarrays in the fifth slot of each element of the 9×9 array and not the device pillars themselves, as imaging the pillars (particularly with the SEM) risks damage to them. Use an AFM to determine the height of the pillars. This gives information as to the degree of success of the first ion mill (the number measured should be close to the calculated

number), and also is important for the final precision polyimide etch. SEM imaging gives information about the shape of the pillar; its cross-sectional area and aspect ratio are important numbers to know when trying to make quantitative comparisons to spin-transfer theory. AFM and SEM also show how uniform the pillar fabrication process is; the imaged arrays should be fairly regular in shape and height if the previous steps have gone well. Image several arrays at different points on a single wafer, to check uniformity across the wafer. See Figs. 2.2 and 2.3 of Chapter 2 for characteristic AFM and SEM images of array pillars.

At this point the pillar, the bottom leads, and part of the top leads have been fabricated. It is now time to prepare for the very last step, which is to deposit the rest of the top leads and complete the device. In order to make sure the top and bottom leads only contact each other through the pillar, however, an insulator has to first be deposited which physically separates the area of overlap of the two leads. The insulator I use is polyimide, which is a polymer that is kept in solvent and can be spun on a wafer like photoresist or PMMA. There are a large varieties of polyimides available; the kind I use (Duramide 285, 2:1 in solvent) requires preapplication of an adhesion promoter, which essentially "primes" the surface of the wafer so that the polyimide will stick better. The adhesion promoter used is labeled QZ3289. This is diluted with another chemical labeled QZ3290, which, despite the arcane name, is nothing more than 5 parts (volume) of DI water mixed with 95 parts of IPA. The chemicals should be mixed in a ratio of 1 part QZ3289 to 9 parts QZ3290; they need to be combined fresh just prior to spinning. The proportions can be determined roughly by using an eyedropper. Try to mix as small an amount as possible, as very little is required per wafer.

Mount the wafer on a chuck in the e-beam resist room at CNF and clean the

surface with acetone and IPA. Before applying the adhesion promoter, make sure the polyimide (Duramide 285 2:1) is within reach, as it will need to be deposited within seconds of applying the promoter. Spin the diluted adhesion promoter on, at a rate of 3500 RPM and a time of 40 seconds. Within several seconds, spin the polyimide on at a rate of 3000 RPM and 40 seconds. This should generate a thickness of 220-240 nm.

After spinning comes the bake, which is extremely important in determining the final polyimide quality. First rest the wafer onto the 170° C hotplate for several seconds. This drives off the solvent from the polyimide, a process that can be seen visually (it's neat!). The remainder of the baking is done in the 170° C oven in the e-beam resist room. The most important quantity during the bake is the final temperature, but it is also important that the baking be ramped to that final temperature in several steps. A sequence that has worked for me, but is not unique to creating successful polyimide films, is to bake at 150° C, then 170° C, then 220° C, all in 20 minute increments, for a total bake time of 60 minutes. The resulting wafer should have a roughly uniform color, except perhaps at the edges. The color itself is determined by the material underneath. Depending on the shade of the silicon oxide (which is blue), I have seen quality polyimide films that are either green or red. The pillar after polyimide deposition is shown in Figure B.4a.

The third photolithography step follows the polyimide spin. The pattern here covers everything in photoresist except for the contact pads and two small squares above the test mesa (Figure B.3c). These two squares will later be used to measure the polyimide thickness. The Buhrman group mask used here is labeled "Clear Polyimide". Follow the procedures of the previous two photolith steps.

The polyimide can be removed in an oxygen plasma; I typically use the Applied

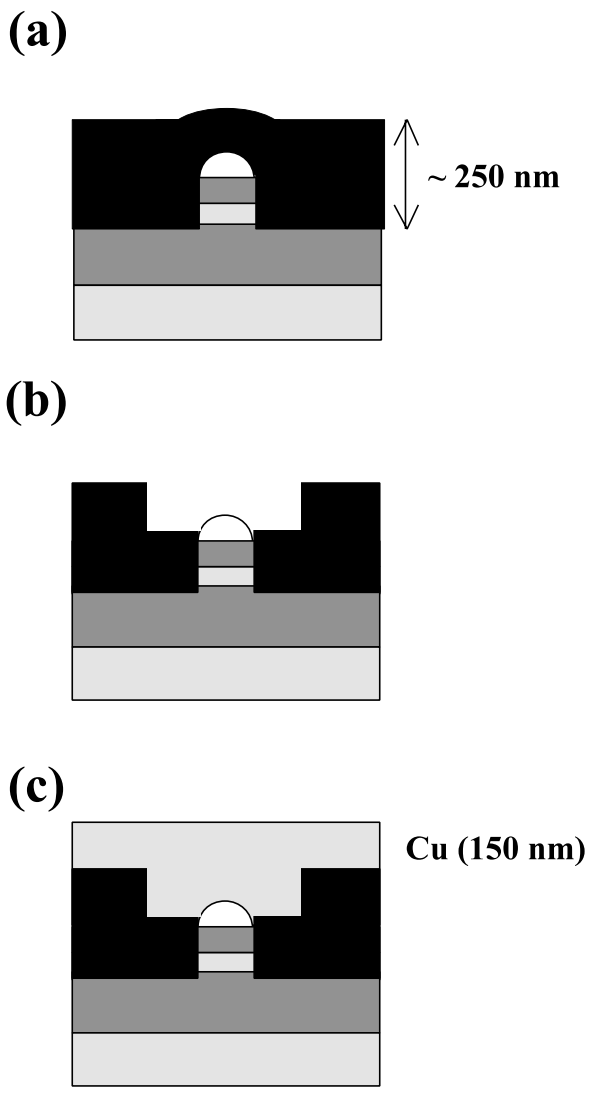


Figure B.4: Schematic of the final steps of the nanopillar process, after the creation of the nanopillar (not to scale). (a) A polyimide insulator is spun on the pillar. (b) Through photolithography and a precision oxygen plasma etch, the top of the pillar is exposed through the insulator. (c) Further photolithography and evaporation/liftoff create the top electrode.

Materials etcher for this. Run a plasma using 40 mTorr of oxygen at 30 SCCM, and a power of 40 watts, for 240 seconds. This will clear the contact pads of the polyimide, and etch squares down to the test mesa. Image the contact pads after etching; they should be gold-colored. If not, etch a little longer.

After removing the photoresist with acetone and IPA (it will be blissfully easy to do so), measure the depth of the polyimide holes on the test mesas. This can be done with a standard profilometer (there are ones in CNF and in TOL at Clark Hall), or with an AFM. Measure at various points on the wafer; the polyimide thickness is typically uniform to within 10-20 nm.

Next comes the fourth photolithography step. This exposes a small window above each device pillar (Figure B.3d). The Buhrman group mask for this step is called "#4". The procedure is identical to the three previous photolith steps.

Following this is the precision etch, which exposes the top of the pillar through the polyimide. An ideal etch will remove enough polyimide so that only the top Au cap is exposed, with the rest safely covered by the polyimide (Figure B.4b). To do this, the height of the pillar, the thickness of the polyimide, and the etch rate must all be known. Even if these numbers are known well, however, there can still be variations due to the deformation in the polyimide caused by the pillar (Figure B.4a). Therefore, a range of etch times need to be tried, to ensure that at least some devices are optimally etched. Use a scriber to cut the wafer into 9 squares, each consisting of a 3×3 array. Label each by scribing a number on them, noting from what region of the wafer they were cut, in case the pillar height or polyimide thickness varies across the wafer. The etching is performed in the Applied Materials etcher, using an oxygen plasma at 40 mTorr, 30 SCCM, and 30 Watts. The default polyimide etch rate with these parameters is 1.2 nm/sec, but this number can vary

by as much as $\pm 20\%$.

This is a tricky and not-always-successful procedure, but I have had some luck by performing the etching steps as follows: Start with one square from the wafer, which will be sacrificed to determine the etch rate. Using the measured pillar height, the measured polyimide thickness, and the default etch rate, calculate the time needed to etch so that the Au cap is roughly halfway exposed. Etch the wafer using a time 10-20 seconds *shorter* than this value; this is done to ensure that the polyimide is not completely removed, in case the actual etch rate is much larger than the default etch rate. Afterwards, immediately measure the etch depth (after removing the photoresist, of course) on the profilometer or AFM, and from this calculate the actual etch rate. Then go back and, using this etch rate, etch several more squares, varying the etch time on each by 5-10 seconds. In general it is desireable to have the average of the etch times slightly smaller (5-10 seconds) than optimal, since the device will be etched a second time after the fifth photolithography step during the descum. The optimal etch time may be different between different squares due to variations in polyimide thickness or pillar height.

Next is the fifth and final photolithography step, which creates a pattern for the top leads above the pillars (Figure B.3e). The Buhrman group mask for this is labeled "Top Lead". This step is different from the previous four photolithography steps in that individual 3×3 squares will be used, rather than the full wafer. There are small spinner chucks designed for chips of this size, so the resist can be spun in the normal way. Center the square on the chuck of the 5X stepper. I have used a process for 3×3 arrays that is in my 5X directory called "mf", with run name "ed". This process aligns using the two alignment marks on the center element of the 3×3 array. They must be located optically. To ensure that I am above the

correct alignment mark, I move the stage until I am along an edge of the square, so that I can count along until I am at the center element. Alignment can be a painstaking process, and will involve many small adjustments of the square by hand so that it is level. Expose and develop in the usual way.

Peform a descum using the same parameters as before. An unknown portion of this descum time etches the polyimide as well, which is why it is safer to underetch by a few seconds during the precision etch. After this, I usually perform a short ion mill in the VEECO to remove the top layers of the Au cap. An *in situ* ion mill can also be performed on the CHA evaporator in the Buhrman group immediately prior to deposition of the top lead. I have not tried this approach with great success, but it appears to make a marked improvement in the contact resistances of the devices made in Buhrman group. I typically run the VEECO at 50 mA for 5 seconds–this should remove roughly 4-5 nm of the Au cap.

Deposit the top Cu lead, about 150 nm of material (Figure B.4c). Place the squares in acetone and soak for 30-60 minutes. The Cu should peel off cleanly; if there are scratch marks in the photoresist, it may become stuck in places. A finished device is depicted in Figure B.3f. Enjoy!

Bibliography

[1] F. J. Albert, Dissertation, Cornell University, Ithaca, NY (2002).